

Dissertation zur Erlangung des Doktorgrades
der Fakultät für Chemie und Pharmazie
der Ludwig-Maximilians-Universität München

Synthesis and Characterization of Novel Perovskite Materials for Solar Cell Applications

Andreas Christian Herbert Binek

aus

Schwabmünchen, Deutschland

2016

Erklärung

Diese Dissertation wurde im Sinne von § 7 der Promotionsordnung vom 01. April 2014 von Herrn Prof. Dr. Thomas Bein betreut.

Eidesstattliche Versicherung

Diese Dissertation wurde eigenständig und ohne unerlaubte Hilfe bearbeitet.

München, 15.02.2017

Andreas Binek

Dissertation eingereicht am 29.12.2016

1. Gutachter: Prof. Dr. Thomas Bein

2. Gutachter: Prof. Dr. Achim Hartschuh

Mündliche Prüfung am 10.02.2017

Danksagung

Ich möchte mich zuerst einmal bei meinem Doktorvater Prof. Dr. Thomas Bein für die Aufnahme in seine Gruppe zur Doktorarbeit bedanken. Er gab mir eine Chance, in der physikalischen Chemie Fuß zu fassen, obwohl ich mein Studium eher in der anorganischen Chemie verbracht habe. Jedoch ermutigte er mich stets, mein angesammeltes Wissen in mein neues Forschungsgebiet mit einzubringen, um somit die Brücke zwischen physikalischer und anorganischer Chemie zu schließen.

Des Weiteren danke ich Prof. Dr. Achim Hartschuh, der sich bereit erklärt hat, meine Doktorarbeit als zweiter Gutachter zu bewerten. Die Zusammenarbeit mit dem AK Hartschuh war stets sehr produktiv und ermöglichte mir, mit Hilfe von modernen Messmethoden viel über Ladungstransport in Solarzellen zu lernen.

Ein großer Dank geht auch an Dr. Pablo Docampo, der mir immer mit Rat und Tat zur Seite stand und sich auch mehrfach Zeit nahm, mir physikalische Zusammenhänge zu erklären. Ohne seine Hilfe wären einige Projekte in eine Sackgasse gelaufen und wären nicht veröffentlicht worden. Seine konstante Ermutigung weiterzumachen, obwohl man „gescooped“ wurde, oder neue Dinge in Angriff zu nehmen (ich sage nur SolarSim) hat dazu geführt, dass ich mich konstant weiterentwickeln konnte während der Doktorarbeit.

Doch nicht nur Pablo war stets an meiner Seite in Sachen Wissenschaft, sondern die ganze Photovoltaik Subgroup. Vielen Dank an Fabi, Enrico, Meltem, Hongi, Nadja, Michiel, Tina, Philipp und Charles. Besonders danke ich aber Fabi, der mir damals einen reibungslosen Eintritt in die Perowskit Gruppe ermöglichte, mir die Basics beibrachte und von Anfang an mir mit Rat und Tat zur Seite stand. Ich weiß nicht, wie oft ich „Fabi, kann ich dich kurz was fragen?“ gesagt habe. Auch Michiel und Hongi möchte ich noch extra für den Besuch von unvergesslichen Konferenzen danken, ich glaube besser als wir kann man eine Konferenz/Urlaub nicht gestalten.

In diesem Zusammenhang möchte ich auch meinen Kollaborationspartnern und Praktikanten danken. Vor allem Matze, Irene und Kathi vom AK Hartschuh, die stets ein offenes Ohr für meine Anliegen hatten und auch jederzeit für einen unwissenschaftlichen Plausch zur Verfügung standen. Vielen Dank an meine Praktikanten Vincent, Niklas und Helen, ohne euch wäre so manches Projekt nicht möglich gewesen.

Preface

Eine Doktorarbeit besteht allerdings nicht nur aus Experimenten, sondern auch aus sehr viel Papierkram. Daher möchte ich Regina und Tina meinen tiefsten Dank aussprechen, die mir bei jeglichen Anliegen geholfen haben - sei es das Ausfüllen von Reisegenehmigungen, das Bestellen von teuren Geräten oder labortechnischen Problemen. Auch Mona möchte ich danken, die mir gerade anfangs eine super Mentorin war und mir gezeigt hat, wie man sich im AK Bein zurechtfindet.

Für die Erholung zwischendurch an anstrengenden Tagen sorgten stets meine Büronachbarn. Danke Erika, Laura, Askhat, Alex, Christian, Cindy, Andi, Noggi, Stefan, Tina und Michiel. Gerade die Zeit mit Andi, Noggi, Stefan und Tina habe ich sehr genossen, es geht doch nichts über blöde Sprüche den ganzen Tag und konstanten Besuch von allen anderen AK Bein Mitgliedern.

Für das Leben neben der Arbeit sorgten meine Freunde aus Nah und Fern. Vielen Dank an die „Geilmenschen“ (Aga, Chrissy, Derya, Domi, Hanne, Jana, Kathi, Kathrin, Meike, Nino, Saskia und Tina), „Die Besten“ (Andi, Börni, Claudi, Dennis, Karli, Saskia, Stefan, Steffi und Stephi) und dem „PIC Schafkopf Team“ (Matze, Philipp, Stefan, Tobi und Ursi). Ihr habt mir stets die nötige Entspannung gegeben, die man braucht, um eine erfolgreiche Doktorarbeit zu schreiben. Auch dem Georg möchte ich danken für seine verrückten Trainingseinheiten, die allerdings immer gut waren, um den Kopf frei zu kriegen.

Ein großer Dank geht an meine Eltern Marianne Binek und Herbert Binek, die mich vor und während meines Studiums und während meiner Doktorarbeit auf jede erdenkliche Weise unterstützt, immer an mich geglaubt und mich ermutigt haben, den großen Schritt ins Studium zu wagen. Meinen Geschwistern Doris und Daniela danke ich auch aus tiefstem Herzen für das stets offene Ohr und das rege Interesse an meiner Forschung. Auch meiner Nichte Franziska danke ich für die vielen schönen Stunden, die ich mit ihr beim Spielen haben durfte (Los Amadeus!).

Mein ganz spezieller Dank gilt Jana für viel Verständnis, Geduld und Zuspruch während meiner Doktorarbeit. Ich konnte mich immer auf dich verlassen und ohne dich hätte ich vermutlich nie meine Doktorarbeit angefangen.

Meiner Mutter

in Liebe und Dankbarkeit

Abstract

The global energy demand is rising due to the rapidly growing world population as well as the inherent necessity of energy for fueling economic progress. Consequently, the human energy economy is facing great challenges in the near future. The challenge is that the power industry of nearly all countries is based on the use of fossil fuels in the form of coal, oil and natural gas. These resources have in common that their availability on our planet is limited and the byproducts formed in the conversion processes are harmful for the environment. Therefore, renewable resources like wind, water or solar energy are needed. In particular, sunlight is an ideal candidate for energy production because of the high incident solar flux, which by far exceeds the actual annual worldwide demand. One possibility to use this energy is the use of crystalline silicon in solar cells, which offers power conversion efficiencies of up to around 25%. However, the production of such solar cells is rather cost and energy intensive. For these reasons, new photovoltaic technologies based on simple preparation procedures as well as the use of cheap and abundant materials are required.

Hybrid metal halide perovskite based solar cells have recently emerged as a serious competitor for large scale and low-cost photovoltaic technologies. State-of-the-art solar cells based on methylammonium lead iodide (MAPbI_3) now reach efficiencies of over 20%.

This thesis addresses the challenges of stability, reproducibility and impact on the environment of these new materials. One important parameter in commercially available solar cells is the reproducibility of the synthesis protocol. In the case of MAPbI_3 , chloride based precursors are known to have a positive influence on the crystallization and the final performance of the perovskite. Thereby, MAPbCl_3 crystallizes directly after the deposition of the starting solution and acts as a template for the formation of MAPbI_3 . Together with controlled and slow crystallization conditions, reproducible, high efficiency solar cells can be produced. Formamidinium lead iodide (FAPbI_3) has the potential to achieve even higher

efficiencies than MAPbI₃, while being more stable at ambient conditions. Stability is another key parameter for the commercial application since solar cells are exposed to fluctuating weather conditions and strong temperature variations. The major drawback for pure FAPbI₃ is that it can crystallize at room temperature as a wide bandgap material with hexagonal symmetry instead of the desired trigonal black phase. With a mixture of methylammonium (MA) and formamidinium (FA) the phase transition of FAPbI₃ can be completely suppressed, while maintaining the superior properties of the material. Not only single junction perovskite based solar cells are potentially industrially relevant. Medium-bandgap perovskite absorber materials, such as MAPbBr₃ or FAPbBr₃, can be used in tandem solar cells or as building-integrated photovoltaic systems. Both compounds can be incorporated in planar heterojunction solar cells exhibiting power conversion efficiencies approaching 7%.

Another big concern in terms of commercial applications is the use of toxic lead in these devices. One potential alternative for lead is bismuth, but because of the oxidation state of 3⁺ these compounds exhibit different structures, with strong absorbance in the red region. However, the inorganic (Cs₃Bi₂I₉) or hybrid (HDABiI₅) compounds are still solution-processable and show photovoltaic efficiencies of 1%. However, the perovskite structure can also be achieved with bismuth by incorporating an element with oxidation state 1⁺. These materials exhibit photoluminescence in the same wavelength range as the lead perovskites. Another way to reduce exposure of the environment to lead is a sustainable procedure for handling the cells after their operational lifetime. Thereby, the toxic lead can be isolated in high yield and the received PbI₂ can be reused for the preparation of new solar cells with comparable performance. Additionally, the most expensive part of the solar cell, the conductive glass (FTO), can also be reused several times without any reduction in the performance.

Table of contents

1	Introduction	15
1.1	Global Energy Demand	15
1.2	Operation Principle of Photovoltaic Systems	16
1.3	Hybrid Perovskite Solar Cells – How to Make Them Industrially Relevant?	22
1.4	Literature	38
2	Characterization	43
2.1	X-Ray Diffraction	43
2.2	Scanning Electron Microscopy (SEM)	44
2.3	UV-Vis Absorption Spectroscopy	46
2.4	Steady State Photoluminescence (ssPL)	48
2.5	Time Correlated Single Photon Counting (TCSPC)	49
2.6	Current-Voltage Measurements	51
2.7	Time of Flight Measurements (ToF)	53
2.8	Inductively Coupled Plasma Optical Emission Spectroscopy (ICP-OES)	55
2.9	Design of a Solar Simulator for the Glovebox	56
2.10	Literature	59
3	Control of perovskite crystal growth by methylammonium lead chloride templating	61
3.1	Introduction	61
3.2	Results and Discussion	62
3.3	Conclusion	74
3.4	Experimental Section	74
3.5	Literature	78
4	Stabilization of the Trigonal High Temperature Phase of Formamidinium Lead Iodide	81
4.1	Introduction	81
4.2	Results and Discussion	83
4.3	Conclusion	92
4.4	Experimental Section	92

4.5	Literature	97
5	Efficient Planar Heterojunction Perovskite Solar Cells Based on Formamidinium Lead Bromide	99
5.1	Introduction	99
5.2	Results and Discussion	100
5.3	Conclusion	113
5.4	Experimental Section	114
5.5	Literature	118
6	Synthesis of Perfectly Oriented and Micrometer-Sized MAPbBr₃ Perovskite Crystals for Thin Film Photovoltaic Applications	121
6.1	Introduction	121
6.2	Results and Discussion	123
6.3	Conclusion	137
6.4	Experimental Section	138
6.5	Literature	141
7	Recycling perovskite solar cells to avoid lead waste	143
7.1	Introduction	143
7.2	Cost Estimation of Perovskite based Solar Cell	144
7.3	Results and Discussion	147
7.4	Conclusion	163
7.5	Experimental Section	163
7.6	Literature	168
8	Antimony and Bismuth Based Materials as Lead-Free Light Absorber	171
8.1	Introduction	171
8.2	Results and Discussion	172
8.3	Conclusion	186
8.4	Experimental Section	188
8.5	Literature	194
9	Conclusions	197
10	Curriculum Vitae	201

11	Publications and Presentations	205
11.1	Journals	205
11.2	Journal Cover	206
11.3	Oral presentations	206
11.4	Poster presentations	208

1 Introduction

1.1 Global Energy Demand

The global energy consumption has rapidly increased during the last half century and is expected to grow even further in the future. The increase in the past was stimulated by “cheap” fossil fuels and the industrialization mostly in North America, Europe and Japan. Furthermore, the contribution of China and India to the global energy consumption raised a lot due to their constantly increasing population, which nowadays stands for a third of the world’s population.^[1] However, most parts of the western world managed to keep their energy consumption constant or even reduce it in the 21st century. Nevertheless, the total energy demand is still growing due to the increased needs in Asia as shown in Figure 1-1a.

These high amounts of energy can not only be harvested from fossil fuels (oil, natural gas and coal) as they will run out sooner or later.^[2] Therefore, new forms of renewable energy have to be developed, not only to cover the energy demand but also to reduce the emission of greenhouse gases in the atmosphere.^[3]

Approximately about 3.5×10^{24} J of solar energy reaches the Earth’s surface every year. In contrast, the yearly consumption of energy in 2015 was 13,423 Mtoe, which corresponds to 5.62×10^{20} J.^[4] The unit toe (tonne of oil equivalent) is defined as the amount of energy released by burning one tonne of crude oil. Wind and solar power are the most commonly used renewable energies, at the moment. Figure 1-1b illustrates the increase of the produced energy from wind and solar energy in this century. Especially, the amount of renewable energy constantly increases in Europa, Pacific and Africa.

1.2 Operation Principle of Photovoltaic Systems

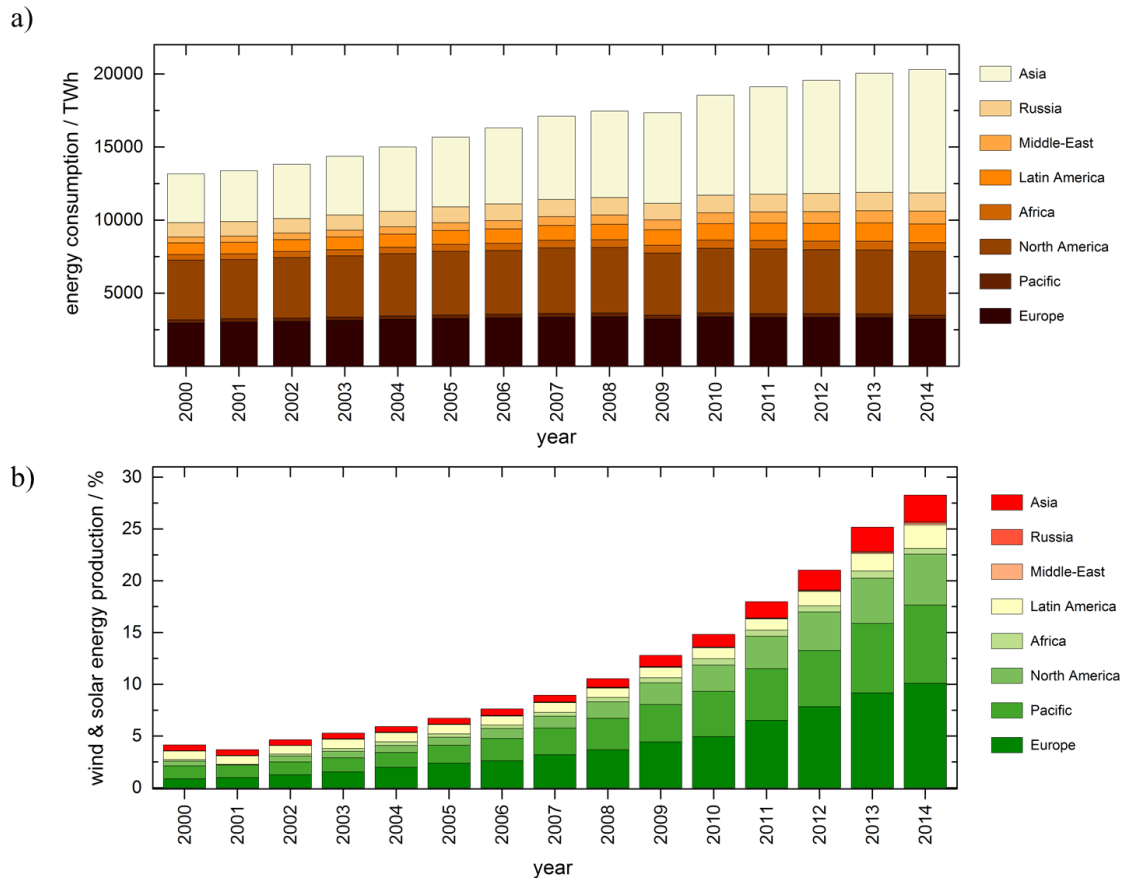


Figure 1-1: Energy consumption from the year 2000 till 2014 and the percentage of the produced energy by wind and solar energy.^[5]

In order to benefit from this solar energy not only existing photovoltaic technologies have to be steadily updated but also new compounds and their application in solar cells have to be investigated. In particular, compounds with cheap, abundant starting materials should be in the main focus of research, as well as easy fabrication routes for applications all over the world.

1.2 Operation Principle of Photovoltaic Systems

The absorption of energy from the sun within a solar material results from an electronic transition from a filled to an empty state, but is limited by an energy threshold below which no photons are absorbed. Such materials are called semiconductors and the threshold is the

bandgap, which corresponds to the minimal photon energy that can be absorbed. This photon energy suffices to promote an electron from the valance band (VB) to the conduction band (CB).^[6] The lack of an electron in the VB is called a hole and can be treated as a quasi-particle. Both electrons and holes can diffuse through the CB and the VB of the material, respectively.^[7]

Figure 1-2a shows the AM1.5 solar spectrum normally reaching photovoltaic systems on the earth with 1.5 atmosphere thickness, which corresponds to a solar zenith angle of $z = 48.2^\circ$. The different radiation areas and the relation between wavelength and intensity are also illustrated. On the one hand, a smaller bandgap material is able to absorb more photons; on the other hand, a wide bandgap will be able to gain more energy from the absorbed photons. Based on the solar spectrum, the highest efficiencies for a single-bandgap system can be achieved for materials with a bandgap between 1.1 and 1.5 eV, which translates to an absorption onset wavelength in the range of 825 – 1125 nm.^[8]

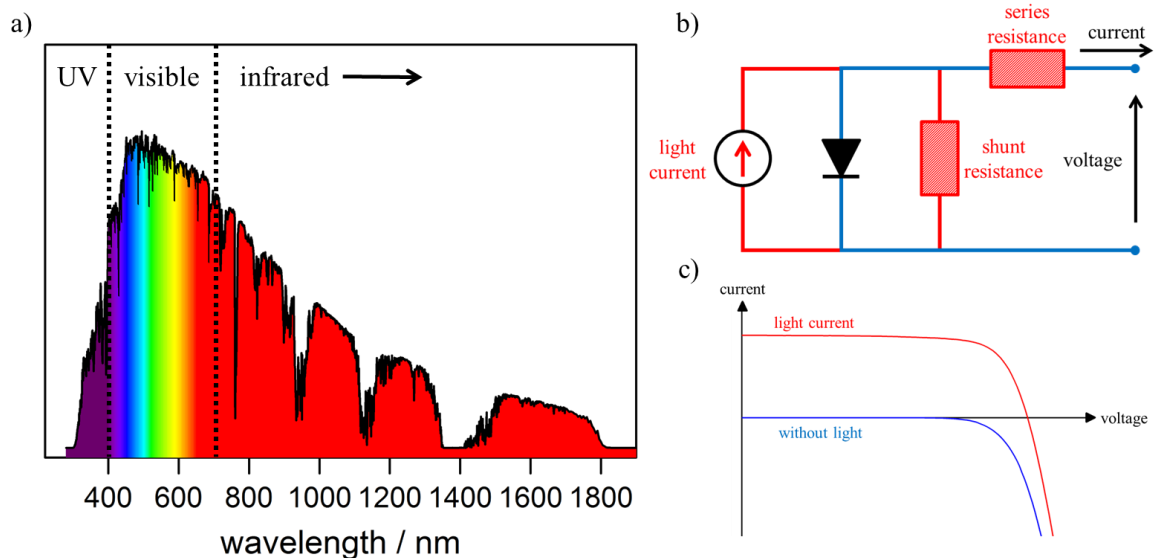


Figure 1-2: Solar spectrum (AM1.5) with the different absorption areas (a), the equivalent circuit diagram of a solar cell (b) and the typical current-voltage curve of a photovoltaic cell (c).

1.2 Operation Principle of Photovoltaic Systems

In the majority of cases, the solar absorber within a photovoltaic device is a semiconductor. If just one kind of semiconductor is used, the most common approach is to make a p-n junction with it. A p-n junction is a boundary between two types of semiconductors, namely p-type (excess of holes) and n-type (excess of electrons). If a p-n-junction is produced of the same material it is called a homojunction. However, it is also possible to make a junction between p- and n-type semiconductors of different materials. These are called heterojunctions.

Ideally, a solar cell can be modeled as a simple electrical circuit with a current source (light-generated current) in parallel with a diode, as depicted in Figure 1-2b. If no light is present to generate the current, the cell will behave like a normal diode, where the current will increase exponentially under forward bias condition and very little current will flow in the reverse bias direction (Figure 1-2c). In case of an illuminated device the current will increase and the current-voltage (J - V) curve will be moved up along the y-axis. However, during operation the efficiency of a solar cell is reduced because of internal resistances. The series resistance (R_S) and shunt resistance (R_{SH}) of a solar cell are shown above in Figure 1-2b. Regarding an ideal cell, R_{SH} would be infinite and would not provide an alternative path for the current, while R_S would be zero. In reality the shape of the J - V curve largely depends upon both resistances and is reflected by the fill factor (FF) and the maximum power point (P_{MAX}) of the solar cell, which will be explained in more detail in the characterization chapter. Thereby, R_{SH} can reduce the open circuit voltage (V_{OC}), while an increasing R_S can cause a drop of FF . The values of both resistances can be estimated by the slopes at V_{OC} and J_{SC} .

1.2.1 First-Generation Technologies

First-generation photovoltaic technologies are primarily crystalline silicon (c-Si), where the material is doped with boron or phosphorus so that one side is p-type with holes as the

dominant electronic species and the other side is n-type with electrons as dominant species. By combining both materials, the electrons from the n-doped side tend to travel to the positively charged p-doped side. In the center of the cell, the electrons and the holes recombine and create a so-called depletion region where no mobile charges are present. As a consequence of this effect, an in-built electric field is generated by the charge difference of the n-doped side (positive side) and the p-doped side (negative side). At this point, there are no mobile charges left in the junction region.^[3] When the cell is illuminated electrons are excited to the conduction band (CB), generating holes in the valence band (VB). Through the internal electric field, the carriers are separated and can be extracted by an external circuit. The Shockley–Queisser limit predicts a maximum theoretical power conversion efficiency of ~30%^[9] under direct AM1.5 sunlight for single-junction devices; with silicon the actual efficiencies are moving close to the theoretical limit.^[10]

1.2.2 Second-Generation Technologies

Initially, one drawback of c-Si based solar cells were the high manufacturing costs. Therefore, considerable efforts were made to develop “second-generation” technologies for photovoltaic applications with reduced production costs. Absorber materials used for the second-generation photovoltaics are cadmium telluride (CdTe), copper indium gallium selenide (CIGS) and amorphous Si (a-Si). These devices are fabricated by using low-cost large-area deposition techniques, such as sputtering, physical vapor deposition and chemical vapor deposition.

Prior to the development of CdTe and CIGS technologies, a-Si based solar cells were commercially successful because of their relatively low production cost and their ability to be integrated into electronics and building materials. An amorphous material has no long-range crystalline order, which in the case of Si results in a “quasi-direct” bandgap and a higher

1.2 Operation Principle of Photovoltaic Systems

optical absorption coefficient. As a result, thinner absorbing layers, which require less material, are needed than for c-Si. The growth technique for a-Si can be adjusted by an additional temperature step to form nanocrystalline or microcrystalline Si, either with or without an accompanying amorphous matrix. As the grain size increases, the film starts to convert in the direction of the characteristics of polycrystalline Si (indirect bandgap, lower optical absorption). CdTe and CIGS solar cells on the other hand are heterojunction devices between a thin n-type cadmium sulfide (CdS) layer and p-type CdTe or CIGS absorber layer. Figure 1-3 shows SEM cross-sections of both device structures.

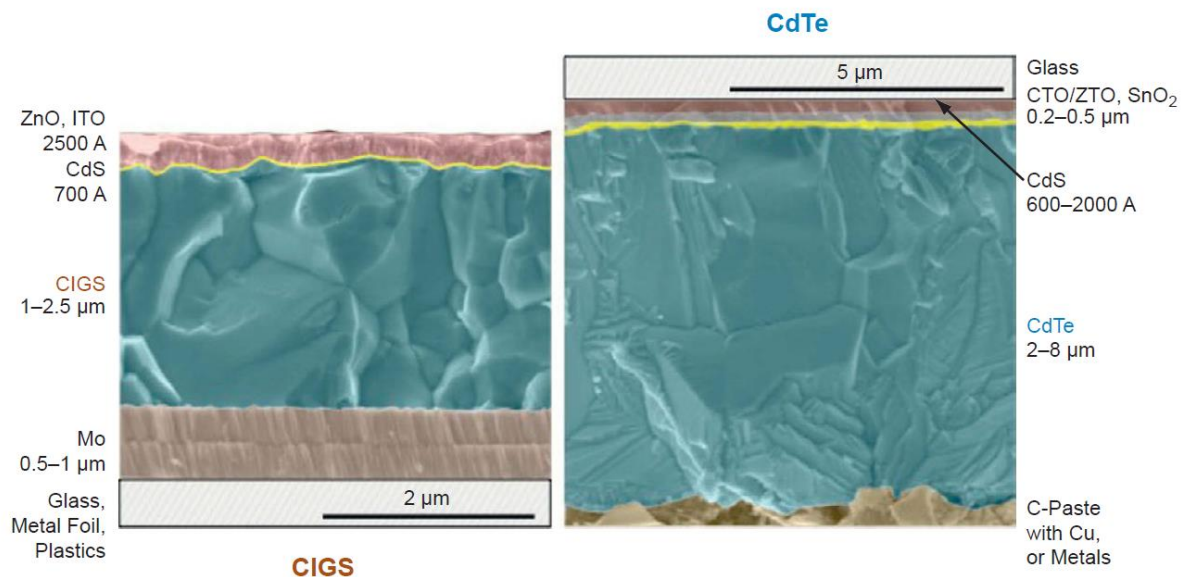


Figure 1-3: SEM cross-sections of a CIGS solar cell (left) and a CdTe solar cell (right).^[3]

The challenges of these systems are the interactions between the different layers and the sensitivity against moisture. Nevertheless, it is possible to get the efficiencies of CdTe cells a bit over 22%^[11] with the aid of the right glass/glass encapsulation, whereas CIGS cells reach efficiencies of up to 22%.^[12]

1.2.3 Organic Photovoltaics (OPV)

OPV is a technology with the chance to produce solar cells at low production costs and without the need for vacuum deposition techniques.^[13] The major difference to the other solar technologies, mentioned above, is the combination of polymers, small molecules and/or inorganic (nano)structures to build an excitonic solar cell. A typical layout of a bulk heterojunction organic solar cell is illustrated in Figure 1-4a, whereby the active area is composed of an organic donor (small-molecules or polymers), which acts as an absorber layer, and an electron acceptor (fullerene or quantum dots). These layers are sandwiched between a metal contact and a hole-transport layer/transparent contact.

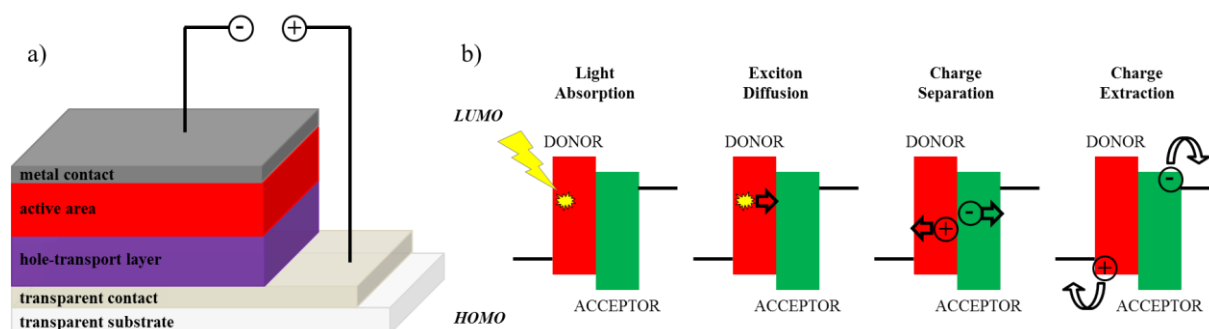


Figure 1-4: Schematic layout (a) and the working principle (b) of a bulk heterojunction organic solar cell.

When illuminated, a photon is absorbed resulting in the excitation of an electron from the HOMO to the LUMO and thereby forming an exciton (bound electron-hole-pair). Subsequently, the excitation diffuses to the interface between donor (Figure 1-4b, red) and acceptor (Figure 1-4b, green) where charge transfer takes place, resulting in a coulombically bound electron-hole pair. Subsequently, the carriers move energetically “downhill” collecting holes and electrons at the electrodes. The hole-transport layer carries holes much easier than electrons and lowers the recombination prior to the extraction of the carriers.

1.3 Hybrid Perovskite Solar Cells – How to Make Them Industrially Relevant?

Although the efficiencies do not match those of crystalline Si-cells, advantages of this technology compared to silicon are the very high optical absorption coefficients, where only thin films are needed, the compatibility with flexible substrates and the possible production in high-throughput and low-temperature roll-to-roll processes. Additionally, OPV has the possibility to be integrated into existing structures, e.g. window units or other commercial PV products as it has the ability to change the device color and the shape of the pattern.

1.3 Hybrid Perovskite Solar Cells – How to Make Them Industrially Relevant?

A new and revolutionary candidate has emerged in the third generation of solar technologies a few years ago with the introduction of organic-inorganic hybrid perovskites based on the general composition ABX_3 , where A represents an organic cation (such as methylammonium or formamidinium), B a divalent heavy metal (Pb^{2+} or Sn^{2+}) and X a halide anion (Cl^- , Br^- , I^-). Especially, methylammonium lead iodide ($MAPbI_3$) has become the focus of research all over the world, because of its simple solution-based synthesis which can be done at room temperature^[14], its high absorption coefficient^[15], the long lifetime of the photogenerated species^[16] and the tunability of its bandgap.^[17] In this structure the lead ions are octahedrally coordinated by 6 iodide ions. Through shared iodide ions the PbI_6 octahedra are connected in all three dimensions, resulting in cavities where the methylammonium ions are located.^[18] The structure of $MAPbI_3$ is depicted in Figure 1-5a.

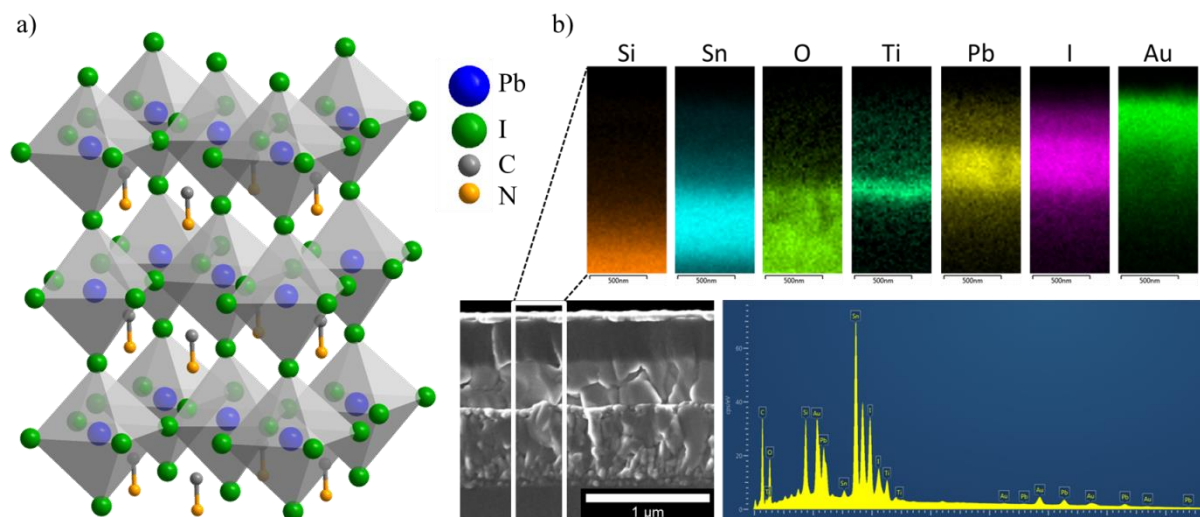


Figure 1-5: Crystal structure of methylammonium lead iodide (a) and an SEM cross-section with EDX-mapping of the typical solar cell layout (b).

To be able to use the above described material in solar cells, it is incorporated in a heterojunction layout. The most common device architecture is glass / FTO / TiO₂ / perovskite / spiro-OMeTAD / Au as illustrated in the SEM cross-section image together with the EDX-mapping (Figure 1-5b). Thereby, titanium dioxide (TiO₂) acts as electron extraction layer and spiro-OMeTAD (2,2',7,7'-tetrakis-(*N,N*-di-4-methoxyphenylamino)-9,9'-spirobifluorene) as hole-transporting layer.^[19] In this layout, the photogenerated electrons can be extracted through the TiO₂, while the holes are transferred by the spiro-OMeTAD to an external circuit.

The hybrid organic-inorganic perovskite exhibits characteristics approaching the quality of commercially available systems, such as GaAs and Si. Since 2009 the power conversion efficiency of MAPbI₃ based solar cells increased from 3.8% to over 20%.^[20, 21] However, before this technology can proceed to industrial production, several challenges have to be addressed. Thereby, the most important challenges to overcome are the sensitivity of the perovskite towards moisture^[22, 23] and the crystal phase transition in the operation regime of solar cells.^[24, 25] Additionally, poor reproducibility of the film formation, resulting in a spread

1.3 Hybrid Perovskite Solar Cells – How to Make Them Industrially Relevant?

in performance, the toxicity and the related bad reputation of lead, as well as the material cost of the hole transporter and top electrode are also important aspects that have to be considered to make perovskite solar cells industrially relevant. In the following chapters recent results in these areas regarding the above-mentioned aspects will be reviewed to illustrate the viability of perovskite optoelectronics.

1.3.1 Stability

A major challenge regarding perovskite PV research is the degradation of the perovskite material, which can be observed when solar cells are exposed to thermal stress, light, oxygen and moisture.^[26, 27] The demand for commercial applications of solar cells is a 10,000 h degradation test, during which the device has to show a constant power output.^[28] Recent studies show that perovskite solar cells are stable up to 1,000 h in accelerated degradation tests,^[29] dropping only to approximately 80% of the initial performance. With the objective of reaching high standards in the commercial sector, the degradation behavior of MAPbI₃ has to be further improved. Thereby, it is crucial to understand the degradation pathways, i.e., the humidity-induced degradation as well as the decomposition of the structure under the influence of heat and light, to be able to improve the stability of the system.

The presence of water causes the decomposition of MAPbI₃ into aqueous hydroiodic acid (HI), solid lead iodide (PbI₂) and methylammonium (MA⁺) either released as gas (as amine) or dissolved in water.^[30] This irreversible process occurs with films exposed to warm humid air with water vapor content over 50% at room temperature and leads to a permanent loss in device efficiencies.^[17] However, when the films are exposed to cool humid air without water condensation on the surface, water is slowly incorporated into the crystal structure accompanied by a separation of the PbI₆ octahedra.^[22] In Figure 1-6 the scheme of the slow

hydration reaction as well as the XRD measurements of the reversible and irreversible hydration of MAPbI₃ films are illustrated.

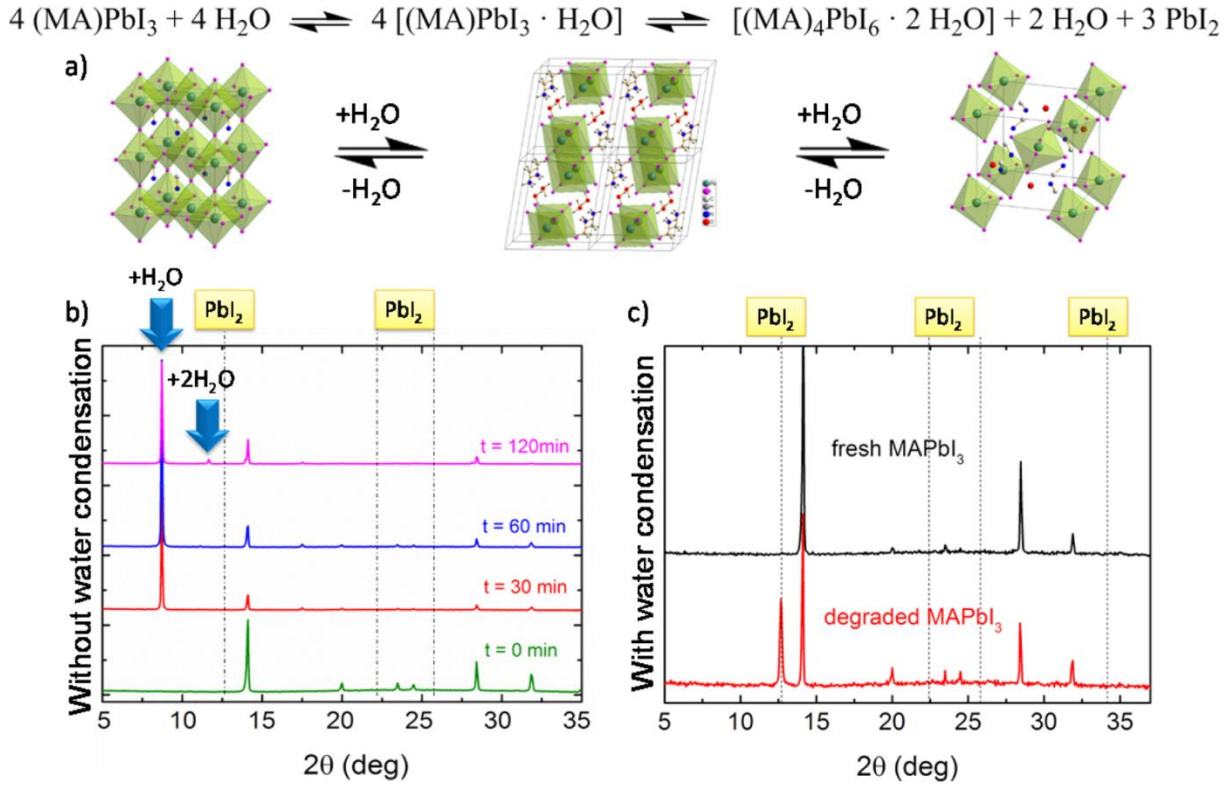


Figure 1-6: Hydration reaction scheme with the corresponding crystal structures (a). XRD patterns of MAPbI₃ thin films exposed to moisture with cold air flow (b) and exposed to moist warm air for 20 min (c).^[28]

The slow hydration reaction of MAPbI₃ is a two-step process, where the 3D arrangement of the PbI₆ octahedra is first saturated with one water molecule per formula unit. Subsequently, a new structure is formed by the inclusion of another water molecule upon longer exposure to humidity. The change in the PbI₆ configuration can be depicted as a transition from a 3D network of octahedra for MAPbI₃ into 1D double-chains of monohydrated MAPbI₃, which finally results in a 0D framework of isolated octahedra of MAPbI₃ dihydrate. In this regard, the monohydrate is an intermediate product that can be easily converted back to MAPbI₃ as shown in the chemical equation of the hydration process.^[31] If the reaction is driven further to the right, the formation of the dihydrate will be initiated, accompanied by the formation of

1.3 Hybrid Perovskite Solar Cells – How to Make Them Industrially Relevant?

PbI₂ and the release of two water molecules. Then, the released water molecules can be reused to convert the remaining MAPbI₃ crystals into the monohydrated MAPbI₃. The complete conversion of a film occurs in the presence of an excess of water, which can dissolve the MA and remove it from the device, resulting in an irreversible hydration process. Nevertheless, the monohydrate-to-dihydrate conversion is reversible but also limited by the phase separation of the reaction products.^[22] If the hydrated MAPbI₃ crystals are exposed to air with low humidity (35% RH) for longer times, the dehydration will be revealed by a color change from yellow to the dark grey of crystalline MAPbI₃.

A number of approaches have been explored to reduce the moisture-sensitivity, including the use of mixed-halide perovskites,^[17] the formation of crystal crosslinking,^[32] the adoption of protective transporting layers or electrodes^[33, 34] and the use of new deposition techniques. Furthermore, protective hole-transporting materials (HTMs)^[33] or hydrophobic materials^[35] have been used to improve the moisture stability of the device.

Not only moisture, but also environmental conditions such as temperature or pressure can lead to structural changes in the commonly employed hybrid perovskite based solar cells. The stability of ABX₃ perovskites can be estimated from the tolerance factor (t) proposed by Goldschmidt (1927).^[36] This value depends on the ionic radii of the ions (A, B and X) and is defined as:

$$t = \frac{r_A + r_X}{\sqrt{2}(r_B + r_X)} \quad (1)$$

Empirically, for the most stable perovskite, t corresponds to values between 0.8 and 1 and an increase in t generally leads to an increase in symmetry.^[37] A tolerance factor between 0.71 – 0.9 results in a distorted perovskite structure with tilted octahedra, while higher (>1) or lower (<0.71) values lead to non-perovskite structures.^[36] Usually, more than one structure is

found for a perovskite material with a given chemical composition, depending on the temperature and preparation methods.^[38] The crystal structure of the commonly employed MAPbI₃ shows tilted octahedra along the *c*-axis and a tetragonal symmetry, for example. With increasing temperature the octahedra start reorganizing into a cubic symmetry. This phase transition occurs between 54 and 57 °C, which corresponds to common solar cell operating temperatures during summer.^[25] MAPbI₃ has a very low thermal conductivity such that the light-deposited heat inside the perovskite cannot be distributed quickly within the film.^[39] The symmetry variation, caused by octahedra tilting, and the heat affect the electronic and optical properties of the perovskite and therefore influence the photovoltaic performance of devices.^[40] Additionally, cycling between two crystal structures during day and night cycles could lead to material fatigue and shorter device lifetimes.

Currently, the best perovskite structure with no phase transition at solar cell operating temperatures is formamidinium lead iodide (FAPbI₃). This compound has a band gap of 1.53 eV for the trigonal α -phase,^[24] which is near the optimum for single junction solar cells, and a phase transition at 125 °C.^[18] The crystal structures and phase transitions of MAPbI₃ und FAPbI₃ are shown in Figure 1-7.

1.3 Hybrid Perovskite Solar Cells – How to Make Them Industrially Relevant?

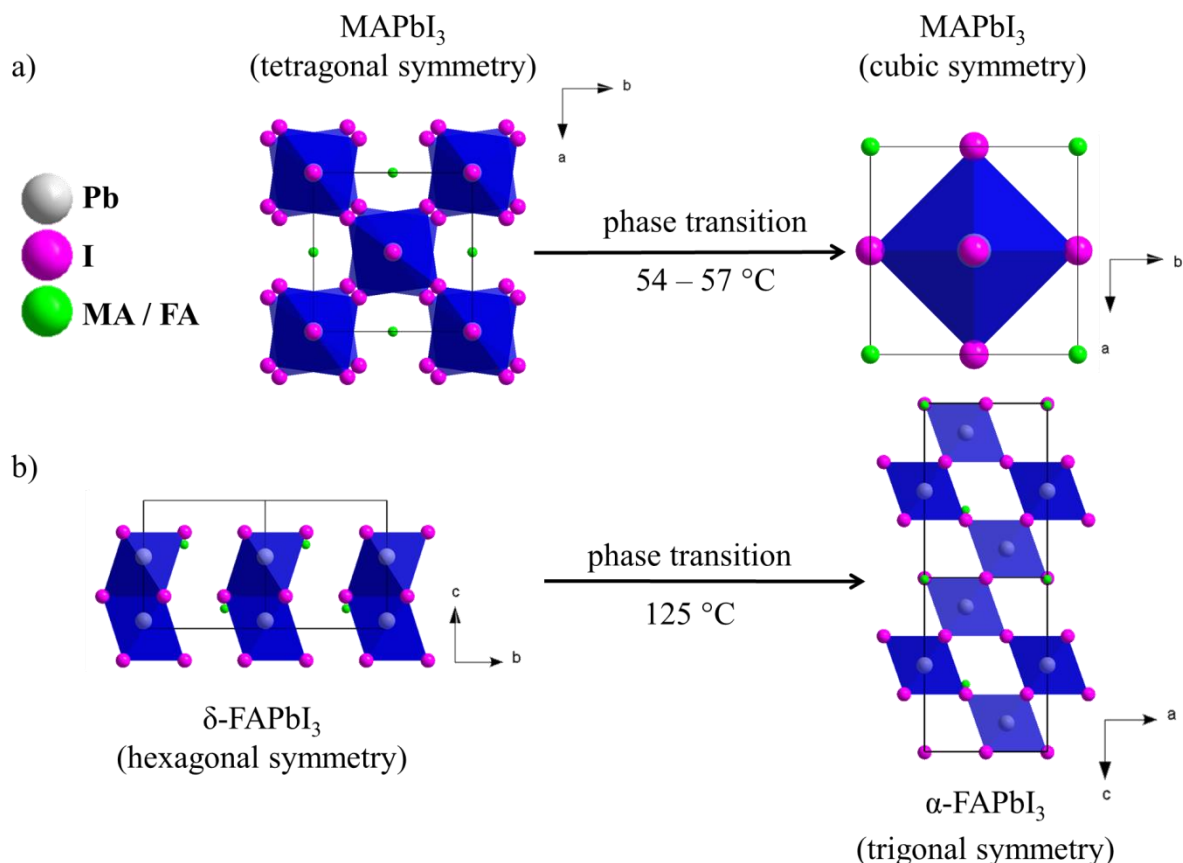


Figure 1-7: Phase transitions with the respective crystal structures of MAPbI₃ (a) and FAPbI₃ (b).

One drawback of FAPbI₃ is the thermodynamically more stable δ -phase, which crystallizes in a hexagonal symmetry where the lead halide octahedra are connected by a shared plane creating a 2D structure. This configuration results in disrupted charge transport and a wide band gap of 2.2 eV. Depending on the synthesis protocol FAPbI₃-type materials can be crystallized directly in the α -phase. One way to crystallize the α -phase is a replacement of approximately 15% of the FA cations with MA. Thereby, the phase transition from trigonal to hexagonal symmetry is completely suppressed between RT and 220 °C and the resulting material exhibits the same lattice parameters, photoluminescence emission peak and band gap as neat FAPbI₃.^[24] This stabilization can be explained by the incorporation of MA and by the accompanied increase in the overall hydrogen bonding strength between iodide and the organic cation and the increase in Madelung energy or the combination of the two. State-of-

the-art solar cells based on this approach now reach power conversion efficiencies above 20%.^[21] Another approach to retard the thermal degradation of perovskite based solar cells is the replacement of the organic hole transport material with polymer-functionalized single-walled carbon nanotubes (SWNTs) embedded in an insulating polymer matrix.^[41]

1.3.2 Toxicity

Currently, one of the major issues still to be solved regarding perovskite based solar cells is the heavy metal lead (Pb) in the absorber layer, which is well-known for its significant hazard to the environment and human health.^[42, 43] In particular, water-soluble salts are very harmful, as they can be easily absorbed by living organisms, where a small daily dose of 1 mg will result in chronic lead poisoning symptoms in humans, such as birth defects.^[44-46] For this reason, the lead content of gasoline, paints and ceramic products, sealing and water pipe solder has been limited. Furthermore, its concentrations have been dramatically reduced in recent years. The maximum accepted levels of lead in drinking water and air are restricted to 15 and 0.15 $\mu\text{g/L}$, respectively, by the US Environmental Protection Agency (EPA).^[47] Lead exists in the 2^+ oxidation state in perovskite solar cells, which makes it soluble in water and thus a hazard to human health in case the cells are employed in large scale applications.

Like most toxic heavy metals, lead interferes with a variety of biological processes and can harm many organs and tissues, including the heart, the intestine, bones, kidneys and the reproductive and nervous systems. The human brain is the organ most sensitive to lead exposure.^[48] Because of the interactions with the nervous system, lead poisoning is particularly toxic to children, causing potentially permanent learning and behavior disorders.^[48] The Centers for Disease Control (US) has set standards regarding the elevated blood lead level for adults to 10 $\mu\text{g/dl}$ and for children to 5 $\mu\text{g/dl}$.^[49] Major treatments include

1.3 Hybrid Perovskite Solar Cells – How to Make Them Industrially Relevant?

the removal of the source of lead and a chelation therapy, where the lead is bound by agents that can be extracted afterwards.^[50]

Looking at the periodic table, the most viable replacements for Pb would seem to be tin (Sn) and germanium (Ge), which are also members of the group 14. The issue regarding elements in this group is the decreasing stability of the 2^+ oxidation state when moving up in the periodic table. For example, Sn-based perovskite materials have shown good mobilities in transistors^[51] and can become metallic.^[52] Noel and co-workers prepared a Sn-based perovskite for the application in solar cells.^[53] With a synthesis procedure like the one for the Pb perovskite, namely dissolving SnI_2 and MAI in dimethylformamide (DMF), they spin-coated films on different substrates to determine the properties of the material. Methylammonium tin iodide (MASnI_3) crystallizes in a tetragonal symmetry with a lattice parameter similar to MAPbI_3 . The structure is shown in Figure 1-8a.

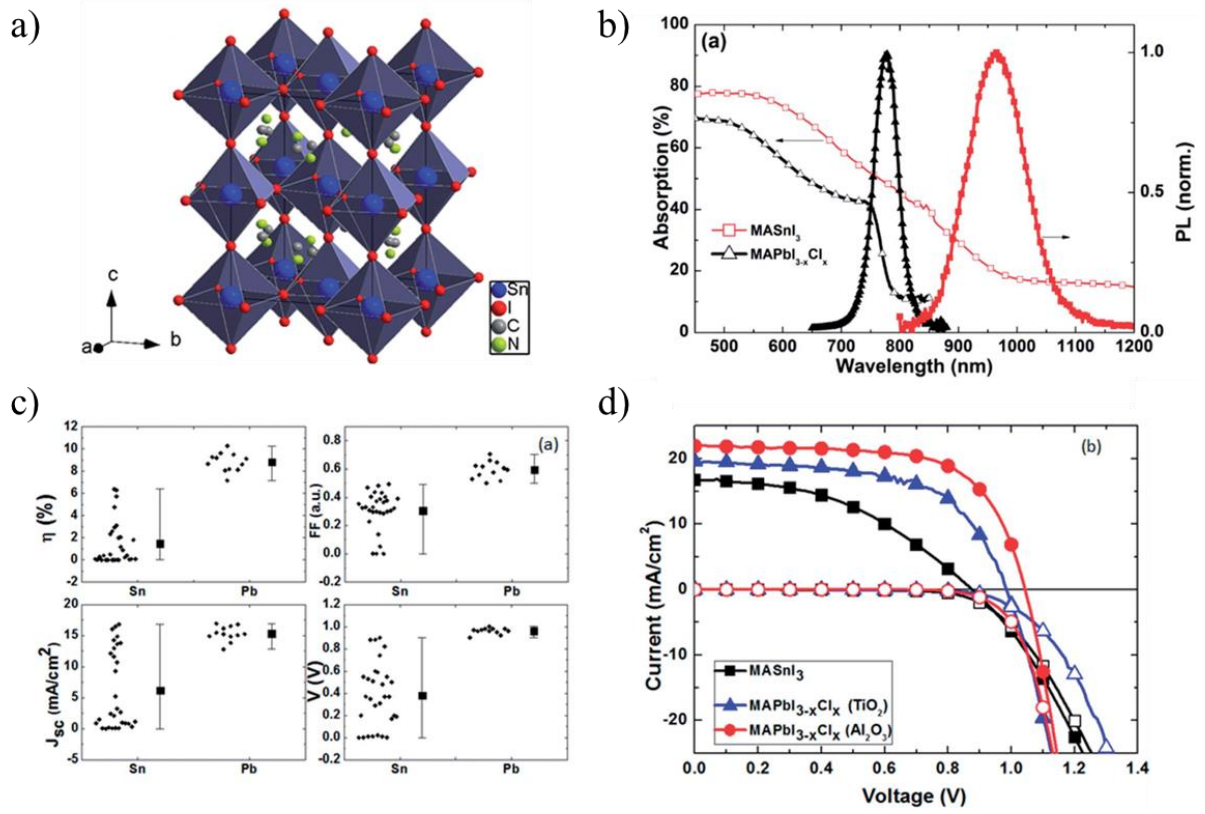


Figure 1-8: Crystal structure (a), normalized steady state photoluminescence (b), device performance parameters (c) and current-voltage characteristics (d) of MASnI₃.^[53]

The absorption spectrum (Figure 1-8b) shows a broad absorption starting at 1000 nm and a broad photoluminescence (PL) peak at 980 nm. In comparison, the lead perovskite shows a sharper absorption edge and a narrower emission spectrum. Photo-thermal deflection spectroscopy (PDS) of MASnI₃ revealed a bandgap of 1.23 eV.^[53] Besides these properties Noel *et al.*^[53] observed a rapid degradation of the material under ambient conditions. The instability is likely to result from the inherent instability of Sn²⁺ ions in the presence of oxygen and moisture. Nevertheless, they incorporated MASnI₃ into a solar stack (FTO / compact TiO₂ / mesoporous TiO₂ / MASnI₃ / spiro-OMeTAD / Au) and together with encapsulation under inert atmosphere, a power efficiency of 6.4% under 1 sun illumination was reported (Figure 1-8d).

1.3 Hybrid Perovskite Solar Cells – How to Make Them Industrially Relevant?

The stability of MASnI_3 still remains a challenge. The necessary next step will be the stabilization of this material to suppress the oxidation of the Sn within the crystal. If this problem can be solved, it will be possible to exploit the full potential of Sn-based perovskites. Potentially the materials can approach the performance of c-Si and GaAs.^[53]

In order to overcome challenges regarding the stability of the oxidation state, first attempts have been made to use elements from group 15 in the periodic table. The general valence shell electronic configuration of these elements is ns^2np^3 . The elements of group 15 generally exhibit 3^- , 3^+ and 5^+ oxidation states. Due to the inert pair effect, the stability of the 5^+ state decreases and that of the 3^+ state increases by moving down the group in the periodic table.^[54] This result suggests a high stability of Bi^{3+} and together with the much lower toxicity compared to lead, bismuth is an interesting alternative candidate in photovoltaics.^[55]

Park *et al.* introduced bismuth-based perovskites for solar cell application with the chemical structure $\text{A}_3\text{Bi}_2\text{I}_9$, where A is a monovalent cation such as cesium (Cs) or MA.^[56] This material consists of bioctahedral $(\text{Bi}_2\text{I}_9)^{3-}$ clusters that are surrounded by the cations. A schematic picture of the structure is shown in Figure 1-9a.

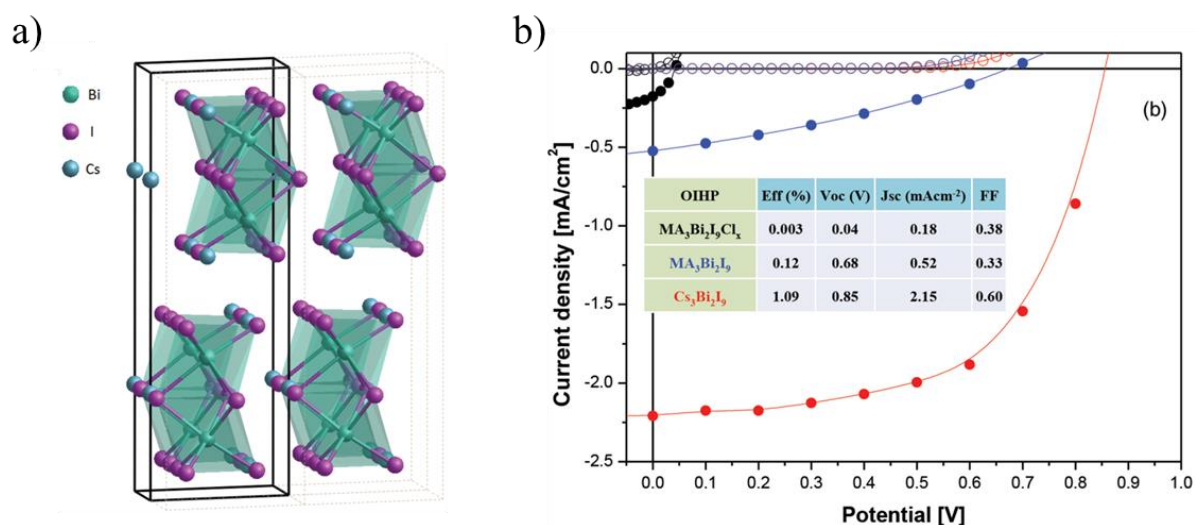


Figure 1-9: Crystal structure of $\text{Cs}_3\text{Bi}_2\text{I}_9$ (a) and the corresponding current-voltage characteristics (b).^[56]

In comparison with MAPbI₃, the bismuth perovskites show lower light absorption for a similar sample thickness and have bandgaps of around 2.1 eV.^[56] For Cs₃Bi₂I₉ a broad PL peak is observed at around 650 nm, which results in a power conversion efficiency of 1.09% in the following solar cell stack: FTO / compact TiO₂ / mesoporous TiO₂ / Cs₃Bi₂I₉ / spiro-OMeTAD / Ag (Figure 1-9b). The MA₂Bi₂I₉ perovskite, with the same solar cell layout, only shows an efficiency of 0.12%.^[56] One big challenge with these materials lies in the film formation, which leads to rather rough surfaces with pinholes in the layer. Although the photovoltaic performances are poor compared to MAPbI₃ and MASnI₃, these perovskites exhibit high stability and the solar cells show no decay of performance after one month.^[56] As a denser homogeneous layer of these materials will probably result in more efficient devices, bismuth perovskites do show promise for applications in solar cells.

Next to using lead-free alternatives, another approach to prevent the release of lead into the environment is the recycling of solar cell devices based on MAPbI₃. This opens up new vistas for the commercialization of perovskite-based devices, as solar cells are not allowed to be depolluted at the end of their working lifetime according to international electronic waste disposal regulations^[57, 58]. By recycling the hazardous materials the waste issue can be solved and additionally the synthesis procedure will be economically more attractive.

In the past, different approaches have been published to reduce lead waste in the energy economy, such as the recycling of lead-based batteries^[59] or perovskite-based solar cells.^[60, 61] The recycling procedures of Poll *et al.*^[60] and Chen *et al.*^[59] are shown in Figure 1-10; they are based on dissolving the active areas with subsequent purification. Then the pure PbI₂ can be reused for the preparation of high quality films of MAPbI₃.

1.3 Hybrid Perovskite Solar Cells – How to Make Them Industrially Relevant?

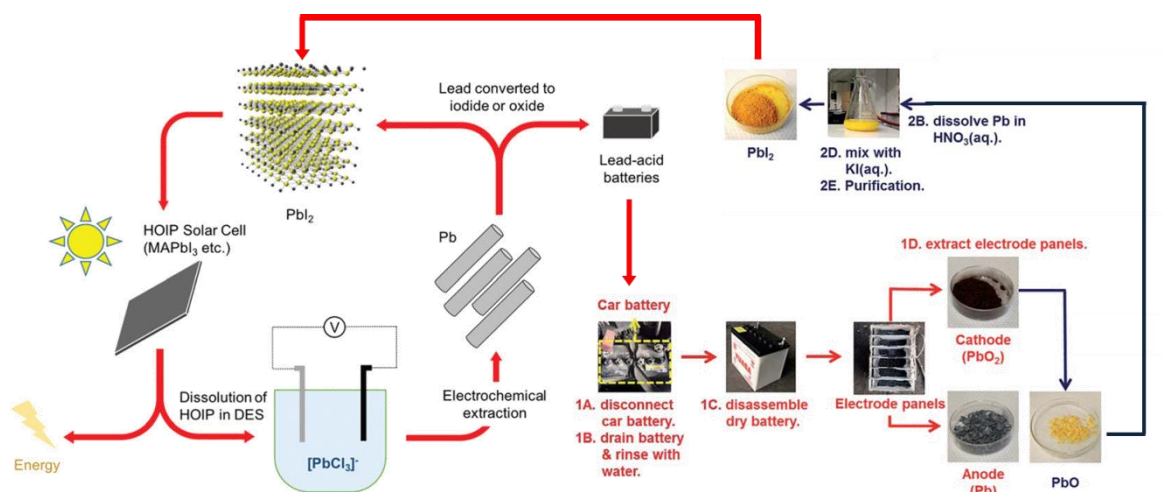


Figure 1-10: The combined recycling procedures of different lead sources for the preparation of perovskite-based solar cells from Poll *et al.*^[60] and Chen *et al.*^[59]

These recycling procedures fulfil requirements regarding the environmental compatibility and the avoidance of expensive high temperature steps, like the traditional lead extraction process.^[62] If deep eutectic solvents (DES) are used for the recycling of lead-based solar cells, a clean, low-cost, electrochemical method will be introduced. In this regard, DESs have shown excellent capability for the dissolution of metal salts^[63] and the subsequent reuse of these materials.^[64] Furthermore, they are considered environmentally friendly.^[65] If it is possible to extend the recycling process to the other layers within a solar cell the cost and environmental impact will be even lower.

1.3.3 Upscaling

Although the reported efficiencies of perovskite-based solar cells (PSC) are comparable to those of silicon solar cells, these cells are mainly prepared by spin-coating on the lab scale. This process is not only difficult to scale up and to apply to flexible and uneven substrates, but it is also a relatively high-cost process because of its inevitable material waste during the spinning process.^[66] Furthermore, it is a non-continuous process, which is inconsistent with low-cost and large scale production.^[67] Although large area MAPbI₃ deposition techniques are

already under investigation, a fully printable module level process still poses a significant challenge.^[68] Like in other photovoltaic systems, the upscaling of device size as well as the use of flexible substrates increases the series resistance and as a result the power conversion efficiencies are lower than on the lab scale.^[69]

A wide range of techniques, such as spray coating,^[70] inkjet printing,^[71] sequential vacuum deposition,^[72] electrodeposition,^[73] slot-die coating,^[74] drop-casting^[75] and slot-die roll-to-roll (R2R) coating,^[76] are being applied to address challenges associated with PSC processing on the large scale. The photovoltaic performances, the active area of the devices as well as the cell configuration of the different preparation techniques are summarized in Table 1-1.

Table 1-1: Photovoltaic performance of perovskite-based photovoltaics concerning large scale.^[77]

cell configuration	PCE (%)	preparation method	active area (mm ²)
ITO / TiO ₂ / MAPbI ₃ / Spiro / Ag	8.1	spray coating	6.5
FTO / TiO ₂ / mp-TiO ₂ / MAPbI ₃ / Spiro / Au	12.3	inkjet printing	4
ITO / PEDOT:PSS / MAPbI ₃ / C ₆₀ / Bphen / Ca / Ag	15.4	seq. vacuum deposition	5
FTO / TiO ₂ / MAPbI ₃ / carbon	10.2	electro-deposition	7.1
	4.5		400
ITO / ZnO / MAPbI ₃ / P3HT / Ag	4.2	slot-die coating	50
FTO / TiO ₂ / mp-TiO ₂ / ZrO ₂ / MAPbI ₃ / Carbon	12.8	drop-casting	7

Among the many options, slot-die R2R coating is the most attractive route for PSC scale-up because the technique is most suitable for high throughput device fabrication.^[69] With this technique, the crystallization kinetics can be tuned via the solution feed, the drum speed and temperature, thus facilitating efficient printing of well-defined stripes for solar modules.

1.3 Hybrid Perovskite Solar Cells – How to Make Them Industrially Relevant?

Furthermore, it is economically viable because of the effective material usage with very little loss during printing.^[68]

Probably the most difficult issue with scalable printing methods is the different drying mechanism compared to the spin coating process. Coating methods form first a wet film, which is dried naturally or afterwards by an air dryer.^[78] During this slow drying period, the solution can lose uniformity and overgrowing crystals can be formed on the substrate.^[74] In order to overcome this problem, an external “quenching” effect is needed to imitate the spin-coating process. Therefore, Hwang *et al.* introduced a second slot-die head into the setup, which was connected to high-pressure nitrogen for rapid drying of the printed film.^[74] The schematic layout of the setup is shown in Figure 1-11a.

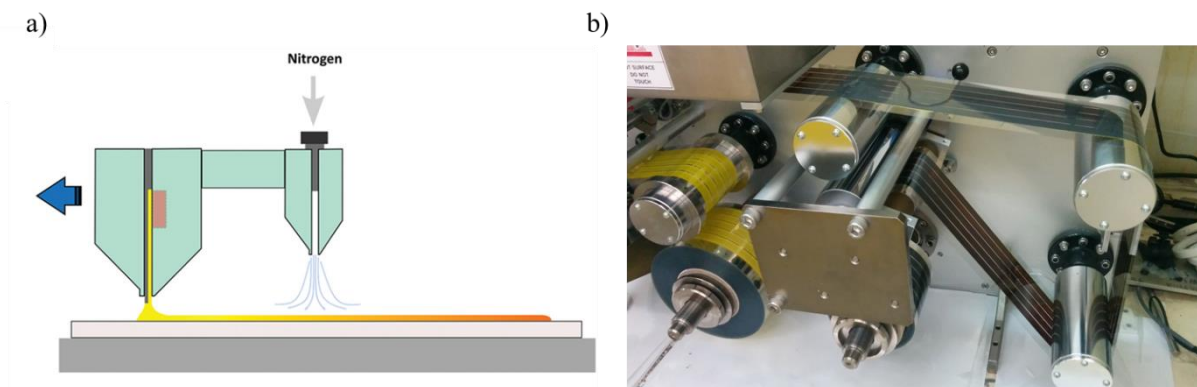


Figure 1-11: Schematic illustration of slot-die coating with a gas-quenching process (a) and the actual roll-to-roll production of perovskite solar cells (b).^[74]

With this method, every layer (except of the metal electrode) of a perovskite-based solar cell with the device layout ITO / ZnO / MAPbI₃ / P3HT / Ag was printed. The perovskite layer was prepared by a slot-die R2R deposition of PbI₂ followed by conversion into the perovskite with MAI, also deposited by a slot-die R2R process. ZnO and doped P3HT charge transporting layers were also successfully fabricated by the slot-die coating. A PV efficiency of around 10 % was obtained for areas up to 10 mm².^[74]

In the near future, techniques like slot-die R2R processing are expected to enable the price point necessary for PSCs to contribute to the photovoltaic markets. This technique is also suitable for other perovskite-based applications, such as tandem devices with silicon or CIGS cells as well as applications in light emitting and detecting technologies.^[74]

1.4 Literature

- [1] D. Y. Goswami, *Principles of Solar Engineering*, CRC Press, Boca Raton **2015**.
- [2] V. Scott, R. S. Haszeldine, S. F. B. Tett, A. Oschlies, *Nature Clim. Change* **2015**, 5, 419.
- [3] D. S. Ginley, D. Cahen, *Fundamentals of Materials for Energy and Environmental Sustainability*, Cambridge University Press, United Kingdom **2012**.
- [4] V. Badescu, *Modeling Solar Radiation at the Earth's Surface: Recent Advances*, Springer Verlag, Berlin **2008**.
- [5] <https://yearbook.enerdata.net/>.
- [6] H. T. Grahn, *Introduction to Semiconductor Physics*, World Scientific, Singapore **1999**.
- [7] P. Würfel, *Physics of Solar Cells: From Basic Principles to Advanced Concepts*, John Wiley & Sons, Weinheim **2009**.
- [8] H. J. Snaith, *Adv. Funct. Mater.* **2010**, 20, 13.
- [9] W. Shockley, H. J. Queisser, *J. Appl. Phys.* **1961**, 32, 510.
- [10] M. A. Green, *Prog. Photovoltaics* **2012**, 20, 472.
- [11] X. Wu, *Sol. Energy* **2004**, 77, 803.
- [12] M. A. Contreras, M. J. Romero, R. Noufi, *Thin Solid Films* **2006**, 511–512, 51.
- [13] S. E. Shaheen, D. S. Ginley, G. E. Jabbour, *MRS Bull.* **2005**, 30, 10.
- [14] J. You, Z. Hong, Y. Yang, Q. Chen, M. Cai, T.-B. Song, C.-C. Chen, S. Lu, Y. Liu, H. Zhou, Y. Yang, *ACS Nano* **2014**, 8, 1674.
- [15] S. De Wolf, J. Holovsky, S.-J. Moon, P. Löper, B. Niesen, M. Ledinsky, F.-J. Haug, J.-H. Yum, C. Ballif, *The Journal of Physical Chemistry Letters* **2014**, 5, 1035.
- [16] S. D. Stranks, G. E. Eperon, G. Grancini, C. Menelaou, M. J. P. Alcocer, T. Leijtens, L. M. Herz, A. Petrozza, H. J. Snaith, *Science* **2013**, 342, 341.
- [17] J. H. Noh, S. H. Im, J. H. Heo, T. N. Mandal, S. I. Seok, *Nano Lett.* **2013**, 13, 1764.
- [18] C. C. Stoumpos, C. D. Malliakas, M. G. Kanatzidis, *Inorg. Chem.* **2013**, 52, 9019.
- [19] M. A. Green, A. Ho-Baillie, H. J. Snaith, *Nat Photon* **2014**, 8, 506.
- [20] A. Kojima, K. Teshima, Y. Shirai, T. Miyasaka, *J. Am. Chem. Soc.* **2009**, 131, 6050.
- [21] N. J. Jeon, J. H. Noh, W. S. Yang, Y. C. Kim, S. Ryu, J. Seo, S. Seok, *Nature* **2015**, 517, 476.

- [22] A. Leguy, Y. Hu, M. Campoy-Quiles, M. I. Alonso, O. J. Weber, P. Azarhoosh, M. van Schilfgaarde, M. T. Weller, T. Bein, J. Nelson, P. Docampo, P. R. F. Barnes, *Chem. Mater.* **2015**, 27, 3397.
- [23] J. A. Christians, P. A. Miranda Herrera, P. V. Kamat, *J. Am. Chem. Soc.* **2015**, 137, 1530.
- [24] A. Binek, F. C. Hanusch, P. Docampo, T. Bein, *The Journal of Physical Chemistry Letters* **2015**, 6, 1249.
- [25] T. Baikie, Y. N. Fang, J. M. Kadro, M. Schreyer, F. X. Wei, S. G. Mhaisalkar, M. Graetzel, T. J. White, *J. Mater. Chem. A* **2013**, 1, 5628.
- [26] T. Leijtens, G. E. Eperon, N. K. Noel, S. N. Habisreutinger, A. Petrozza, H. J. Snaith, *Adv. Energy Mater.* **2015**, 5, 1.
- [27] Y. Rong, L. Liu, A. Mei, X. Li, H. Han, *Adv. Energy Mater.* **2015**, 5, 1.
- [28] P. Docampo, T. Bein, *Acc. Chem. Res.* **2016**, 49, 339.
- [29] A. Mei, X. Li, L. Liu, Z. Ku, T. Liu, Y. Rong, M. Xu, M. Hu, J. Chen, Y. Yang, M. Grätzel, H. Han, *Science* **2014**, 345, 295.
- [30] J. M. Frost, K. T. Butler, F. Brivio, C. H. Hendon, M. van Schilfgaarde, A. Walsh, *Nano Lett.* **2014**, 15, 2584.
- [31] F. Hao, C. C. Stoumpos, R. P. H. Chang, M. G. Kanatzidis, *J. Am. Chem. Soc.* **2014**, 136, 8094.
- [32] S. Luo, W. A. Daoud, *J. Mater. Chem. A* **2015**, 3, 8992.
- [33] J. H. Kim, P.-W. Liang, S. T. Williams, N. Cho, C.-C. Chueh, M. S. Glaz, D. S. Ginger, A. K. Y. Jen, *Adv. Mater.* **2015**, 27, 695.
- [34] Y. S. Kwon, J. Lim, H.-J. Yun, Y.-H. Kim, T. Park, *Energy & Environmental Science* **2014**, 7, 1454.
- [35] Y. Hu, J. Schlipf, M. Wussler, M. L. Petrus, W. Jaegermann, T. Bein, P. Müller-Buschbaum, P. Docampo, *ACS Nano* **2016**, 10, 5999.
- [36] V. M. Goldschmidt, *Naturwissenschaften* **1926**, 14, 477.
- [37] D. B. Mitzi, *Synthesis, Structure, and Properties of Organic-Inorganic Perovskites and Related Materials*, John Wiley & Sons, Canada **2007**.
- [38] Z. Li, M. Yang, J.-S. Park, S.-H. Wei, J. J. Berry, K. Zhu, *Chem. Mater.* **2016**, 28, 284.
- [39] A. Pisoni, J. Jaćimović, O. S. Barišić, M. Spina, R. Gaál, L. Forró, E. Horváth, *The Journal of Physical Chemistry Letters* **2014**, 5, 2488.

1.4 Literature

- [40] A. Amat, E. Mosconi, E. Ronca, C. Quarti, P. Umari, M. K. Nazeeruddin, M. Grätzel, F. De Angelis, *Nano Lett.* **2014**, *14*, 3608.
- [41] S. N. Habisreutinger, T. Leijtens, G. E. Eperon, S. D. Stranks, R. J. Nicholas, H. J. Snaith, *Nano Lett.* **2014**, *14*, 5561.
- [42] L. Patrick, *Altern Med Rev* **2006**, *11*, 2.
- [43] I. R. Benmessaoud, A.-L. Mahul-Mellier, E. Horvath, B. Maco, M. Spina, H. Lashuel, L. Forro, *Toxicol Res* **2015**, *5*, 407.
- [44] R. A. Goyer, T. W. Clarkson, *Toxic Effects of Metals*, Vol. 1236, McGraw-Hill, New York **1996**.
- [45] A. Demayo, M. C. Taylor, K. W. Taylor, P. V. Hodson, P. B. Hammond, *Crit. Rev. Env. Contr.* **1982**, *12*, 257.
- [46] R. A. Goyer, *Environ. Health Perspect.* **1990**, *86*, 177.
- [47] USA Environmental Protection Agency Lead Laws and Regulations, <http://www2.epa.gov/lead/lead-laws-and-regulations> (retrieved on 08/11/2016).
- [48] K. M. Cecil, C. J. Brubaker, C. M. Adler, K. N. Dietrich, M. Altaye, J. C. Egelhoff, S. Wessel, I. Elangovan, R. Hornung, K. Jarvis, B. P. Lanphear, *PLoS Med* **2008**, *5*, 112.
- [49] Advisory Committee On Childhood Lead Poisoning Prevention (ACCLPP), http://www.cdc.gov/nceh/lead/ACCLPP/acclpp_main.htm (retrieved on 08/13/2016).
- [50] K. Kalia, S. J. S. Flora, *Journal of Occupational Health* **2005**, *47*, 1.
- [51] C. Kagan, D. Mitzi, C. Dimitrakopoulos, *Science* **1999**, *286*, 945.
- [52] D. B. Mitzi, C. Feild, Z. Schlesinger, R. Laibowitz, *J. Solid State Chem.* **1995**, *114*, 159.
- [53] N. K. Noel, S. D. Stranks, A. Abate, C. Wehrenfennig, S. Guarnera, A.-A. Haghighirad, A. Sadhanala, G. E. Eperon, S. K. Pathak, M. B. Johnston, A. Petrozza, L. M. Herz, H. J. Snaith, *Energy & Environmental Science* **2014**, *7*, 3061.
- [54] R. S. Drago, *The Journal of Physical Chemistry* **1958**, *62*, 353.
- [55] H. Suzuki, N. Komatsu, T. Ogawa, T. Murafuji, T. Ikegami, Y. Matano, *Organobismuth chemistry*, Elsevier, Netherlands **2001**.
- [56] B.-W. Park, B. Philippe, X. Zhang, H. Rensmo, G. Boschloo, E. M. J. Johansson, *Adv. Mater.* **2015**, *27*, 6806.
- [57] European Parliament, Off. J. Eur. Union, L37 2003, 24.
- [58] European Parliament, Off. J. Eur. Union L197 2012, 38.

- [59] P.-Y. Chen, J. Qi, M. T. Klug, X. Dang, P. T. Hammond, A. Belcher, *Energy & Environmental Science* **2014**, 7, 3659.
- [60] C. G. Poll, G. Nelson, D. M. Pickup, A. V. Chadwick, J. Riley, D. Payne, *Green Chemistry* **2016**, 18, 2946.
- [61] A. Binek, M. L. Petrus, N. Huber, H. Bristow, Y. Hu, T. Bein, P. Docampo, *ACS App. Mater. Interfaces* **2016**, 8, 12881.
- [62] R. Jolly, C. Rhin, *Resources, Conservation and Recycling* **1994**, 10, 137.
- [63] A. P. Abbott, G. Capper, D. L. Davies, K. J. McKenzie, S. U. Obi, *Journal of Chemical & Engineering Data* **2006**, 51, 1280.
- [64] A. P. Abbott, G. Capper, D. L. Davies, R. K. Rasheed, V. Tambyrajah, *Green Chemistry* **2002**, 4, 24.
- [65] K. Haerens, E. Matthijs, A. Chmielarz, B. Van der Bruggen, *Journal of Environmental Management* **2009**, 90, 3245.
- [66] S. Günes, H. Neugebauer, N. S. Sariciftci, *Chem. Rev.* **2007**, 107, 1324.
- [67] J. W. Jung, W. H. Jo, *Adv. Funct. Mater.* **2010**, 20, 2355.
- [68] S. T. Williams, A. Rajagopal, C.-C. Chueh, A. K. Y. Jen, *The Journal of Physical Chemistry Letters* **2016**, 7, 811.
- [69] F. C. Krebs, T. Tromholt, M. Jorgensen, *Nanoscale* **2010**, 2, 873.
- [70] S. Das, B. Yang, G. Gu, P. C. Joshi, I. N. Ivanov, C. M. Rouleau, T. Aytug, D. B. Geohegan, K. Xiao, *ACS Photonics* **2015**, 2, 680.
- [71] Z. Wei, H. Chen, K. Yan, S. Yang, *Angew. Chem. Int. Ed.* **2014**, 53, 13239.
- [72] C.-W. Chen, H.-W. Kang, S.-Y. Hsiao, P.-F. Yang, K.-M. Chiang, H.-W. Lin, *Adv. Mater.* **2014**, 26, 6647.
- [73] Y. Deng, E. Peng, Y. Shao, Z. Xiao, Q. Dong, J. Huang, *Energy & Environmental Science* **2015**, 8, 1544.
- [74] K. Hwang, Y.-S. Jung, Y.-J. Heo, F. H. Scholes, S. E. Watkins, J. Subbiah, D. J. Jones, D.-Y. Kim, D. Vak, *Adv. Mater.* **2015**, 27, 1241.
- [75] A. Mei, X. Li, L. Liu, Z. Ku, T. Liu, Y. Rong, M. Xu, M. Hu, J. Chen, Y. Yang, M. Grätzel, H. Han, *Science* **2014**, 345, 295.
- [76] T. M. Schmidt, T. T. Larsen-Olsen, J. E. Carlé, D. Angmo, F. C. Krebs, *Adv. Energy Mater.* **2015**, 5, 1.
- [77] M. Ye, X. Hong, F. Zhang, X. Liu, *J. Mater. Chem. A* **2016**, 4, 6755.
- [78] F. C. Krebs, *Sol. Energy Mater. Sol. Cells* **2009**, 93, 394.

2 Characterization

2.1 X-Ray Diffraction

X-ray diffraction (XRD) is the commonly used method for the characterization of the atomic structure and the composition of crystalline materials. The principle of XRD measurements is based on the scattering of electromagnetic waves (X-rays) on structures in the Ångström range (10^{-10} m), which have about the same physical dimension as the wavelength of the incident radiation (Figure 2-1).

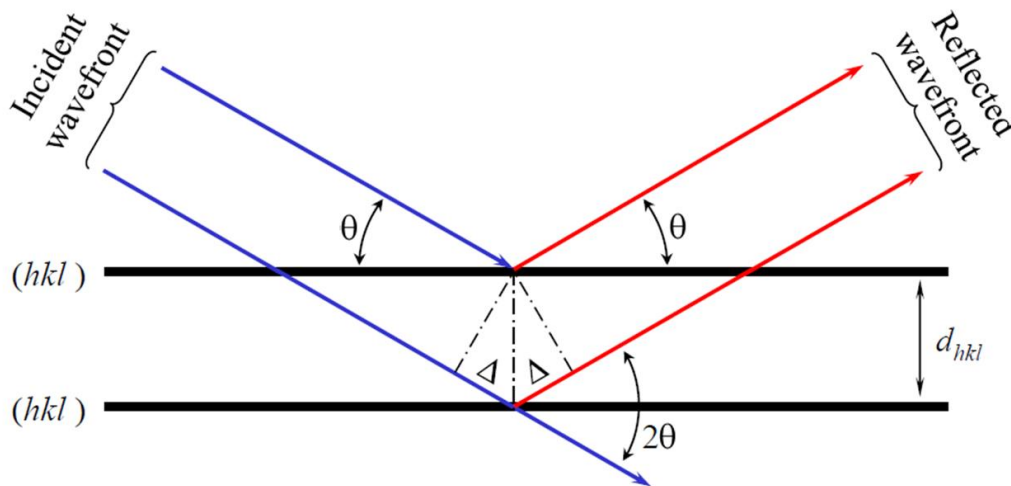


Figure 2-1: Schematic representation of the scattering processes in a XRD measurement.

The observed diffraction pattern originates from the elastic scattering of X-rays by atoms in a periodic three-dimensional structure. The relationship between the scattering angle and the distance of lattice planes is given by Bragg's law:

$$n \lambda = 2d \sin(\theta) \quad (2)$$

where n is the order of interference, λ the wavelength of X-rays (usually Cu $K_{\alpha 1} = 1.540562$ Å), d the lattice spacing of the material and θ the angle of incidence. The

2.2 Scanning Electron Microscopy (SEM)

resolution of this technique is given by the measurable angles between $0.5^\circ 2\theta$ and $100^\circ 2\theta$, which correlate to lattice spacings of 0.1 nm to 20 nm.^[1]

2.2 Scanning Electron Microscopy (SEM)

Besides the crystallographic properties of materials, the morphology and the surface of the nanoscale structure are also important parameters, especially in the case of solar cells. One technique to characterize materials concerning the structure of solar cells is scanning electron microscopy (SEM). Thereby, an electron beam is generated by either a heated tungsten filament or a field emission gun with acceleration voltages of about 1 to 30 kV. Afterwards, the produced electrons are focused on the sample with the aid of various condenser lenses and an objective lens. The scanning coils enable the motion of the beam on the sample, which results in a variety of different types of interactions between the beam of electrons and the atoms in the sample. Accelerated electrons can pass through the sample without interaction, undergo elastic scattering or can be scattered inelastically. Other types of signals are back-scattered electrons (BSE), characteristic X-rays, light (cathodoluminescence) and specimen current. The imaging in the SEM measurements is performed by absorbed electrons, which relax within the sample and are emitted again as electrons with lower energy, so called secondary electrons (SE). These SE can be detected by a detector, which is placed at a certain angle to the sample holder. The typical setup of a SEM is shown in Figure 2-2.

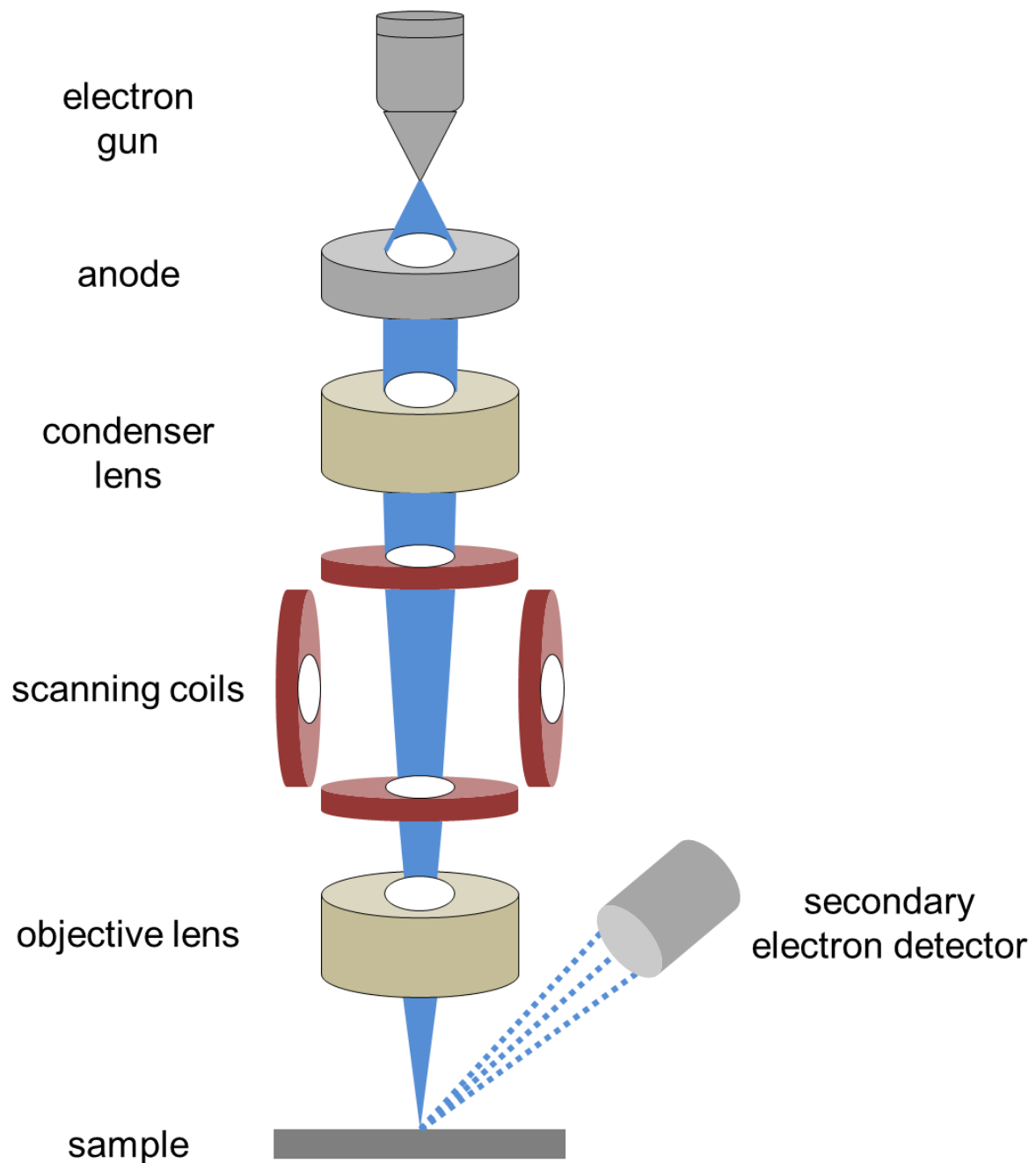


Figure 2-2: Schematic setup of a scanning electron microscope (SEM).

The number of SE reaching the detector depends on the surface height and orientation of the material as well as on the composition of the illuminated spot. Thus, by scanning the surface of the sample with the electron beam point by point it is possible to generate a microscopic image.^[2]

2.3 UV-Vis Absorption Spectroscopy

As mentioned above, characteristic X-rays are also produced by the electron beam. These X-rays correspond to the atomic composition of the material and can be sorted in a detector according to their wavelength. It is possible to determine the quantity of the included atoms of the analyzed sample with the obtained spectrum. This technique is called energy dispersive X-ray spectroscopy (EDX).^[3]

2.3 UV-Vis Absorption Spectroscopy

In addition to the structure and the morphology of the material, the electronic properties are another important feature of the absorber materials studied for PV applications. By means of ultraviolet-visible (UV-Vis) spectroscopy the optical transitions from the ground state to various excited states can be investigated. It is possible to apply this method for the quantitative and qualitative determination of the absorption properties of liquid as well as solid samples.

The absorbance A at a certain wavelength is defined in equation 3, where I is the measured intensity and I_0 the intensity of the incident beam (measured without inserted sample).

$$A(\lambda) = -\log \frac{I(\lambda)}{I_0(\lambda)} \quad (3)$$

In case of a sample dissolved in a suitable solvent at a concentration where molecular interactions are small, the absorbance is also related to the concentration of the absorbing species via the Lambert-Beer-Law (equation 4), where A is the absorbance at a certain wavelength, λ , ϵ the specific absorption coefficient, c the concentration and L the optical path length.

$$A(\lambda) = \epsilon(\lambda) c L \quad (4)$$

Normally solar cells consist of several layers with different refractive indices, which makes the determination of the amount of absorbed light more difficult. This becomes even more complicated in a fully assembled solar cell, as a solar cell typically not only contains various charge selective layers but also a reflective metal electrode. Thereby, the light is scattered and refracted at the interfaces between the different layers. In a simple model geometry for the determination of the absorption in the active layer of a solar cell (sample on glass substrate), there exist three interfaces that involve scattering of light, namely the air-substrate, the substrate-sample and the sample-air interface.

As the Lambert-Beer-Law is not applicable for the determination of the absorbance in such more complex samples, a reliable determination of the absorbance can only be obtained by optical modelling based on the optical constants of each individual layer^[4], or measurements using an integrating sphere, corrected by choosing a suitable reference.^[5]

A procedure has been developed to produce reliable results for a wide variety of thin film samples and has been applied throughout this thesis to estimate absorption in thin films.^[6] There are three possibilities of interactions between light and the sample: either the light is absorbed, transmitted or reflected. Therefore, the intensity of the incident light can be written as percentages of absorbed (%A), reflected (%R) and transmitted (%T) light.

$$\%A + \%R + \%T = 1 \quad (5)$$

The different components of the light can be determined by transmission and reflectance measurements of the reference and sample by an integration sphere. For the reflectance measurement the sample is positioned outside of the exit port of the integrating sphere. This way, only light reflected from the surface will be taken into account. Regarding the transmittance measurement, the sample has to be positioned just within the entrance port of

2.4 Steady State Photoluminescence (ssPL)

the integration sphere. Thus, all the transmitted light and the light scattered towards the edges of the sample is collected. These measurements have to be performed with the reference and the sample. In case of thin film solar cells, the reference would be the supporting transparent substrate without the active layer. Additionally, the instrument transmission baseline (100% T) has to be acquired without any optical obstacles in the beam path and a Spectralon white standard (100% R).

Through adapting equation 5 the absorbance for each sample can be calculated by the sum of reflectance and transmittance subtracted from 1. Afterwards, the absorption can be calculated by the absorbance following equation 6.

$$A = -\log(1 - \%A) \quad (6)$$

For this reason and in summary, the absorption of the active layer is the absorption of the complete sample reduced by the absorption of the substrate (reference).

2.4 Steady State Photoluminescence (ssPL)

If a chromophore or an electron is excited in a semiconductor, it will relax to its ground state after a certain time, while the excess energy will be released as phonons or photons. The energy of the emitted photon depends on the energy difference between the excited state and the ground state (band gap). A schematic representation of the absorption and emission processes is represented in Figure 2-3.

The detection of the emitted photons can provide valuable information not only about the energy levels of a certain sample but also about the effectiveness of processes like charge transfer.

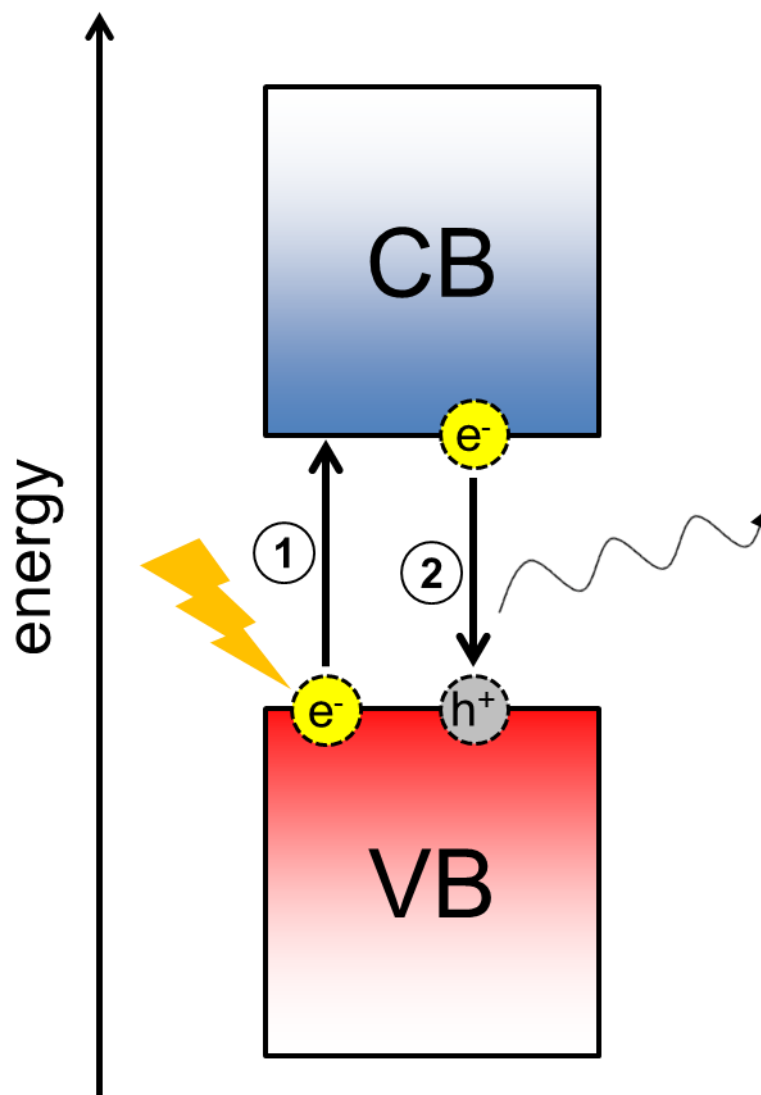


Figure 2-3: Schematic representation of absorption (1) and relaxation (2) processes leading to photoluminescence.

2.5 Time Correlated Single Photon Counting (TCSPC)

The photoluminescence (PL) signal cannot only be used to illustrate the absolute energy and the intensity of the emitted photons (ssPL), but also to record the time-resolved kinetics of photoemission from the band edge. One of the techniques used to measure this process is called time correlated single photon counting (TCSPC) and is based on the repetitive and precisely timed registration of single photons created by the sample.

2.5 Time Correlated Single Photon Counting (TCSPC)

In order to realize the experimental setup, a pulsed laser source is needed. Thereby, the time between a laser pulse and the detection of a photon is measured. However, this time is not a constant value, as shown in Figure 2-4, because it is not possible to predict the exact time when the relaxation process will happen. As a consequence, the decay mechanisms cannot be investigated by a single experiment.

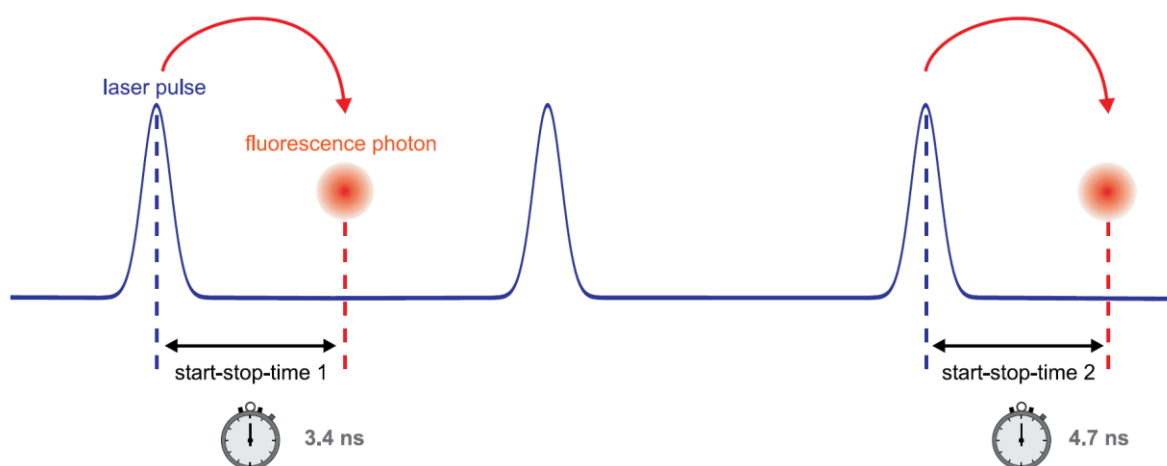


Figure 2-4: Measurement of start-stop times in a time-resolved fluorescence measurement with TCSPC.^[7]

Therefore, the laser is pulsed in the frequency range of 100 kHz to 80 MHz in order to collect a multitude of individual single photon measurements. In the evaluation, every single decay time is sorted in a histogram consisting of a range of time bins (Figure 2-5).

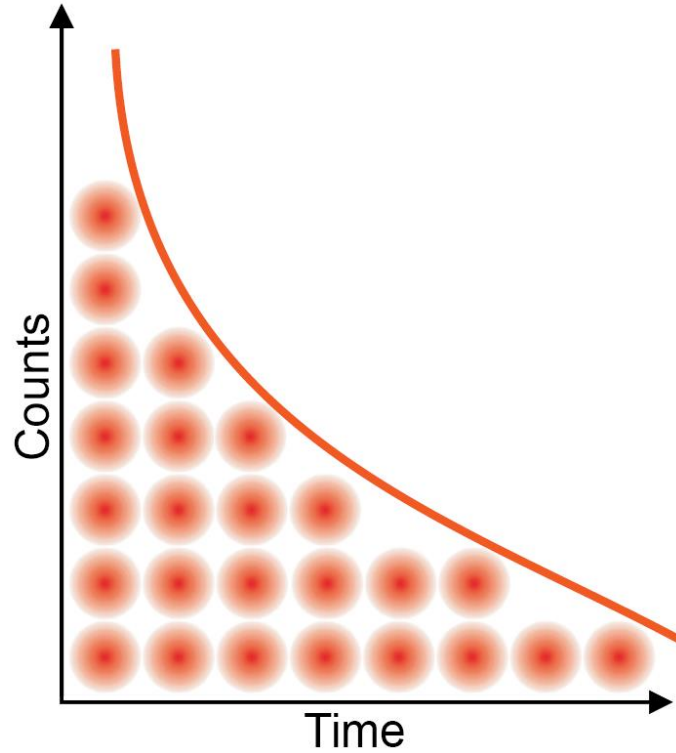


Figure 2-5: Histogram of start-stop times in time-resolved fluorescence measurement with TCSPC.^[7]

Thereby, typically an exponential decay is observed by plotting the count rates against time. The half-life time of the photoexcited species can be extracted with a matching function of the exponential decay.

2.6 Current-Voltage Measurements

After the PL investigations the sample can be incorporated into a stack of electron- and hole-extraction layers to facilitate the determination of the power conversion efficiency (PCE, η) of the device. To be able to compare different type of architectures, samples and results of different laboratories, the testing takes place under standardized conditions. One important parameter is the light intensity, which is standardized to a total light intensity of 100 mW/cm^2 (1 sun).^[8] This standard is called ASTM G173-03 air mass 1.5 global (AM1.5G) and

2.6 Current-Voltage Measurements

corresponds to the spectrum emitted by the sun and corrected for absorption and scattering by the atmosphere.

During the illumination with 1 sun current-voltage (J - V), measurements are performed to obtain the efficiency of the solar cell. Thereby, different voltages are applied to the device during the measurement of the resulting current. A typical J - V -curve for a perovskite solar cell is shown in Figure 2-6.

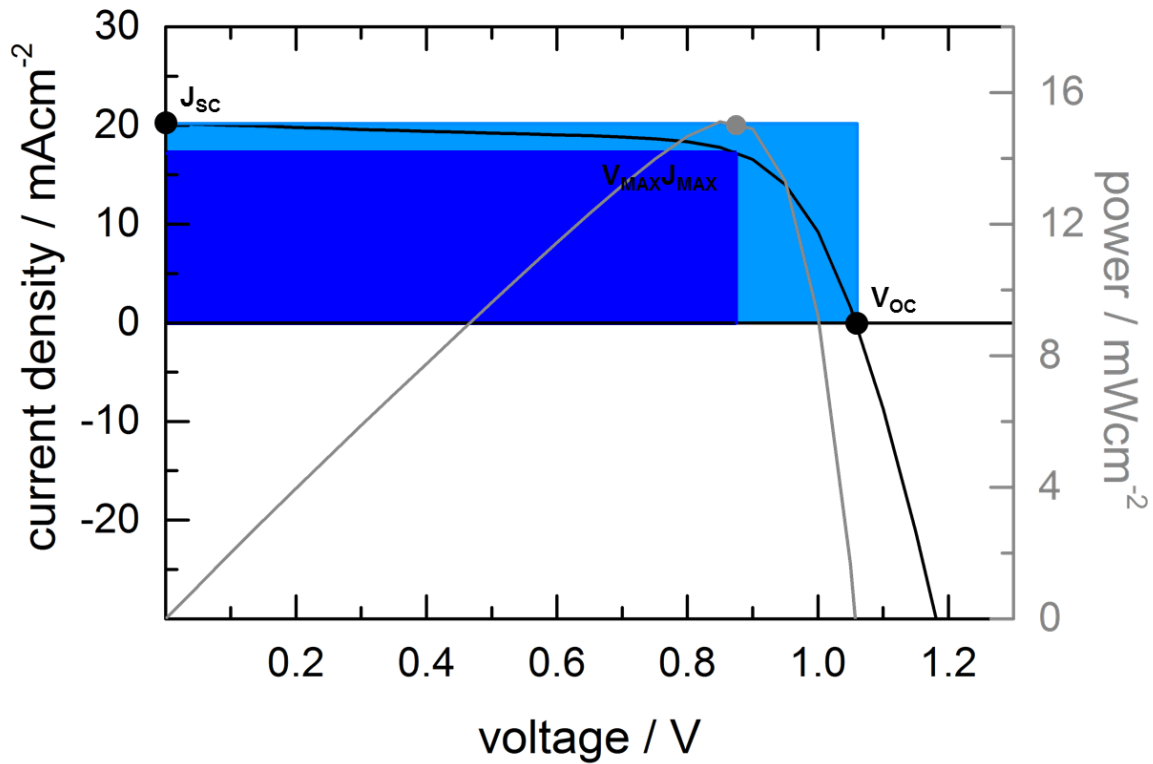


Figure 2-6: Typical J - V and power curve for a perovskite solar cell.

Important factors characterizing solar cells are the short circuit current (J_{sc}) and the open circuit voltage (V_{oc}). J_{sc} represents the current of the cell with no applied bias voltage. Furthermore, it provides insights in the absorption behavior, the charge carrier production and the charge carrier transport within the absorber layer. On the other hand, V_{oc} is the needed

voltage to compensate the internal electrical field of the solar cell, which means that no current is flowing at that voltage.

The power produced by the solar cell is determined as the product of the current and the applied voltage (grey curve). The maximum of this parabolic power curve is called maximum power point (P_{MAX}). At this voltage the solar cell performs with highest efficiency. The power conversion efficiency (PCE) is directly proportional to the quotient of P_{MAX} and the power of the incident light (P_{IN}).

$$PCE = \frac{P_{MAX}}{P_{IN}} = \frac{V_{MAX} \cdot J_{MAX}}{P_{IN}} \quad (7)$$

The fill factor (FF) is introduced as another quality factor, which will vary as a function of the shunt and serial resistance of the device. It is defined as

$$FF = \frac{V_{MAX} \cdot J_{MAX}}{V_{OC} \cdot J_{SC}} = \frac{P_{MAX}}{V_{OC} \cdot J_{SC}} \quad (8)$$

This equals the ratio between the areas of the light blue and dark blue rectangles in Figure 2-6 (see above).

2.7 Time of Flight Measurements (ToF)

In addition to the number of excited species (excitons) within the absorber layer, splitting of the excitons and the mobility of the resulting charge carriers is crucial for the photovoltaic performance of the material, too. With the measurement of the time of flight (ToF), the mobility of charge carriers in either a single charge-transporting layer or in multiple layers, consisting of charge carrier generation and transport layers sandwiched between the two electrodes, can be investigated.

2.7 Time of Flight Measurements (ToF)

The ToF method is based on the measurement of the carrier transit time (τ), that is the required time for charge carriers generated by pulsed light irradiation to travel from one electrode to the other under an applied electric field (Figure 2-7). In case of measuring a hole drift mobility, the transparent electrode (FTO) is held at a positive potential, while the other electrode (gold) is grounded through a resistor R that has a much smaller resistance than the sample. This leads to an applied potential U in the material so that the photo-generated charges will start moving towards the negative electrode. An advantage of using the ToF technique is that hole and electron mobility can be studied separately.

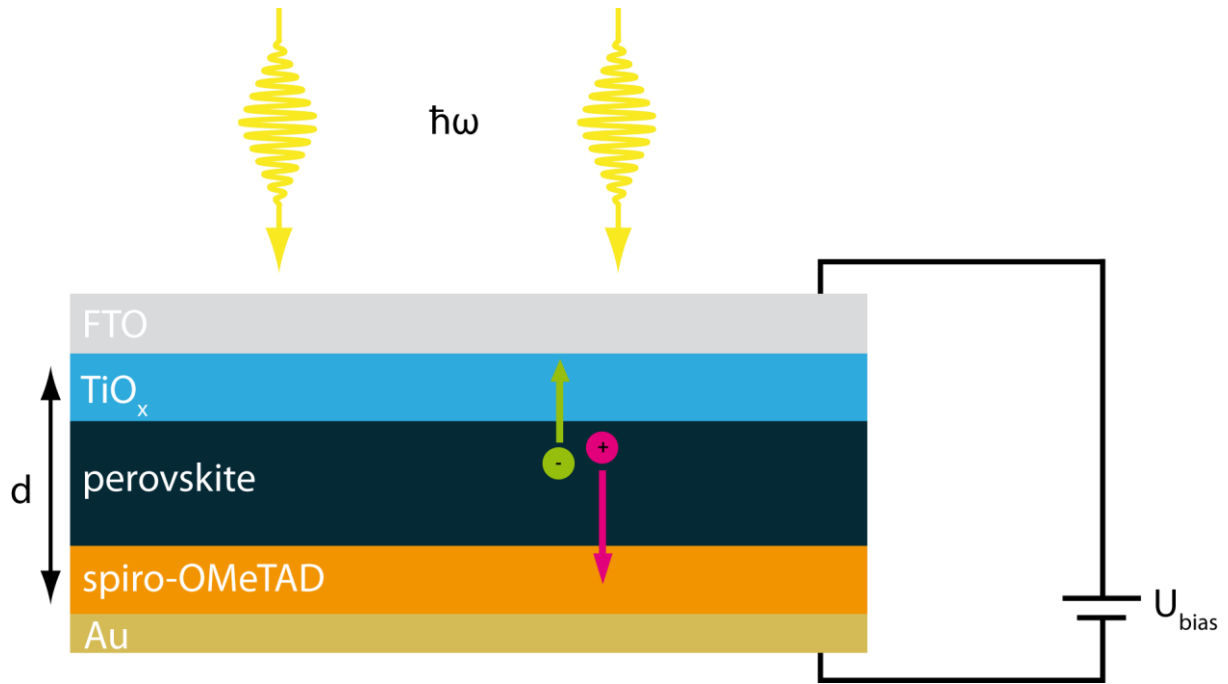


Figure 2-7: Principle of the time of flight measurement on a perovskite based solar cell.

If charge carriers start to drift, photocurrent will flow until the charge carriers arrive at the other electrode. Then the transit time can be extracted from the double logarithmic plot of transient photocurrents and the time, according to the *Scher-Montroll* theory.^[9] With the obtained transit time τ , the sample thickness d and the applied potential U the mobility can be calculated according to equation 9.^[10]

$$\mu = \frac{d^2}{U \cdot \tau} \quad (9)$$

The mobility gives insights in the quality of the absorber and connects it with the power conversion efficiency of the device.

2.8 Inductively Coupled Plasma Optical Emission Spectroscopy (ICP-OES)

Optical emission spectroscopy (OES) provides a measurement to investigate atoms, ions and molecules within a plasma, causing the sample to emit light and thereby revealing their presence and concentration by distinct spectral signatures. Here, the excitation of electrons to higher energy levels within the sample is achieved by inductively coupled plasma (ICP). ICP is plasma that is ionized by heating a gas (Ar) inductively with an electromagnetic coil. Furthermore, the sample chamber contains a sufficient concentration of ions and electrons to make the gas conductive. Plasma temperatures can range between 6000 K and 10000 K.^[11] This is why almost every chemical element is ionized so it can emit its characteristic photons. Afterwards, the generated light is transferred to a diffraction grid, which separates the radiation in monochromatic components as shown in Figure 2-8.

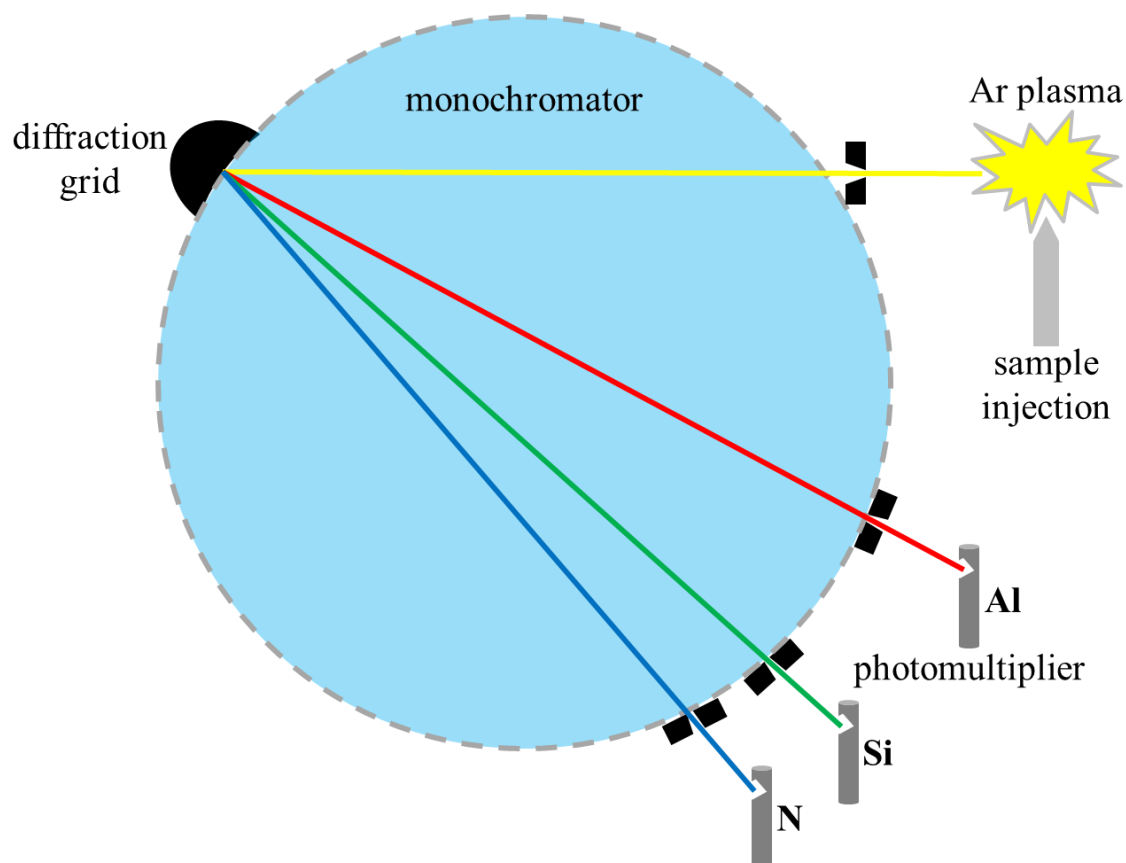


Figure 2-8: Schematic setting of ICP-OES measurement.

Small photoengraved plates are set on the grey circle (Rowland Circle) to isolate the spectral lines belonging to the selected elements for the analysis. The intensity of each emission spectrum depends on the concentration of the element. Therefore, it is possible to perform qualitative and quantitative analysis of the elements within the sample.

2.9 Design of a Solar Simulator for the Glovebox

During the process of this thesis, we developed a setup for obtaining J - V curves under inert atmosphere (N_2) and simulated solar irradiation (Figure 2-9).

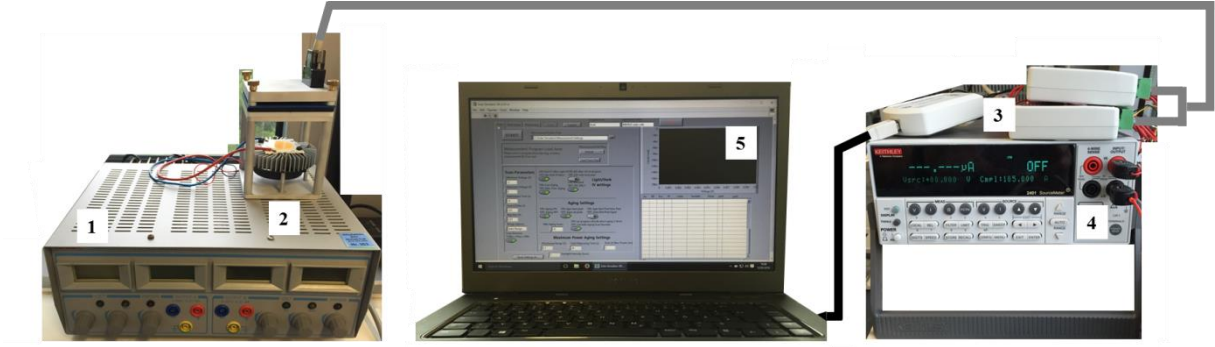


Figure 2-9: Layout of the solar simulator.

Solar irradiation is obtained by a LED array (Bridgelux, 6600 lm), which emits warm white light with an intensity between 50 and 250 mW/cm². The LED is thermally coupled to a ventilator (SUNON) to prevent an overheating of the system (2). The intensity of the light can be modified by a power supply (1). At normal working conditions the LED is calibrated to 100 mW/cm² with a Fraunhofer ISE certified silicon cell. However, the spectrum of the LED differs from the simulated AM1.5G solar spectrum, so a mismatch factor has to be calculated in order to get reliable *J-V* characteristics.

To be able to estimate the spectral mismatch the fractional variation between the test cell short-circuit current measured under the solar simulator and the test cell short-circuit current measured under AM1.5 sun light of 100 mWcm⁻² intensity has to be calculated. The equation from Snaith *et al.*^[12] is used for the calculation of the mismatch factor.

$$M = \frac{\int E_R(\lambda) S_R(\lambda) d\lambda}{\int E_S(\lambda) S_R(\lambda) d\lambda} \times \frac{\int E_S(\lambda) S_T(\lambda) d\lambda}{\int E_R(\lambda) S_T(\lambda) d\lambda} \quad (10)$$

Here $S_R(\lambda)$ and $S_T(\lambda)$ are the spectral responses of the reference diode and the test cell, which is in this case a Methylammonium lead iodide (MAPbI₃) based solar cell with a strong absorption starting from 850 nm to 350 nm. These values can be calculated from the IPCE (incident photon to current efficiency) ratio. The term $E_S(\lambda)$ is the output spectrum of the used solar source (in this case an LED) and $E_R(\lambda)$ is the AM1.5G spectrum. A mismatch factor of

2.9 Design of a Solar Simulator for the Glovebox

0.9 is obtained for this setup as a result of the difference between the LED spectrum and the solar spectrum. With this value the solar simulator is calibrated in order to get reliable results for the devices.

Up to 12 individual devices per substrate can be measured automatically via computer-controlled relays (3). The corresponding pins on the circuit board (Figure 2-10b) are bumped onto on the gold contacts of the substrate by bolting a metal lid on top (Figure 2-10a). The circuit for the measurement is closed by connecting the back contact (pin 13-16) with the desired pixel (pin 1-12) of the solar cell. Afterwards, J - V curves are recorded with a Keithley 2400 sourcemeter (4) and plotted with the aid of LabView (5). Each device of the substrate has an active area of 0.0831 cm^2 defined by a square metal aperture mask on the white teflon layer (Figure 2-10a).

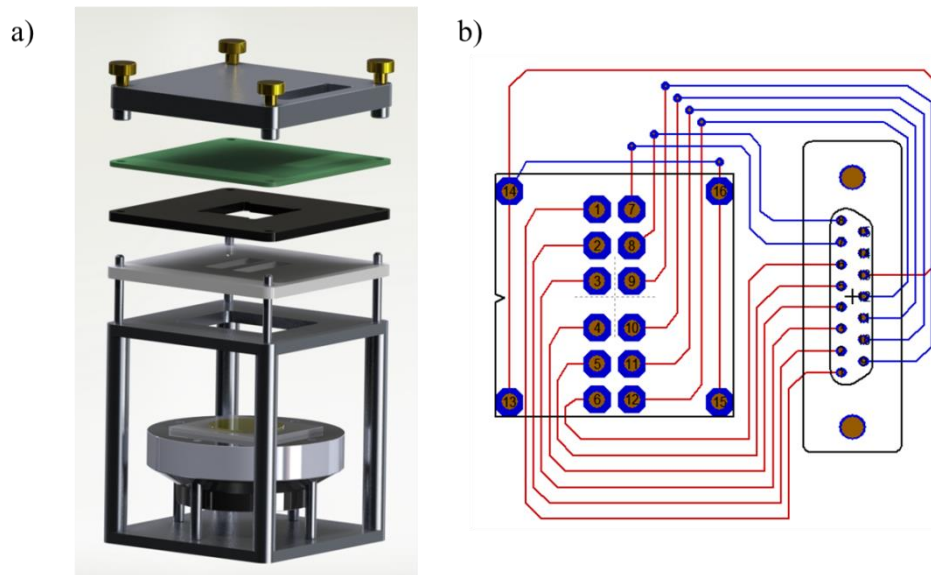


Figure 2-10: a) LED setup (2) and b) layout of the circuit board.

2.10 Literature

- [1] W. H. Bragg, W. L. Bragg, *Proc. R. Soc. London, Ser. A* **1913**, 88, 428.
- [2] M. v. Ardenne, *Z. Physik* **1938**, 109, 553.
- [3] C. G. Barkla, C. A. Sadler, *Philos. Mag.* **1909**, 17, 739.
- [4] G. F. Burkhard, E. T. Hoke, M. D. McGehee, *Adv. Mater.* **2010**, 22, 3293.
- [5] H. J. Snaith, C. Ducati, *Nano Lett.* **2010**, 10, 1259.
- [6] B. M. Klahr, A. B. F. Martinson, T. W. Hamann, *Langmuir* **2011**, 27, 461.
- [7] M. Wahl, PicoQuant GmbH, Berlin 2014.
- [8] <http://rredc.nrel.gov/solar/spectra/am1.5/>.
- [9] H. Scher, E. W. Montroll, *Physical Review B* **1975**, 12, 2455.
- [10] S. Tiwari, N. C. Greenham, *Opt. Quantum Electron.* **2009**, 41, 69.
- [11] E. V. Shunko, D. E. Stevenson, V. S. Belkin, *IEEE Transactions on Plasma Science* **2014**, 42, 774.
- [12] H. J. Snaith, *Energy & Environmental Science* **2012**, 5, 6513.

3 Control of perovskite crystal growth by methylammonium lead chloride templating

This chapter is based on the following publication:

Andreas Binek^{*}, Irene Grill^{*}, Niklas Huber^{*}, Kristina Peters, Alexander G. Hufnagel, Matthias Handloser, Pablo Docampo, Achim Hartschuh and Thomas Bein, *Chemistry – An Asian Journal*, **2016**, 11, 1199-1204.

^{*}These authors contributed equally to this work

3.1 Introduction

With rising global energy demand and the decline of fossil fuels reserves, there is great need to develop renewable energy resources. Lately, solar cells based on organic-inorganic trihalide perovskites, e.g. $(\text{CH}_3\text{NH}_3)\text{PbI}_3$, have emerged as a highly efficient and inexpensive photovoltaic technology.^[1-4] Through optimization of the fabrication processes,^[5-7] the annealing process^[8, 9] and the interfaces,^[10] perovskite solar cells have already exceeded 20 % power conversion efficiency (PCE).^[11]

Recently, several novel crystallization methods have been exploited to fabricate perovskite photovoltaic devices with high and reproducible performance.^[12, 13] In particular, previous studies show that control of the macroscopic morphology and the crystalline domain size has a strong influence on the resulting device performance.^[14-16] Hence, understanding the crystallization mechanism of the active layer is a crucial factor. In grain boundaries and defects, traps for the photoexcited species are located and recombination can occur..^[17] Thus, a good strategy to maximize device efficiency is the reduction of the number of grain boundaries in the perovskite layer by tuning the deposition technique.^[18] A common approach

3.2 Results and Discussion

to improve the performance of perovskite solar cells is the use of a chloride-based precursor in the casting solution. In particular, lead chloride (PbCl_2) and methylammonium iodide (MAI) mixtures lead to highly efficient devices when employed in planar heterojunction solar cells.^[19] This enhancement is generally attributed to the formation of bigger crystal domains of the perovskite compared to other precursors and the related reduction of grain boundaries and defects in the bulk material.^[16] However, the role of chloride during the crystallization process is still unclear, with many groups reporting no or only small amounts of chloride in the final structure.^[20-23] Thus, understanding the crystallization mechanism and, therefore, gaining additional handles to tune the crystal morphology of these systems can open up new strategies to maximize the device performance. Here, we investigate the crystallization of the perovskite immediately after deposition in order to understand and control the crystallization kinetics of the system. Our *in-situ* X-ray diffraction measurements show that initially MAPbCl_3 crystallizes on the substrates to be fully converted into MAPbI_3 after a certain time under heating. Furthermore, we show the positive influence of the slow evaporation of the solvent on the crystal size, morphology, and also on the charge-carrier mobility in the perovskite layer. Our results help to understand the influence of chloride during the crystallization process of the perovskite and the origin of the improved performance of the system.

3.2 Results and Discussion

The MAPbI_3 samples were prepared according to the synthesis route of Eperon *et al.*^[8] In short, a mixture of lead chloride (PbCl_2) and methylammonium iodide (MAI) was dissolved at a ratio of 1:3, and was then spin-coated on a TiO_2 -covered fluorine-doped tin oxide (FTO) substrate. Afterwards, the sample was kept at room temperature (RT) for different times to allow for the slow evaporation of the residual solvent, and then heated to different

temperatures to complete the conversion to the MAPbI_3 crystal phase. With this procedure we enabled slow formation of the perovskite, leading to uniform crystallites. In order to examine the influence of different evaporation times of the solvent at RT on the perovskite morphology, cross-sections were prepared (Figure 3-1). Short exposure times between 1 min and 20 min resulted in crystallites that are not uniform in size and shape, and a large number of grain boundaries are visible. In contrast, the SEM images of samples with a longer crystallization time show larger and more uniform crystallites, and consequently a reduction of grain boundary density.

To substantiate the uniformity of the MAPbI_3 crystals, smooth cross sections showing high contrast were also prepared with a focused ion beam (FIB). In the FIB cross-sections (Figure 3-1b) the noticeable difference between fast and slow evaporation of the solvent is even more visible. The 5 min sample exhibits a rough surface due to non-uniform crystal formation. In comparison, the 40 min sample shows a regular brick-like morphology of the perovskite on the substrate.

3.2 Results and Discussion

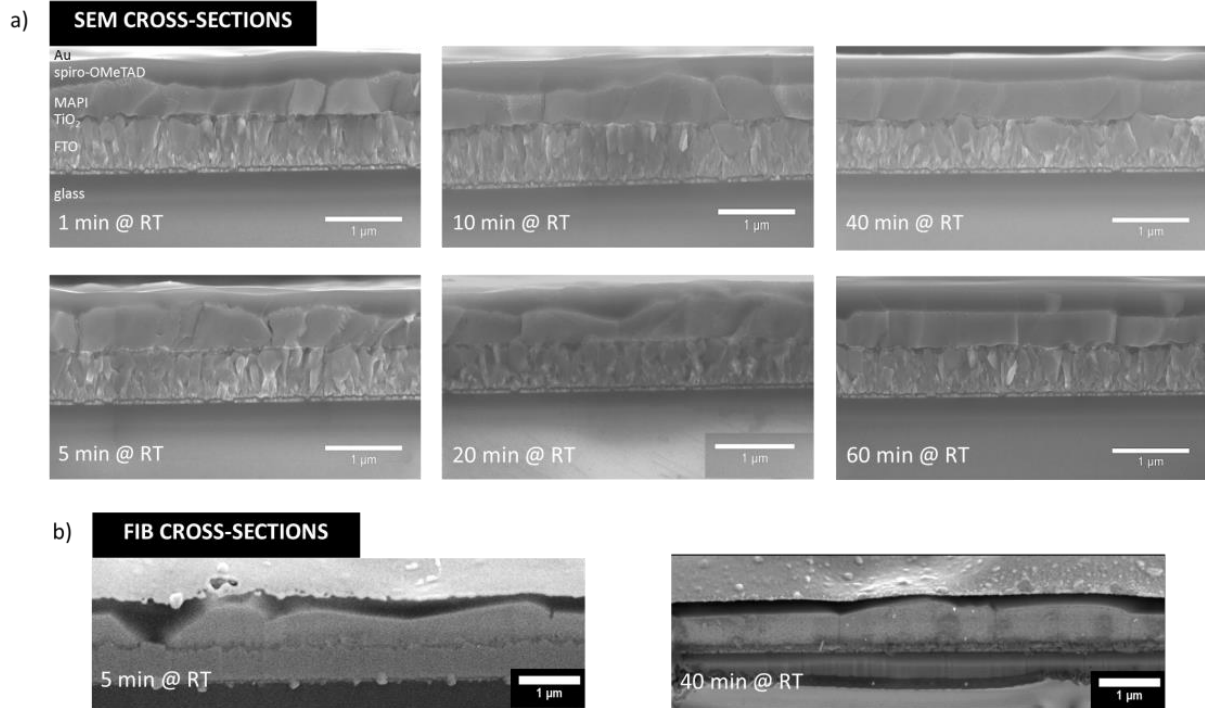


Figure 3-1: SEM images of cross-sections of samples with different evaporation times at RT (a) and SEM images of FIB cross-sections of a 5 min and a 40 min sample, respectively (b).

In order to further understand the crystallization and the influence of the different temperature treatments during the synthesis, *in-situ* X-Ray diffraction measurements (XRD) were performed under a nitrogen atmosphere with freshly spin-coated samples. Additionally, we investigated the effect of heating steps on the perovskite crystal structure; such steps are often used to achieve highly efficient devices for a range of exposure times (Figure 3-2). In the first XRD pattern, after 5 min at RT, an intense reflection at around $16^\circ 2\theta$ is observed. Over time, an additional reflection at $14^\circ 2\theta$ appears and slowly increases at RT. The first reflection at higher angles ($16^\circ 2\theta$) is attributed to the (200) plane of the MAPbCl₃ perovskite structure, while the second reflection ($14^\circ 2\theta$) is attributed to the (002) plane of MAPbI₃ (Figure 3-2d); no shift is present in either reflection, therefore ruling out MAPbI_{3-x}Cl_x mixed phases. The broad reflection between 11.2 and $12.6^\circ 2\theta$ is likely the result of the formation of PbI_n⁽²⁻ⁿ⁾ complexes, which arise as a result of employing non-stoichiometric perovskite mixtures with an excess of the organic cation.^[24]

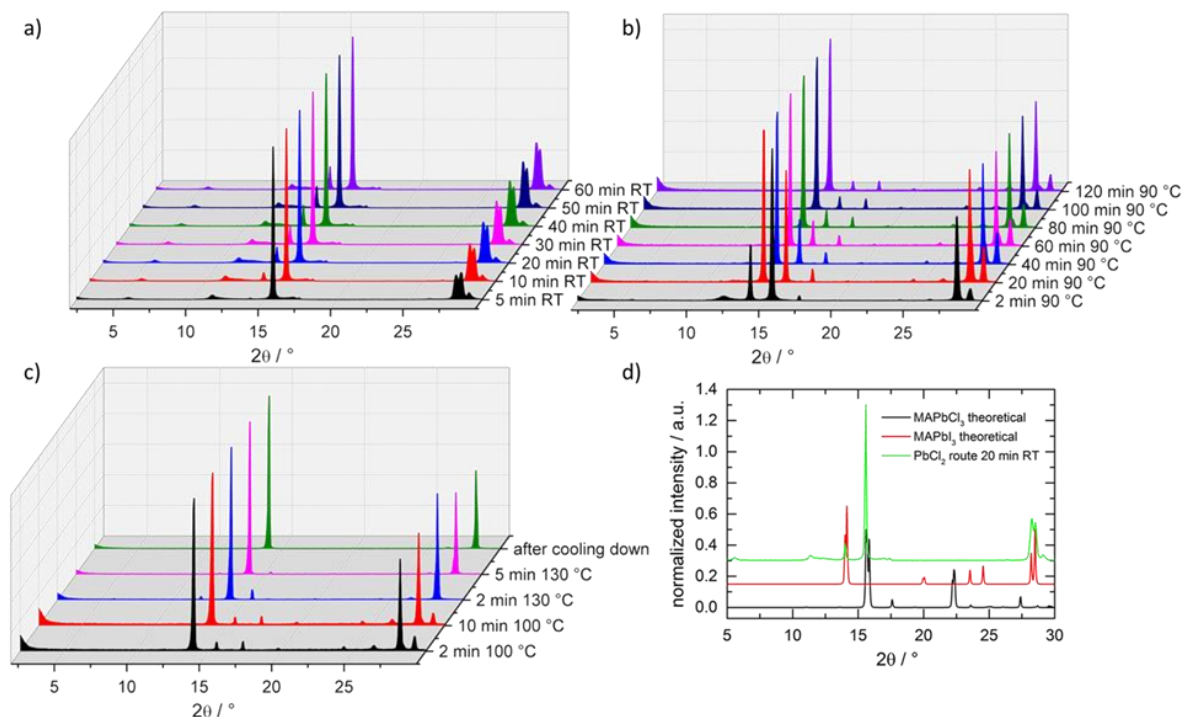


Figure 3-2: *In-situ* X-ray diffraction measurements with samples prepared according to the PbCl₂ route. XRD patterns for the RT step from 5 min to 60 min (a), 90 °C step from 2 min to 120 min (b), 100 °C / 130 °C at different times and after cooling down (c). Theoretical patterns of MAPbI₃ and MAPbCl₃ compared with XRD pattern of the sample after 20 min at RT (d).

The difference between both structures is not only the halide but also the arrangement of the PbX₆ octahedra. Heating to 90 °C leads to a reversal of reflection intensity of both perovskite structures, and thus conversion from one structure to the other. Thereby, the intensity of MAPbCl₃ is quickly decreased while the reflection of MAPbI₃ gains in intensity. Furthermore, the second reflection of the iodide perovskite at around 28 °2θ also increases during the heat treatment. In the following two temperature steps (Figure 3-2c), the intensity of MAPbCl₃ reflections is further decreased and the orientation of the MAPbI₃ crystals is enhanced as the number of reflections is reduced, and only reflections arising from *c*-axis orientation remain. After cooling down to RT, only two reflections are observed, indexed as (001) and (002) from MAPbI₃, indicating that the crystals exhibit a preferred orientation along the *c*-axis and therefore parallel to the substrate. The same orientation is also observed in samples having been exposed to different evaporation times at RT, as shown in Figure 3-3.

3.2 Results and Discussion

From a crystallographic point of view the samples are very similar, however, the cross-sections show different morphologies.

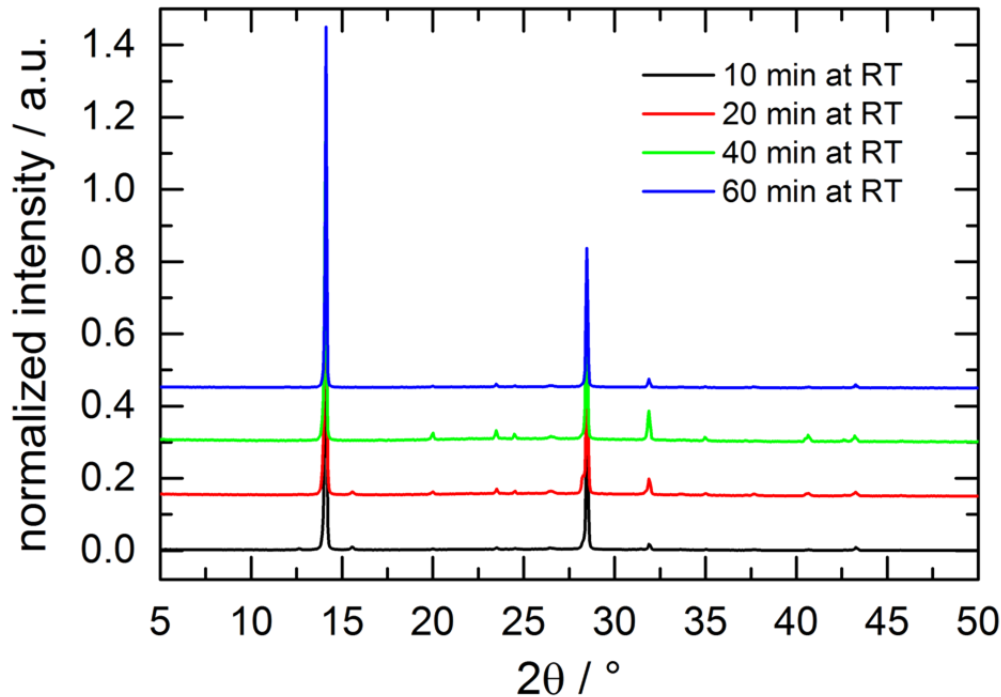


Figure 3-3: XRD patterns of samples prepared by the PbCl_2 route with different resting times at RT. All samples were heated up to 90°C for 2 h, 100°C for 10 min and 130°C for 5 min after each RT step.

Crystallization of a material from a solution can occur by cooling down the solution or through evaporation of the solvent.^[25] This is achieved through spinning of the substrate, which then leads to the formation of the nuclei. Afterwards, the crystallites grow due to the heating of the substrate. The fact that chloride, which improves the crystal quality of the perovskite,^[26] is not incorporated into the structure of MAPbI_3 , indicates that its effect must take place during the crystallization process.

The crystallization order of the two perovskite structures can be explained with the Ostwald–Volmer rule, which states that the system with the lower density crystallizes first.^[27] Here, the density of MAPbCl_3 ^[28] was estimated as 1.576 g/cm^3 , while a value of 4.119 g/cm^3 was obtained for the MAPbI_3 ^[29] compound, and therefore the chloride-containing material is

3 Control of perovskite crystal growth by methylammonium lead chloride templating

expected to crystallize first, as observed experimentally. We show a schematic of the proposed mechanism in Figure 3-4.

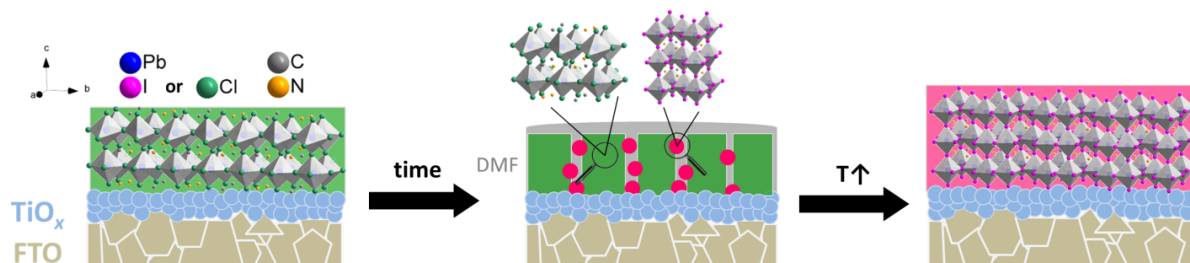


Figure 3-4: Schematic mechanism of the crystallization of the perovskite based on the PbCl_2 synthesis route established from Ostwald-Volmer rule.

Here, the sample is left at RT for the slow evaporation of the solvent, where MAPbCl_3 forms on the surface and acts as a template for MAPbI_3 . Additionally, some crystallites of MAPbI_3 emerge during the RT treatment as observed in the *in-situ* XRD. These can then act as seeds for the formation of the MAPbI_3 layer while heating up the system. Over time, the solvent as well as the excess of MA and chloride are evaporated, and highly oriented MAPbI_3 crystals are formed on the surface of the substrate with the orientation induced by the MAPbCl_3 template. With this crystallization mechanism, the morphological differences in the SEM cross-sections can be explained with the time required by the MAPbCl_3 template to form on the surface. A short time of 5 min at RT appears to be insufficient to create an oriented and fully formed MAPbCl_3 template. Therefore, in this case, the deposition of MAPbI_3 during the heat treatment leads to less uniform and smaller crystals. The difference between samples treated for 5 min and 40 min at room temperature was further investigated by incorporating the resulting perovskite layers in a planar heterojunction photovoltaic device architecture with TiO_2 and spiro-OMeTAD serving as the charge extraction contacts.^[30] The current/voltage curves and the efficiency distributions of the devices are displayed in Figure 3-5a and b, respectively.

3.2 Results and Discussion

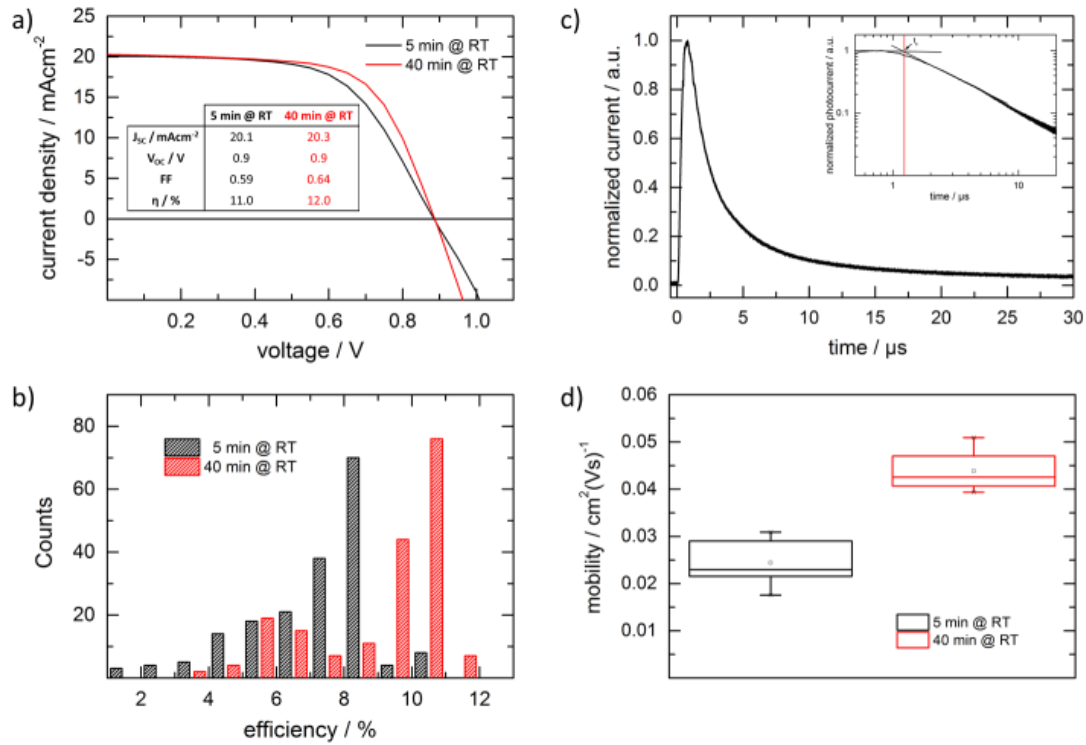


Figure 3-5: *J-V* characteristics of MAPbI₃-based solar cell devices prepared with 5 min and 40 min evaporation time at RT (a) and their distribution of efficiencies from 200 solar cells (b). Figure c shows a representative ToF transient. The inset is a double logarithmic zoom in of the region used to fit the data to obtain the transit time t_{tr} (see text). The respective mobilities obtained by ToF measurements of both sample types are depicted in d). Here it is observed that the incorporation of the material treated for 40 min at RT in the solar cell leads to an increase of charge carrier mobility by a factor of 2.

We show that the film treated for 40 min at RT exhibits enhanced PCE values in comparison to the film treated for 5 min at RT. We attribute this difference to the higher crystallinity and more uniform size distribution of crystals within the film during the MAPbCl₃ template-assisted growth process, as illustrated by our *in-situ* XRD measurements depicted in Figure 3-2. In the SEM top-view images (Figure 3-6) of both films we observe that the domain sizes of the perovskite crystals are increased while the surface density of pinholes is decreased for the film treated for 40 min at RT as compared to the film treated for 5 min, leading to an enhanced PCE and reduced hysteresis of the device (Figure 3-7).^[16]

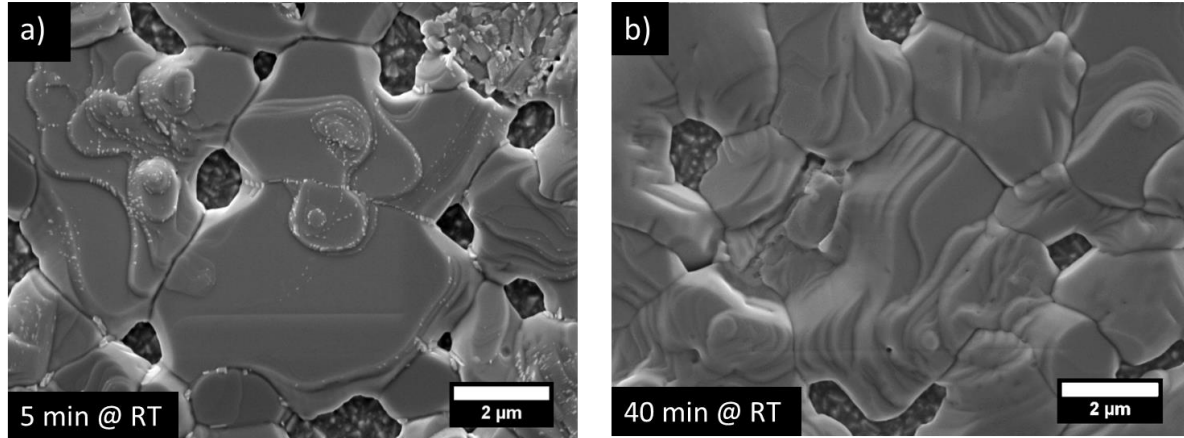


Figure 3-6: SEM images of samples with resting times of 5 min at RT (a) and 40 min at RT (b).

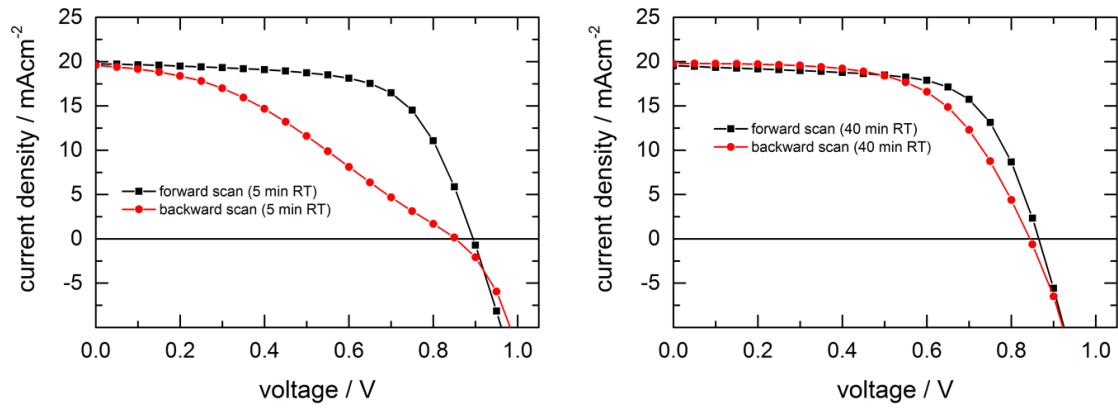


Figure 3-7: $J-V$ curves (forward and backward scan) of samples with 5 min and 40 min resting times at RT.

The trend observed for the best device $J-V$ curves, as presented in Figure 3-5, also holds for averaged devices as shown in Figure 3-8. Additionally, the greater number of pinholes present in the film treated for 5 min at RT also results in a small open circuit voltage loss due to higher recombination losses, similar to previous results reported in the literature.^[8]

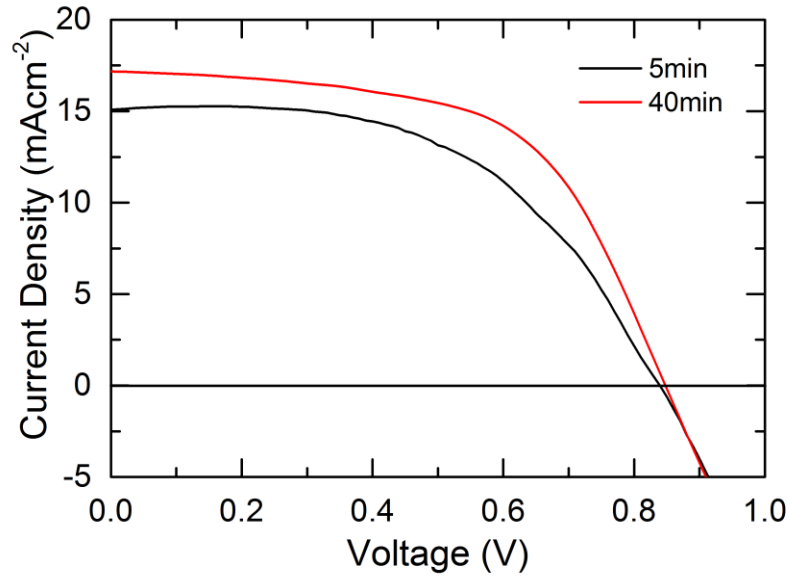


Figure 3-8: Averaged J - V curve of all prepared cells for both sample types fabricated within this work.

In order to investigate the relationship between crystal quality and transport dynamics in our solar cells, we carried out time-of-flight (ToF) studies for the devices fabricated from perovskite films treated for 5 and 40 min at room temperature. ToF is a well-established method to extract the mobility of charge carriers in semiconductors and solar cells. Based on the generation of charge carriers by short laser pulses and subsequent drifting due to an applied bias, the resulting time-resolved photocurrent is used for the determination of the corresponding mobility.^[31] A representative ToF transient is depicted in Figure 3-5. From this transient, the transit time t_{tr} is obtained. A detailed description of the fitting procedure and the measurement setup used, including the transit time as a function of applied bias, see Figure 3-9, Figure 3-10 and Figure 3-11.

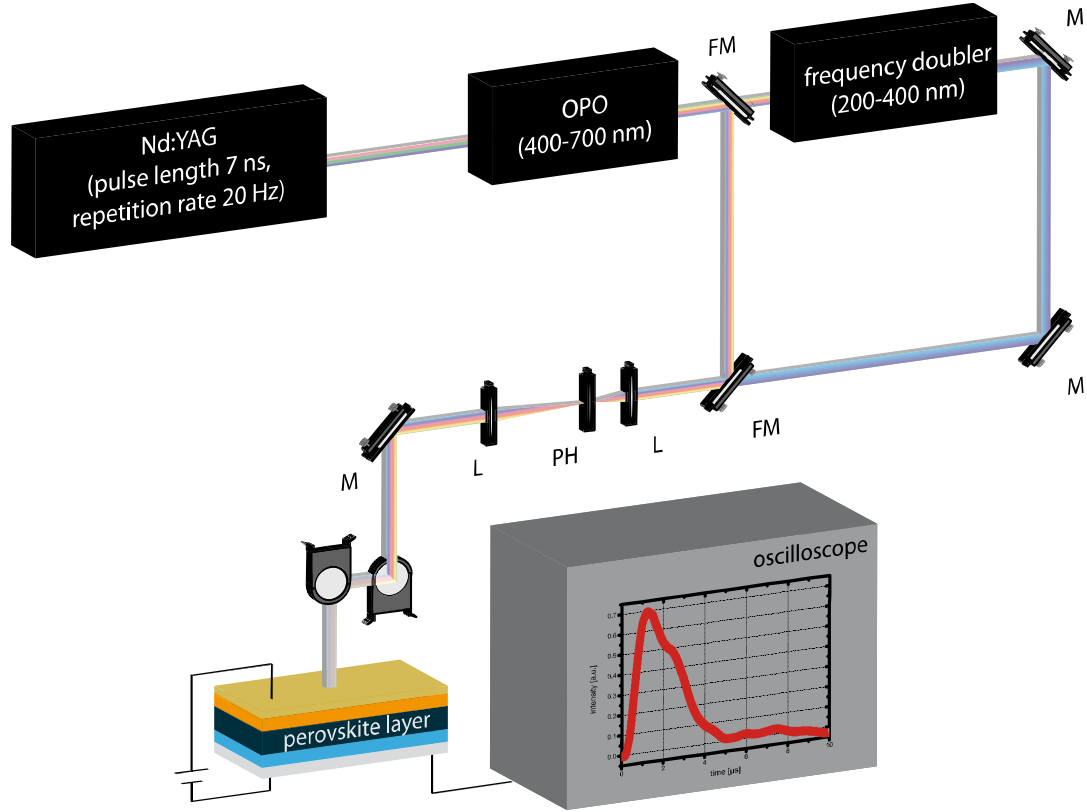


Figure 3-9: The ToF setup used in this study (schematic).

The extraction of the transit times that are necessary to calculate the charge carrier mobility according to $\mu = d^2/U \cdot t_{tr}$ (d : perovskite layer thickness, U : bias voltage) was done by linearly fitting the plateau and the decay of the transient in a double-log-plot (see Figure 3-5). The transit time of the charge carriers was extracted from the intersection of both lines.^[31] In the presented experiments we could not observe any difference for the mobilities of electrons and holes due to our temporal resolution of ~ 2 ns.^[32]

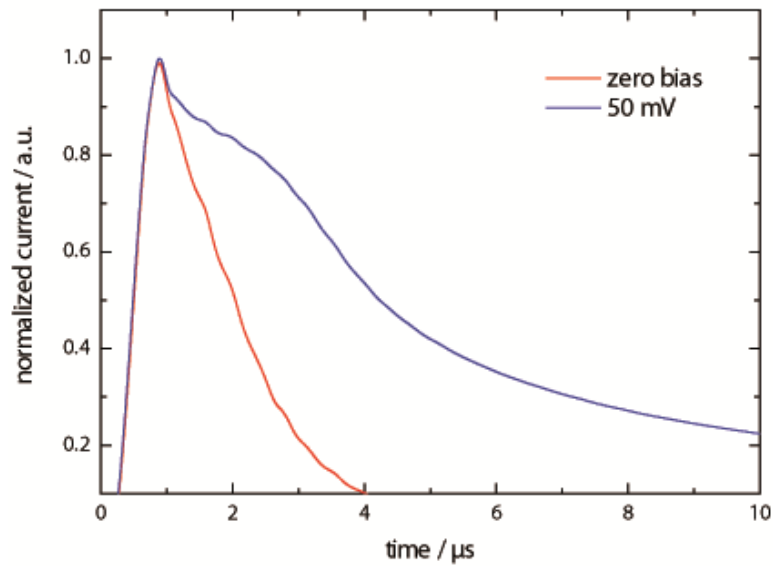


Figure 3-10: Transient characteristics for a ToF measurement performed with an applied bias voltage of 50 mV compared to the generated photocurrent at zero bias under pulsed laser excitation.

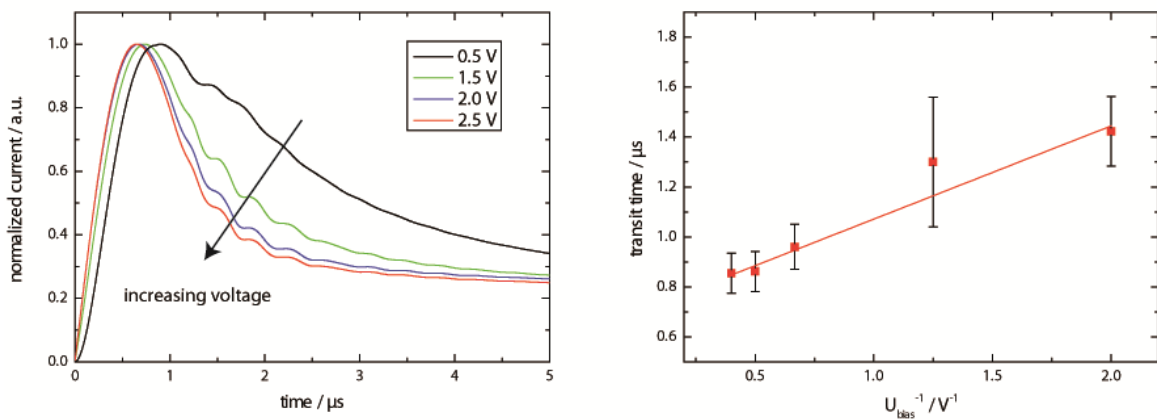


Figure 3-11: ToF transients obtained at different applied bias voltages (left) and corresponding transit times as a function of the reciprocal bias values (right), extracted by the before mentioned procedure.

In the current device structure, we predominantly measure hole transport, as most charges are generated in close proximity to the electron collection layer (TiO_2), while the holes must travel throughout the whole thickness of the film. We note that the resulting ToF transient characteristics in a thin film device fabricated for supporting electron transport, for instance, by using PEDOT:PSS (poly(3,4-ethylenedioxythiophene)- polystyrene sulfonate) and PCBM (phenyl- C_{61} -butyric acid methyl ester), would lead to similar results, since electron and hole

mobility in MAPbI₃ thin films have been shown to be similar.^[32] Further, the penetration depth of light in MAPbI₃ thin films at 550 nm is 0.66 μm , as measured by Park.^[33]

The results extracted from ToF data can be found in Figure 3-5d. We note that the experimental error is mainly caused by the determination of the layer thickness. The slow evaporation of the solvent and the associated formation of uniform and big crystals of the perovskite for the 40 min at RT sample can be connected to the enhancement of the mobility of the charge carriers within the photoactive layer, as observed in the ToF measurements. The higher mobility in the 40 min at RT sample is also observable in the J - V characteristic since the series resistance of the solar cell is lowered, which leads to a higher fill factor (FF). The series resistance was estimated by fitting the ohmic regime of the J - V curve and yields $12.5 \Omega\text{cm}^2$ for the 5 min and $8.2 \Omega\text{cm}^2$ for the 40 min device. With this increased conductivity of the sample, the charge extraction by the selective contacts is enhanced, resulting in higher device efficiency. The results presented here show mobility values two orders of magnitude higher than previous ToF studies on perovskite solar cells.^[34] We note that the morphology of the perovskite plays an important role for the mobility, as demonstrated here, and hence we expect that the much smaller crystals and thus higher grain boundary density present in the previous study account for the discrepancy. On the other hand, values obtained from THz ($8.1 \text{ cm}^2\text{V}^{-1}\text{s}^{-1}$)^[35] and microwave ($6.2 \text{ cm}^2\text{V}^{-1}\text{s}^{-1}$)^[36] conductivity measurements on the active perovskite layer only are up to three orders of magnitude higher than the present results that have been obtained for complete devices. We attribute these differences to the different transport processes and probing dimensions associated with THz and microwave measurements, in comparison with the complete through-layer transport probed with ToF methods. Moreover, as the ToF measurement probes the entire device, there could also be a minor influence of the transport layer (spiro-OMeTAD) and the relevant interfaces on the apparent mobility of the material.

3.4 Experimental Section

3.3 Conclusion

In summary, we have studied the crystallization of MAPbI₃ based on a one-step approach with a chloride-based precursor. Based on *in-situ* XRD measurements, we propose a crystallization mechanism for the synthesis procedure. Thereby, MAPbCl₃ is assembled on the substrate during the slow evaporation of the solvent, and over time some MAPbI₃ crystals are also formed. While heating up the substrate, MAPbI₃ grows at the expense of MAPbCl₃, which leads to crystals oriented parallel to the substrate. Furthermore, we show that a slow evaporation of the solvent during the formation of the MAPbCl₃ template influences the morphology, size, and uniformity of the resulting MAPbI₃ crystals. Advanced electro-optical characterization by time-of-flight studies in this work showed that the charge-carrier mobility is doubled for devices based on MAPbI₃ that were fabricated with more controlled evaporation of the solvent at RT. This indicates that slow evaporation of the solvent before the heat treatment benefits the solar cell efficiency through enhanced conductivity and a corresponding increased device performance.

3.4 Experimental Section

Preparation of the precursors

Methylammonium iodide was prepared by adapting a recipe published earlier.^[37] In short, 24 mL of methylamine solution (33% in ethanol, Sigma-Aldrich) was diluted with 100 mL of absolute ethanol in a 250 mL roundbottom flask. To this solution, 10 mL of hydroiodic acid (33 wt%) was added under constant stirring. After a reaction time of one hour at room temperature, the solvents were removed by rotary evaporation. The obtained white solid was washed with dry diethyl ether and finally recrystallized from ethanol.

Solar cell preparation

Fluorine doped tin oxide (FTO) coated glass sheets (7 Ω /sq, Pilkington, USA) were patterned by etching with zinc powder and 3 M HCl. They were subsequently cleaned with a 2% Hellmanex solution and rinsed with de-ionized water, ethanol and acetone. Directly before applying the blocking layer, last organic residues were removed by an oxygen plasma treatment for 5 min. The dense TiO₂ layer was prepared from sol-gel precursor solution by spin-coating onto the substrates and calcining at 500 °C in air.^[38] For the sol-gel solution a 27.2 mM solution of HCl in 2-propanol was added dropwise to a vigorously stirred 0.43 mM solution of titanium isopropoxide (99.999%, Sigma-Aldrich) in 2-propanol. The solution stayed clear during the addition and was discarded otherwise.

The precursor solution for the synthesis of MAPbI₃ was prepared by dissolving 1.685 g of MAI in 4 mL dry *N,N*-dimethylformamide (DMF, 99.8%, Sigma-Aldrich). This solution was then added to 973 mg of PbCl₂ (98%, Sigma-Aldrich) and heated to 100 °C in order to fully dissolve the lead precursor. Subsequently, 100 mL of this solution was spin-coated onto the TiO₂-covered substrates at 1000 rpm for 45 s. After varying the resting times at RT, the samples were placed on a hotplate at 90 °C for 2 h. Afterwards, two additional heating steps were performed, first 10 min at 100 °C and then 5 min at 130 °C. Next, the films were covered with a layer of spiro-OMeTAD (Borun Chemicals, 99.5% purity). Typically, 100 mg of spiro-OMeTAD were dissolved in 1 mL chlorobenzene (99.8%, Sigma-Aldrich). The solution was filtered and mixed with 10 μ L 4-*tert*-butylpyridine (tBP, 96%, Sigma-Aldrich) and 30 μ L of a 170 mg/mL bis(trifluoromethane)sulfonamide lithium salt (LiTFSI, 99.95%, Sigma-Aldrich) solution in acetonitrile. This solution was spin-coated dynamically at 1500 rpm for 45 s. In a second step the sample rotation was accelerated to 2000 rpm for 5 s to allow the solvent to dry completely. Before depositing the gold electrodes by evaporation,

3.4 Experimental Section

spiro-OMeTAD was left to oxidize in air overnight at room temperature and <20% relative humidity.

Characterization details:

X-ray diffraction analysis was carried out in reflection mode using a Bruker D8 Discover with Ni-filtered Cu-K α -radiation ($\lambda = 1.5406 \text{ \AA}$) and a position-sensitive semiconductor detector (LynxEye). The XRD patterns were offset in y-direction.

In-situ X-ray diffraction measurements were also performed on the Bruker D8 Discover with Ni-filtered Cu-K α -radiation ($\lambda = 1.5406 \text{ \AA}$) and a position-sensitive semiconductor detector (LynxEye). An Anton Paar heating stage (DHS1100) coupled to an Anton Paar TCU200 control unit was used. The sample was placed on the heating stage and covered with an X-ray transparent foil, which was flushed with N₂ (99.999%, Air Liquide) constantly during all temperature steps. The heating rate for this experiment was 60 °C/min.

Scanning electron microscopy images were acquired on a JEOL JSM-6500F microscope. The perovskite layer was deposited on FTO-coated glass. The latter was then fixed with silver paint on an aluminum holder. The silver paint was allowed to dry for 3 h in a desiccator. The samples were prepared 10 to 16 h before the measurement and were always stored in a desiccator with <20% relative humidity to avoid decomposition of the moisture-sensitive materials.

J-V curves were recorded with a Keithley 2400 sourcemeter under simulated AM 1.5 sunlight, calibrated to 100 mW/cm² with a Fraunhofer ISE certified silicon cell. The active area of the solar cells was defined with a square metal aperture mask of 0.0831 cm². The devices were light-soaked at 2 V for 10 s, and then they were scanned from forward to reverse bias with a step size of 50 mV and 100 ms setting time; then from short circuit to open circuit.

3 Control of perovskite crystal growth by methylammonium lead chloride templating

Time-of-flight (ToF) studies were performed by using a Nd:YAG laser with a pulse length of 7 ns and a repetition rate of 20 Hz, pumping an optical parametric oscillator (OPO) which allows for tuning of the excitation wavelength to 550 nm. All solar cell devices were illuminated from the transparent FTO side at ambient conditions and low laser light intensity (order of one sun). The generated photocurrent was detected via an oscilloscope after applying a bias voltage of 50 mV to force drifting of the charge carriers to the respective Au electrode.

FIB cross-sections were prepared with a JEOL JEM-9320 focused ion beam setup.

3.5 Literature

- [1] H. J. Snaith, *J. Phys. Chem. Lett.* **2013**, 3623.
- [2] M. Liu, M. B. Johnston, H. J. Snaith, *Nature* **2013**, 501, 395.
- [3] J. Burschka, N. Pellet, S.-J. Moon, R. Humphry-Baker, P. Gao, M. K. Nazeeruddin, M. Grätzel, *Nature* **2013**, 499, 316.
- [4] S. Kazim, M. K. Nazeeruddin, M. Grätzel, S. Ahmad, *Angew. Chem. Int. Ed.* **2014**, 126, 2854.
- [5] M. Xiao, F. Huang, W. Huang, Y. Dkhissi, Y. Zhu, J. Etheridge, A. Gray-Weale, U. Bach, Y.-B. Cheng, L. Spiccia, *Angew. Chem. Int. Ed.* **2014**, 126, 10056.
- [6] Z. Xiao, C. Bi, Y. Shao, Q. Dong, Q. Wang, Y. Yuan, C. Wang, Y. Gao, J. Huang, *Energy Environ. Sci.* **2014**, 7, 2619.
- [7] W. Nie, G. Gupta, B. K. Crone, F. Liu, D. L. Smith, P. P. Ruden, C.-Y. Kuo, H. Tsai, H.-L. Wang, H. Li, S. Tretiak, A. D. Mohite, *Adv. Sci.* **2015**, 2, 1.
- [8] G. E. Eperon, V. M. Burlakov, P. Docampo, A. Goriely, H. J. Snaith, *Adv. Funct. Mater.* **2013**, 151.
- [9] F. X. Xie, D. Zhang, H. Su, X. Ren, K. S. Wong, M. Grätzel, W. C. H. Choy, *ACS Nano* **2015**, 9, 639.
- [10] P. Docampo, J. M. Ball, M. Darwich, G. E. Eperon, H. J. Snaith, *Nat. Commun.* **2013**, 4, 2761.
- [11] M. A. Green, K. Emery, Y. Hishikawa, W. Warta, E. D. Dunlop, *Prog. Photovoltaics* **2015**, 23, 1.
- [12] N. J. Jeon, J. H. Noh, Y. C. Kim, W. S. Yang, S. Ryu, S. I. Seok, *Nat. Mater.* **2014**, 13, 897.
- [13] H. Zhou, Q. Chen, G. Li, S. Luo, T.-b. Song, H.-S. Duan, Z. Hong, J. You, Y. Liu, Y. Yang, *Science* **2014**, 345, 542.
- [14] M. Saliba, K. W. Tan, H. Sai, D. T. Moore, T. Scott, W. Zhang, L. A. Estroff, U. Wiesner, H. J. Snaith, *J. Phys. Chem. C* **2014**, 118, 17171.
- [15] K. W. Tan, D. T. Moore, M. Saliba, H. Sai, L. A. Estroff, T. Hanrath, H. J. Snaith, U. Wiesner, *ACS Nano* **2014**, 8, 4730.
- [16] W. Nie, H. Tsai, R. Asadpour, J.-C. Blancon, A. J. Neukirch, G. Gupta, J. J. Crochet, M. Chhowalla, S. Tretiak, M. A. Alam, H.-L. Wang, A. D. Mohite, *Science* **2015**, 347, 522.

- [17] X. Wu, M. T. Trinh, D. Niesner, H. Zhu, Z. Norman, J. S. Owen, O. Yaffe, B. J. Kudisch, X. Zhu, *J. Am. Chem. Soc.* **2015**, *137*, 2089.
- [18] N. K. Noel, A. Abate, S. D. Stranks, E. Parrott, V. Burlakov, A. Goriely, H. J. Snaith, *ACS Nano* **2014**, *8*, 9815.
- [19] F. K. Aldibaja, L. Badia, E. Mas-Marza, R. S. Sanchez, E. M. Barea, I. Mora-Sero, *J. Mater. Chem. A* **2015**, *3*, 9194.
- [20] Y. Li, W. Sun, W. Yan, S. Ye, H. Peng, Z. Liu, Z. Bian, C. Huang, *Adv. Funct. Mater.* **2015**, *25*, 4867.
- [21] V. L. Pool, A. Gold-Parker, M. D. McGehee, M. F. Toney, *Chem. Mater.* **2015**, *27*, 7240.
- [22] P. Docampo, F. Hanusch, S. D. Stranks, M. Döblinger, J. M. Feckl, M. Ehrensperger, N. K. Minar, M. B. Johnston, H. J. Snaith, T. Bein, *Adv. Energy Mater.* **2014**, *4*, 1400355.
- [23] A. E. Williams, P. J. Holliman, M. J. Carnie, M. L. Davies, D. A. Worsley, T. M. Watson, *J. Mater. Chem. A* **2014**.
- [24] J. S. Manser, B. Reid, P. V. Kamat, *The Journal of Physical Chemistry C* **2015**, *119*, 17065.
- [25] H. P. Wirges, *Chem. Ing. Tech.* **1995**, *67*, 1513.
- [26] C. Huang, N. Fu, F. Liu, L. Jiang, X. Hao, H. Huang, *Sol. Energy Mater. Sol. Cells* **2016**, *145*, Part 3, 231.
- [27] W. Ostwald, *Z. Phys. Chem.* **1897**, 289.
- [28] L. Chi, I. Swainson, L. Cranswick, J.-H. Her, P. Stephens, O. Knop, *J. Solid State Chem.* **2005**, *178*, 1376.
- [29] C. C. Stoumpos, C. D. Malliakas, M. G. Kanatzidis, *Inorg. Chem.* **2013**, *52*, 9019.
- [30] D. Liu, T. L. Kelly, *Nat. Photonics* **2014**, *8*, 133.
- [31] S. Tiwari, N. C. Greenham, *Opt. Quantum Electron.* **2009**, *41*, 69.
- [32] D. Shi, V. Adinolfi, R. Comin, M. Yuan, E. Alarousu, A. Buin, Y. Chen, S. Hoogland, A. Rothenberger, K. Katsiev, Y. Losovyj, X. Zhang, P. A. Dowben, O. F. Mohammed, E. H. Sargent, O. M. Bakr, *Science* **2015**, *347*, 519.
- [33] N.-G. Park, *Mater. Today*.
- [34] Y. Chen, J. Peng, D. Su, X. Chen, Z. Liang, *ACS App. Mater. Interfaces* **2015**, *7*, 4471.
- [35] C. Wehrenfennig, G. E. Eperon, M. B. Johnston, H. J. Snaith, L. M. Herz, *Adv. Mater.* **2014**, *26*, 1584.

3.5 Literature

- [36] T. J. Savenije, C. S. Ponseca, L. Kunneman, M. Abdellah, K. Zheng, Y. Tian, Q. Zhu, S. E. Canton, I. G. Scheblykin, T. Pullerits, A. Yartsev, V. Sundström, *The Journal of Physical Chemistry Letters* **2014**, 5, 2189.
- [37] M. M. Lee, J. Teuscher, T. Miyasaka, T. N. Murakami, H. J. Snaith, *Science* **2012**, 338, 643.
- [38] J. M. Ball, M. M. Lee, A. Hey, H. J. Snaith, *Energy & Environmental Science* **2013**, 6, 1739.

4 Stabilization of the Trigonal High Temperature Phase of Formamidinium Lead Iodide

This chapter is based on the following publication:

Andreas Binek, Fabian C. Hanusch, Pablo Docampo and Thomas Bein, *The Journal of Physical Chemistry Letters*, **2015**, 6, 1249-1253.

4.1 Introduction

With the recent rise in awareness of environmental and energy issues, the development of renewable energy sources have been the focus of a large number of research groups. Over the last two years, solar cells based on alkylammonium lead halide perovskites have distinguished themselves as a highly efficient and inexpensive photovoltaic technology.^[1-4] Since these materials are solution processable in a facile way at low temperatures, solar cells on flexible substrates can be prepared with high photovoltaic performance.^[5-8] Current state-of-the-art devices are based on the methylammonium lead iodide (MAPbI₃) perovskite, with a certified power conversion efficiency (PCE) of 19.3%.^[9]

However, the long-term stability of the prepared devices is an open question since MAPbI₃ undergoes a reversible phase transition between tetragonal and cubic symmetry in a temperature range between 54 and 57 °C, corresponding to common solar cell operating temperatures during summer.^[10] This structural phase transition is expected to influence the electronic band structure of the material and therefore impact the photovoltaic properties.^[10] In order to achieve a stable solar cell in the long term, the development of a perovskite without temperature-induced phase transitions in this temperature range is required.

4.1 Introduction

The exchange of the organic cation of the perovskite from methylammonium (MA) to formamidinium (FA) results in a material with either a trigonal structure (black color, α -phase) or a hexagonal structure (yellow color, δ -phase) depending on the synthesis temperature. For the δ -phase, no significant phase transition is expected within the solar cell operating temperature range since the phase transition from the δ -phase to the α -phase takes place at around 125 °C.^[11] Furthermore, the larger cation influences the metal-halide-metal bond angle, which leads to a narrower bandgap relative to MAPbI₃.^[12] Therefore, FAPbI₃ is closer to the optimum bandgap for a single junction solar cell derived from the Shockley-Queisser limit, which in turn leads to potentially higher theoretical efficiencies.^[13] Pellet and co-workers used this concept to extend the optical-absorption onset of MAPbI₃ into the red region by incorporating FA into the structure.^[14] Jeon *et al.* have recently adapted this strategy by mixing FAPbI₃ with MAPbBr₃, achieving power conversion efficiencies of 18%.^[15] However, in this instance, one of advantages of using FAPbI₃, i.e. its narrower bandgap, is lost by the combination with a bromide compound.^[16, 17] Moreover, the introduction of bromide will per se change the lattice constant of the perovskite, thus making it more challenging to isolate the impact of the inclusion of methylammonium in the structure. Additionally, the devices developed in Jeon *et al.*'s study incorporate a mesoporous titania photoanode, which could precludes its inclusion in tandem or flexible applications. Concluding from Pellet's and Jeon's studies, a transition from tetragonal (i.e. similar to MAPbI₃) to trigonal symmetry (i.e. similar to α -FAPbI₃) is observed when the methylammonium content in the structure is reduced to below 20%.^[14, 15]

Here, we explore this route to stabilize the α -phase of FAPbI₃ for its application in planar heterojunction solar cells without the need for high annealing temperatures. We show that incorporation of a smaller cation (MA) with a high dipole moment stabilizes the trigonal phase of FAPbI₃ without any lattice shrinkage or changes in the optical properties. We ascribe

this finding to the enhancement of I-H hydrogen bonds between the cation and the inorganic cage or to an increase of the Madelung energy of the structure. Thereby, the δ -phase transition can be completely suppressed as shown by temperature-dependent X-ray diffraction. Our results help to elucidate the origin of the improved performance and the stability of the newly developed systems.

4.2 Results and Discussion

The stabilized FAPbI₃ samples were prepared via a two-step deposition/conversion process. A layer of lead iodide (PbI₂) was initially deposited on an FTO covered glass substrate via spin-coating and subsequently converted into the perovskite phase in a second step by immersion in a solution of 85% FAI and 15% MAI in isopropanol (IPA). In order to illustrate the differences between MAPbI₃ and FAPbI₃, the crystal structures of the starting material, PbI₂, as well as of MAPbI₃ and FAPbI₃ are shown in Figure 4-1. For PbI₂, the PbI₆ octahedra are connected via a shared plane of three iodide ions. Through the incorporation of MA, the layered octahedra form a 3D-network by reducing the number of shared iodide ions from three to only one. However, at room temperature the octahedra are not perfectly aligned, which results in an identical twist of every second octahedral layer in the *c*-direction. When the temperature increases, the unit cell expands and the octahedra will arrange perfectly along the *c*-axis. This effect can also be observed when filling the unit cell with a mixture of MA and FA. While still maintaining the tetragonal room temperature structure, the unit cell is enlarged. This was observed in X-ray diffraction measurements by a shift of the diffraction pattern to lower angles.^[14] With more than 80% of FA in the perovskite structure, the tetragonal symmetry collapses and the trigonal structure of α -FAPbI₃ is formed. In this configuration the octahedra form a 3D-network. However, at room temperature the neat FAPbI₃ compound can also crystalize in a hexagonal structure (δ -FAPbI₃), where the

4.2 Results and Discussion

octahedra form a network similar to PbI_2 . In Figure 4-1b and c the XRD patterns of the synthesized yellow FAPbI_3 and stabilized black FAPbI_3 , and their theoretical patterns^[11] are illustrated.

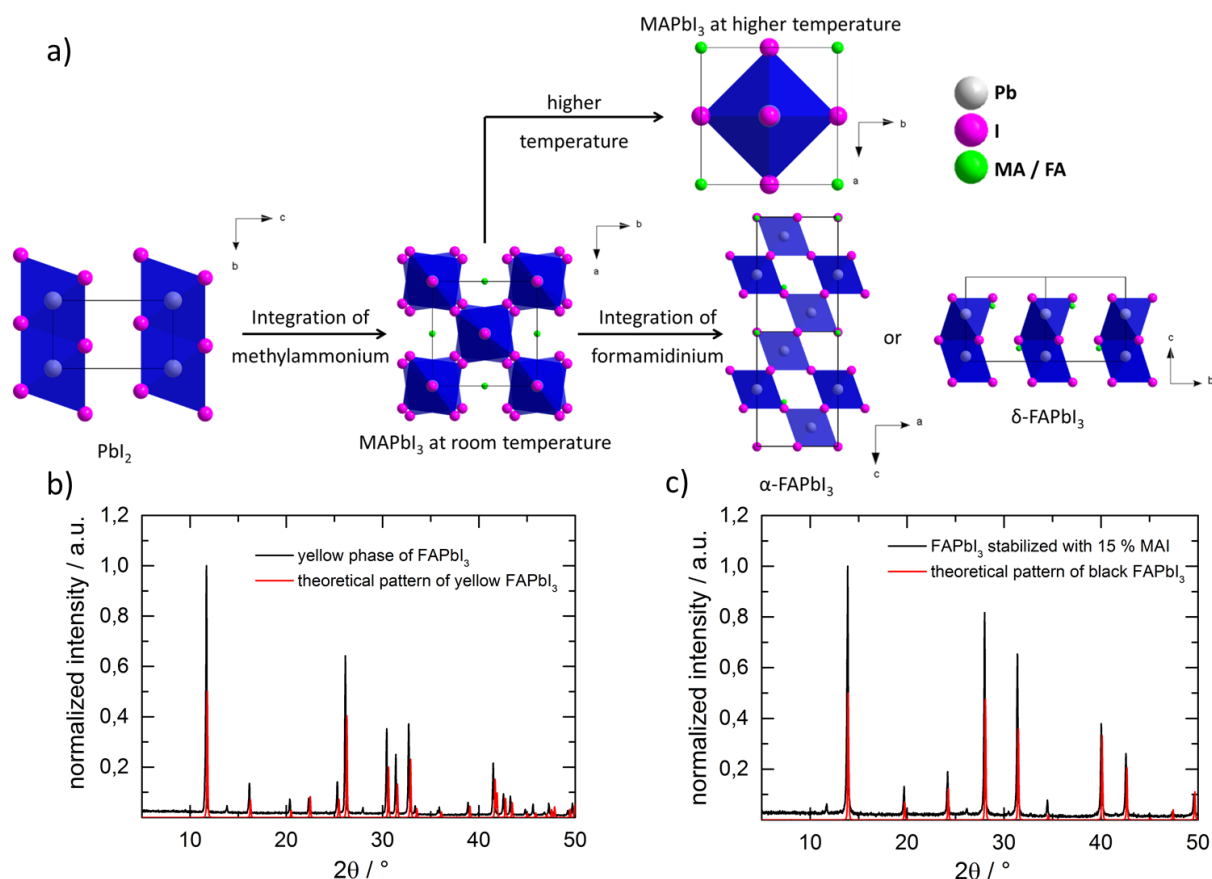


Figure 4-1: Crystal structure of PbI_2 and MAPbI_3 at different temperatures, $\alpha\text{-FAPbI}_3$ and $\delta\text{-FAPbI}_3$ (a) and the corresponding wide angle XRD pattern of the yellow δ -phase (b) and the stabilized black α -phase (c) of FAPbI_3 . The intensity of the theoretical patterns was reduced by half to illustrate the comparison of the XRD patterns.

The comparison of theoretical and experimental XRD patterns for the prepared samples shows that both FAPbI_3 structures were successfully prepared. In order to monitor the stabilization of the α -phase of FAPbI_3 , temperature-dependent X-ray diffraction measurements were performed on both a non-stabilized and a stabilized sample. The phase transition can be observed in the shift of the main reflection to higher angles (from 5.4° 2θ to 6.3° 2θ), since the unit cell of the α -phase is larger than the unit cell of the δ -phase.

4 Stabilization of the Trigonal High Temperature Phase of Formamidinium Lead Iodide

Temperature-dependent XRD measurements with powder samples (Figure 4-2) were performed with a molybdenum source. The diffraction pattern is therefore shifted to lower angles compared to the XRD patterns in Figure 4-1, which were obtained using Cu-K α radiation. The main reflection for the δ -phase is at $5.4^\circ 2\theta$ and for the α -phase this reflection is at $6.3^\circ 2\theta$.

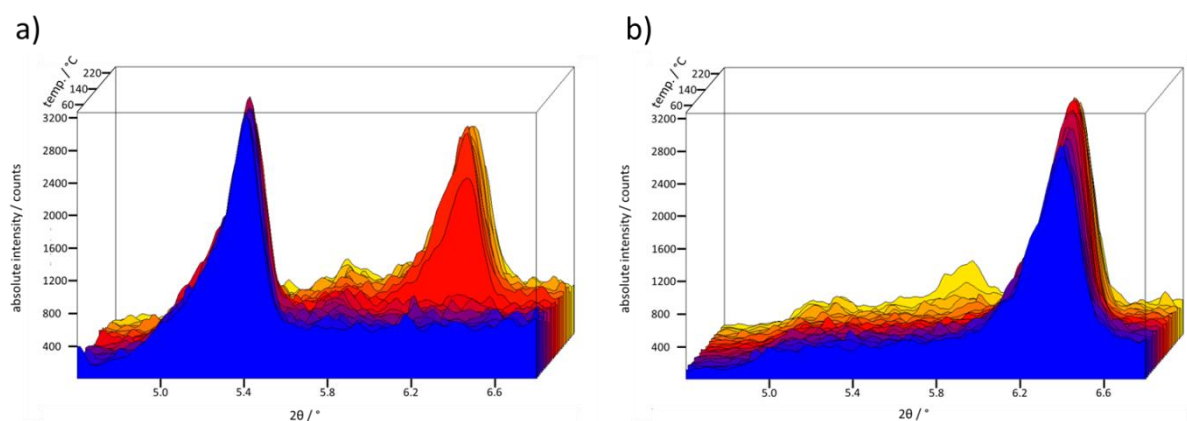


Figure 4-2: Temperature-dependent X-ray diffraction measurements of non-stabilized FAPbI₃ with phase transition (a) and stabilized FAPbI₃ (b) without phase transition.

In the non-stabilized sample, the phase transition occurs at 130°C , which is slightly higher than the observed temperature for single crystals of FAPbI₃ (125°C).^[11] The phase transition was reversible, where upon cooling down to room temperature the sample returned to the original δ phase. The measurement of the MA-stabilized sample of FAPbI₃ was performed in the same temperature range. In contrast to the neat FAPbI₃ sample, no phase transition from the trigonal α -FAPbI₃ was observed in this temperature range. We note here that previous studies demonstrate phase pure α -FAPbI₃ at room temperature,^[10] however these films were prepared on mesoporous TiO₂. The use of a mesoporous scaffold may influence the crystal structure of the perovskite and possibly alter its phase transition due to the confinement in TiO₂ mesopores.^[18] The sample preparation and the temperature-dependent XRD measurements were performed under a nitrogen atmosphere, and thus the influence of water

4.2 Results and Discussion

can be excluded as a cause for the formation of δ -FAPbI₃. At concentrations of MA below 15% in the conversion solution, both α -FAPbI₃ and δ -FAPbI₃ were formed, see Figure 4-3.

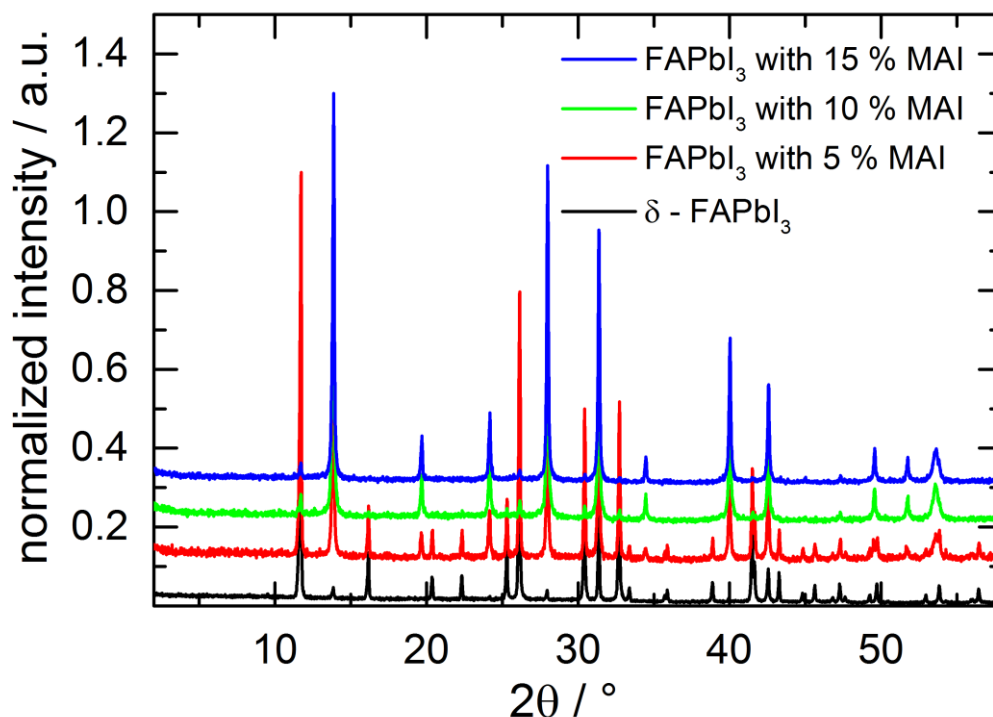


Figure 4-3: XRD patterns of pure yellow δ -FAPbI₃ and stabilized FAPbI₃ with different MAI concentrations.

The disappearance of the yellow δ -FAPbI₃ phase can also be monitored via the SEM micrographs in Figure 3 d-f. Here, the needle-like crystals formed at lower MA content can be assigned to the δ -FAPbI₃ phase, as they correlate with the disappearance of the XRD reflections corresponding to the hexagonal structure when α -FAPbI₃ is stabilized with higher amounts of MA.

The photophysical properties of the materials were measured to further understand the origin of the higher photovoltaic performance. The photoluminescence (PL) spectra of the stabilized samples are illustrated in Figure 4-4a. In the non-stabilized samples, a PL emission maximum at 798 nm can be observed. With increasing MAI content, the emission is shifted and matches

the position of neat α -FAPbI₃ at 813 nm with 10% MAI and 15% MAI in the conversion solution. For the neat δ -phase the PL signal was below the detection limit of the instrument and is therefore not shown. Additionally, time-correlated single photon counting (TCSPC) measurements were performed to obtain the lifetime of the photoexcited species in the prepared films. Figure 4-4b shows the drastic increase in lifetime for samples with 10% and 15% MAI compared to the non-stabilized FAPbI₃, the neat α -FAPbI₃ and the 5% MAI sample. This striking difference in lifetime can be attributed to the stabilization of the crystal structure of α -FAPbI₃ and the disappearance of the δ -phase. We note here that the decay dynamics found for the neat α -FAPbI₃ compound are very similar to those found for the standard MAPbI₃ compound.^[19] As already mentioned above, both structures of FAPbI₃ were observed in the XRD measurements for samples with lower MA concentration, with a large number of grain boundaries between both phases. In these crossover samples, traps for the photoexcited species may be located and recombination can occur.^[20] By reducing the number of grain boundaries in the perovskite layer, the lifetime of the photoexcited species can be enhanced. Similar behavior was also reported for a passivation of surface trap states in MAPbI₃.^[21]

4.2 Results and Discussion

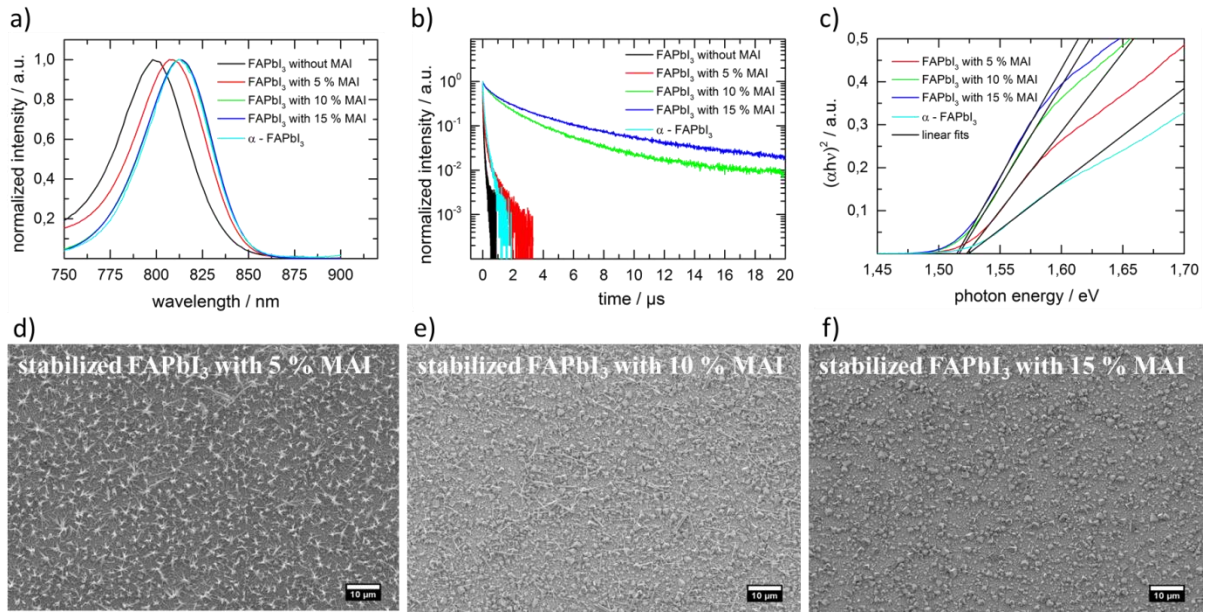


Figure 4-4: Photoluminescence measurements (a), time-correlated single photon counting measurements (b) and Tauc-plots (c) of samples with different concentration of MAI. The estimated bandgap for all MAI concentrations and α -FAPbI₃ is 1.52 ± 0.02 eV. SEM micrographs of stabilized FAPbI₃ with 5% MAI (d), 10% MAI (e) and 15% MAI (f). With increasing MA content the needle-like structure disappears and is replaced by a cubic structure.

The corresponding UV-Vis measurements are shown in Figure 4-5. By fitting the linear part of the plots, a bandgap of 1.52 ± 0.02 eV was estimated for all films (Figure 4-4). The bandgap energy found for the films presented here is in good agreement with the value of 1.48 eV estimated by Eperon and coworkers.^[16]

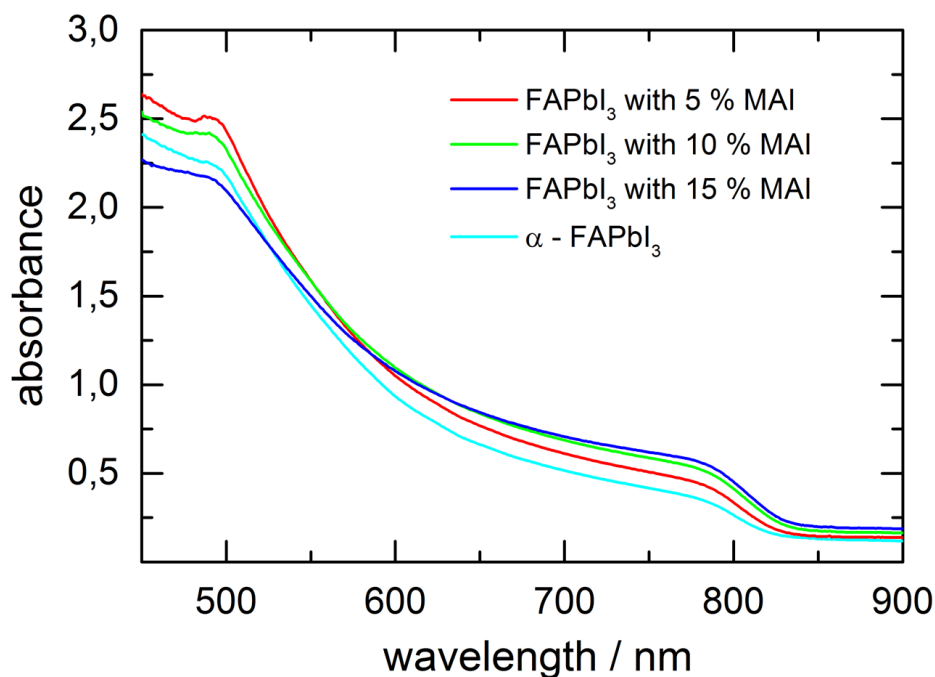


Figure 4-5: UV-Vis measurements of α -FAPbI₃ and stabilized FAPbI₃ with different concentrations of MAI.

Since the bandgap of the prepared films was found to be the same for all MAI contents, there is a possibility that no MA was introduced in the crystal structure. To probe this, we performed elemental analysis of the stabilized sample. Neat FAPbI₃ should have a nitrogen content of 4.5% and a carbon content of 1.9% of the total compound mass; however, in the stabilized FAPbI₃ prepared by substitution with 15% MAI relative to FAI in the conversion solution, the nitrogen content is lower (4.2%) and the carbon content is higher (2.1%), which corresponds to a composition of FA_{0.87}MA_{0.13}PbI₃.

The stabilization of the α -phase of FAPbI₃ can also be monitored in the performance of the solar cells with different MAI concentrations. With increasing MAI content, the short circuit current (J_{SC}), the open circuit voltage (V_{OC}) and the fill factor (FF) is enhanced (Figure 4-6). The most efficient device contains 15% MAI and exhibits a high short circuit current of 15.7 mA and a fill factor of 56% with a voltage of 1 V, resulting in power conversion efficiency (η) of 8.7%. We note here that the maximum performance of the devices prepared

4.2 Results and Discussion

in this work is limited by the rough perovskite layer. The SEM micrographs shown in Figure 4-4d-f show a full surface coverage for all prepared samples, while all samples exhibit similar absorbance (Figure 4-5). We can therefore exclude shunting between the electron and hole selective contacts or thickness variations as the causes for the differences in short circuit current for the prepared devices. However, the needle-like crystals lying on top of the perovskite layer suggest the formation of the hexagonal structure of FAPbI₃ at this interface. This wide-bandgap material may then reduce charge transfer from α -FAPbI₃ into the hole transporter and consequently diminish the charge collection efficiency, thus accounting for the observed short circuit photocurrent differences.

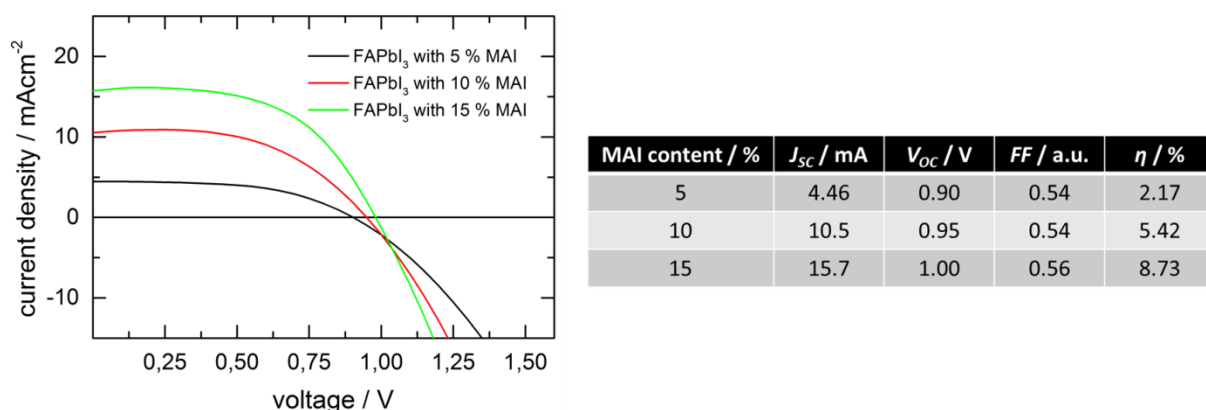


Figure 4-6: *J-V* curves for devices with different MAI content measured under AM 1.5 solar irradiation conditions. The table summarizes the photovoltaic parameters (short circuit current, J_{sc} ; open circuit voltage, V_{oc} ; fill factor, FF ; and power conversion efficiency, η).

In order to understand the stabilization of the α -phase of FAPbI₃, we consider two possibilities. Firstly, the structure can be made more stable by increasing the number of hydrogen bonds between the iodide ions and the hydrogen of the ammonium moiety in the cation. The probability of hydrogen bond formation may be related to the number of hydrogen atoms of the molecule, and with four FA ions present in the pseudocubic α -FAPbI₃ unit cell^[22], bearing 4 hydrogen atoms each, this is already quite likely. However, molecules with a higher dipole moment tend to form stronger hydrogen bonds.^[22, 23] Since MA exhibits a

4 Stabilization of the Trigonal High Temperature Phase of Formamidinium Lead Iodide

dipole moment ten times higher than FA, 2.3 Debye compared with 0.21 Debye,^[24] with 3 hydrogen atoms, we suggest that it is more likely that stronger hydrogen bonds are formed when MA is introduced into the α -FAPbI₃ structure. The low dipole moment in FA is due to the resonance-stabilization of the structure.^[24] In this case, the electron density is homogeneous distributed over the nitrogen-carbon-nitrogen bond as reported by Frost *et al.*^[24] In contrast, the electron density of the MA molecule is concentrated at the nitrogen atom. Secondly, the structure can be made more stable through the increase of the Madelung energy.^[25] Since the Coulombic interaction between charges and dipoles is proportional to the strength of the dipole, in this second scenario it is possible that the stronger interaction between MA and the lead iodide octahedra results in an increase of the Madelung energy and therefore to an enhanced stability of the system.^[26] Both cations and their interactions with the inorganic “cage” are shown in Figure 4-7.

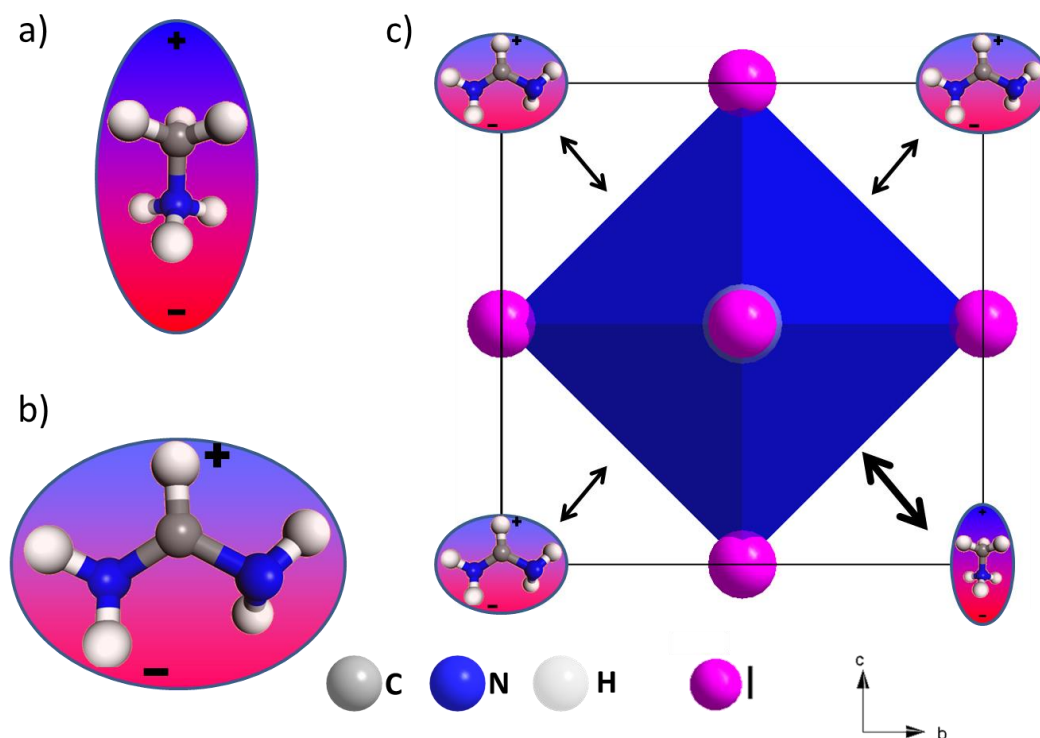


Figure 4-7: Illustration of the dipole moments of MA (a) and FA (b) and their different influence on the inorganic cage of the perovskite (c).

4.4 Experimental Section

4.3 Conclusion

Summarizing, we have studied the phase transition of the yellow δ -phase to the dark α -phase of FAPbI_3 in perovskite films prepared by a 2-step deposition/conversion method. By exchanging a small amount of 15% MA relative to FA in the immersion solution, we show that the resulting films exhibit a fully stabilized α phase in the temperature range studied (25-250 °C). Elemental analysis of the prepared samples shows a composition of $\text{FA}_{0.87}\text{MA}_{0.13}\text{PbI}_3$. Strikingly, no accompanying lattice shrinkage was observed, while the transition to the yellow δ -phase of FAPbI_3 was completely suppressed in the temperature range examined. We suggest that the smaller MA cation, which exhibits a dipole moment 10 times larger than FA, stabilizes the 3D arrangement of the PbI_6 octahedra with a pseudocubic symmetry via I-H hydrogen bonding and/or the increase of Coulomb interactions within the structure. This results also in additional benefits for solar cell performance in the form of a drastic increase of the lifetime of the photoexcited species generated within the film, and a corresponding high device performance. The dipole moment of the cation is an important parameter for the formation of hybrid perovskites and therefore this approach is expected to be suitable for the stabilization of other perovskite systems for further enhancement of the crystallization of the active layer and their application in photovoltaic devices.

4.4 Experimental Section

Preparation of the precursors

Methylammonium iodide was prepared by adapting a recipe published earlier.^[8] In short, 24 mL of methylamine solution (33% in ethanol, Sigma-Aldrich) was diluted with 100 mL of absolute ethanol in a 250 mL roundbottom flask. To this solution, 10 mL of hydroiodic acid

4 Stabilization of the Trigonal High Temperature Phase of Formamidinium Lead Iodide

(33 wt%) was added under constant stirring. After a reaction time of one hour at room temperature, the solvents were removed by rotary evaporation. The obtained white solid was washed with dry diethyl ether and finally recrystallized from ethanol.

Solar cell preparation

Fluorine doped tin oxide (FTO) coated glass sheets (7 Ω /sq, Pilkington, USA) were patterned by etching with zinc powder and 3 M HCl. They were subsequently cleaned with a 2% Hellmanex solution and rinsed with de-ionized water, ethanol and acetone. Directly before applying the blocking layer, last organic residues were removed by an oxygen plasma treatment for 5 min. The dense TiO₂ layer was prepared from sol-gel precursor solution by spin-coating onto the substrates and calcining at 500 °C in air.^[1] For the sol-gel solution a 27.2 mM solution of HCl in 2-propanol was added dropwise to a vigorously stirred 0.43 mM solution of titanium isopropoxide (99.999%, Sigma-Aldrich) in 2-propanol. The solution stayed clear during the addition and was discarded otherwise.

The PbI₂ (99%, Sigma-Aldrich) layer was prepared by spin-coating 75 μ L of a 1 M PbI₂ solution in dry *N,N*-dimethylformamide (DMF, 99.8%, Sigma-Aldrich) onto the TiO₂-covered substrates at 3000 rpm for 15 s. To obtain smooth, homogeneous layers it was important to heat both, the PbI₂ solution and the substrates, to 60 °C before spin-coating and to perform the deposition dynamically with hot solution onto hot substrates.

The lead iodide layer was transformed into the stabilized FAPbI₃ perovskite by immersing it into a 20 mM solution of FAI (Dyesol) mixed with a 20 mM solution of MAI in isopropanol. The substrates were immersed into 40 ml of the solution. The mixing ratios of the different MAI concentrations are shown in Table 4-1.

4.4 Experimental Section

Table 4-1: Contents of FAI and MAI used to prepare the dipping solutions for the different MAI concentrations.

MAI concentration	FAI content	MAI content
5%	38 mL	2 mL
10%	36 mL	4 mL
15%	34 mL	6 mL

The solutions were heated up to 60 °C and the substrates were placed in the reaction vessel for 7 min. After taking the films out of the solution, they were washed in an isopropanol bath and carefully dried in a nitrogen stream.

Afterwards, the films were covered with a layer of spiro-OMeTAD (Borun Chemicals, 99.5% purity). Typically 100 mg of Spiro were dissolved in 1 mL chlorobenzene (99.8%, Sigma-Aldrich). The solution was filtered and mixed with 10 μ L 4-*tert*-butylpyridine (*t*BP, 96%, Sigma-Aldrich) and 30 μ L of a 170 mg/mL bis(trifluoromethane)sulfonamide lithium salt (LiTFSI, 99.95%, Sigma-Aldrich) solution in acetonitrile. This solution was spin-coated dynamically at 1500 rpm for 45 s. In a second step the sample rotation was accelerated to 2000 rpm for 5 s to allow the solvent to dry completely. Before evaporating the gold electrodes, spiro-OMeTAD was left to oxidize in air over night at room temperature and <20rel% humidity.

PL sample preparation

Perovskite samples for steady state and time resolved PL measurements were prepared as described in the preparations mentioned above. In this case non-conductive glass substrates were used and the perovskite was covered with a poly(methylmethacrylate) (PMMA) layer to prevent degradation by ambient moisture. The layer was deposited by spin coating 75 μ L of a 10 mg/mL solution of PMMA in chlorobenzene at 1000 rpm for 45 s.

4 Stabilization of the Trigonal High Temperature Phase of Formamidinium Lead Iodide

Characterization details:

The X-ray diffraction patterns were obtained on a Stoe powder diffractometer in transmission geometry (Cu-K α_1 , $\lambda = 1.5406 \text{ \AA}$) equipped with a position-sensitive Mythen-1K detector. The XRD patterns were offset in y-direction in order to better visualize changes in the crystal structure. The powder samples were prepared by removing films from glass substrates.

Steady-state absorption spectra were acquired with a Lambda 1050 UV-Vis spectrophotometer (Perkin Elmer) using an integration sphere.

Steady state and time resolved PL measurements were performed with a Fluotime 300 Spectrofluorometer (Picoquant GmbH). The excitation wavelength was fixed at 510 nm. The emission for time resolved measurements was monitored at the maximum intensity of the steady state photo-emission.

J-V curves were recorded with a Keithley 2400 sourcemeter under simulated AM 1.5 sunlight, calibrated to 100 mW/cm^2 with a Fraunhofer ISE certified silicon cell. The active area of the solar cells was defined with a square metal aperture mask of 0.0831 cm^2 .

Temperature-dependent powder diffraction experiments in the range of 25 to 400 °C were performed with a Stoe Stadi P powder diffractometer equipped with an imaging plate detector system using MoK α_1 radiation ($\lambda = 0.71093 \text{ \AA}$) in a modified Debye-Scherrer geometry. Powdered samples were filled into silica glass capillaries with 0.5 mm diameter and sealed under nitrogen atmosphere. During the measurements, the samples were heated up to 250 °C with a heating rate of 2 °C/min.

SEM images were acquired on a Jeol JSM-6500F microscope. The perovskite layer was deposited on FTO-coated glass. It was then fixed with silver paint on an aluminum holder. The silver paint was allowed to dry for 3 h in the desiccator. The samples were prepared 10 to

4.4 Experimental Section

16 h before the measurement and were always stored in a desiccator with <20% relative humidity to avoid decomposition of the moisture-sensitive material.

4.5 Literature

- [1] J. M. Ball, M. M. Lee, A. Hey, H. J. Snaith, *Energy & Environmental Science* **2013**, 6, 1739.
- [2] M. Liu, M. B. Johnston, H. J. Snaith, *Nature* **2013**, 501, 395.
- [3] J. Burschka, N. Pellet, S.-J. Moon, R. Humphry-Baker, P. Gao, M. K. Nazeeruddin, M. Grätzel, *Nature* **2013**, 499, 316.
- [4] S. Kazim, M. K. Nazeeruddin, M. Grätzel, S. Ahmad, *Angew. Chem.* **2014**, 126, 2854.
- [5] P. Docampo, J. M. Ball, M. Darwich, G. E. Eperon, H. J. Snaith, *Nat. Commun.* **2013**, 4, 2761.
- [6] J. You, Z. Hong, Y. Yang, Q. Chen, M. Cai, T.-B. Song, C.-C. Chen, S. Lu, Y. Liu, H. Zhou, Y. Yang, *ACS Nano* **2014**, 8, 1674.
- [7] Y.-F. Chiang, J.-Y. Jeng, M.-H. Lee, S.-R. Peng, P. Chen, T.-F. Guo, T.-C. Wen, Y.-J. Hsu, C.-M. Hsu, *PCCP* **2014**, 16, 6033.
- [8] M. M. Lee, J. Teuscher, T. Miyasaka, T. N. Murakami, H. J. Snaith, *Science* **2012**, 338, 643.
- [9] H. Zhou, Q. Chen, G. Li, S. Luo, T.-b. Song, H.-S. Duan, Z. Hong, J. You, Y. Liu, Y. Yang, *Science* **2014**, 345, 542.
- [10] T. Baikie, Y. N. Fang, J. M. Kadro, M. Schreyer, F. X. Wei, S. G. Mhaisalkar, M. Graetzel, T. J. White, *J. Mater. Chem. A* **2013**, 1, 5628.
- [11] C. C. Stoumpos, C. D. Malliakas, M. G. Kanatzidis, *Inorg. Chem.* **2013**, 52, 9019.
- [12] M. R. Filip, G. E. Eperon, H. J. Snaith, F. Giustino, *Nat. Commun.* **2014**, 5, 5757.
- [13] W. Shockley, H. J. Queisser, *J. Appl. Phys.* **1961**, 32, 510.
- [14] N. Pellet, P. Gao, G. Gregori, T.-Y. Yang, M. K. Nazeeruddin, J. Maier, M. Grätzel, *Angew. Chem., Int. Ed.* **2014**, 53, 3151.
- [15] N. J. Jeon, J. H. Noh, W. S. Yang, Y. C. Kim, S. Ryu, J. Seo, S. I. Seok, *Nature* **2015**, 517, 476.
- [16] G. E. Eperon, S. D. Stranks, C. Menelaou, M. B. Johnston, L. Herz, H. Snaith, *Energy Environ. Sci.* **2014**, 7, 982.
- [17] J. H. Noh, S. H. Im, J. H. Heo, T. N. Mandal, S. I. Seok, *Nano Lett.* **2013**, 13, 1764.
- [18] J. J. Choi, X. Yang, Z. M. Norman, S. J. L. Billinge, J. S. Owen, *Nano Lett.* **2014**, 14, 127.

4.5 Literature

- [19] P. Docampo, F. C. Hanusch, S. D. Stranks, M. Döblinger, J. M. Feckl, M. Ehrensperger, N. K. Minar, M. B. Johnston, H. J. Snaith, T. Bein, *Adv. Energy Mater.* **2014**, 4.
- [20] X. Wu, M. T. Trinh, D. Niesner, H. Zhu, Z. Norman, J. S. Owen, O. Yaffe, B. J. Kudisch, X. Zhu, *J. Am. Chem. Soc.* **2015**, 137, 2089.
- [21] N. K. Noel, A. Abate, S. D. Stranks, E. Parrott, V. Burlakov, A. Goriely, H. J. Snaith, *ACS Nano* **2014**, 8, 9815.
- [22] A. Amat, E. Mosconi, E. Ronca, C. Quarti, P. Umari, M. K. Nazeeruddin, M. Grätzel, F. De Angelis, *Nano Lett.* **2014**, 14, 3608.
- [23] W. Li, A. Thirumurugan, P. T. Barton, Z. Lin, S. Henke, H. H. M. Yeung, M. T. Wharmby, E. G. Bithell, C. J. Howard, A. K. Cheetham, *J. Am. Chem. Soc.* **2014**, 136, 7801.
- [24] J. M. Frost, K. T. Butler, F. Brivio, C. H. Hendon, M. van Schilfgaarde, A. Walsh, *Nano Lett.* **2014**, 14, 2584.
- [25] E. Madelung, *Physikalische Zeitschrift* **1919**, 19, 524.
- [26] W. A. Harrison, *Electronic Structure and the Properties of Solids*, **1980**.

5 Efficient Planar Heterojunction Perovskite Solar Cells Based on Formamidinium Lead Bromide

This chapter is based on the following publication:

Fabian C. Hanusch, Erwin Wiesenmayer, Erich Mankel, Andreas Binek, Philipp Angloher, Christina Fraunhofer, Nadja Giesbrecht, Johann M. Feckl, Wolfram Jaegermann, Dirk Johrendt, Thomas Bein and Pablo Docampo, *The Journal of Physical Chemistry Letters*, **2014**, 5, 2791-2795.

Initial experiments and basic material characterization have been performed by Fabian Hanusch. Optimization of the sample preparation have been performed by Andreas Binek. Rietveld refinements have been performed by Erwin Wiesenmayer. XPS/UPS measurements have been performed by Erich Mankel.

5.1 Introduction

Solar cells based on alkylammonium lead halide perovskites have recently garnered a large amount of interest in the photovoltaics community.^[1] This class of materials exhibits a very high absorption coefficient of more than 10^4 cm^{-2} above their bandgap energy range and extremely long lifetimes of the charge carriers,^[2-5] making them comparable to established inorganic solar cell materials. One possible application of these materials is in tandem solar cells with a conventional Si or CIGS bottom cell, where the latter established technologies could be improved by as much as 30% in this configuration at almost no extra cost.^[6] Moreover, building-integrated photovoltaics can also benefit from absorber materials displaying different colors, i.e. band gaps.

5.2 Results and Discussion

Recently, Eperon *et al.* reported on the substitution of iodide with bromide for a formamidinium-based system.^[7] They observed a band gap of 2.23 eV for the resulting FAPbBr₃ material, which makes it a more suitable candidate for tandem applications than either MAPbBr₃ or MAPbI₃.^[6] Although high efficiency MAPbBr₃-based solar cells have been reported by Ryu *et al.*,^[8] their device architecture includes a high-temperature sintered titania layer, which makes them unsuitable for tandem and flexible applications. As our results show, a striking advantage of the FAPbBr₃ system is that it can be processed in a planar heterojunction configuration, without a mesoporous scaffold for charge extraction. In this material, the lifetime of photoexcited species, measured via TCSPC, is long enough to enable diffusion to the charge selective contacts and therefore efficient charge separation. The fabricated devices exhibit over 6.5 mA short circuit currents (J_{SC}), a 1.35 V open circuit voltage (V_{OC}) and an overall efficiency approaching 7%. This comparably high efficiency, in combination with its facile, low temperature processability makes FAPbBr₃ an ideal candidate for wide bandgap photovoltaics.

The structure of alkylammonium lead halide perovskites can be readily adjusted to tune the material's absorption and electronic properties. For example, elemental substitution of the halide can vary the material's bandgap in a range of 1.55 to 2.35 eV,^[9] extend the photoexcited species lifetime^[2, 10] and enhance charge transport through the layer.^[10, 11] The choice of the organic cation can also strongly impact the structural parameters and therefore the performance in photovoltaic devices.^[7, 12]

5.2 Results and Discussion

Here we focus on the cation exchange of methylammonium by formamidinium in lead bromide systems, resulting in the FAPbBr₃ perovskite structure. This material is very similar

to MAPbBr₃, which has been widely investigated over the last years, as both compounds crystallize in the pseudocubic perovskite structure $Pm-3m$.^[9, 11, 13]

Figure 5-1a shows the wide angle powder X-ray diffraction patterns for both materials. We have performed Rietveld analysis on these powder diffraction patterns and obtained the crystal structures shown in

Figure 5-1b. As previously reported for the MAPbBr₃ structure, the lead atoms are coordinated octahedrally by bromide with the organic cation sitting in the voids between the octahedra. However, due to its larger size, the FA cation spaces the PbBr₆ octahedra further. This increases the lattice constant from 5.92 Å for MAPbBr₃ to 5.99 Å for FAPbBr₃. The PbBr₆ octahedra share one corner with their nearest neighbor, where the Pb-Br-Pb bond angle deviates from the ideal value of 180° by about 15°. This displacement is visible in the crystal structure, where for each bromide ion two of the four possible positions are shown. The tilting of the rigid PbBr₆ building blocks leads to a higher degree of space filling and therefore to a higher stability of the whole structure.^[14, 15]

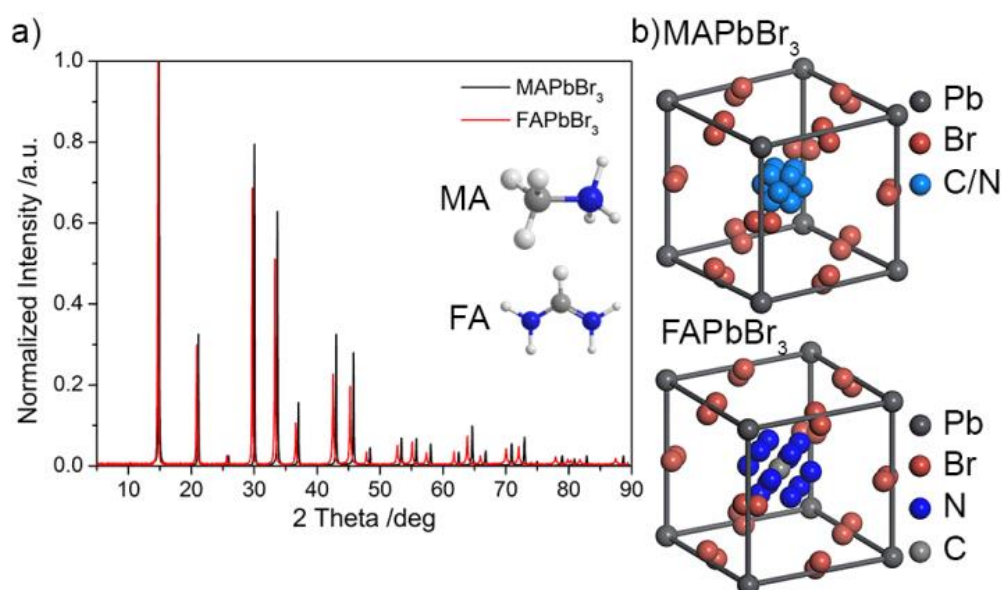


Figure 5-1: Wide angle XRD pattern of MAPbBr₃ and FAPbBr₃ (a) and refined crystal structures obtained from the XRD patterns (b). The rotation of the organic cations in the center of the unit cell is illustrated by 12 different positions for the nitrogen atoms.

While the lead and bromide ions form the stable backbone of the structure, the MA or FA ions can rotate in the center of the unit cell.^[16] The position of the carbon and nitrogen atoms cannot be precisely determined, since the cation is rotating freely along and perpendicular to the C-N axis.^[13] For the FAPbBr₃ the rotation center lies in the carbon atom, which is fixed in the center of the unit cell. The nitrogen atoms are distributed around the center in a distance of about 117 pm. The results of the Rietveld refinement, including the refined atom positions and fit parameters, are summarized in Table 5-1 and

Table 5-2.

Table 5-1: Results of the Rietveld refinement of MAPbBr₃.

MAPbBr ₃	
space group	<i>Pm-3m</i> (No.221)
<i>Z</i>	1
lattice parameter [Å]	5.923 (1)
volume [Å ³]	207.8 (1)

5 Efficient Planar Heterojunction Perovskite Solar Cells Based on Formamidinium Lead Bromide

atomic parameters		<i>x</i>	<i>y</i>	<i>z</i>	<i>occ</i>
Pb	1a	0	0	0	1
Br	12h	0	0.0724 (2)	0.5	0.25
C	12j	0.4143 (4)	0.4143 (4)	0.5	0.0833
N	12j	0.5857 (4)	0.5857 (4)	0.5	0.0833
U_{iso} [pm ²]		Pb		301 (2)	
		Br		241 (4)	
C/N not refined					
$R_{\text{wp}}/R_{\text{p}}$		2.747/2.036			
χ^2/R_{Bragg}		1.930/2.916			

Table 5-2: Results of the Rietveld refinement of FAPbBr₃.

FAPbBr ₃					
space group		<i>Pm-3m</i> (No.221)			
<i>Z</i>		1			
lattice parameter [Å]		5.992 (1)			
volume [Å ³]		215.2 (1)			
atomic parameters		<i>x</i>	<i>y</i>	<i>z</i>	<i>occ</i>
Pb	1a	0	0	0	1
Br	12h	0	0.0617 (3)	0.5	0.25
C	1b	0.5	0.5	0.5	1
N	12j	0.3633 (5)	0.3633 (5)	0.5	

5.2 Results and Discussion

U_{iso} [pm ²]	Pb	403 (3)
	Br	286 (6)
	C/N not refined	
$R_{\text{wp}}/R_{\text{p}}$	3.198/2.287	
χ^2/R_{Bragg}	2.115/2.342	

The SEM micrographs in Figure 5-2a,b show the high surface coverage of the prepared perovskite layers. The top-view images show a dense layer with no gaps and occasional larger crystals, which appear lighter in the micrograph. The same can be seen from the cross-section images in Figure 5-2c, where the perovskite layer uniformly coats the FTO substrate, without any dips or pinholes. It has been shown previously that a high degree of film coverage is beneficial for light absorption of the perovskite layers and is a requirement for efficiently working solar cells.^[17, 18] We have recently demonstrated that in the case of the methylammonium lead iodide perovskite, a high surface coverage can be achieved with a solution deposition-conversion technique.^[10] Here, the prepared MAPbBr₃ and FAPbBr₃ films consist of crystallites ranging from several tens to hundreds of nanometers in size. After the conversion, the film thickness is approximately 400 nm, as can be estimated from the cross section images in Figure 5-2c, and complete surface coverage is achieved.

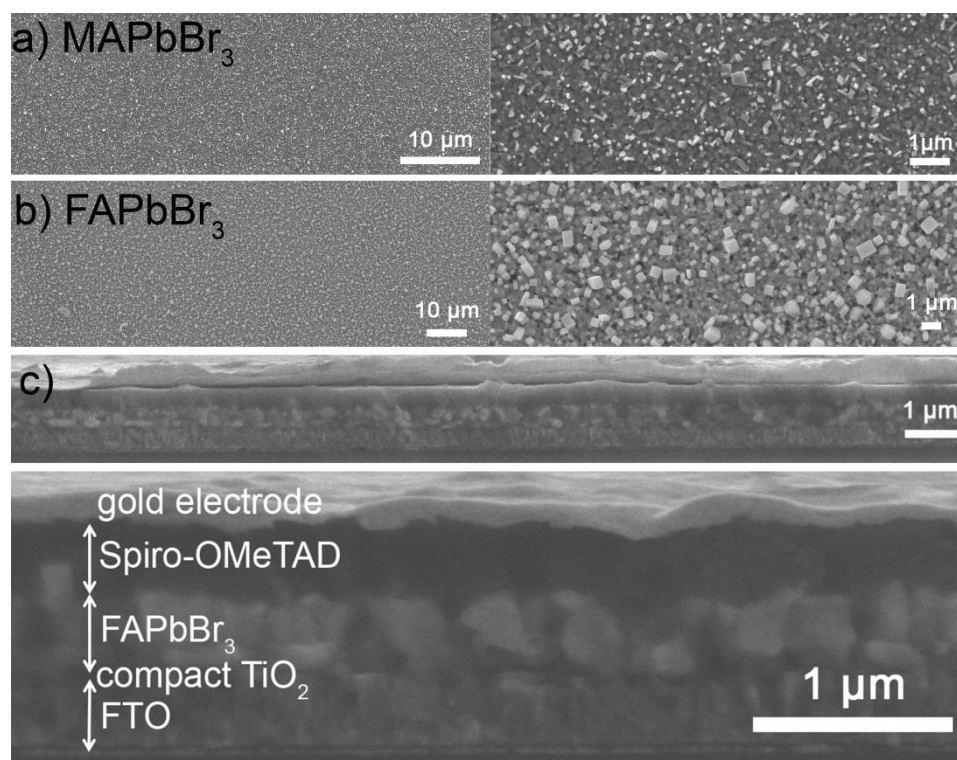


Figure 5-2: SEM top view micrographs of MAPbBr₃ (a) and FAPbBr₃ (b) films. Below cross section of a FAPbBr₃ film on a compact TiO₂ blocking layer, covered with spiro-OMeTAD and a gold electrode(c).

We have prepared solar cells based on these materials according to a previously reported layout.^[19] In short, FTO-coated glass slides were covered with a non-porous TiO₂ layer as the electron selective contact. Over this layer, the MAPbBr₃ or FAPbBr₃ layer was deposited via a deposition/conversion approach.^[10, 20] Firstly, a PbBr₂ film was deposited via spin-coating and was then immersed in MABr or FABr solutions in 2-propanol, respectively. The state-of-the-art p-type hole transporter spiro-OMeTAD was then deposited by spin-coating from chlorobenzene and the whole device was contacted with thermally evaporated gold electrodes under high vacuum. A scheme of the solar cell layout and the energy levels of the used materials are displayed in Figure 5-3a,b. The energy levels of FAPbBr₃ were obtained through ultraviolet photoelectron spectroscopy (UPS). The obtained spectra are depicted in Figure 5-4. The current voltage curves obtained for both types of materials are displayed in Figure 5-3c.

5.2 Results and Discussion

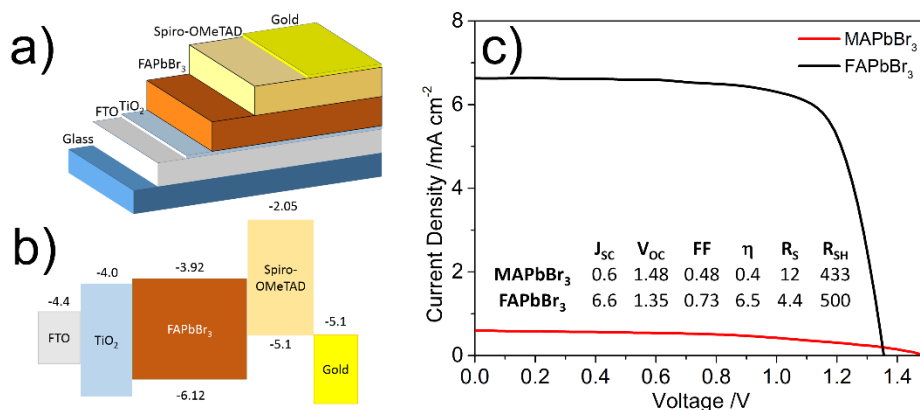


Figure 5-3: Schematic display of the prepared solar cell layout (a) and energy levels for all layers (b). The HOMO and LUMO levels for FAPbBr₃ were determined by ultraviolet photoelectron spectroscopy (UPS). *J-V* curves under AM1.5 solar irradiation conditions for both MAPbBr₃ (red) and FAPbBr₃ (black)-based solar cells (c). The inset table summarizes the photovoltaic parameters (short circuit current, J_{SC} (mAcm⁻²); open circuit voltage, V_{OC} (V); fill factor, *FF*; power conversion efficiency, η ; series resistance, R_s (Ohm cm²) and shunt resistance, R_{SH} (Ohm cm²)).

The energy levels of FAPbBr₃ were obtained through ultraviolet photoelectron spectroscopy (UPS). The obtained spectra are depicted in Figure 5-4, as well as a comparison for the energy level of both investigated materials (Figure 5-5).

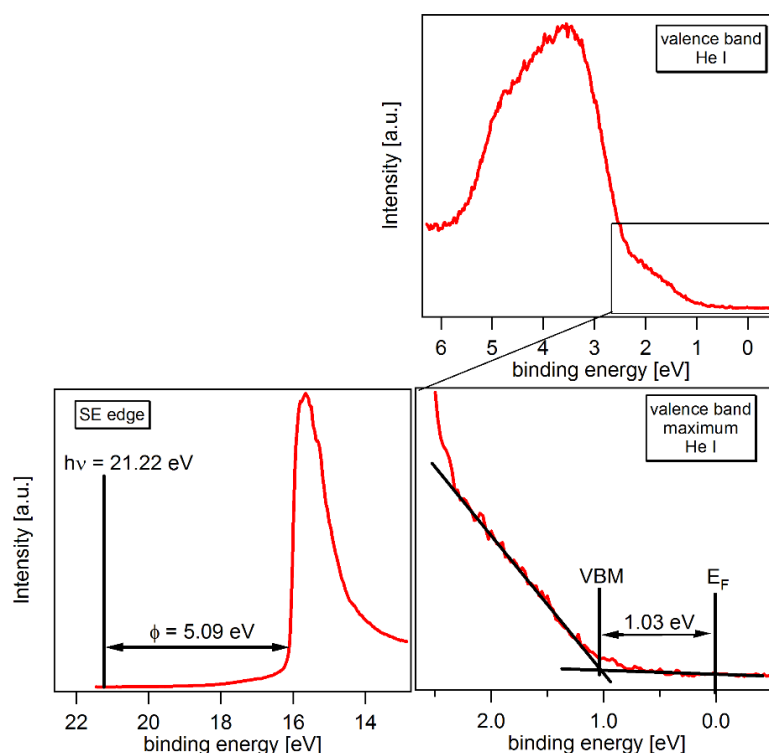


Figure 5-4: XPS spectra obtained for FAPbBr₃. The graph on the left describes the Fermi level E_F relative to vacuum. The images on the right show the energetic position of the valence band relative to the Fermi level E_F .

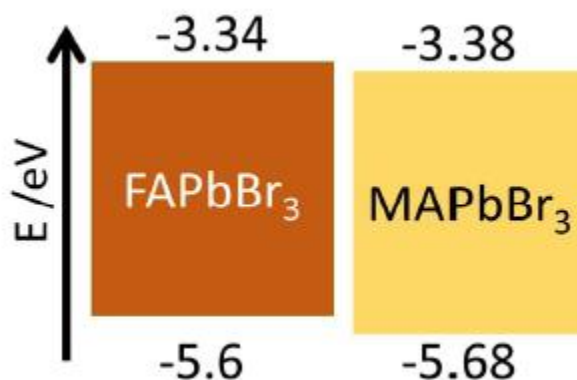


Figure 5-5: Comparison of the energy levels of FAPbBr₃ and MAPbBr₃. The values for MAPbBr₃ were taken from literature.^[21]

The current voltage curves obtained for both types of materials are displayed in Figure 5-3c. Additionally, forward and backward scans for FAPbBr₃ are shown in Figure 5-6.

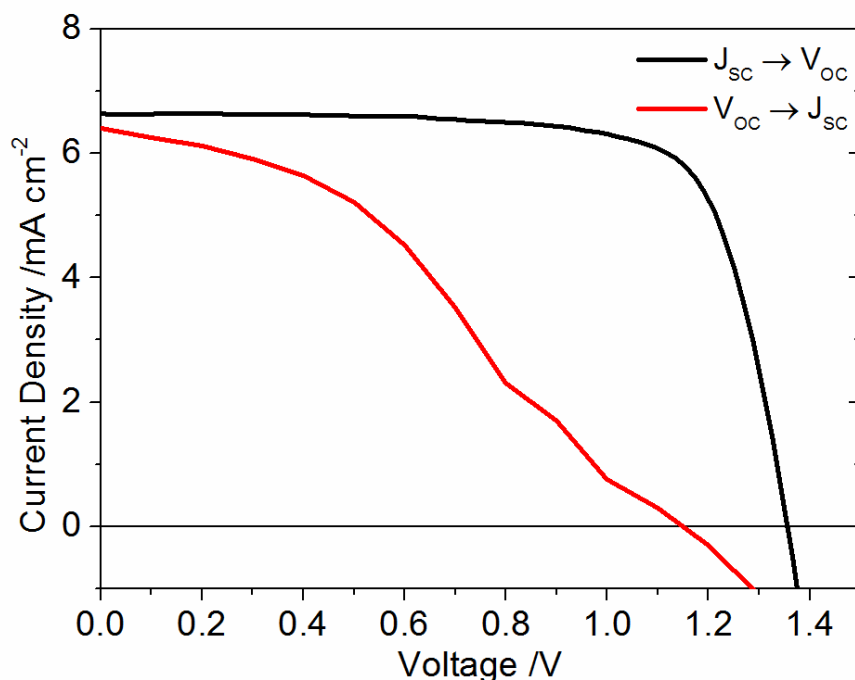


Figure 5-6: Forward and backward current-voltage sweep for a FAPbBr₃ solar cell.

The MAPbBr₃ solar cells show a very high open circuit voltage of 1.5 V, matching previously reported record values. Both, the short circuit current and fill factor, however, are low, compared to the theoretical maximum, resulting in a power conversion efficiency of only 0.4%. The FAPbBr₃ devices, on the other hand, exhibit high short circuit currents of over 6.5 mA and a fill factor exceeding 70%. Additionally the FAPbBr₃ devices exhibit lower series resistance compared to the MAPbBr₃ devices and also highly efficient MAPbI₃ prepared in a similar way in our laboratory.^[10] This compensates for the slightly lower voltage of 1.35 V and results in an overall power conversion efficiency of 6.5%. Statistics on a batch of 36 solar cells are depicted in Figure 5-7.

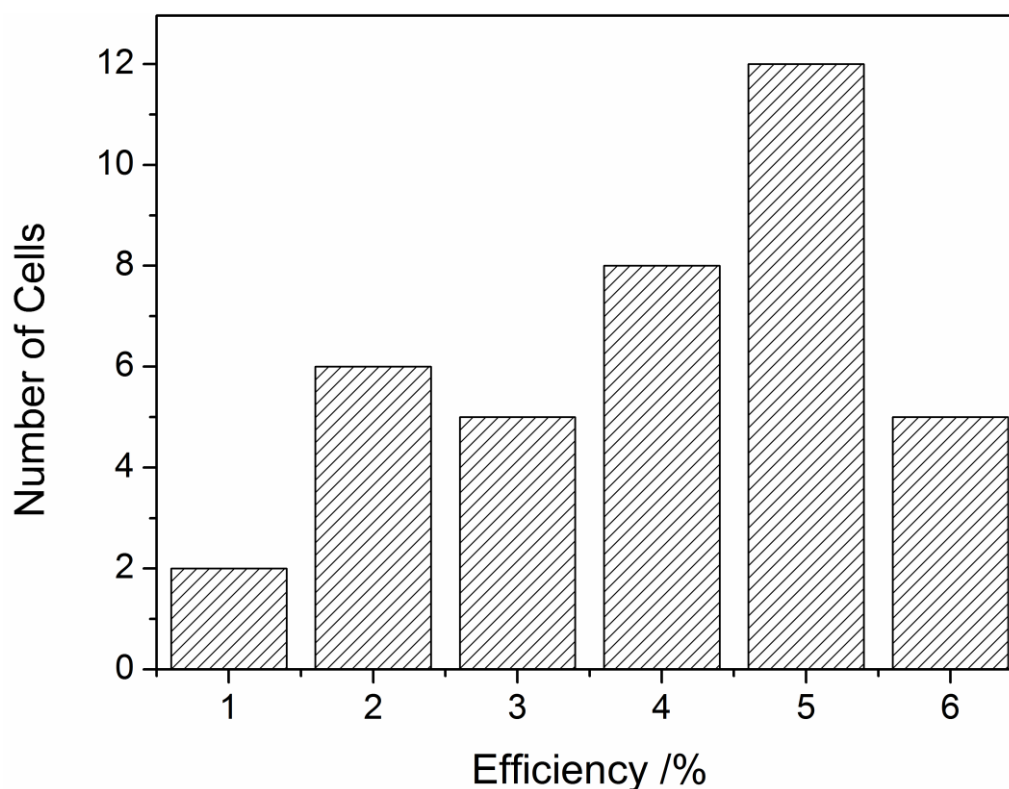


Figure 5-7: Power conversion efficiency (PCE) histogram of a batch of 40 devices.

We can attribute the lower voltage to the narrower band gap of the FAPbBr_3 of 2.26 eV compared to 2.34 eV for the MA compound. We note here that the open circuit voltage of the devices is limited to a large extent by the use of spiro-OMeTAD, which exhibits a HOMO level of 5.1 eV. This energy level is optimum for the MAPbI_3 perovskite, but in the systems presented here, this results in a rather large voltage loss. Hence, before high voltage perovskite solar cells can be achieved, new hole transporting materials need to be developed. A step in this direction was presented in recent work by Ryu *et al.*, where high performance devices based on the MAPbBr_3 perovskite were prepared by employing various triarylamine polymers.^[8] However, the voltages in that study were still low and further progress is required.

In order to understand the differences in short circuit current, the light absorption of both materials was studied. The UV-Vis absorbance spectrum for FAPbBr_3 in Figure 5-8a shows a

5.2 Results and Discussion

strong increase of absorbance at the band edge and an excitonic feature centered on 532 nm. The absorption band onset and the photoluminescence signal at 550 nm are overlapping, indicating that there is no significant vibronic relaxation and therefore no sub-band gap states in the material.^[2] The optical band gap of the prepared structure is estimated to be 2.26 eV by a Tauc-plot (Figure 5-9). For the MAPbBr₃ system the absorption onset and PL are shifted 10 nm to shorter wavelengths as compared with the MA system. Both materials show comparable absorption coefficients for energies higher than the band gap, and both prepared films absorb over 90% of the incident light. We calculated the maximum achievable short circuit current for solar cells prepared from both materials by integrating the absorption spectra with the AM1.5G solar spectrum to be 9.0 mA cm⁻² for FA based films and 7.5 mA cm⁻² for the MA system. Therefore, the substantial differences in short circuit current in the devices cannot be explained by light absorption differences.

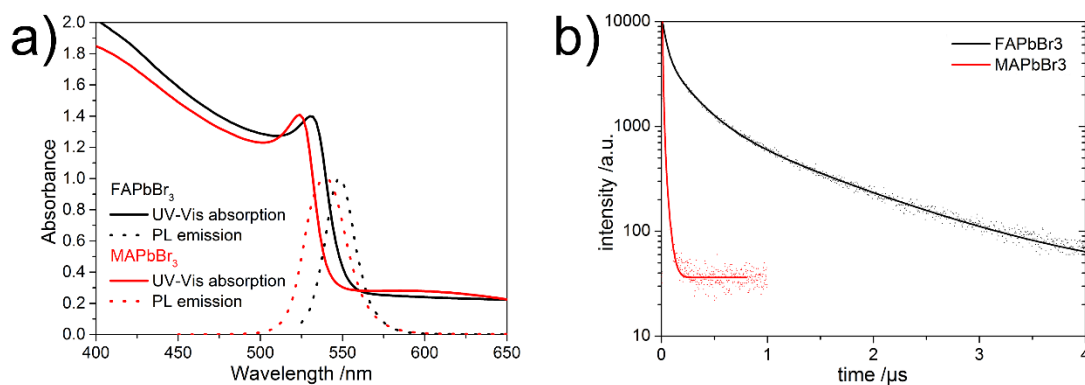


Figure 5-8: (a) UV-Vis absorption in transmission and PL emission spectra for 400 nm thick FAPbBr₃ (black) and MAPbBr₃ (red) films. (b) Photoluminescence (PL) decay curves for FAPbBr₃ and MAPbBr₃. The samples were illuminated at 510 nm with a pump fluence of $\sim 0.3 \mu\text{Jcm}^{-2}$; the emission was monitored at the maximum of the PL emission at 548 nm for FAPbBr₃ and at 540 nm for MAPbBr₃.

It is possible that the device photocurrent in MAPbBr₃ is limited by insufficient charge collection. It has recently been shown that measurements of photoluminescence (PL) dynamics yield important information about the diffusion length of the photoexcited species in the devices, with longer PL lifetimes indirectly indicating longer charge diffusion

lengths.^[2, 3] We show such data in Figure 5-8b. The FAPbBr₃ films show an unusually long decay lifetime τ_e of about 200 ns, much slower than the lifetime exhibited by MAPbBr₃ films (17 ns). Stranks *et al.* attribute a comparable lifetime for the MAPbI_{3-x}Cl_x perovskite to a free diffusion length of electrons and holes of more than 1 μm .^[2] In contrast, the MAPbBr₃ variant exhibits a similar lifetime to that of the non-Cl treated MAPbI₃ perovskite, and therefore diffusion lengths closer to ~ 100 nm.^[2, 3] It is not clear at this point why the FA-based perovskite exhibits longer diffusion lengths than the MA variant, as both crystallize in the same crystal phase and only minor differences in the size of the unit cell exist. While differences in the nature and behavior of the cations, be it limited cation rotation or a smaller dipole moment,^[22] could certainly play a role. It has also been shown recently that processing conditions,^[10] crystal quality and orientation can significantly influence the electronic properties of the final devices.^[23] More experiments to clarify this aspect are currently under way.

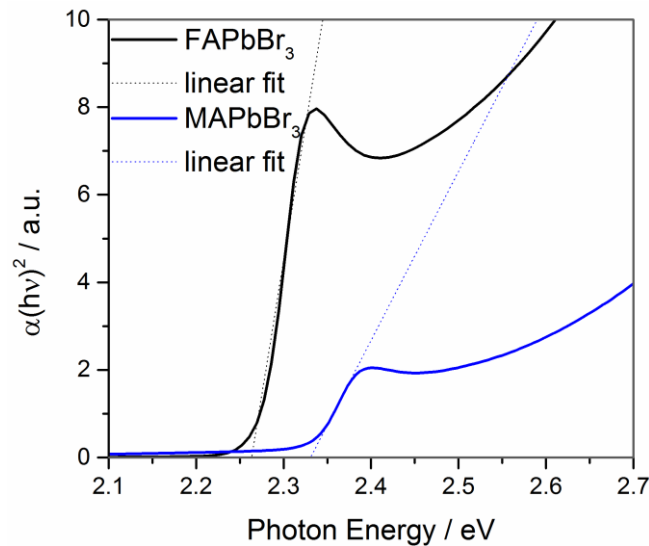


Figure 5-9: Tauc-plot for FAPbBr₃ and MAPbBr₃. The estimated band gaps are 2.26 eV and 2.34 eV, respectively.

5.2 Results and Discussion

Our results are consistent with the recent report by Ryu *et al.*, who showed high short circuit currents for devices based on the MAPbBr₃ material.^[8] In their study, the short diffusion length of the MA-based perovskite was overcome by the use of a mesoporous TiO₂ scaffold. In this case, due to the interpenetrating nature of the titania framework and the perovskite material, efficient charge collection was possible as charges only need to travel the pore diameter (typically under 30 nm) in order to be collected.^[2-4] In our study, however, the MAPbBr₃ perovskite was deposited in a planar configuration and therefore the photoexcited species must travel the whole thickness of the film (>400 nm) in order to be collected. Since the diffusion length is shorter than the thickness of the film, we can conclude that poor charge collection limits the photocurrent in this system. This is not the case for the FA-based perovskite, which works efficiently even without a high temperature sintered titania scaffold. This is particularly important in order to integrate the perovskite technology into tandem devices with inorganic bottom cells or flexible applications, neither of which can sustain heating processes above 150 °C. Additionally, the FA-based perovskites show favorable chemical stability, where the photovoltaic performance of the devices improved by over 50% after storage in the dark in a desiccator for over 72 h. Additionally, we have performed thermogravimetric measurements on both MA- and FA-based perovskites as shown in Figure 5-10. We can clearly observe a shift of +50 degrees for the decomposition onset, clearly indicating that the FA perovskite is more thermally stable than both MAPbBr₃ and MAPbI₃. Since solar cells under real working conditions will usually heat up to over 60 degrees during the course of the day,^[24] high thermal stability is likely to extend the long-term stability of perovskite solar cells fabricated from formamidinium variants.

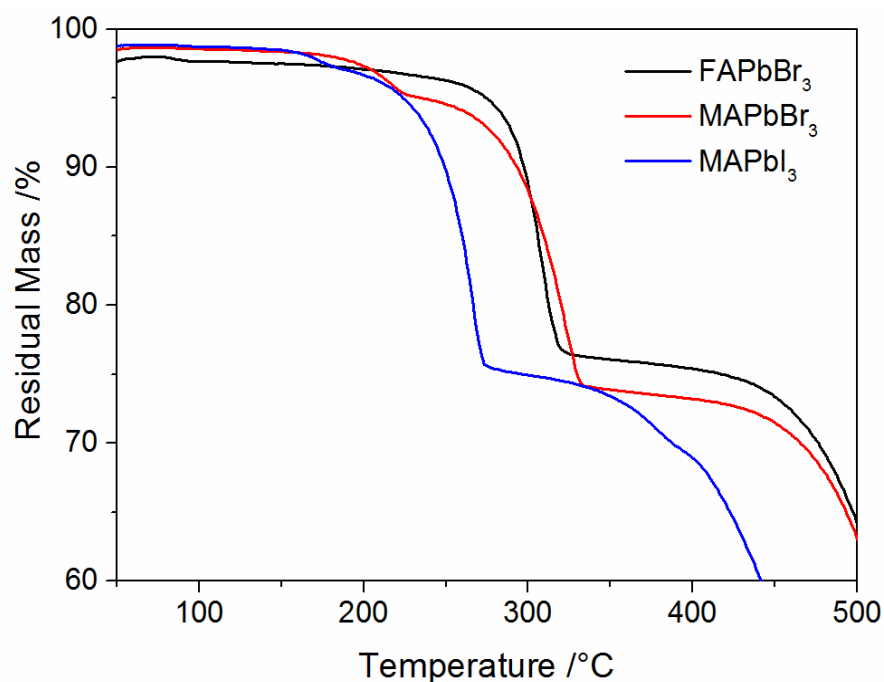


Figure 5-10: Thermogravimetric analysis (TGA) of MA and FAPbBr₃. For comparison we include the TGA for the literature known methylammonium lead iodide perovskite.

5.3 Conclusion

We have studied the novel wide bandgap perovskite material FAPbBr₃ and fully characterized its crystal structure as well as optical and electronic properties. We have shown that FAPbBr₃ can achieve for the first time high power conversion efficiencies of up to 7% in a planar heterojunction architecture, without the need for a mesoporous scaffold. Our results show that devices fabricated from MAPbBr₃ in the same configuration are charge collection limited, while the formamidinium variant exhibits diffusion lengths that are orders of magnitude longer, and therefore is able to achieve high charge collection efficiency. Additionally, we have performed thermogravimetric analysis and find that the FA variant exhibits a shift of +50 degrees in the decomposition onset, showcasing the higher stability of this system. This renders the FAPbBr₃ system suitable as the absorber for flexible photovoltaic applications as well as the top cell in a tandem configuration with a commercially available silicon or CIGS bottom cell.

5.4 Experimental Section

Preparation of the precursors

Methylammonium bromide was prepared by adapting a recipe published earlier.^[25] In short, 24 mL of methylamine solution (33% in ethanol) was diluted with 100 mL of absolute ethanol in a 250 mL roundbottom flask. To this solution, 8 mL of an aqueous solution of hydrobromic acid (48 wt%) was added under constant stirring. After a reaction time of one hour at room temperature, the solvents were removed by rotary evaporation. The obtained white solid was washed with dry diethyl ether and finally recrystallized from ethanol.

Formamidinium bromide was synthesized following a known procedure.^[7] Formamidinium acetate was dissolved in a double molar excess of aqueous HBr (48 wt%), and stirred at 50 °C for 60 minutes. The solvent and remaining HBr was removed by rotary evaporation to obtain a slightly yellow powder. Washing with dry diethyl ether and recrystallization from ethanol led to the white, crystalline product.

Solar cell preparation

Fluorine doped tin oxide (FTO) coated glass sheets (15 Ω /sq, Dyesol Italy) were patterned by etching with zinc powder and 3 M HCl. They were subsequently cleaned with a 2% Hellmanex solution and rinsed with de-ionized water, acetone and ethanol. Directly before applying the blocking layer, last organic residues were removed by an oxygen plasma treatment for 5 minutes. The dense TiO₂ layer was prepared from a sol-gel precursor solution by spin-coating onto the substrates and calcining at 500 °C in air.^[19] For the sol-gel solution a 27.2 mM solution of HCl in 2-propanol was added dropwise to a vigorously stirred 0.43 mM solution of titanium isopropoxide in 2-propanol. The solution stayed clear during the addition and was discarded otherwise.

An approximately 250 nm thick layer of PbBr_2 was prepared by spin-coating 75 μL of a 1 M PbBr_2 solution in dry *N,N*-Dimethylformamide (DMF) onto the TiO_2 covered substrates at 2000 RPM for 15 seconds. To obtain smooth, homogeneous layers it was important to heat both, the PbBr_2 solution and the substrate, to 60 °C before spin-coating and to perform the deposition dynamically with hot solution onto the hot substrate.

The lead bromide layer was transformed into either the MAPbBr_3 or FAPbBr_3 perovskite by immersing it into a 20 mM solution of either MABr or FABr in isopropanol respectively. For the MAPbBr_3 perovskite, the PbBr_2 coated substrates were immersed into 40 mL of the solution, which was heated to 60 °C for 5 minutes. For FAPbBr_3 the solution had to be heated to 70 °C and the immersion was performed for 30 minutes. After taking the films out of the solution, they were rinsed in an isopropanol bath and carefully dried in a nitrogen stream.

Afterwards, the films were covered with a 400 nm layer of spiro-OMeTAD (Borun Chemicals, 99.1% purity). 75 mg of spiro-OMeTAD were dissolved in 1 mL of chlorobenzene and mixed with 10 mL 4-*tert*-Butylpyridine (*t*BP) and 30 μL of a 170 mg mL^{-1} bis(trifluoromethane)sulfonimide lithium salt (LiTFSI) solution in acetonitrile. This solution was spin-coated dynamically at 800 rpm for 45 seconds. In a second step the sample rotation was accelerated to 2000 rpm for 5 seconds to allow the solvent to dry completely. Before evaporating the gold electrodes, spiro-OMeTAD was left to oxidize in air over night at room temperature and 15 – 20% relative humidity.

PL sample preparation

Perovskite samples for steady state and time resolved PL measurements were prepared as described for the solar cell preparation. In this case non-conductive glass substrates were used and the perovskite was covered with a poly(methyl methacrylate) (PMMA) layer to prevent

5.4 Experimental Section

degradation by ambient moisture. The layer was deposited by spin coating 75 μL of a 10 mg mL^{-1} solution of PMMA in chlorobenzene at 1000 rpm for 45 seconds.

Characterization details:

J-V curves were recorded with a Keithley 2400 sourcemeter under simulated AM 1.5 sunlight, calibrated to 100 mWcm^{-2} with a Fraunhofer ISE certified silicon cell. The active area of the solar cells was defined with a square metal aperture mask of 0.0831 cm^2 .

Steady-state absorption spectra were acquired with a Lambda 1050 UV/Vis spectrophotometer (Perkin Elmer) using an integrating sphere.

Steady state and time resolved PL measurements were performed with a Fluotime 300 Spectrofluorometer (Picoquant GmbH). The excitation wavelength was fixed at 510 nm. The emission for time resolved measurements was monitored at the maximum intensity of the steady state photo emission.

Scanning electron microscopy (SEM) images were obtained using a Jeol JSM-6500F microscope equipped with a secondary electron detector.

Samples for powder XRD measurements were obtained by preparing perovskite films on glass substrates following the procedure described for solar cells and removing them from the glass. The measurements were performed on a Huber Imaging Plate Guinier Diffractometer G670 (Cu- $K_{\alpha 1}$ -radiation). Rietveld refinement was performed using the Bruker TOPAS package.^[26] The refinements are based on a structure published by Mashiyama *et al.*^[16] To describe the rotation of methylammonium in MAPbBr_3 , the nitrogen and carbon atoms were displaced around the center of the unit cell. For FAPbBr_3 , the carbon atom was placed in the center of the unit cell and the nitrogen atoms were dislocated around it. As a consequence of the fast rotation of the organic cation, the U_{iso} of C and N was restrained in both cases.

The photoelectron spectroscopy experiments were performed using an Escalab 250 spectrometer equipped with a monochromatized Al anode X-ray source ($h\nu = 1486.6$ eV), and a helium discharge lamp ($h\nu = 21.2$ eV) as excitation sources for X-ray photoelectron spectroscopy (XPS) and UV photoelectron spectroscopy (UPS), respectively. The energetic resolution determined by the 2σ Gaussian broadening used to fit the Fermi edge of a freshly sputter-cleaned silver sample measured at room temperature is 0.35 eV for XPS and 0.13 eV for UPS. All spectra are referenced in binding energy to the Fermi level. The core level lines of *in-situ* cleaned Au, Ag and Cu metal foils were used to calibrate the XPS binding energy scale.

5.5 Literature

- [1] H. J. Snaith, *J. Phys. Chem. Lett.* **2013**, 4, 3623.
- [2] S. D. Stranks, G. E. Eperon, G. Grancini, C. Menelaou, M. J. P. Alcocer, T. Leijtens, L. M. Herz, A. Petrozza, H. J. Snaith, *Science* **2013**, 342, 341.
- [3] G. Xing, N. Mathews, S. Sun, S. S. Lim, Y. M. Lam, M. Grätzel, S. Mhaisalkar, T. C. Sum, *Science* **2013**, 342, 344.
- [4] C. Wehrenfennig, M. Liu, H. J. Snaith, M. B. Johnston, I. Herz, *Energy Environ. Sci.* **2014**, 7, 2269.
- [5] S. De Wolf, J. Holovsky, S.-J. Moon, P. Löper, B. Niesen, M. Ledinsky, F.-J. Haug, J.-H. Yum, C. Ballif, *The Journal of Physical Chemistry Letters* **2014**, 5, 1035.
- [6] Z. M. Beiley, M. D. McGehee, *Energy Environ. Sci.* **2012**, 5, 9173.
- [7] G. E. Eperon, S. D. Stranks, C. Menelaou, M. B. Johnston, L. M. Herz, H. J. Snaith, *Energy Environ. Sci.* **2014**, 7, 982.
- [8] S. Ryu, J. H. Noh, N. J. Jeon, Y. C. Kim, W. S. Yang, J. W. Seo, S. I. Seok, *Energy Environ. Sci.* **2014**, 7, 2614.
- [9] J. H. Noh, S. H. Im, J. H. Heo, T. N. Mandal, S. I. Seok, *Nano Lett.* **2013**, 13, 1764.
- [10] P. Docampo, F. Hanusch, S. D. Stranks, M. Döblinger, J. M. Feckl, M. Ehrensperger, N. K. Minar, M. B. Johnston, H. J. Snaith, T. Bein, *Advanced Energy Materials* **2014**.
- [11] E. Edri, S. Kirmayer, M. Kulbak, G. Hodes, D. Cahen, *J. Phys. Chem. Lett.* **2014**, 5, 429.
- [12] K. Liang, D. B. Mitzi, M. T. Prikas, *Chem. Mater.* **1998**, 10, 403.
- [13] R. Wasylishen, O. Knop, J. Macdonald, *Solid State Commun.* **1985**, 56, 581.
- [14] A. M. Glazer, *Acta Crystallogr., Sect. B* **1972**, 28, 3384.
- [15] A. Poglitsch, D. Weber, *The Journal of Chemical Physics* **1987**, 87, 6373.
- [16] H. Mashiyama, Y. Kurihara, T. Azetsu, *J. Korean Phys. Soc* **1998**, 32, 156.
- [17] G. E. Eperon, V. M. Burlakov, P. Docampo, A. Goriely, H. J. Snaith, *Adv. Funct. Mater.* **2014**, 24, 151.
- [18] P. Docampo, J. M. Ball, M. Darwich, G. E. Eperon, H. J. Snaith, *Nat Commun* **2013**, 4, 2761.
- [19] J. M. Ball, M. M. Lee, A. Hey, H. J. Snaith, *Energy Environ. Sci.* **2013**, 6, 1739.
- [20] J. Burschka, N. Pellet, S.-J. Moon, R. Humphry-Baker, P. Gao, M. K. Nazeeruddin, M. Grätzel, *Nature* **2013**, 499, 316.

- [21] S. Ryu, J. H. Noh, N. J. Jeon, Y. Chan Kim, W. S. Yang, J. Seo, S. I. Seok, *Energy & Environmental Science* **2014**, 7, 2614.
- [22] J. M. Frost, K. T. Butler, F. Brivio, C. H. Hendon, M. van Schilfgaarde, A. Walsh, *Nano Lett.* **2014**, 14, 2584.
- [23] M. Saliba, K. W. Tan, H. Sai, D. T. Moore, T. Scott, W. Zhang, L. A. Estroff, U. Wiesner, H. J. Snaith, *The Journal of Physical Chemistry C* **2014**.
- [24] N. Kato, Y. Takeda, K. Higuchi, A. Takeichi, E. Sudo, H. Tanaka, T. Motohiro, T. Sano, T. Toyoda, *Sol. Energy Mater. Sol. Cells* **2009**, 93, 893.
- [25] H. S. Kim, C. R. Lee, J. H. Im, K. B. Lee, T. Moehl, A. Marchioro, S. J. Moon, R. Humphry-Baker, J. H. Yum, J. E. Moser, M. Gratzel, N. G. Park, *Scientific Reports* **2012**, 2.
- [26] R. Cheary, A. Coelho, J. Cline, *J. Res. Natl. Inst. Stand. Technol.* **2004**, 109, 1.

6 Synthesis of Perfectly Oriented and Micrometer-Sized MAPbBr₃ Perovskite Crystals for Thin Film Photovoltaic Applications

This chapter is based on the following publication:

Nadja Giesbrecht, Johannes Schlipf, Lukas Oesinghaus, Andreas Binek, Thomas Bein, Peter Müller-Buschbaum and Pablo Docampo, *Energy Letters*, **2016**, *1*, 150–154.

Initial experiments and basic material characterization have been performed by Nadja Giesbrecht. Optical characterization with SEM measurements have been performed by Andreas Binek. GIWAXS measurements have been performed by Johannes Schlipf.

6.1 Introduction

Perovskite based solar-cell development has been very impressive with power conversion efficiencies already exceeding 20% after only a few years of development.^[1] This fast development can be attributed to the excellent properties of the perovskite material, mainly its very high absorption coefficient^[2] and long charge carrier diffusion length.^[3, 4] Furthermore, the perovskite material is easy to process from solution, with no high temperature steps required.^[5] Although alternatives based on the exchange of iodide for bromide are interesting for applications in multijunction and photoelectrochemical devices, their fabrication has not been studied in detail.^[6-9] Bromide-based compounds are interesting since they exhibit a wider bandgap of approximately 2.3 eV and thus can achieve much higher values compared to the iodide counterpart.^[6, 8]

To date, the most efficient devices employing methylammonium lead bromide (MAPbBr₃) utilize a mesoscopic titania scaffold as the electron extraction layer.^[6, 8] However, a planar

6.1 Introduction

architecture provides higher flexibility for device optimization, multijunction construction and thus can be employed in a wider variety of applications.^[10, 11] The main challenges for planar heterojunction solar cells, which we will focus on, are the perovskite film coverage, grain size and crystal orientation.^[12]

Recent studies have highlighted the importance of the perovskite morphology, which determines to a large extent the performance of the final device.^[13, 14] In particular, further understanding of the crystallization processes has been the driving force behind the recent impressive device performance improvements in the iodide perovskite system.^[15-18] Thus, a wide variety of deposition techniques has been developed, such as the fast deposition-crystallization procedure, vapor-assisted solution process, or the interdiffusion of solution-processed precursor stacking layers, respectively.^[13,19,20] To improve the solar cell performance in the bromide perovskite system, a similar improvement in morphology is expected to be necessary.

Recently, we have highlighted the importance of perovskite crystal orientation in the performance of the assembled devices.^[21] A higher degree of preferential orientation of the crystallites in the perovskite film generally leads to higher device photocurrents and more reproducible solar cells overall.^[21] Therefore, further understanding on the crystallization process for the bromide system will not only provide a path to enhanced performance with higher voltages of this system, but will also give insights applicable to other hybrid halide perovskite structures.

In this work, we introduce a new synthesis approach for MAPbBr₃ and incorporate this material into a planar device structure. We achieve extended control over crystallization such that the perovskite film exhibits densely packed and highly-ordered grains with crystallite sizes between 5 and 10 μm . We present the first grazing-incidence wide angle X-ray

scattering (GIWAXS) investigation of the MAPbBr₃ perovskite and the highest orientation of the crystallites in a perovskite film ever reported for this family of materials. Such highly-ordered crystallites, in combination with the perovskite film quality in solar devices, maximize the charge collection efficiency leading to internal quantum efficiencies of over 95%.

6.2 Results and Discussion

In order to understand the impact of morphology and crystal orientation of methylammonium lead bromide based solar cells, we have prepared films via the state-of-the-art spin-coating the PbBr₂ and MABr precursors from γ -butyrolactone:dimethylsulfoxide solution (BD),^[8] vapor-assisted solution process (VASP)^[19] and via spin-coating from a lead acetate precursor, which we have termed controlled solvent drying (CSD). To deposit the perovskite via the state-of-the-art process, referred to as BD from here on, we spin-coated the perovskite from the precursor solution and added toluene during the spin-coating process with a subsequent heating step.^[8] The deposition steps for the VASP technique are illustrated in Figure 6-1.

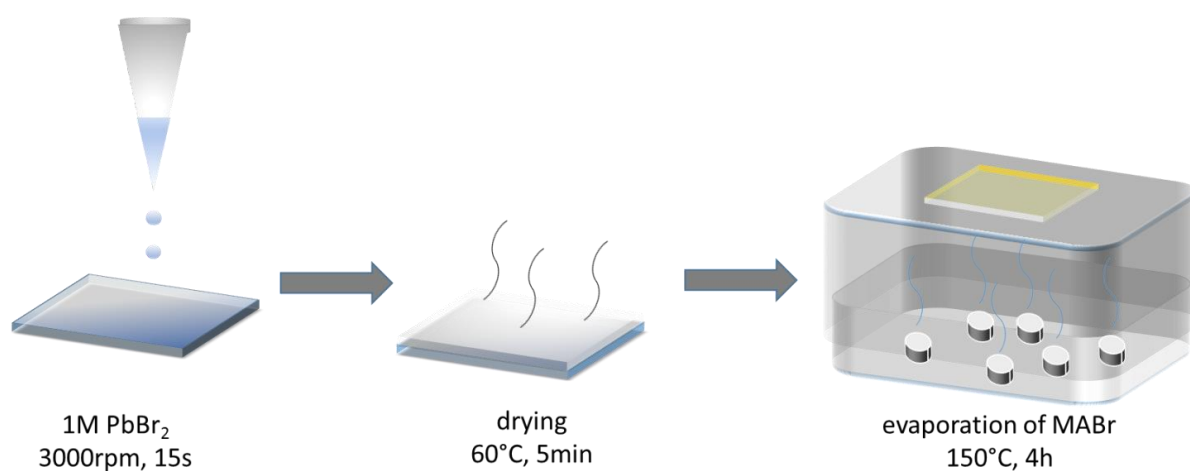


Figure 6-1: Schematic illustration of the perovskite-layer synthesis approach via evaporation; first: PbBr₂ was deposited via spin-coating; second: the PbBr₂ film was dried on a hotplate; third: conversion of the PbBr₂ to the perovskite in a MABr vapor.

6.2 Results and Discussion

In this case, an initial lead bromide layer is deposited directly on TiO₂-coated ITO substrates and afterwards converted to the perovskite with methylammonium bromide (MABr) vapor.^[19]

In Figure 6-2 we show a schematic illustration of the deposition-route via the CSD process. Our approach involves two stages wherein the solution of Pb(Ac)₂ and MABr precursors is spin-coated in a nitrogen-rich environment and is annealed under a glass cover. Here, we find that control of the solvent atmosphere during the whole crystallization process is crucial to maximize crystal size.

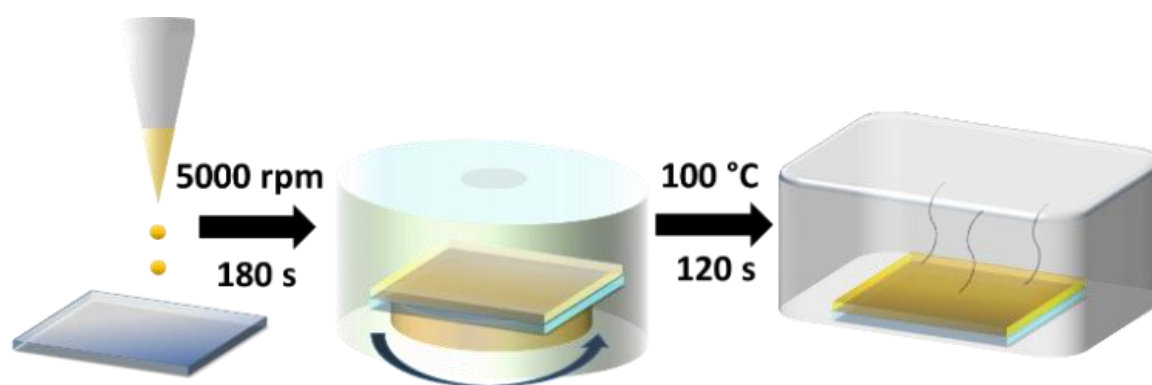


Figure 6-2: Schematic illustration of the perovskite-layer synthesis approach via CSD

In particular, films undergo gentle solvent annealing during the 3 minute spin-coating process as a result of the solvent coating the walls of the spin-coater. To achieve high-quality films, excess of solvent in the spin-coater must be removed between samples. Exposure to too much solvent or traces of alcoholic solvents, such as methanol, leads to secondary nucleation and inhomogeneous films, as shown in Figure 6-3.

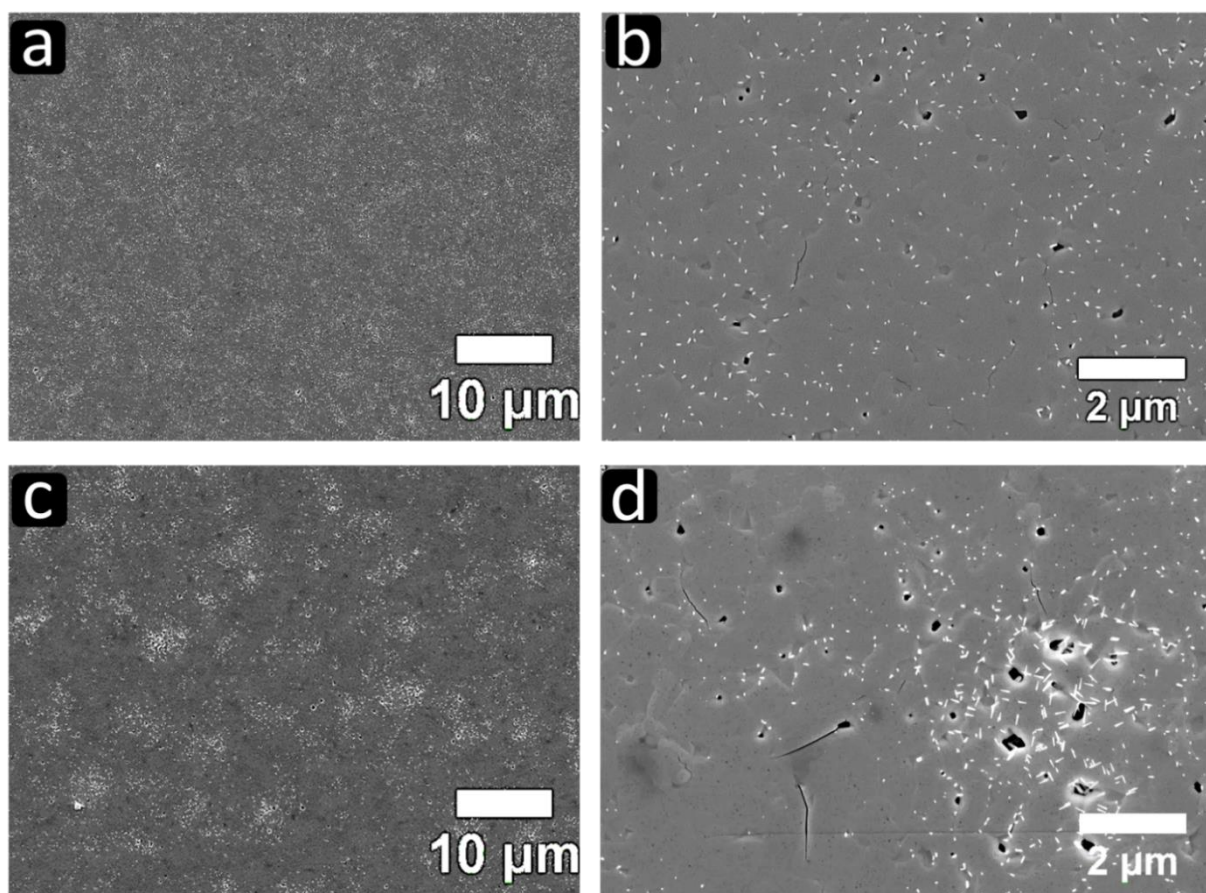


Figure 6-3: SEM top views of MAPbBr₃ perovskite films deposited via CSD; a, b) films deposited with an excess of perovskite solution, c, d) films deposited in a MeOH containing environment in the glove-box.

In Figure 6-4a, c, e we illustrate the morphology of the perovskite films prepared via VASP which has been shown in previous studies to achieve high performance when employed in solar cells.^[7, 22] This morphology is comparable with the state-of-the-art films on top of a mesoporous scaffold with full surface coverage and grain sizes of approximately 1 μm, and is similar to that achieved for the iodide system.^[19, 22]

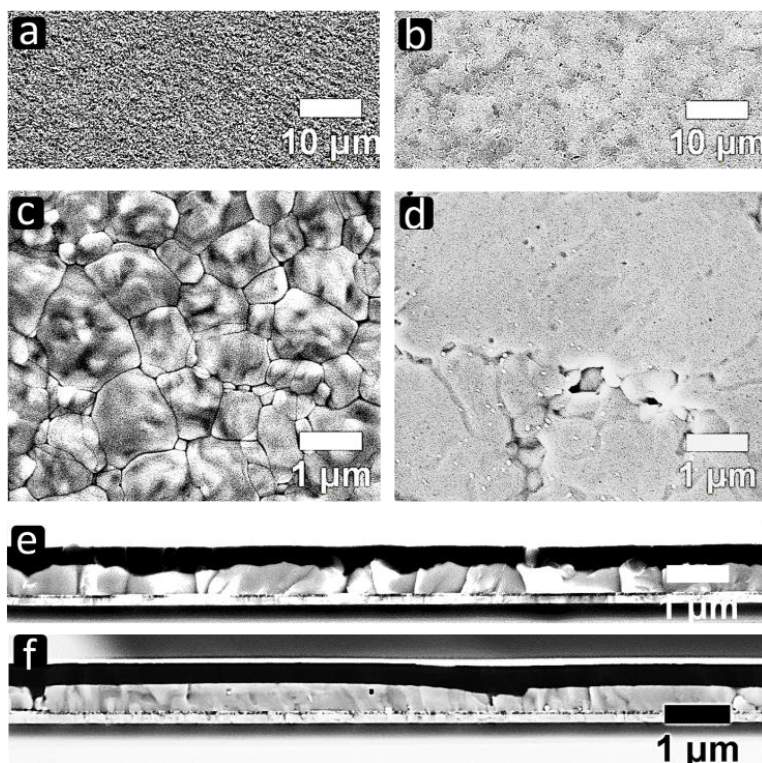


Figure 6-4: SEM top-view and cross-sectional images of MAPbBr₃ perovskite-film a, c, e) deposited on a TiO₂/ITO substrate by VASP, and b, d, f) deposited on TiO₂/ITO by spin-coating with a lead acetate precursor.

On the other hand, films deposited via the CSD method are very smooth and also achieve full surface coverage with large crystals between 5 and 10 μm, as shown in Figure 6-4 and Figure 6-5 and Figure 6-6.

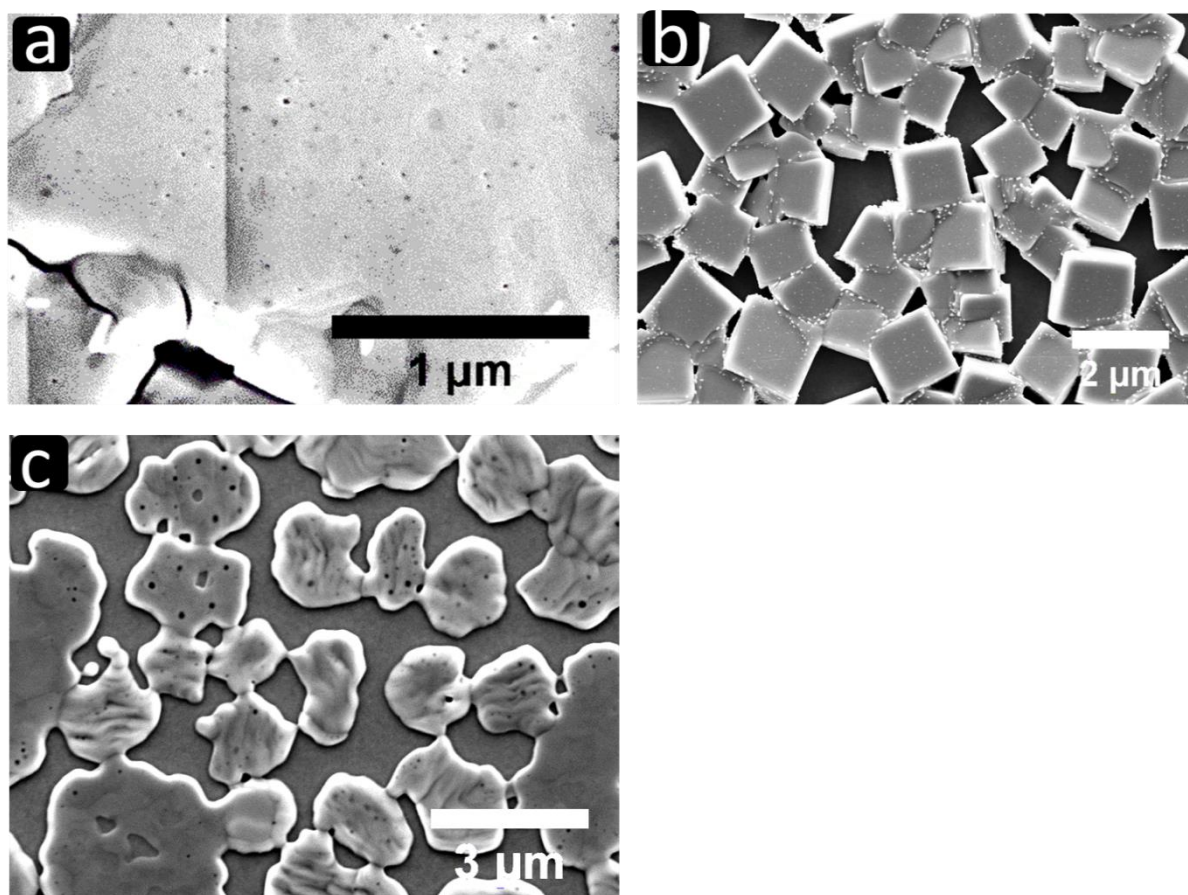


Figure 6-5: a) SEM images of MAPbBr₃ perovskite films deposited via CSD, b) SEM top-view of MAPbBr₃ perovskite-film deposited by spin-coating from lead acetate precursor with a short spin-coating duration of 30 s, c) SEM top view of FAPbBr₃ deposited with the CSD method on TiO₂/ITO coated glass.

We have also prepared films through the BD process, as shown in the Figure 6-7. In this case, the crystal sizes are very small, in the range of 100 nm.^[8]

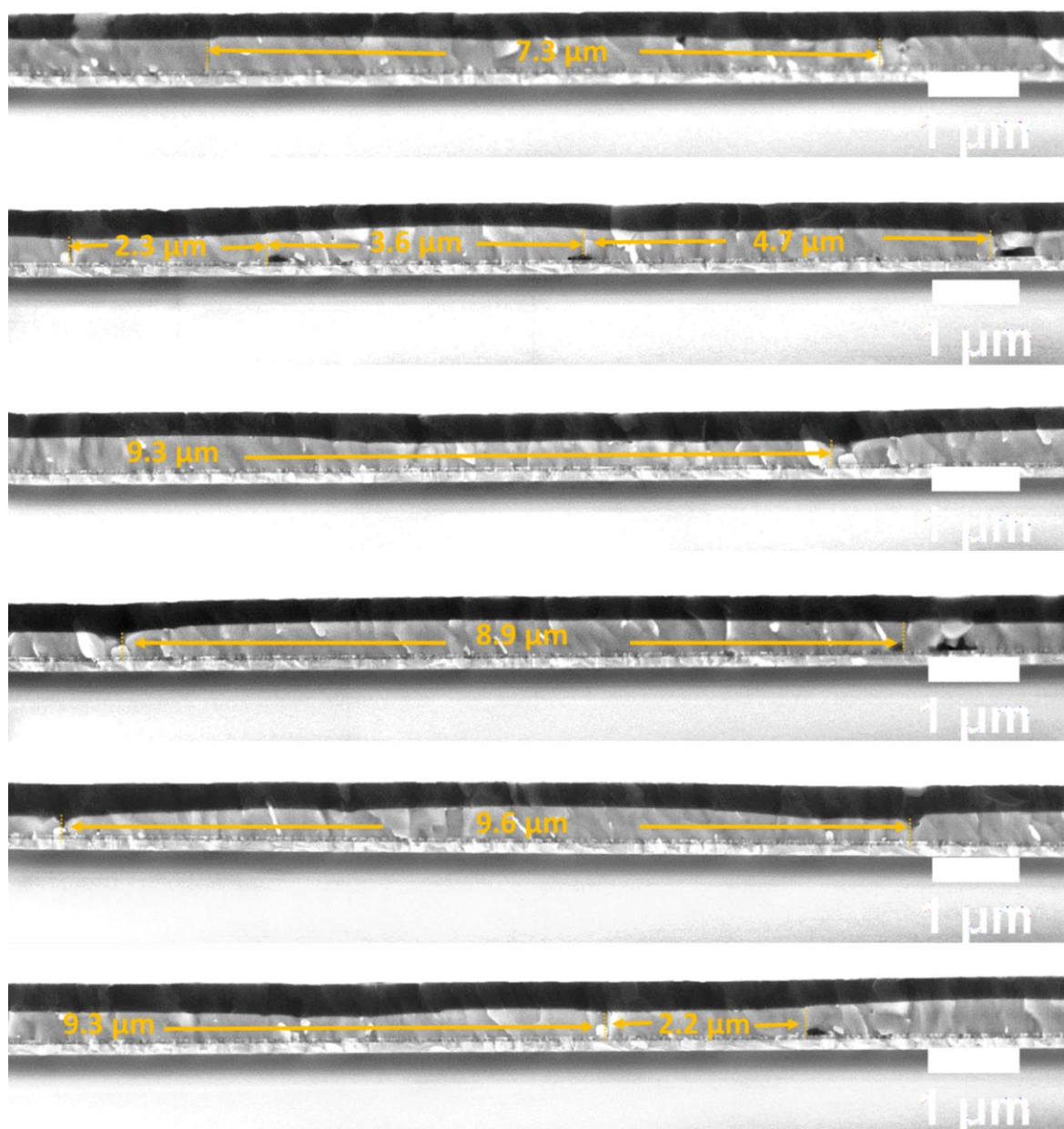


Figure 6-6: SEM cross-sectional images of MAPbBr₃ perovskite solar cells in the configuration ITO / TiO₂ / MAPbBr₃ / spiro-OMeTAD / Au.

6 Synthesis of Perfectly Oriented and Micrometer-Sized MAPbBr₃ Perovskite Crystals for Thin Film Photovoltaic Applications

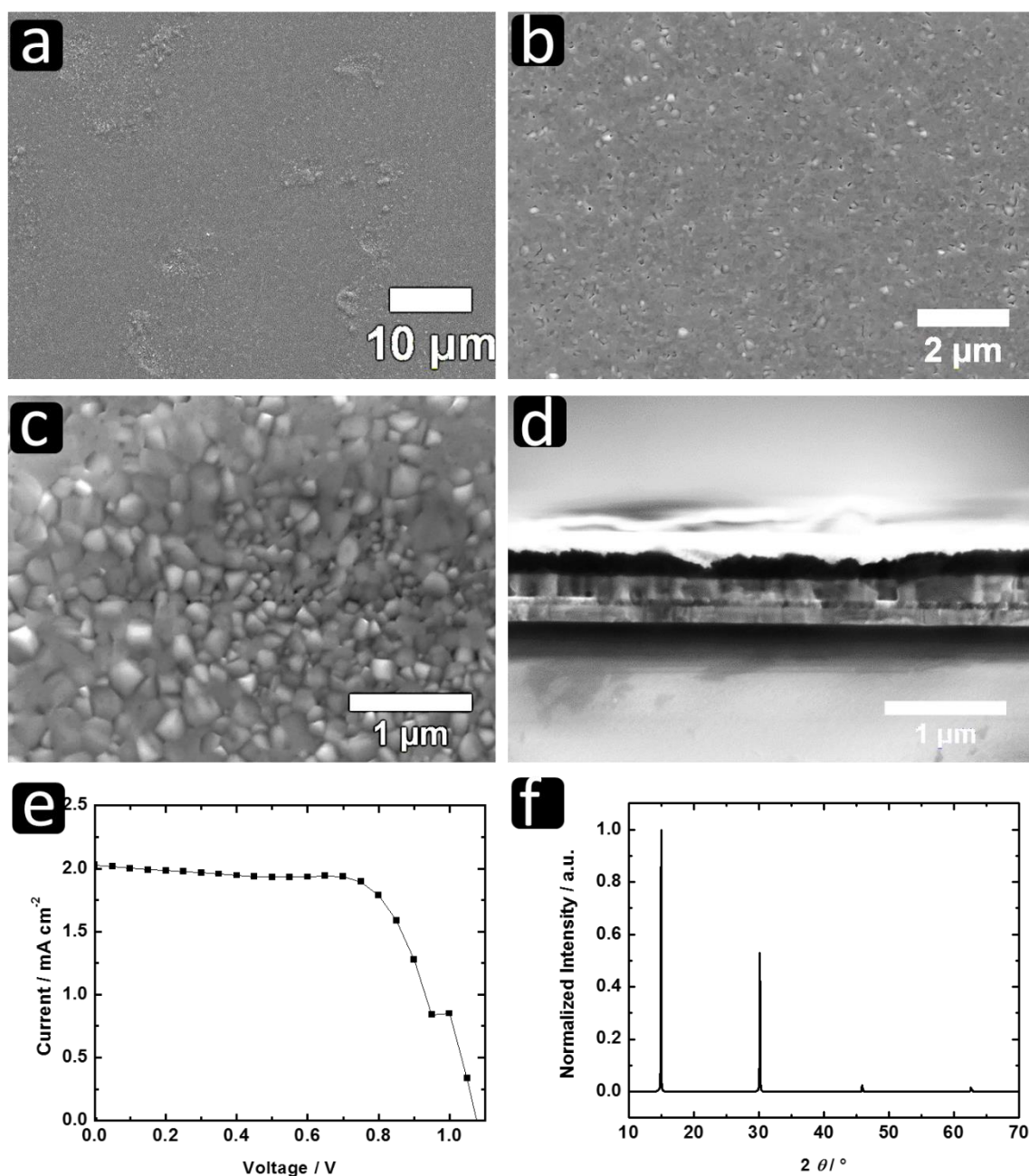


Figure 6-7: SEM images of MAPbBr₃ perovskite films deposited via the state-of-the-art BD method; a,b,c) top view on a film prepared on ITO, d) cross-sectional image of a solar cell device prepared on ITO, e) *J-V* curve under AM1.5 solar irradiation conditions of the best performing device, f) XRD pattern normalized to the reflex at $2\theta = 14.9^\circ$.

We attribute the full surface coverage and large grain size to our newly developed synthesis approach, which results in improved control over the crystallization of the perovskite. Low volatile solvents, such as dimethylformamide (DMF) are good candidates to grow large crystals at temperatures around 100 °C. However, achieving perovskite films with full surface

6.2 Results and Discussion

coverage is challenging.^[23, 24] In our developed CSD method $\text{Pb}(\text{Ac})_2$ and MABr react to form the perovskite structure and the excess organic components react to form methylammonium acetate, methylamine and acetic acid. All the expected organic components formed during the reaction are liquid at room temperature, which keep the films wet during the process. This in turn likely allows a certain degree of precursor mobility, and enables the very large crystal growth observed in the final films. Further evidence that this is the case is given by the structurally related formamidinium lead halide perovskite (FAPbX_3). Here, a solid formamidinium acetate salt is formed, and thus the films completely dry within the spin-coating step. In turn this results in the formation of a non-continuous perovskite film with large voids between the crystals (see Figure 6-5).

To further investigate the crystalline quality of the films with the large domains, X-ray diffraction (XRD) experiments were performed for both CSD and VASP derived films. The X-ray patterns, shown in Figure 6-8a, confirm for both films a phase-pure MAPbBr_3 compound crystallized in the cubic $Pm\bar{3}m$ structure type. However, most of the reflections for the CSD sample are not present, which indicates a high degree of crystal orientation. A good tool to fully determine this parameter is grazing incidence wide-angle X-ray scattering (GIWAXS) which captures a two-dimensional slice through reciprocal space, allowing the reconstruction of the crystal structure and extraction of information on the orientation of the crystal planes from the azimuthal intensity distribution.^[25, 26] In Figure 6-8b and d we show GIWAXS data for VASP and CSD derived perovskite films. In case of VASP films very homogeneous rings with no pronounced peaks are found. This implies no preferential orientation of the crystallites in the perovskite film. In contrast, films fabricated via the CSD process show very intense *Bragg* peaks and no rings. This implies that all crystallites are very well oriented with the $\{001\}$ planes parallel to the glass substrate. This is remarkable for a thin polycrystalline film processed from solution. The orientation distribution is shown

6 Synthesis of Perfectly Oriented and Micrometer-Sized MAPbBr₃ Perovskite Crystals for Thin Film Photovoltaic Applications

schematically in Figure 6-8c. We suggest that such high order derives from the pre-crystallization step with the presence of a solvent layer on top. We note that a similar effect was observed for the iodide system when an ionic liquid was used to crystallize the perovskite.^[27]

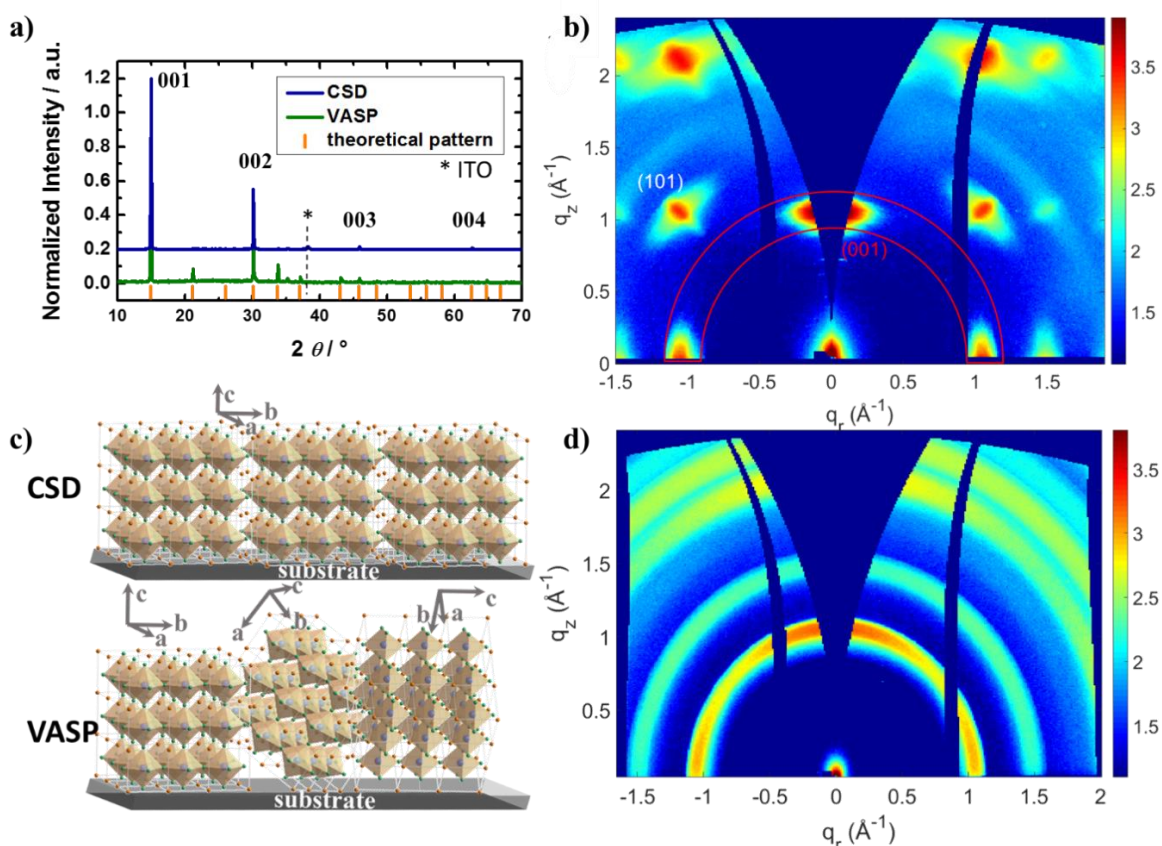


Figure 6-8: XRD patterns normalized to the reflex at $2\theta = 14.9^\circ$, perovskite-film prepared via CSD and via VASP and the theoretical pattern, b) 2D GIWAXS patterns of the sample produced via CSD ((001) and (101) peaks are marked in red and white, respectively). The data are corrected as outlined in the experimental section., c) schematic illustration of the crystal orientation of the perovskite film prepared via CSD and disorder of the film prepared via VASP, d) 2D GIWAXS pattern of the sample produced via VASP.

To correlate the effect of morphology and crystal orientation with the solar cell performance, we prepared devices with the developed perovskite layer in the standard device configuration, employing TiO₂ and spiro-OMeTAD as the charge extraction contacts, as shown schematically in Figure 6-9a. To exclude variations in the optical absorption of the films due

6.2 Results and Discussion

to different perovskite film thicknesses, we have fixed this value for both techniques to 350 nm. The corresponding photovoltaic performance for perovskite films deposited via CSD and VASP is shown in Figure 6-9b, and the data are summarized in Table 6-1.

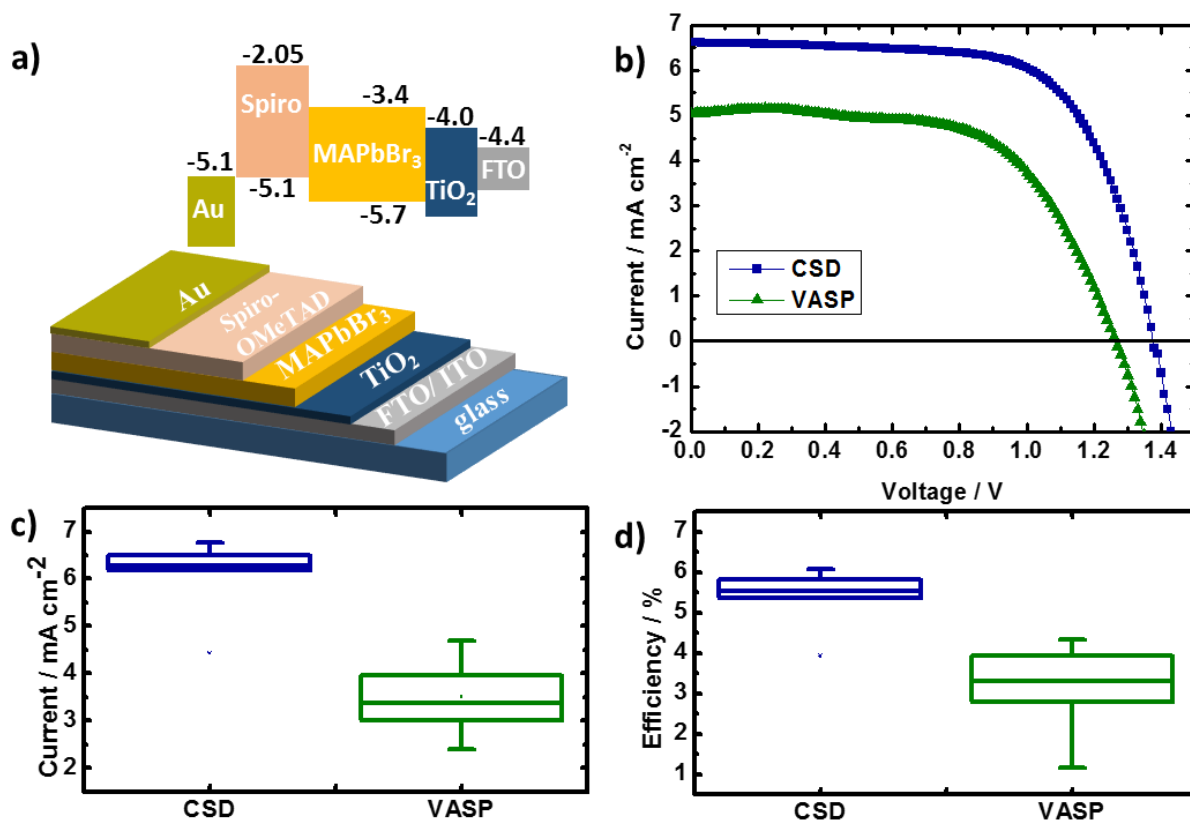


Figure 6-9: a) Scheme of the regular solar cell layout and energy diagram, b) J - V curves under AM1.5 solar irradiation conditions for solar cell employing MAPbBr₃ derived from CSD or VASP processes, c) photocurrent and d) efficiency box plots of 20 devices employing VASP- or CSD-derived perovskite films. The edges of the box represent the 25/75 percentile, while the horizontal line represents the median value. Whiskers represent minimum and maximum values.

Table 6-1: Photovoltaic performance data of devices employing CSD- or VASP-derived perovskite films.

Method	V_{OC} / V	J_{SC} / mAcm ⁻²	FF / %	PCE / %
CSD	1.38	6.60	67	6.08
VASP	1.26	5.05	62	4.00

In general, the performance of devices employing VASP-derived films is lower compared to those employing CSD-derived films. In Figure 6-9c, d and in Figure 6-10 we show the

6 Synthesis of Perfectly Oriented and Micrometer-Sized MAPbBr₃ Perovskite Crystals for Thin Film Photovoltaic Applications

distribution of the photovoltaic performance for the fabricated devices. The difference in device performance may arise from the different crystallization processes of the film leading to disparities in perovskite surface and in defect density. However, the VASP technique leads to the highest performance reported,^[22] thus we expect the amount of defects to not be the major factor behind the variation in device performance.

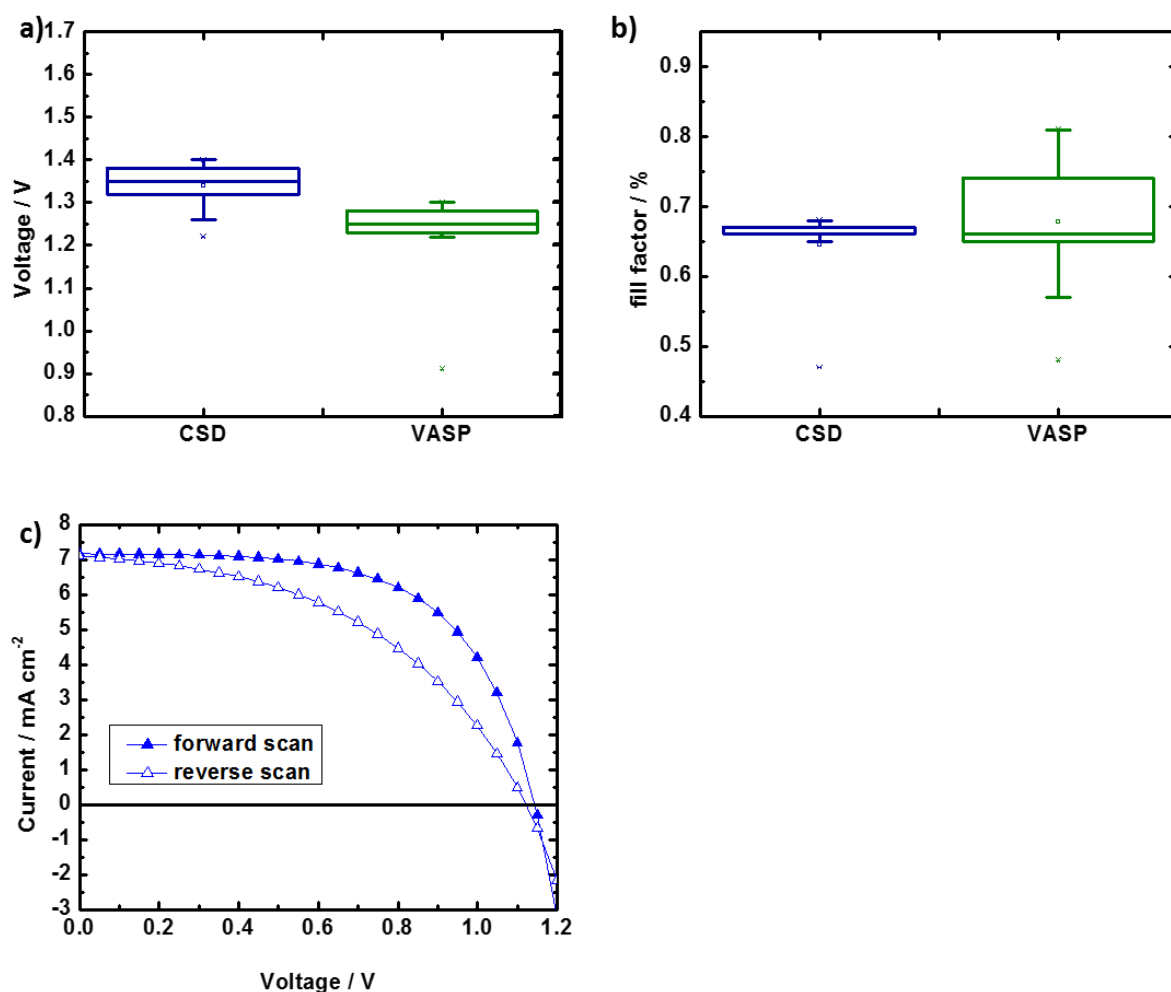


Figure 6-10: Distribution of device performance data of 20 devices with perovskite films prepared via VASP or spin-coating from a lead acetate precursor (CSD), a) open circuit voltage, b) fill factor, c) forward and reverse scanning results for solar cells employing MAPbBr₃ derived from CSD.

Here, devices employing perfectly oriented perovskite films, derived via the CSD process, exhibit photocurrents between 6 and 7 mA cm⁻², which is twice the average value found for

6.2 Results and Discussion

devices employing non-oriented perovskite crystals, prepared via the VASP process. We note that the theoretical limit for the short-circuit current extracted from light absorption measurements on devices is 7.15 mA cm^{-2} which implies an internal quantum efficiency of over 95% (Figure 6-11).

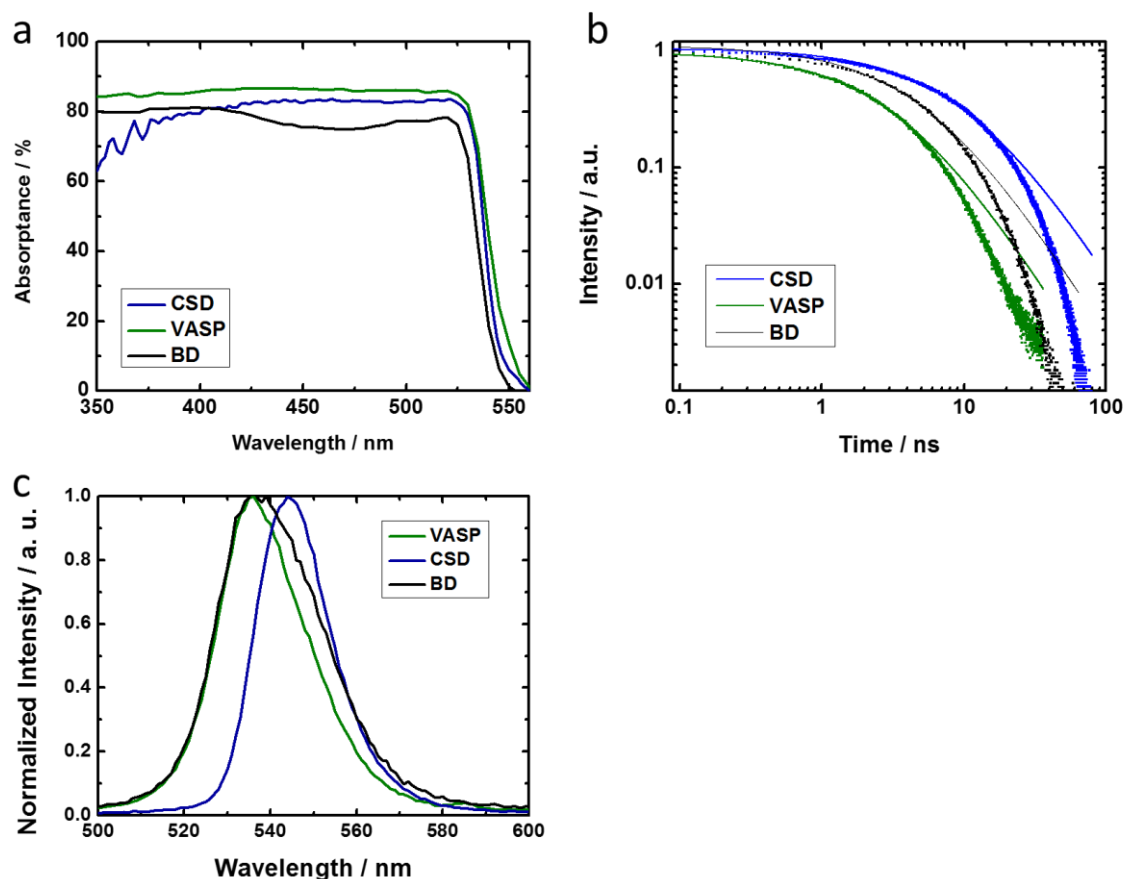


Figure 6-11: a) Absorbance of MAPbBr_3 prepared via VASP or spin-coating from lead acetate precursor, b) PL decay curves for MAPbBr_3 prepared via VASP or spin-coating from lead acetate precursor. The samples were illuminated at 510 nm with a pump fluence of $\sim 0.3 \mu\text{Jcm}^{-2}$; the emission was monitored at the maximum of PL emission at 549.5 nm for CSD and 540 nm for VASP; c) PL emission.

To further understand the differences in crystalline quality between films obtained from the CSD process and VASP derived films, we performed time-correlated single photon counting (TCSPC) to obtain the lifetime of the photoexcited species. Recent investigations showed that time resolved photoluminescence (PL) measurements yield not only important information about the diffusion length of the photoexcited species in the devices but also correlate with

perovskite layer morphology. In particular, larger crystals present narrower band gaps and longer lifetimes, which points towards a smaller radiative bimolecular recombination coefficient.^[28] Our results presented in Figure 6-11 agree with these findings, since we also observed a red shift of the steady-state PL maximum for the CSD-derived sample with respect to the BD- and VASP-derived sample. We also observed a slower bimolecular recombination process for films prepared with CSD, which is a strong indicator for good crystalline quality with fewer defects and lower disorder compared to the BD- and VASP-derived film.^[29, 30]

The higher current for our CSD-derived films may be a result of either their larger crystal size, or their enhanced crystal order, as compared to those deposited via the VASP technique. In order to investigate this further, we have prepared devices with the rougher bottom contact FTO. This enhanced surface roughness hinders horizontal crystal growth and reduces the domain sizes in the perovskite layer, leading to crystal sizes comparable to those derived with the VASP approach, as shown in Figure 6-12.

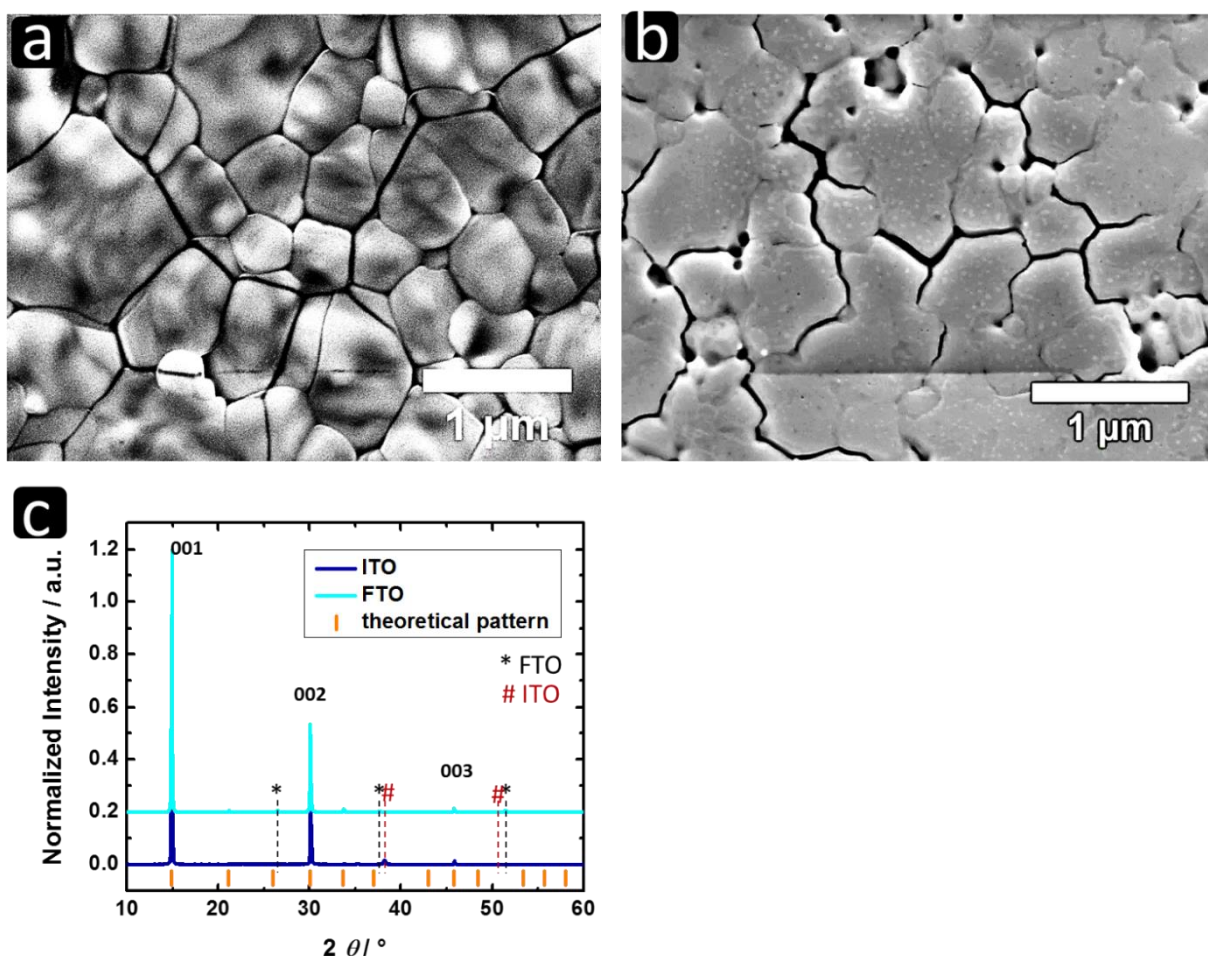


Figure 6-12: a) SEM top views of MAPbBr₃ perovskite films deposited via VASP, b) SEM top views of MAPbBr₃ perovskite films deposited via CSD on FTO, c) XRD pattern normalized to the reflex at $2\theta = 14.9^\circ$.

However, these films maintain their high degree of orientation with the (001) plane parallel to the substrate, allowing us to discriminate between effects arising from the crystal size or the crystal orientation. We show histograms of all photovoltaic parameters in Figure 6-13. Here, we observe that the short circuit current is not affected by the crystal size of the films, leading us to postulate that the degree of crystal order in the film is the parameter affecting the short circuit current. This may be a result of a lower number of defects at the grain boundaries as all neighboring crystals exhibit the same facets with the same orientation.

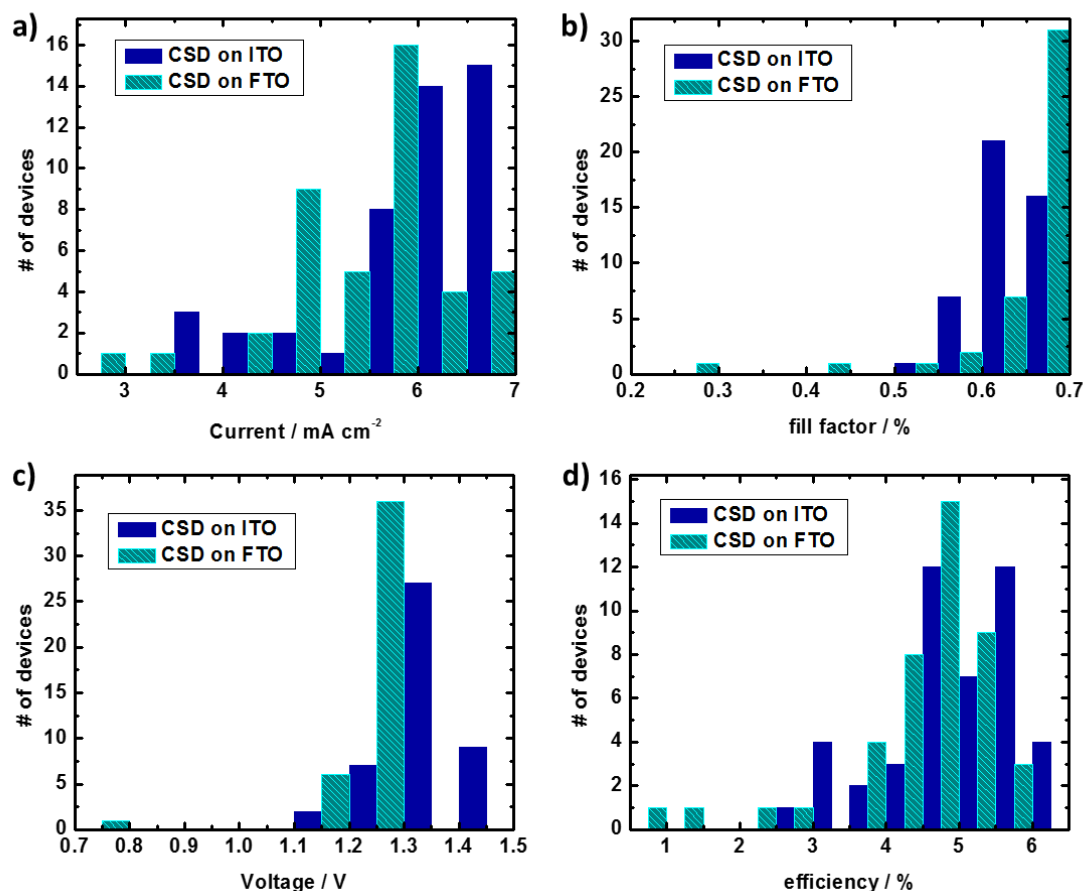


Figure 6-13: Distribution of device performance data of 45 devices with perovskite films prepared via spin-coating from a lead acetate precursor (CSD) with an FTO- or ITO-coated substrate, a) short circuit current output, b) fill factor, c) open circuit voltage, d) power conversion efficiencies.

6.3 Conclusion

In summary, we have studied the role of morphology and crystal order in the photovoltaic performance of MAPbBr₃ deposited via three different deposition techniques. We developed a new fabrication method based on solvent drying with a halide-free lead precursor controlling the crystallization atmosphere. Here, the reaction of the precursors yields liquid organic by-products at RT which enable large crystal growth with perfectly oriented crystal planes parallel to the substrate as shown by GIWAXS measurements. Our results show that large crystal sizes can only be achieved for smooth ITO substrates, whereas perovskite films on FTO result in crystals limited to hundreds of nanometers due to the enhanced surface

6.4 Experimental Section

roughness which limits horizontal growth. In addition, we examine the role of perovskite crystallite orientation in planar heterojunction solar cells by comparing non-oriented VASP-derived films with our newly developed oriented CSD-derived films. We show that this perfect alignment of the cubic crystal planes parallel to the substrate of the CSD-derived film leads to reproducible high performance and enhanced short circuit currents approaching (7 mA cm^{-2}) their theoretical limit, compared to non-oriented VASP-derived perovskite films. The photocurrents generated in these devices correlate with the degree of crystal orientation rather than the crystal size. Thus, this work demonstrates that crystal orientation and morphology are key parameters to maximize the short-circuit current in perovskite solar cells.

6.4 Experimental Section

Preparation of the precursors

$\text{CH}_3\text{NH}_3\text{Br}$ was synthesized by reacting 8 mL of hydrobromic acid (48 vol% in water) with 24 mL of methylamine (33 vol% in methanol, Sigma-Aldrich) in ethanol in a round-bottom flask at room temperature for 1 h. To recover the precipitates, solvent evaporation at 60°C at a pressure of 200 mbar was used and the products were recrystallized in ethanol, filtered and dried with diethylether and under vacuum afterwards.

Solar cell preparation

Fluorine-doped tin oxide (FTO, Pilkington, $7 \Omega \text{ sq}^{-1}$) substrates or indium-doped tin oxide (ITO, Zhuhai Kaivo Optoelectronic Technology Co., Ltd., $<15 \Omega \text{ sq}^{-1}$) were etched with 2 M HCl and zinc powder and cleaned in 2% Hallmanex detergent, acetone and ethanol. The TiO_2 layer was deposited via a sol-gel approach where a solution containing 0.23 M titanium isopropoxide (Sigma Aldrich, 99.999%) and 0.013 M HCl in isopropanol was spin-coated on

6 Synthesis of Perfectly Oriented and Micrometer-Sized MAPbBr₃ Perovskite Crystals for Thin Film Photovoltaic Applications

FTO or ITO at 2000 rpm for 30 s and annealed at 150 °C for 10 min and for 45 min at 400 °C for the ITO and at 500 °C for the FTO in ambient air conditions.

BD: A 1.2 M solution of the perovskite precursors PbBr₂ and MABr (1:1 ratio) was prepared in a solvent mixture of γ -butyrolactone and dimethylsulfoxide in a 7:3 ratio. The precursor solution was deposited in a 3-step spin-coating program. The first step of the program was at 500 rpm for 5 s, the second step was at 1000 rpm for 40 s and the third step was at 5000 rpm for 50 s. At the beginning of the last step toluene was dripped on the substrate. Afterwards the films were annealed at 100 °C for 10 min.

VASP: In the vapor-assisted-solution process first the lead bromide precursor layer was deposited. The PbBr₂ was dissolved in DMF (1 M) and preheated together with the substrates at 60 °C before spin-coating the layer at 3000 rpm for 15 s. Afterwards the PbBr₂ was dried at 60 °C for 10 min and converted in a closed vial to the perovskite in MABr vapor for 2 hours at 150 °C.

CSD: The perovskite layer was deposited at room temperature kept substrate via dynamically spin-coating 50 μ L solution (1.5 M Pb(Ac)₂ + 4.5 M MABr in DMF) per 9 cm² of substrate dimension at 5000 rpm for 3 min. The samples were then annealed at 100 °C for 2 min with a glass lid covering the substrate in order to avoid defects caused by gas circulation.

On top of the perovskite a 100 mg/mL solution of spiro-OMeTAD in chlorobenzene was spin-coated at 1500 rpm for 45 s and a second step at 2000 rpm for 5 s. Finally a 40 nm thick Au counter electrode was thermally evaporated under high vacuum conditions ($<10^{-6}$ mbar) through a metal aperture leading to devices in the range of 0.10 cm². The active area was determined with a 0.083 ± 0.001 cm² metal aperture.

6.4 Experimental Section

Characterization details:

X-ray diffraction patterns were obtained from samples of perovskite deposited on TiO₂-coated FTO or ITO glass using an X-ray diffractometer (Bruker D8 Discover).

GIWAXS measurements were performed using a Ganesha 300XL SAXS-WAXS with an 8 keV Cu-K_α X-ray source. The incident angle of 0.4° and the sample-detector distance (SDD) of approximately 106 mm were chosen according to the material properties. The exact value of the SDD was determined for each measurement by careful calibration using XRD data. For data evaluation we used the software GIXSGUI by the Advanced Photon Source (APS) of the Argonne National Laboratory, USA.^[31] The applied corrections include the solid angle correction, the efficiency correction and the polarization correction.^[32, 33]

A scanning microscope (JSM-6500F) was used to acquire SEM images of perovskite layers prepared on TiO₂-coated FTO / ITO glass.

The absorbance of the perovskite films on TiO₂-coated ITO glass was measured with a Lambda 1050 UV/Vis spectrometer (Perkin Elmer) using an integrating sphere.

Steady-state and time-correlated single photon counting measurements of the perovskite films coated on non-conductive glass were performed with a Fluotime 300 Spectrofluorometer (Picoquant GmbH); the excitation wavelength was fixed to 510 nm with a pump fluence of ~0.3 μJcm⁻² and the emission was monitored at the maximum at 550 nm, the maximum intensity of the steady state photo emission.

Photovoltaic device performance was measured with a Keithley 2400 sourcemeter in air at 25 °C under illumination by an Newport Oriel Sol2A solar simulator, which was calibrated to 100 mW/cm⁻² with a Fraunhofer ISE certified silicon cell with a mismatch factor of 1.01. The active area of the solar cell was defined with a square metal aperture mask of 0.0831 cm².

6.5 Literature

- [1] W. S. Yang, J. H. Noh, N. J. Jeon, Y. C. Kim, S. Ryu, J. Seo, S. I. Seok, *Science* **2015**, 348, 1234.
- [2] S. De Wolf, J. Holovsky, S.-J. Moon, P. Löper, B. Niesen, M. Ledinsky, F.-J. Haug, J.-H. Yum, C. Ballif, *The Journal of Physical Chemistry Letters* **2014**, 5, 1035.
- [3] S. D. Stranks, G. E. Eperon, G. Grancini, C. Menelaou, M. J. P. Alcocer, T. Leijtens, L. M. Herz, A. Petrozza, H. J. Snaith, *Science* **2013**, 342, 341.
- [4] G. Xing, N. Mathews, S. Sun, S. S. Lim, Y. M. Lam, M. Grätzel, S. Mhaisalkar, T. C. Sum, *Science* **2013**, 342, 344.
- [5] D. Liu, T. L. Kelly, *Nat. Photon.* **2014**, 8, 133.
- [6] E. Edri, S. Kirmayer, D. Cahen, G. Hodes, *J. Phys. Chem. Lett.* **2013**, 4, 897.
- [7] F. C. Hanusch, E. Wiesenmayer, E. Mankel, A. Binek, P. Angloher, C. Fraunhofer, N. Giesbrecht, J. M. Feckl, W. Jaegermann, D. Johrendt, T. Bein, P. Docampo, *J. Phys. Chem. Lett.* **2014**, 5, 2791.
- [8] S. Ryu, J. H. Noh, N. J. Jeon, Y. Chan Kim, W. S. Yang, J. Seo, S. I. Seok, *Energy Environ. Sci.* **2014**, 7, 2614.
- [9] J. H. Noh, S. H. Im, J. H. Heo, T. N. Mandal, S. I. Seok, *Nano Lett.* **2013**, 13, 1764.
- [10] P. Docampo, J. M. Ball, M. Darwich, G. E. Eperon, H. J. Snaith, *Nat. Commun.* **2013**, 4, 2761.
- [11] C. D. Bailie, M. G. Christoforo, J. P. Mailoa, A. R. Bowring, E. L. Unger, W. H. Nguyen, J. Burschka, N. Pellet, J. Z. Lee, M. Gratzel, R. Noufi, T. Buonassisi, A. Salleo, M. D. McGehee, *Energy Environ. Sci.* **2015**, 8, 956.
- [12] W.-J. Yin, J.-H. Yang, J. Kang, Y. Yan, S.-H. Wei, *J. Mater. Chem. A* **2015**, 8926.
- [13] M. Xiao, F. Huang, W. Huang, Y. Dkhissi, Y. Zhu, J. Etheridge, A. Gray-Weale, U. Bach, Y.-B. Cheng, L. Spiccia, *Angew. Chem.* **2014**, 126, 10056.
- [14] K. Handloser, I. Grill, F. Hanusch, N. Giesbrecht, Y. Hu, T. Bein, P. Docampo, M. L. Petrus, M. Handloser, A. Hartschuh, **2016**.
- [15] J.-H. Im, I.-H. Jang, N. Pellet, M. Grätzel, N.-G. Park, *Nat. Nano* **2014**, 9, 927.
- [16] N. J. Jeon, J. H. Noh, W. S. Yang, Y. C. Kim, S. Ryu, J. Seo, S. I. Seok, *Nature* **2015**, 517, 476.
- [17] N. J. Jeon, J. H. Noh, Y. C. Kim, W. S. Yang, S. Ryu, S. I. Seok, *Nat. Mater.* **2014**, 13, 897.

- [18] N. Ahn, D.-Y. Son, I.-H. Jang, S. M. Kang, M. Choi, N.-G. Park, *J. Am. Chem. Soc.* **2015**, *137*, 8696.
- [19] Q. Chen, H. Zhou, Z. Hong, S. Luo, H.-S. Duan, H.-H. Wang, Y. Liu, G. Li, Y. Yang, *J. Am. Chem. Soc.* **2013**, *136*, 622.
- [20] Z. Xiao, C. Bi, Y. Shao, Q. Dong, Q. Wang, Y. Yuan, C. Wang, Y. Gao, J. Huang, *Energy Environ. Sci.* **2014**, *7*, 2619.
- [21] P. Docampo, F. C. Hanusch, N. Giesbrecht, P. Angloher, A. Ivanova, T. Bein, *APL Mat.* **2014**, *2*, 081508.
- [22] R. Sheng, A. Ho-Baillie, S. Huang, S. Chen, X. Wen, X. Hao, M. A. Green, *J. Phys. Chem. C* **2015**, *119*, 3545.
- [23] F. X. Xie, D. Zhang, H. Su, X. Ren, K. S. Wong, M. Grätzel, W. C. H. Choy, *ACS Nano* **2014**, 639.
- [24] W. Zhang, M. Saliba, D. T. Moore, S. K. Pathak, M. T. Hörantner, T. Stergiopoulos, S. D. Stranks, G. E. Eperon, J. A. Alexander-Webber, A. Abate, A. Sadhanala, S. Yao, Y. Chen, R. H. Friend, L. A. Estroff, U. Wiesner, H. J. Snaith, *Nat Commun* **2015**, *6*.
- [25] M. Saliba, K. W. Tan, H. Sai, D. T. Moore, T. Scott, W. Zhang, L. A. Estroff, U. Wiesner, H. J. Snaith, *J. Phys. Chem. C* **2014**, *118*, 17171.
- [26] P. Müller-Buschbaum, *Adv. Mater.* **2014**, *26*, 7692.
- [27] D. T. Moore, K. W. Tan, H. Sai, K. P. Barteau, U. Wiesner, L. A. Estroff, *Chem. Mater.* **2015**, *27*, 3197.
- [28] V. D’Innocenzo, A. R. Srimath Kandada, M. De Bastiani, M. Gandini, A. Petrozza, *J. Am. Chem. Soc.* **2014**, *136*, 17730.
- [29] D. W. de Quilettes, S. M. Vorpahl, S. D. Stranks, H. Nagaoka, G. E. Eperon, M. E. Ziffer, H. J. Snaith, D. S. Ginger, *Science* **2015**, *348*, 683.
- [30] X. Wu, M. T. Trinh, D. Niesner, H. Zhu, Z. Norman, J. S. Owen, O. Yaffe, B. J. Kudisch, X. Y. Zhu, *J. Am. Chem. Soc.* **2015**, *137*, 2089.
- [31] Z. Jiang, *J. Appl. Crystallogr.* **2015**, *48*, 917.
- [32] W. Chen, M. P. Nikiforov, S. B. Darling, *Energy & Environmental Science* **2012**, *5*, 8045.
- [33] C. M. Schleputz, R. Herger, P. R. Willmott, B. D. Patterson, O. Bunk, C. Bronnimann, B. Henrich, G. Hulsen, E. F. Eikenberry, *Acta Crystallographica Section A* **2005**, *61*, 418.

7 Recycling perovskite solar cells to avoid lead waste

This chapter is based on the following publication:

Andreas Binek*, Michiel L. Petrus*, Niklas Huber, Helen Bristow, Yinghong Hu, Thomas Bein and Pablo Docampo, *Applied Materials and Interfaces*, **2016**, 8, 12881–12886.

*These authors contributed equally to this work

7.1 Introduction

Solar energy is the most abundant renewable energy source; its harvesting on a global scale shows the potential to fulfill the world's energy demand at low cost while minimizing greenhouse gas emissions, in accordance with the United Nations' Paris Agreement.^[1] Presently, hybrid halide perovskite materials such as methylammonium lead iodide (MAPbI₃) have emerged as extremely efficient light harvesters in solid-state solar cells.^[2, 3] Through optimization of the fabrication process,^[4-6] the annealing process^[7, 8] and the interfaces,^[9, 10] perovskite solar cells have already exceeded 20% power conversion efficiency (PCE), comparable to established commercial technologies such as CIGS, CdTe or poly-Si, and further improvements are expected.^[11]

Despite their high PCEs, perovskite solar cells still have not entered commercial markets at this time. One of the current major issues is the heavy metal lead used in the perovskite structure in high efficiency devices, which is known to be a significant hazard to the environment and human health.^[12, 13] The toxic effects of lead are ascribed to its harmful interactions with proteins, which cause changes in the folding of the proteins resulting in reduced activity and loss of function. Because of this, lead is harmful to all living organisms.^[14-16] While researchers worldwide have made progress towards developing

7.2 Cost Estimation of Perovskite based Solar Cell

perovskite photovoltaics based on lead alternatives,^[17] these devices show poorer photovoltaic performance and lower stability, making them less likely to be used on a large scale. It is thus important to prevent release of lead into the environment through device encapsulation.

Nevertheless, at the end of their working lifetime, the devices will have to be collected according to international electronic waste disposal regulations.^[18, 19] Recycling protocols have been published for other solar technologies.^[20, 21] For instance, recycling CdTe or CIGS solar cells requires fragmentation of the modules in a first step and then the metals are stripped in successive steps of chemical dissolution, mechanical separation and precipitation or electrodeposition.^[20] After that, (toxic) metals need to be isolated before they can be reused or handled in a waste stream. Reusing the hazardous materials is particularly interesting since the disposal of hazardous waste is expensive (about 1.10 \$/kg).^[22] Developing a recycling strategy in which all the different layers of the panels can be separately collected and reused could thus resolve the waste issues and make the procedure economically attractive.

Here we study the feasibility of recycling different layers of perovskite solar cells with respect to their environmental and cost impact. In our approach, the layers of a planar perovskite-based solar cell can be removed and recovered one by one, greatly simplifying the recycling process. In addition, we demonstrate that the expensive conductive glass as well as the toxic lead precursor can be reused. We believe that this approach could bring perovskite solar cells one step closer to their introduction into commercial systems.

7.2 Cost Estimation of Perovskite based Solar Cell

We estimated the cost of the different layers in a perovskite-based solar cell with planar architecture. In order to make a realistic comparison between the different layers, the price of the chemicals was taken for large lab-scale quantities from different commercial suppliers. In this cost estimation we omitted the solvents since their cost contribution is expected to be

negligible. Also the energy needed for the preparation is not included in the calculations, expect for the heating step in the TiO_2 blocking layer, which was annealed at 500 °C. We note that this is a very rough estimation, and upscaling of the production of perovskite solar cells is expected to have a significant influence on the price of starting materials. Nevertheless, the estimated costs can be used as a guide pointing out which layers are the most promising to recycle from an economical point of view.

Gold

We assume a 40 nm thick gold layer and no loss during the process. With the current gold price (32.414 €/kg in December 2015) this results in a price of 25 \$/m².

HTM (Spiro-OMeTAD)

The calculation for the hole transporting material spiro-OMeTAD has been published by Petrus *et al.* and was estimated to be 40 \$/m².^[23]

Perovskite (MAPbI_3)

We assume a layer thickness of 300 nm and a density of the perovskite^[24] of 4.092 g/cm³, which results in a weight of $1.23 \cdot 10^{-3}$ kg/m². Assuming a full conversion of PbI_2 and MAI into MAPbI_3 , and a cost of 915 \$/kg for PbI_2 (Fisher Chemicals) and of 850 \$/kg for MAI (DyeSol), results in a cost of 898 \$/kg. This results in a cost of 1.10 \$/m² for the perovskite layer.

Blocking layer (TiO₂)

The price for the titanium (IV) isopropoxide precursor is 3,336 \$/kg (Sigma Aldrich). The thickness of the TiO₂ is assumed to be 20 nm and the density $3.89 \cdot 10^3 \text{ kg/m}^3$,^[25] resulting in a cost of 0.31 \$/m². Additionally, we estimated the price for the calcination of the TiO₂ layer, since this is assumed to have a significant impact on the cost of this layer. For annealing on a lab-scale we used a hot plate (area 0.043 m²) and measured the required energy for the heating step (0.9 kWh). With these values an energy demand of 20.8 kWh/m² was obtained, which was multiplied by the energy cost of 0.10 \$/kWh (assumed) resulting in a cost of 2.08 \$/m² for the heating step and a full price for the blocking layer of 2.39 \$/m².

FTO

The cost of FTO / glass strongly varies depending on the supplier; we found cost estimates in the range of 100-850 \$/m² when ordered on a square meter scale. As we compare the lowest cost for lab scale we report a price of 100 \$/m² for the FTO / glass substrate. That makes the substrate by far the most expensive layer within the solar cell stack.

As a result of the large price variations, we also requested a quote from Pilkington for industrial amounts of FTO / glass, in order to estimate a minimum cost. In this case the minimum price would be around 18 \$/m² when ordered in very large quantities. Despite the fivefold lower price when ordered at this scale compared to the lab scale, the FTO / glass is still among the most expensive layers. And while low-cost alternatives for the hole transporter and top electrode are under development and being published, there is only little progress in replacing the FTO / glass substrate with low-cost alternatives. This emphasizes the potential of recycling the FTO / glass substrate.

7.3 Results and Discussion

In order to recycle perovskite solar cells, we have developed a procedure to strip down the device layer by layer. We performed this protocol on freshly prepared methylammonium lead iodide (MAPbI₃) perovskite solar cells with a planar device architecture, which were prepared following the synthetic route described by Xiao *et. al.*^[5] In the first step, the gold contact is removed using adhesive tape (step I, Figure 7-1). Secondly, the spiro-OMeTAD based hole-transporting layer is selectively removed via immersion of the device substrate into chlorobenzene (step II, Figure 7-1). This step selectively removes the hole transporter without removing the perovskite structure, as shown in Table 7-1.

Table 7-1: Metal concentrations measured by ICP in different fractions.

Solution	Pb_{217 nm} ($\mu\text{g mL}^{-1}$)	Pb_{220 nm} ($\mu\text{g mL}^{-1}$)	Ti_{335 nm} ($\mu\text{g mL}^{-1}$)	Ti_{336 nm} ($\mu\text{g mL}^{-1}$)
Chlorobenzene	<L.O.D.	0.068	<L.O.D.	<L.O.D.
Water	4.22	4.35	<L.O.D.	<L.O.D.
DMF	157.4	155.1	<L.O.D.	<L.O.D.
Detection limit	0.090	0.040	0.004	0.005

L.O.D. = limit of detection

Additionally, we showed that it is also possible to combine these two steps by delaminating the gold electrode by using ethyl acetate, after which the gold can be isolated via filtration. This would be particularly interesting for industrial processes where large volumes are required. Brief immersion in doubly distilled water then reconverts the perovskite layer into PbI₂ and methylammonium iodide (MAI), and the MAI is directly extracted into the water (step III, Figure 7-1). The short immersion time combined with the low solubility of PbI₂ in water results in a low lead concentration in the water ($4 \mu\text{g mL}^{-1}$), which is below the maximum concentration of contaminants for toxicity characteristic according to the US

7.3 Results and Discussion

Environmental Protection Agency (EPA).^[26] In step IV (Figure 7-1), PbI_2 is removed from the substrate by immersing the sample for a short time in dimethylformamide (DMF). Analysis shows that the PbI_2 was recovered quantitatively. Extended washing of the device in DMF will also result in the removal of the TiO_2 layer, resulting in a clean FTO substrate (step V, Figure 7-1).

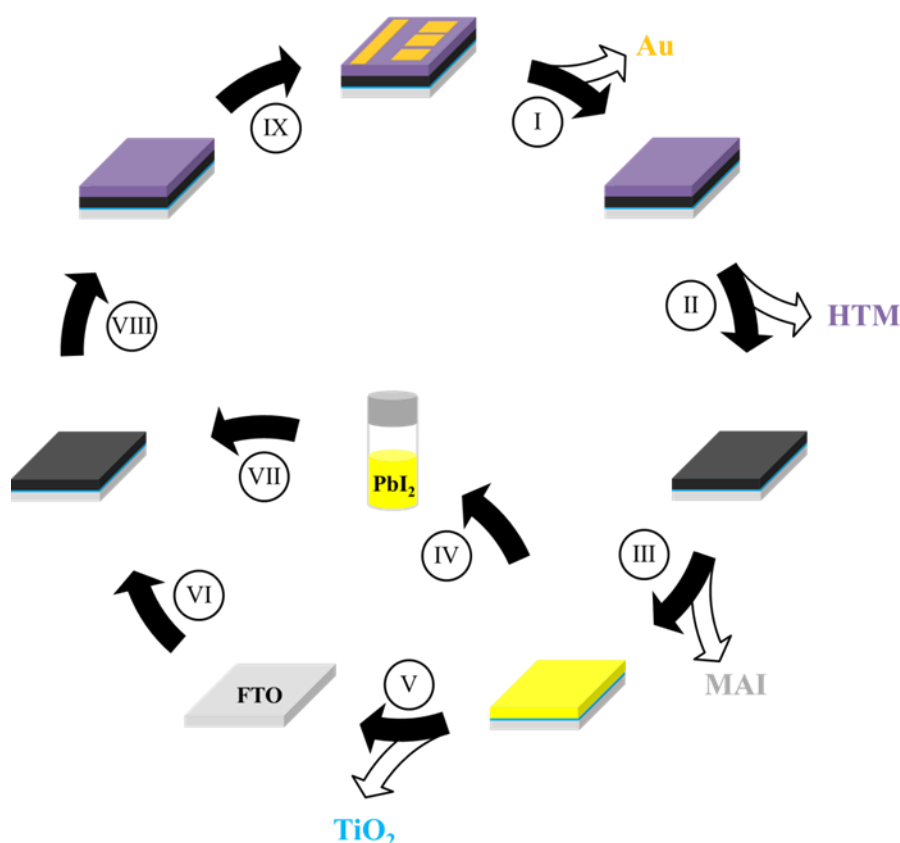


Figure 7-1: Recycling procedure for perovskite solar cells. I: Removing Au electrode with adhesive tape. II: Removing the HTM by immersing in chlorobenzene. III: Transformation of the perovskite into MAI and PbI_2 and extraction of MAI in water. IV & V: Removal of PbI_2 and TiO_2 using DMF. VI: Preparing a new TiO_2 film. VII: Formation of the perovskite film on recycled FTO from recycled PbI_2 . VIII: Preparation of the HTM layer. IX: evaporation of the Au top electrode.

The isolation of toxic lead iodide is important because of its harmful effects to the environment.^[11] However, by reusing the collected PbI_2 , the environmental impact would be even further reduced, leaving no toxic waste. In addition, the described process opens the possibility to recycle the FTO substrate, MAI, spiro-OMeTAD and gold layers.

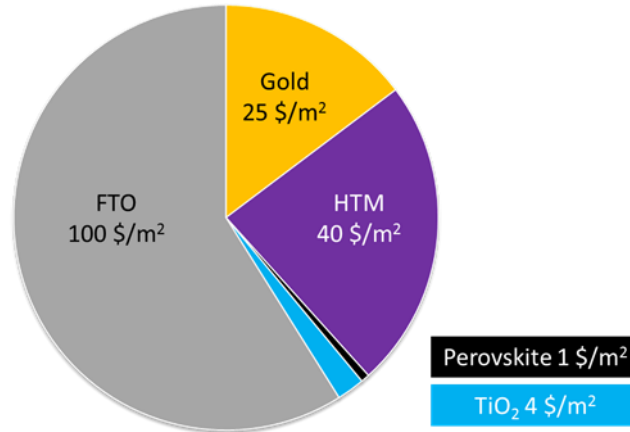


Figure 7-2: Pie chart displaying the estimated cost of the different layers in perovskite solar cells.

Cost analysis for different solar technologies such as organic (OPV), cadmium telluride (CdTe) and dye sensitized (DSSC) photovoltaics shows that the FTO / glass is a major factor of between 20-60% of the module cost.^[27, 28] In our cost estimation (depicted in Figure 7-2) we have determined that this is also the case for perovskite solar cells. Alternatives for the commonly used FTO substrates have been reported in the literature, including ITO / glass, PEDOT:PSS^[29] or graphene.^[30] However, to date, the best performance is still achieved with FTO substrates. Additionally, these alternatives are either more expensive, not commercially available or have not been scaled up yet. The hole transporting material is also a significant cost factor; however, recent publications have shown that several materials that can be produced at a fraction of the cost show the potential to compete with the current state-of-the-art spiro-OMeTAD,^[23, 31, 32] making recycling of this material less critical. The gold top electrode will most likely also be replaced by other materials when perovskite solar cells are scaled up, for example by silver paste.^[33, 34] The cost contribution of the perovskite layer consisting of PbI₂ and MAI and the titanium dioxide layer is relatively small, and the recycling of these layers is less interesting from an economic point of view. Based on the above considerations, here we focus on the recycling of PbI₂ for environmental reasons and on the FTO / glass for economic reasons.

Recycling of PbI₂

In the recycling process, PbI₂ was removed from the substrate through DMF extraction (Step IV, Figure 7-1). UV-vis absorption and ICP analyses show a quantitative recovery of the PbI₂, indicating that the process is very efficient. The solvents used for the recycling could get contaminated with other materials. In example, the water layer containing the MAI could contain traces of lead, since PbI₂ is slightly soluble in water (0.0756 g/100 mL at RT). Here we analyzed the purity of the different fractions using different techniques.

The solvents used for recycling of the solar cells were studied using UV-vis and the results are presented in Figure 7-3. For these measurements 225 cm² of solar cells were recycled. 14 mL of chlorobenzene was used to remove the spiro-OMeTAD, 14 mL of water to remove the MAI and 14 mL of DMF to remove the PbI₂. The chlorobenzene solution was diluted 20 times and clearly showed the absorption of spiro-OMeTAD and its oxidized species, which gives a signal in the range of 450-550 nm. MAI and PbI₂ are considered to be insoluble in chlorobenzene. The water solution containing the MAI did not show any absorption in the range from 350-800 nm and a small onset near 300 nm. A small increase in the absorption is measured near 300 nm, which we assume to originate from PbI₂, however, this signal hardly exceeds the noise. As reference two solutions containing 0.25 mg mL⁻¹ and 0.075 mg mL⁻¹ lead iodide have been added to the spectrum. These reference solutions absorb stronger at 300 nm than our solution, indicating that the PbI₂ concentration is below 0.075 mg mL⁻¹. The noise in the signal does not allow more precise analyses of the concentration of PbI₂ in this sample. We ascribe the low concentration of the lead iodide in the water, to the rather low temperature of the water (~20 °C) and very short immersion time. The DMF solution containing PbI₂ showed absorption with an onset around 410 nm. No absorption in the range of 450-550 nm was observed, indicating the absence of (oxidized) spiro-OMeTAD.

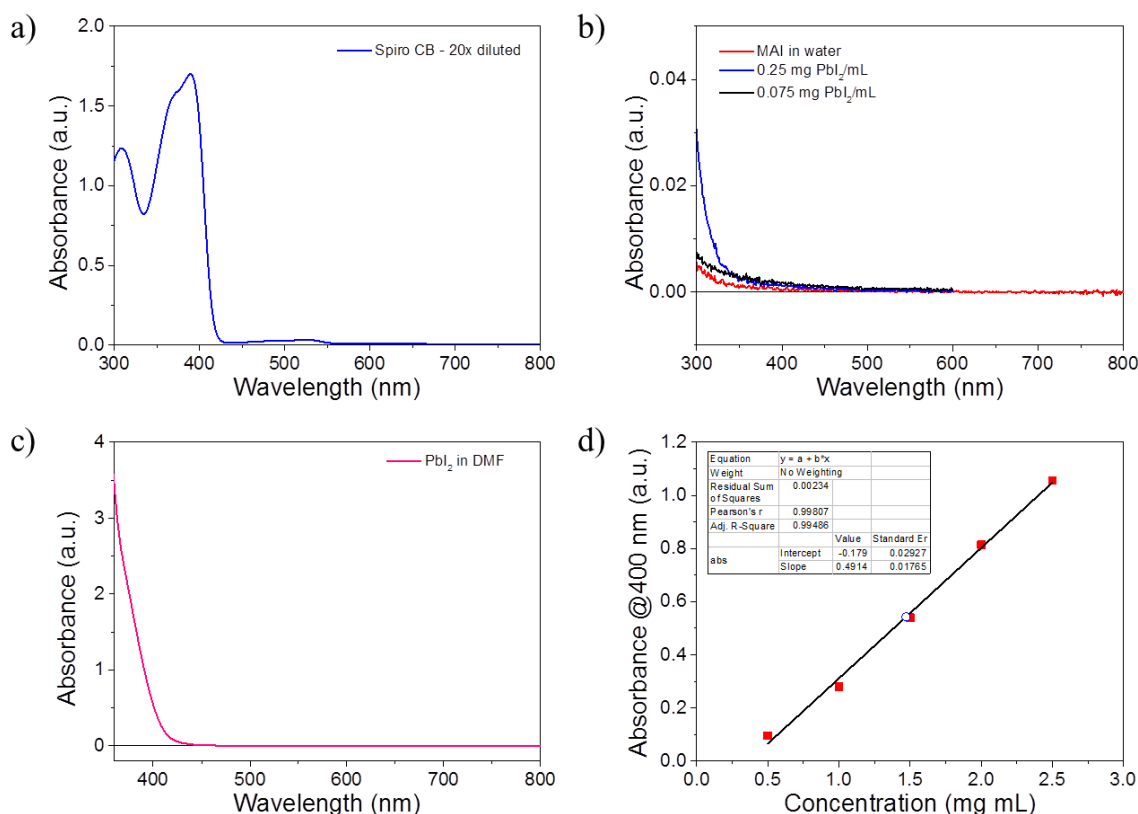


Figure 7-3: UV-vis absorption spectra of a) the chlorobenzene fraction (diluted 20 times) containing spiro-OMeTAD, b) the water fraction containing the extracted methyl ammonium iodide and traces of PbI₂, c) The DMF fraction containing lead iodide and d) the calibration line to determine the lead iodide concentration of the recovered PbI₂. The blue circle indicates the recycled DMF solution.

We prepared a calibration line of PbI₂ in DMF to determine the concentration of the solution. The absorption of the DMF solution from the recycling is marked with a blue circle in the graph (Figure 7-3d). The recycled solution has a concentration of 1.47 mg PbI₂ per mL of DMF. In total 14 mL of DMF was used for recycling 225 cm² of perovskite solar cell, which results in a recovery of 20.6 mg. Since the layer thickness is 300 ± 21 nm, we calculated the recovery rate of the PbI₂ to be $100 \pm 7\%$. We like to point out that the error in the (measured) layer thickness is relatively large, and therefore the error in the recovery rate is also relatively high. Nevertheless we show that the PbI₂ can be recovered quantitatively.

The solutions used for the UV-vis experiments were also used for the ICP measurements. The chlorobenzene was removed from the recovered spiro-OMeTAD under vacuum and then the

7.3 Results and Discussion

possibly present PbI_2 was dissolved in 15 mL of water. The recovered MAI solution in water was measured without workup. The DMF was removed from the recovered PbI_2 under vacuum and the solids were redissolved in 55 mL of water. These solutions were measured with ICP to check for the presence of lead and titanium. The concentration of titanium in all samples was below the detection limit ($<0.004 \mu\text{g mL}^{-1}$), indicating that the electron blocking layer does not dissolve during the recycling process and is simply delaminated. This is also expected since TiO_2 is considered insoluble in these solvents. The concentration of lead was determined at two different wavelengths (214 and 220 nm). The chlorobenzene fraction used to remove the spiro-OMeTAD practically contains no lead. The measurement at 217 nm showed no detectable amount of lead, while the measurement at 220 nm resulted in a concentration just above the detection limit of $0.068 \mu\text{g mL}^{-1}$. According to ICP measurements the water fraction used for extraction of MAI contains 4.22 to $4.35 \mu\text{g mL}^{-1}$ lead. This is in agreement with the UV-vis absorption measurements, which indicated that the concentration would be below $75 \mu\text{g PbI}_2 \text{ mL}^{-1}$. We ascribe the very low concentrations of lead in the water to the short immersion time and relatively low solubility of PbI_2 in water. Additionally we like to point out that the concentration of lead in the water is strongly influenced by the amount of water used (in our experiments around 700 mL per square meter of solar cell). Water containing $5 \mu\text{g mL}^{-1}$ lead or more are considered hazardous according to the US Environmental Protection Agency (EPA, Federal Hazardous Waste code D008).^[35] The water fraction containing the recovered MAI is therefore below the maximum concentration of contaminants for toxicity characteristic according to EPA. For the DMF fraction, which was used for extraction of the lead iodide, concentrations of 155.1 to $157.4 \mu\text{g Pb mL}^{-1}$ were measured. This would result in a total recovery of 19.0 - 19.3 mg PbI_2 for 225 cm^2 of solar cell (92 – 94%). Comparable to the results from the UV-vis experiments, a near quantitative recovery rate was obtained (see Table 7-1).

Recycling 70 dm² of perovskite film yields around 600 mg of PbI₂, which is enough to prepare 1 mL of a 1.25 M PbI₂ solution. This permits the production of recycled MAPbI₃ films with an area of around 2 dm². The large amount of perovskite film required to prepare the recycled PbI₂ solution is the result of the significant material loss when preparing films using spin-coating techniques. On an industrial scale, spin-coating will most likely be replaced by other techniques, such as slot die coating, where material loss can be close to negligible thus making the recycling more efficient.

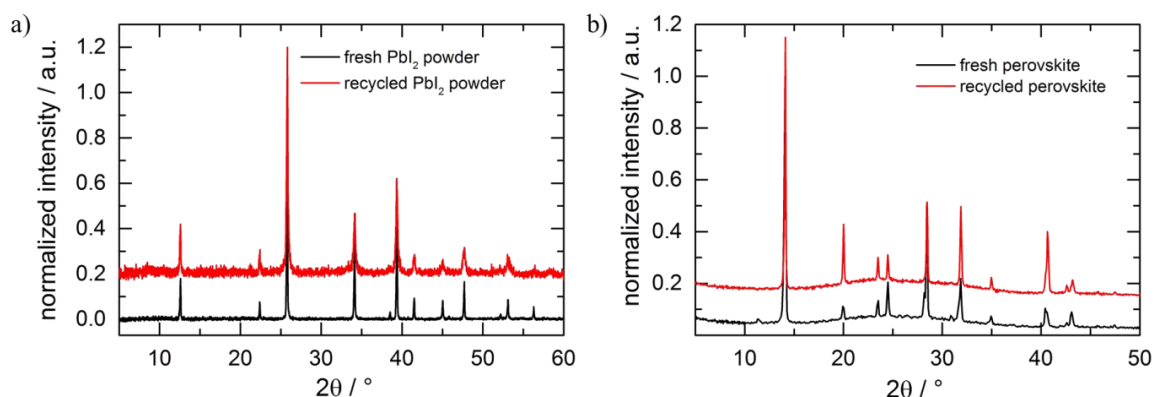


Figure 7-4: Comparison of the XRD patterns of recycled PbI₂ and fresh PbI₂ (a), and MAPbI₃ perovskite films prepared from fresh PbI₂ and from recycled PbI₂ (b). The normalized XRD patterns are offset for clarity.

The recycled PbI₂ was studied by ¹H-NMR (in DMSO-d₆) and UV-vis and no traces of spiro-OMeTAD or other organic compounds were observed in its spectrum (Figure 7-5), while ICP measurements indicate the absence of titanium dissolved in the DMF (Table 7-1). The recycled PbI₂ and perovskite films prepared from the recycled PbI₂ were characterized by XRD and compared to the films prepared from fresh starting materials (Figure 7-4). No changes in the XRD patterns were observed for the recycled PbI₂ and the resulting perovskite film. The observed reflections also correspond to the theoretical reflections of PbI₂ and MAPbI₃.

7.3 Results and Discussion

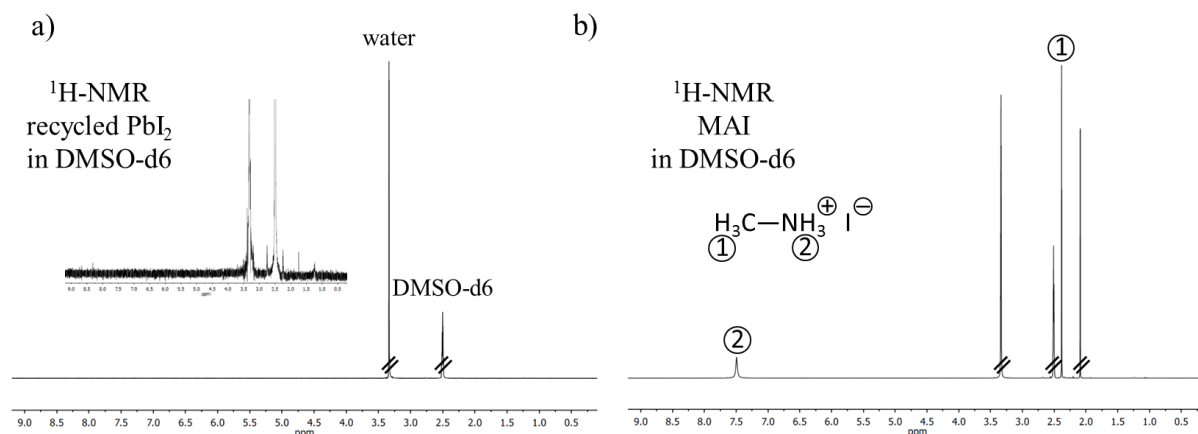


Figure 7-5: ^1H -NMR spectra of recycled PbI_2 (a) and MAI as reference (b) both in DMSO-d_6 .

Photovoltaic devices prepared using the recycled PbI_2 were characterized and their J - V characteristics are shown in Figure 7-6. Although the devices show good performance with best efficiencies exceeding 12%, their PCE is lower than that of devices prepared from highly pure PbI_2 purchased from Sigma-Aldrich (99%+), termed “fresh” in the rest of the article. The lower PCE mainly originates from a lower open circuit voltage (V_{OC} 0.95 vs 1.03 V) and fill factor (FF, 65 vs 74%). This most likely originates from a very small amount of impurities in the PbI_2 solution, which were undetectable with NMR, UV-vis absorption, XRD or ICP measurements. The trace contaminations are probably MAI and/or TiO_2 particles. To examine this hypothesis, we recrystallized the recycled PbI_2 from water in order to remove possible impurities in the material.^[36] Solar cells prepared from this recycled and recrystallized PbI_2 (from here on termed “recrystallized”) show improved device performance with PCEs up to 13.5% and an average of 12.5% (compared to an average of 13.0% for the fresh PbI_2 ,

Table 7-4) and a significant improvement in the V_{OC} and FF (see inset Figure 7-6). Scanning electron microscopy (SEM) cross-sectional images of the devices prepared from fresh and recycled PbI_2 show similar morphology (Figure 7-6b, c), which is in line with the comparable device performance. This demonstrates (i) that our recycling process is able to isolate the

toxic PbI_2 from the perovskite solar cells, and (ii) that the recycled PbI_2 can be reused for the preparation of efficient new solar cells.

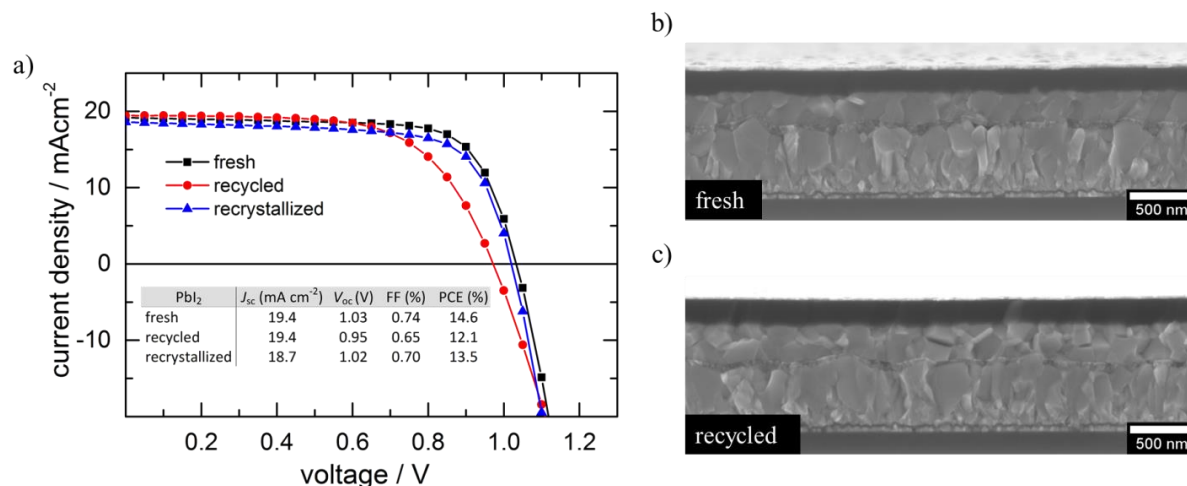


Figure 7-6: a) *J-V* characteristics of perovskite solar cells prepared from fresh, recycled and recycled and recrystallized PbI_2 . SEM cross-section of solar cells prepared from b) fresh PbI_2 and c) recycled PbI_2 .

Recycling the glass/FTO

The cost analysis discussed above shows that the FTO / glass substrate is the most expensive part of the perovskite solar cells, and thus the most economically interesting layer to recycle. In a first approach, the TiO_2 -coated FTO / glass substrate was recycled directly after removing the PbI_2 with DMF. Photovoltaic devices prepared on these substrates showed a significant decrease in device performance over several recycling cycles (Figure 7-7).

7.3 Results and Discussion

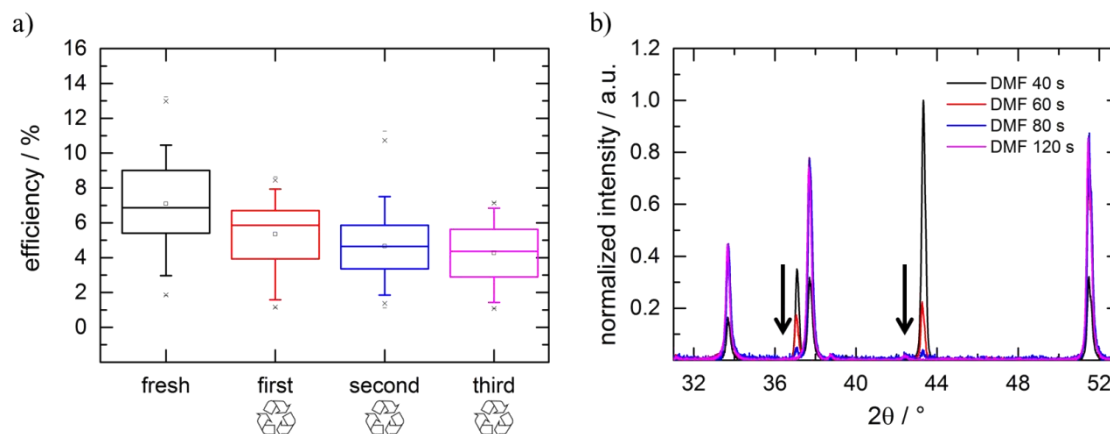


Figure 7-7: Box plot of the PCEs for the devices prepared on fresh and recycled $\text{TiO}_2/\text{FTO}/\text{glass}$. The box plot displays the average, median, minimum, maximum and 75 and 95% deviation, respectively (a). XRD pattern of $\text{FTO} / \text{TiO}_2$ substrates immersed into DMF for different times (b). The decrease of the TiO_2 reflections is illustrated with two black arrows.

XRD studies showed that removing the PbI_2 with DMF also degrades the underlying TiO_2 layer, suggesting that this is the reason behind the lower device. However, the XRD study also revealed that complete removal of the TiO_2 underlayer is possible by prolonged immersion in DMF, which was confirmed by energy dispersive X-ray spectroscopy (EDX) and UV-vis (Figure 7-3 and Figure 7-8).

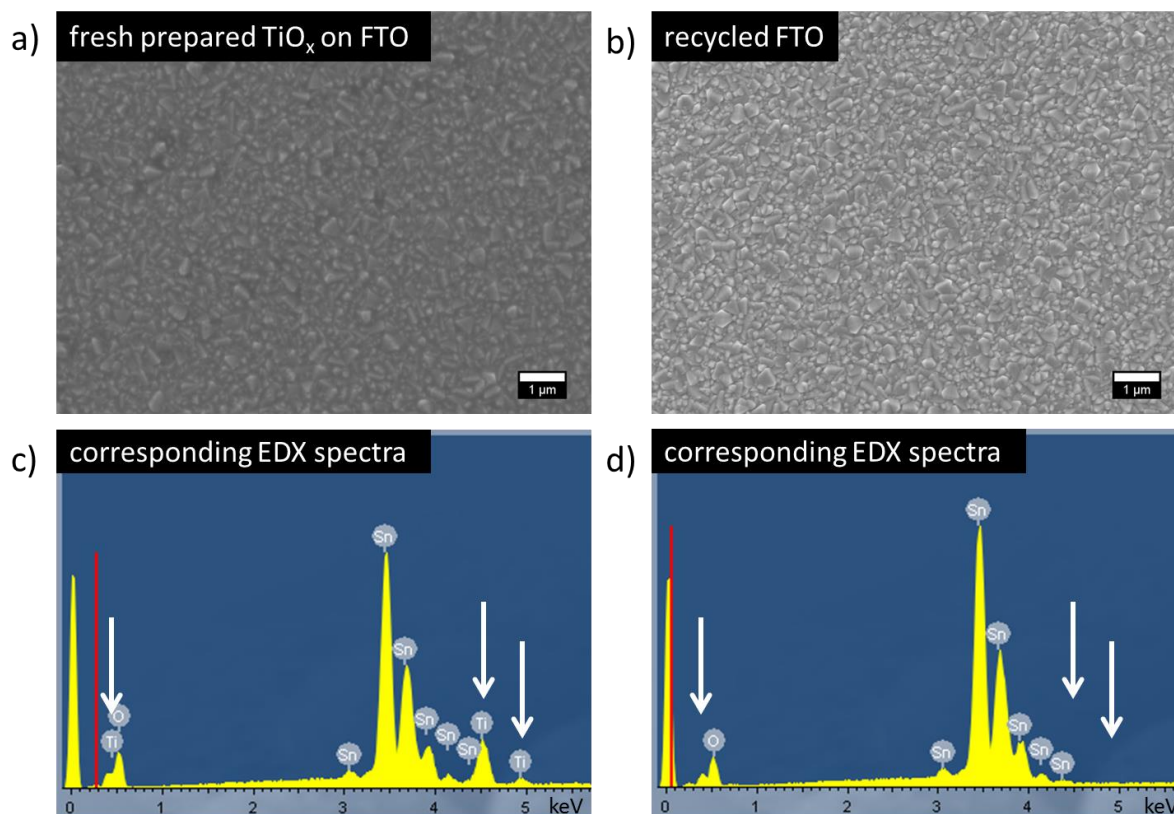


Figure 7-8: SEM top view image of a FTO-TiO₂ substrate (a) and a recycled FTO substrate (b) and the corresponding EDX spectra (c-d). The white arrows mark the peaks of Ti.

Since TiO₂ is insoluble in DMF^[37] we expect that the solvent penetrates through pores in the TiO₂, resulting in the delamination of the layer (see Figure 7-9). In order to see the effect of the DMF treatment on the TiO₂, cross-sections of a 600 nm thick blocking layer were analyzed by SEM. The extra-thick blocking layer was prepared by spin-coating several layers using the standard sol-gel approach with heating steps (150 °C/10 min) in between. One of these samples was afterwards immersed in DMF for 3 min and dried at 100 °C. In Figure 7-9 the images of both a DMF treated and a non-treated sample are shown. The SEM images indicate that the DMF delaminates the TiO_x layer by infiltrating the interface. Further studies regarding the delamination process are ongoing.

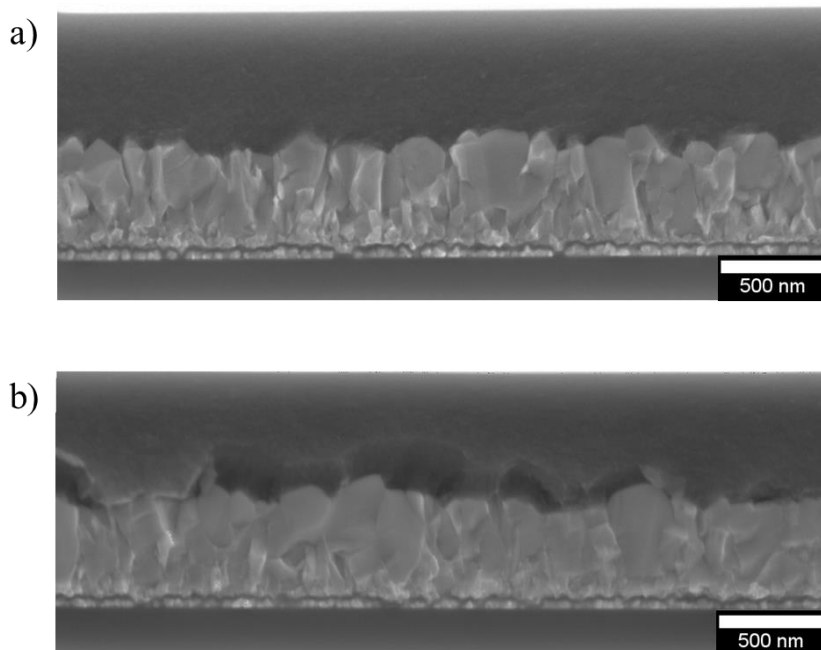


Figure 7-9: Cross-sections of non-calcined TiOx blocking layers before (a) and after the DMF treatment (b).

The transmittance of the substrate was studied by UV-vis absorption for fresh FTO, FTO with TiO₂ and recycled FTO and the results are presented in Figure 7-10. The transmittance for all films is around 80% for most of the visible spectrum. The thin layer of TiO₂, most clearly affects the spectrum in the region of 350-500 nm. On the recycled substrate the TiO₂ was successfully removed as can be seen in the transmission spectrum.

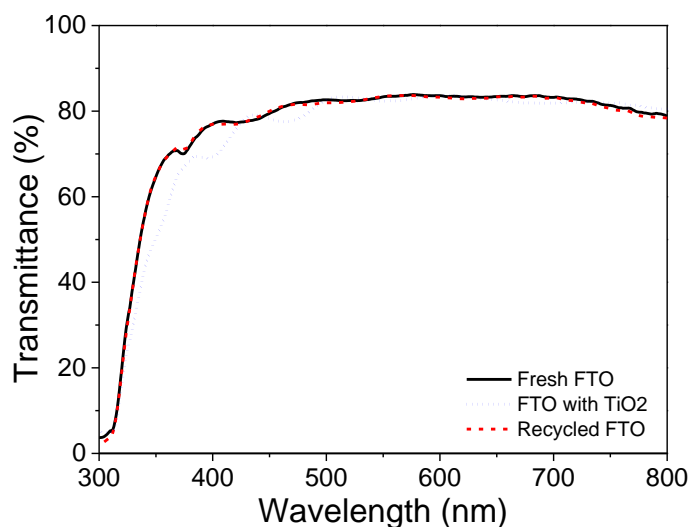


Figure 7-10: Transmittance spectra of fresh FTO, FTO with TiO₂ and recycled FTO substrates.

To address this issue, a fresh electron-selective TiO_2 layer was prepared on the recycled and cleaned FTO / glass substrate using the same deposition protocol. These devices show no loss in performance even after several recovery cycles (Figure 7-11 and Table 7-2). The devices show a relatively narrow distribution of PCEs (standard deviations just above 1%) over a large set of 24 individual devices and no significant drop in any of the device performance parameters (Figure 7-12, Figure 7-13 and

Table 7-4).

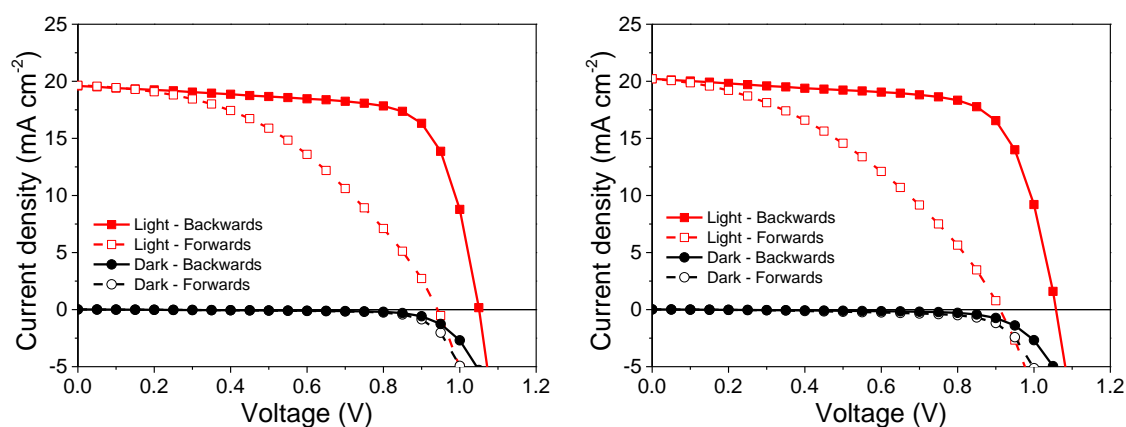


Figure 7-11: *J-V* curves of the record cells on fresh FTO and 3x recycled FTO, showing no significant differences in the hysteresis or the dark measurements.

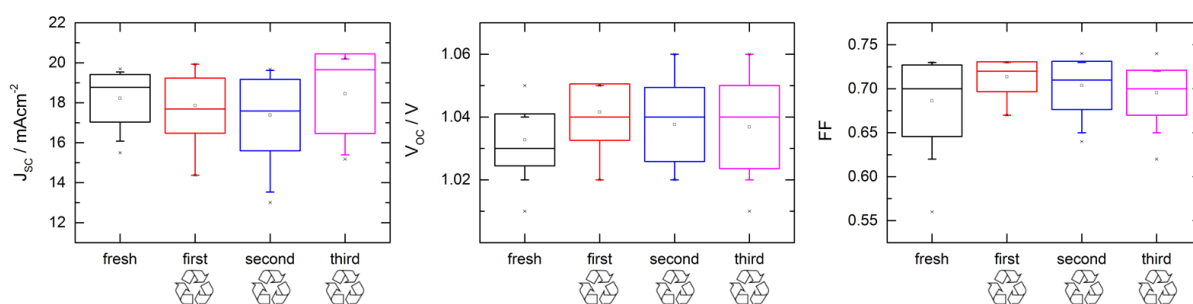


Figure 7-12: Box plot of the J_{sc} , V_{oc} and FF with displaying the average, median, minimum, maximum and 75 and 95% deviation of solar cells prepared on fresh, one, two and three times recycled FTO, respectively.

7.3 Results and Discussion

Table 7-3: Device performance of device after recycling the FTO / glass substrate over various cycles.

Freshly prepared	$J_{SC} / \text{mA cm}^{-2}$	PCE / %	V_{OC} / V	FF
Average values	18.2	13.0	1.03	0.69
Standard deviation	1.2	1.1	0.01	0.04
Best cell	19.2	14.6	1.03	0.73
Shorted cells	2 out of 24			

First recycling	$J_{SC} / \text{mA cm}^{-2}$	PCE / %	V_{OC} / V	FF
Average values	17.9	13.4	1.04	0.71
Standard deviation	1.4	1.1	0.01	0.02
Best cell	19.6	15.1	1.05	0.72
Shorted cells	5 out of 24			

Second recycling	$J_{SC} / \text{mA cm}^{-2}$	PCE / %	V_{OC} / V	FF
Average values	17.4	12.8	1.04	0.70
Standard deviation	1.8	1.3	0.01	0.03
Best cell	19.6	14.7	1.03	0.72
Shorted cells	3 out of 24			

Third recycling	$J_{SC} / \text{mA cm}^{-2}$	PCE / %	V_{OC} / V	FF
Average values	18.5	13.5	1.04	0.70
Standard deviation	2.0	1.5	0.01	0.03
Best cell	20.2	15.4	1.06	0.71
Shorted cells	2 out of 24			

The best cells show similar power conversion efficiencies between 14.6 and 15.4% for all batches, where the highest PCE was obtained on a three-times recycled substrate. The slightly higher PCEs on the recycled substrates may be the result of an improved coverage of TiO_2 over the FTO substrate.

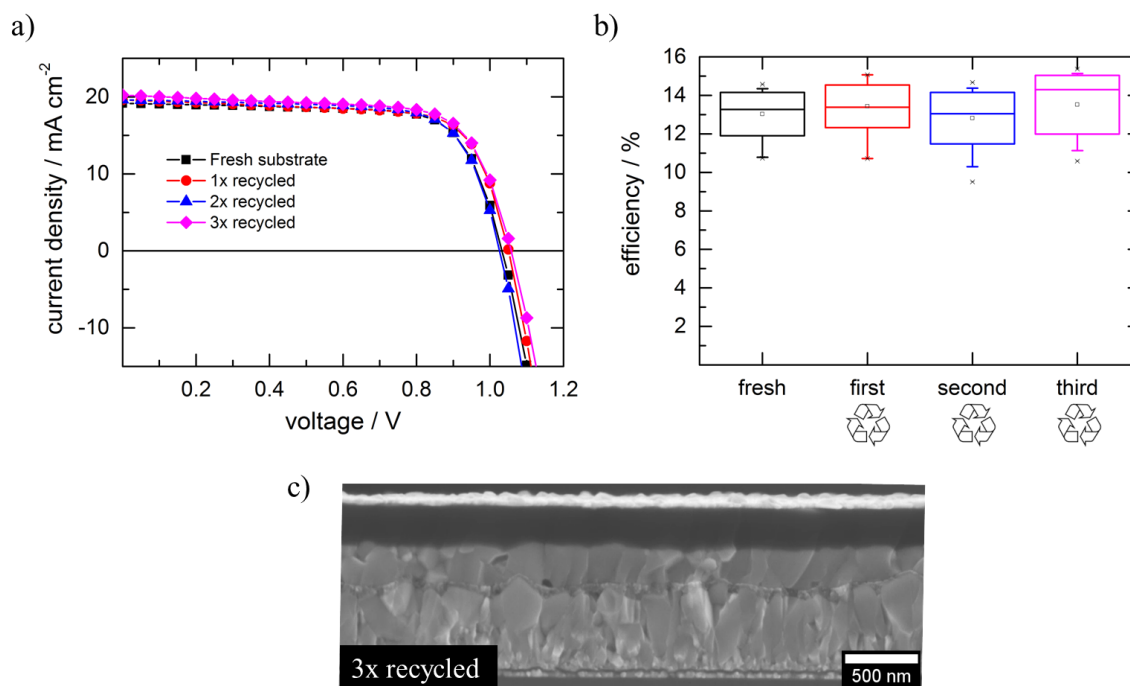


Figure 7-13: Device performance of solar cells prepared on recycled FTO / glass substrates. a) J - V characteristics, b) bar diagram showing the average (circle), median (middle line), maximum, minimum (crosses) and 75 (box) and 95% (small error bar) distribution of 24 individual cells for each of the recycling steps. c) SEM cross-section of a record cell prepared on a three-times recycled substrate.

Table 7-4: Device performance after recycling the FTO substrate.

		J_{sc} (mA cm^{-2})	V_{oc} (V)	FF (%)	PCE (%)
Fresh	Record	19.2	1.03	73	14.6
	Average	18.2 ± 1.2	1.03 ± 0.01	69 ± 4	13.0 ± 1.1
First recycled	Record	19.6	1.05	72	15.1
	Average	17.9 ± 1.4	1.04 ± 0.01	71 ± 2	13.4 ± 1.1
Second recycled	Record	19.6	1.03	72	14.7
	Average	17.4 ± 1.8	1.04 ± 0.01	70 ± 3	12.8 ± 1.3

7.3 Results and Discussion

Third recycled	Record	20.2	1.06	71	15.4
	Average	18.5 ± 2.0	1.04 ± 0.01	70 ± 3	13.5 ± 1.5

Lead has been commonly used in households for millennia in all kinds of applications, such as in pots, pans, pipes and paints. However, since the 19th century the toxic effects of non-metallic lead have become apparent. In particular, water soluble lead salts are potentially very harmful, as they can be easily taken up by living organisms, where a small daily dose of 1 mg results in chronic lead poisoning symptoms in humans, such as birth defects.^[38-40] In the case of perovskite solar cells, lead is present in the 2⁺ oxidation state, which makes it soluble in water and thus a hazard to human health if the cells are employed in large scale applications.

As shown in the cost estimation above, each square meter of solar panel would contain approximately 1.2 g of perovskite absorber. MAPbI₃ consist of 34 wt% lead, which leads to a lead content 0.42 g/m² solar cell. When considering a single solar park, which can easily exceed more than 200 hectares (2 x 10⁶ m²), the total lead content of such a solar park would be over 800 kg. Without a proper way of handling these large amounts, general support for such a park would be unlikely due to the well-known dangers of lead.

An accurate cost estimation of the recycling procedure at this point is challenging since many assumptions have to be made. Both the cost of the recycling process and the cost of perovskite based solar panels, produced on an industrial scale, are difficult to evaluate. However, the cost of transportation and dismantling are unavoidable since the panels have to be collected after their operation lifetime in accordance with international electronic waste disposal laws. The additional costs for the recycling are expected to be relatively low since the process presented here is entirely based on low temperature solution steps. In addition to being economically attractive once perovskite solar cells are produced on a large scale, the recycling of the FTO

substrate is already of interest for research facilities and startup companies. As demonstrated, the expensive FTO substrates can be recycled in a simple and low-cost process, which reduces the overall material cost and also saves production time since the recycled substrates are already patterned and cut to the appropriate size.

7.4 Conclusion

In conclusion, we have demonstrated an environmentally responsible and cost-efficient recycling process for solar cells based on MAPbI₃. Our results show that perovskite solar cells can be stripped down in a layer-by-layer approach, and that the collected materials can be reused without significant losses to device performance. In particular, we show that the toxic PbI₂ can be recycled and, after recrystallization, can be employed to prepare devices exhibiting power conversion efficiencies up to 13.5%. With this approach, the risk of lead contaminating the environment can be decreased, while still retaining PbI₂ as the starting material for the production of highly efficient solar cells. In addition, we were able to recycle the expensive FTO / glass substrates several times without significant loss of device performance on solar cells exhibiting PCEs exceeding 15%. This work demonstrates a process to address the environmental and health issues of lead based-perovskite solar cells and combines this with a cost-reducing recycling process, bringing perovskite solar cells one step closer to their introduction into commercial systems.

7.5 Experimental Section

All materials were obtained from commercial sources and used as received, unless stated otherwise.

7.5 Experimental Section

Solar cell preparation

Fluorine doped tin oxide (FTO) coated glass sheets (7 Ω /sq, Pilkington, USA) were patterned by etching with zinc powder and 3 M HCl. They were subsequently cleaned with a 2% Hellmanex solution and rinsed with de-ionized water, ethanol and acetone. Directly before applying the blocking layer, last organic residues were removed by an oxygen plasma treatment for 5 minutes. The dense TiO₂ layer was prepared from a sol-gel precursor solution by spin-coating onto the substrates and calcining at 500 °C in air.^[41] For the sol-gel solution a 27.2 mM solution of HCl in 2-propanol was added dropwise to a vigorously stirred 0.43 mM solution of titanium isopropoxide (99.999%, Sigma-Aldrich) in dry 2-propanol. The solution remained clear during the addition and was discarded otherwise. After cooling down, the substrate was transferred to a nitrogen-filled glovebox. A solution consisting of PbI₂ (1.25 M) and methylammonium iodide (1.25 M) in DMF was spin-coated dynamically (at 5000 rpm, total 15 s) onto the substrate. After 5 s, 100 μ L of chlorobenzene was added on top of the spinning substrate and afterwards the substrate was placed on a hotplate (100 °C for 10 min). After cooling down to room temperature, the films were covered with a layer of spiro-OMeTAD (Borun Chemicals, 99.5% purity). For this purpose, spiro-OMeTAD was dissolved in 1 mL chlorobenzene. The solution was filtered and 10 μ l 4-*tert*-butylpyridine (*t*BP) and 30 μ l of a 170 mg/mL bis(trifluoromethane)sulfonamide lithium salt (LiTFSI) solution in acetonitrile were added. This solution was spin-coated dynamically at 1500 rpm for 45 s. The devices were stored overnight under air at room temperature and <30 rel% humidity to allow for oxidation of the spiro-OMeTAD. The top electrode was deposited by thermal evaporation of gold under vacuum (at $\sim 10^{-6}$ mbar), with a thickness of 40 nm.

Recycling of the solar cells

In the first step the gold top electrode was removed with scotch tape, which was lightly pressed on the surface of the solar cell before pulling off. Alternatively, the gold can be removed by dissolving the hole transporter as described below, which resulted in delamination of the gold electrodes. Afterwards the gold can be collected via filtration.

The removal of the hole-transporter was done by immersing the whole substrate in chlorobenzene while slowly swirling the solution. After 1 min. the substrate was removed from the solution and was dried under a nitrogen stream. As a more environmentally friendly alternative to chlorobenzene, ethyl acetate can be used as solvent to remove the hole transporter using the same protocol as describe above. In order to extract the methylammonium iodide from the perovskite, the surface of the substrate was dipped in distilled water for approximately 1 s and dried under a nitrogen stream afterwards. To evaporate the residual water, the substrate was placed on a hot plate at 100 °C for 10 min. The obtained PbI_2 layer was immersed for 40 s in DMF to dissolve the PbI_2 . The concentration of this solution was studied by UV-Vis spectroscopy (for more details see Figure 7-3). This solution was used for recycling the PbI_2 . For the recycled and recrystallized batch of PbI_2 , the DMF was removed under vacuum. The solids were dissolved in refluxing water and the solution was filtered to remove insoluble particles. The solution was slowly cooled down to 4 °C resulting in the crystallization of the PbI_2 as golden flakes. The PbI_2 was collected by filtration and dried under vacuum prior to use. The PbI_2 solutions of the recycled and recrystallized PbI_2 looked clear and bright yellow. The glass / FTO / TiO_2 substrate resulting from the above removal steps was placed in a fresh DMF bath for at least 4 min to remove the TiO_2 layer, after which the FTO substrate was dried at 100 °C. After cooling down, the FTO / glass substrate can be used for the preparation of new devices.

7.5 Experimental Section

Characterization details:

Scanning electron microscopy images were acquired on a Jeol JSM-6500F microscope. The cross-sections were freshly cut directly before the measurement. The investigation of the elemental composition was performed by energy dispersive X-ray (EDX) analysis with an EDX-detector from OXFORD INSTRUMENTS.

The X-ray diffraction patterns of the PbI_2 powder were obtained on a STOE powder diffractometer in transmission geometry ($\text{Cu K}\alpha_1$, $\lambda = 1.5406 \text{ \AA}$) equipped with a position-sensitive Mythen-1K detector. X-ray diffraction analysis of perovskite films was carried out in reflection mode using a Bruker D8 Discover with Ni-filtered $\text{Cu K}\alpha_1$ -radiation ($\lambda = 1.5406 \text{ \AA}$) and a position-sensitive semiconductor detector (LynxEye).

^1H -NMR measurements were performed using a Bruker WM-400, 400 MHz. The PbI_2 was dissolved in DMSO-d_6 and the recorded spectra were referenced to the solvent (DMSO-d_6 : ^1H , 2.50 ppm) relative to TMS.

Steady-state UV-Vis absorption spectra were acquired with a Lambda 1050 UV-Vis spectrophotometer (Perkin Elmer) using an integration sphere.

Inductively coupled plasma optical emission spectrometry (ICP-OES) measurements were carried out using a Varian Vista RL.

J - V curves were recorded with a Keithley 2400 source meter under simulated AM1.5G sunlight, with an incident power of approximately 100 mW cm^{-2} , which was corrected for the exact light intensity using a Fraunhofer ISE certified silicon cell. The reported device characteristics were estimated from the measured J - V curves obtained from the backwards scan (from V_{OC} to J_{SC}). All our devices show a significant amount of hysteresis between the

forward and backwards scan, which is comparable for all prepared samples. The active area of the solar cells was defined with a square metal aperture mask of 0.0831 cm^2 .

7.6 Literature

- [1] United Nations Framework Convention on Climate Change (UNFCCC), Paris 2015.
- [2] M. M. Lee, J. Teuscher, T. Miyasaka, T. N. Murakami, H. J. Snaith, *Science* **2012**, 338, 643.
- [3] J. Burschka, N. Pellet, S.-J. Moon, R. Humphry-Baker, P. Gao, M. K. Nazeeruddin, M. Grätzel, *Nature* **2013**, 499, 316.
- [4] M. Xiao, F. Huang, W. Huang, Y. Dkhissi, Y. Zhu, J. Etheridge, A. Gray-Weale, U. Bach, Y.-B. Cheng, L. Spiccia, *Angew. Chem. Int. Ed.* **2014**, 126, 10056.
- [5] Z. Xiao, C. Bi, Y. Shao, Q. Dong, Q. Wang, Y. Yuan, C. Wang, Y. Gao, J. Huang, *Energy Environ. Sci.* **2014**, 7, 2619.
- [6] W. Nie, G. Gupta, B. K. Crone, F. Liu, D. L. Smith, P. P. Ruden, C.-Y. Kuo, H. Tsai, H.-L. Wang, H. Li, S. Tretiak, A. D. Mohite, *Adv. Sci.* **2015**, 2, 1.
- [7] G. E. Eperon, V. M. Burlakov, P. Docampo, A. Goriely, H. J. Snaith, *Adv. Funct. Mater.* **2013**, 24, 151.
- [8] F. X. Xie, D. Zhang, H. Su, X. Ren, K. S. Wong, M. Grätzel, W. C. H. Choy, *ACS Nano* **2015**, 9, 639.
- [9] P. Docampo, J. M. Ball, M. Darwich, G. E. Eperon, H. J. Snaith, *Nat. Commun.* **2013**, 4, 2761.
- [10] H. Zhou, Q. Chen, G. Li, S. Luo, T.-b. Song, H.-S. Duan, Z. Hong, J. You, Y. Liu, Y. Yang, *Science* **2014**, 345, 542.
- [11] M. A. Green, K. Emery, Y. Hishikawa, W. Warta, E. D. Dunlop, *Prog. Photovoltaics* **2015**, 23, 1.
- [12] L. Patrick, *Altern Med Rev* **2006**, 11, 2.
- [13] I. R. Benmessaoud, A.-L. Mahul-Mellier, E. Horvath, B. Maco, M. Spina, H. Lashuel, L. Forro, *Toxicol Res* **2015**, 5, 407.
- [14] H. Needleman, *Annu Rev Med* **2004**, 55, 209.
- [15] C. D. Toscano, T. R. Guilarte, *Brain. Res. Rev.* **2005**, 49, 529.
- [16] B. Pourrut, M. Shahid, C. Dumat, P. Winterton, E. Pinelli, *Reviews of Environmental Contamination and Toxicology* **2011**, 213, 113.
- [17] F. Hao, C. C. Stoumpos, D. H. Cao, R. P. H. Chang, M. G. Kanatzidis, *Nat Photon* **2014**, 8, 489.
- [18] European Parliament, Off. J. Eur. Union, L37 2003, 24.

- [19] European Parliament, Off. J. Eur. Union L197 2012, 38.
- [20] V. M. Fthenakis, *Energy Policy* **2000**, 28, 1051.
- [21] T. Y. Wang, Y. C. Lin, C. Y. Tai, R. Sivakumar, D. K. Rai, C. W. Lan, *J. Cryst. Growth* **2008**, 310, 3403.
- [22] V. Fthenakis, P. Moskowitz, *Prog. Photovoltaics* **2000**, 8, 27.
- [23] M. L. Petrus, T. Bein, T. J. Dingemans, P. Docampo, *J. Mater. Chem. A* **2015**, 3, 12159.
- [24] C. C. Stoumpos, C. D. Malliakas, M. G. Kanatzidis, *Inorg. Chem.* **2013**, 52, 9019.
- [25] T. E. Weirich, M. Winterer, S. Seifried, J. Mayer, *Acta Crystallogr. Sect. A* **2002**, 58, 308.
- [26]
- [27] C. Candelise, M. Winkler, R. Gross, *Prog. Photovoltaics* **2012**, 20, 816.
- [28] J. Kalowekamo, E. Baker, *Sol. Energy* **2009**, 83, 1224.
- [29] K. Sun, P. Li, Y. Xia, J. Chang, J. Ouyang, *ACS App. Mater. Interfaces* **2015**, 7, 15314.
- [30] H. Sung, N. Ahn, M. S. Jang, J.-K. Lee, H. Yoon, N.-G. Park, M. Choi, *Adv. Energy Mater.* **2015**, 6, 1.
- [31] J. Liu, S. Pathak, T. Stergiopoulos, T. Leijtens, K. Wojciechowski, S. Schumann, N. Kausch-Busies, H. J. Snaith, *J. Phys. Chem. Lett.* **2015**, 6, 1666.
- [32] M. Saliba, S. Orlandi, T. Matsui, S. Aghazada, M. Cavazzini, J.-P. Correa-Baena, P. Gao, R. Scopelliti, E. Mosconi, K.-H. Dahmen, F. De Angelis, A. Abate, A. Hagfeldt, G. Pozzi, M. Grätzel, M. K. Nazeeruddin, *Nature Energy* **2016**, 1, 1.
- [33] M. Lee, Y. Ko, B. K. Min, Y. Jun, *ChemSusChem* **2015**, 9, 31.
- [34] A. Kim, H. Lee, H.-C. Kwon, H. S. Jung, N.-G. Park, S. Jeong, J. Moon, *Nanoscale* **2015**, 8, 6308.
- [35] V. J. Brown, *Environ. Health Perspect.* **2004**, 112, 734.
- [36] J. P. Ponpon, M. Amann, *Cryst. Res. Technol.* **2007**, 42, 253.
- [37] K. Othmer, *Encyclopedia of Chemical Technology*, Vol. 27, John Wiley & Sons, New York 2007.
- [38] R. A. Goyer, T. W. Clarkson, *Toxic Effects of Metals*, Vol. 1236, McGraw-Hill, New York 1996.
- [39] A. Demayo, M. C. Taylor, K. W. Taylor, P. V. Hodson, P. B. Hammond, *Crit. Rev. Env. Contr.* **1982**, 12, 257.

7.6 Literature

- [40] R. A. Goyer, *Environ. Health Perspect.* **1990**, 86, 177.
- [41] J. M. Ball, M. M. Lee, A. Hey, H. J. Snaith, *Energy & Environmental Science* **2013**, 6, 1739.

8 Antimony and Bismuth Based Materials as Lead-Free Light Absorber

8.1 Introduction

One of the current major issues for perovskite based solar cells is the heavy metal lead (Pb) in the absorber layer, which is known to be a significant hazard to the environment and human health.^[1, 2] In particular, water soluble salts are potentially very harmful, as they can be easily taken up by living organisms.^[3-5] Previously it has been reported that tin (Sn) can replace lead to form the less toxic MASnI_3 , and solar cells with an efficiency of over 6% were reported.^[6] The challenge with this compound is the low stability of the 2^+ oxidation state of Sn and the associated easy oxidation to the preferred tetravalent 4^+ state through exposure to air and humidity.^[6]

In order to overcome the problem with the stability of the oxidation state while maintaining the reduced toxicity of the metal ion within the perovskites structure, first attempts have been made to use elements from the group 15 in the periodic table. The general valence shell electronic configuration of these elements is ns^2np^3 . The elements of group 15 generally exhibit 3^- , 3^+ and 5^+ oxidation states. Due to the inert pair effect, the stability of the 5^+ state decreases and that of the 3^+ state increases by moving down the group in the periodic table,^[7] which implies a high stability of Bi^{3+} and Sb^{3+} . Additionally, bismuth and antimony are significantly less toxic than lead.^[8]

Here we report the synthesis and characterization of different bismuth and antimony based compounds and their applicability as photovoltaic absorbers. Thereby, we will focus on the inorganic compound $\text{Cs}_3\text{M}_2\text{I}_9$ ($\text{M} = \text{Bi}^{3+}$, Sb^{3+}), the hybrid organic-inorganic compound HDABiI_5 ($\text{HAD} = 1.6\text{-hexanediammonium}$) and the halide double perovskite $\text{Cs}_2\text{M}^{\text{I}}\text{M}^{\text{III}}\text{X}_6$ ($\text{M}^{\text{I}} = \text{Cu}^+$, Ag^+ ; $\text{M}^{\text{III}} = \text{Bi}^{3+}$, Sb^{3+} ; $\text{X} = \text{I}$, Br). Together with X-ray diffraction (XRD),

8.2 Results and Discussion

UV-Vis and photoluminescence (PL) measurements the crystallographic as well as the optoelectronic properties of the materials were characterized. We believe that these results can be a foundation for finding suitable replacements for Pb in the absorber layer of third-generation photovoltaic technologies.

8.2 Results and Discussion

$\text{Cs}_3\text{M}_2\text{I}_9$ ($\text{M} = \text{Bi}^{3+}, \text{Sb}^{3+}$)

The $\text{Cs}_3\text{M}_2\text{I}_9$ samples were prepared according to the synthesis route of Park *et al.*^[9] In short, a mixture of bismuth iodide (BiI_3) or antimony iodide (SbI_3) and cesium iodide (CsI) was dissolved either in a DMF/DMSO mixture (7:3) or in pure DMSO. The solution was then dynamically spin-coated on a substrate and afterwards annealed at 110 °C. This procedure leads to films with the known crystal structure of $\text{Cs}_3\text{Bi}_2\text{I}_9$.^[10] Thereby, bioctahedral $(\text{Bi}_2\text{I}_9)^{3-}$ clusters surrounded by cesium cations are formed, resulting in a hexagonal symmetry with the space group $P63/mmc$. A schematic picture of the $\text{Cs}_3\text{Bi}_2\text{I}_9$ structure, as well as the X-ray diffraction (XRD) patterns of $\text{Cs}_3\text{Bi}_2\text{I}_9$ and $\text{Cs}_3\text{Sb}_2\text{I}_9$ are shown in Figure 8-1.

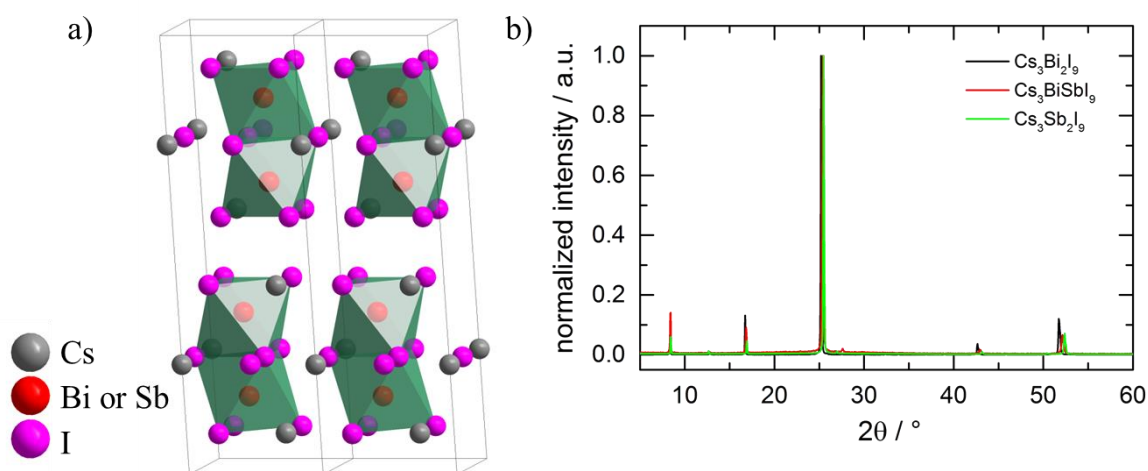


Figure 8-1: (a) Crystal structure of $\text{Cs}_3\text{M}_2\text{I}_9$ ($\text{M} = \text{Bi}^{3+}, \text{Sb}^{3+}$) and (b) the corresponding XRD patterns of both compounds and their mixed phase.

The XRD patterns of $\text{Cs}_3\text{Bi}_2\text{I}_9$ and $\text{Cs}_3\text{Sb}_2\text{I}_9$ show sharp reflections with a small shift to higher angles for the Sb-compound. This shift is most visible for the reflection at around $53^\circ 2\theta$ and can be explained with the contraction of the unit cells due to the smaller metal ion in the structure. Furthermore, a preferred orientation along the *c*-axis of the structure is observed for the spin-coated samples since the first three reflections are indexed as (002), (004) and (006), respectively. Despite the small shift in 2θ values, the three samples are similar from a crystallographic point of view. Nevertheless, these films exhibit different colors and morphologies on an FTO substrate.

In Figure 8-2c these differences are illustrated together with the semi-transparency of the spin-coated films. For $\text{Cs}_3\text{Bi}_2\text{I}_9$, the used solvent seems to be a crucial parameter for the crystal formation leading to either a red or a brownish color. On the other hand, the smaller Sb ion produces yellow crystals of $\text{Cs}_3\text{Sb}_2\text{I}_9$. In order to explain these differences, scanning electron microscopy (SEM) images were recorded to determine the morphologies of these films. The images are presented in Figure 8-2a,b and d.

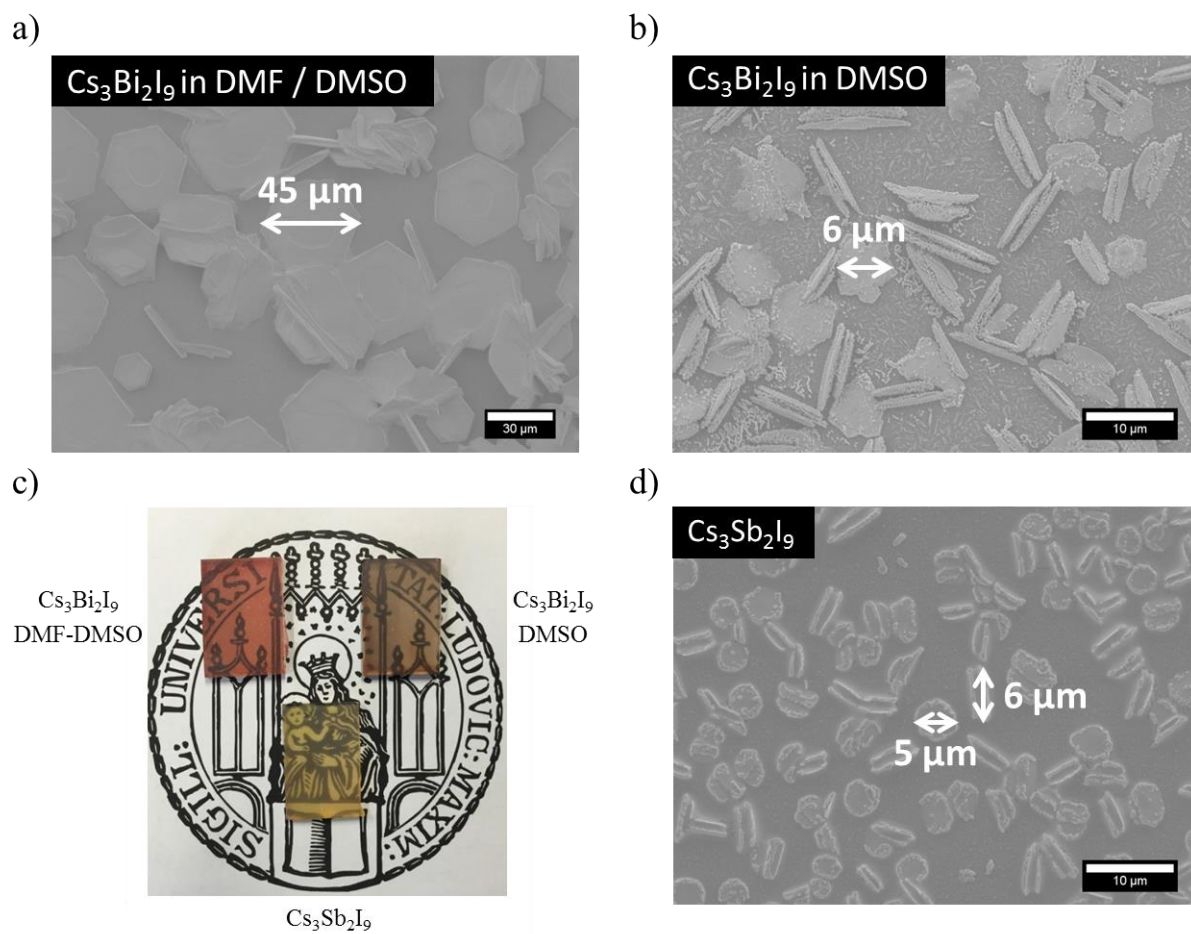


Figure 8-2: SEM topview images of $\text{Cs}_3\text{Bi}_2\text{I}_9$ prepared with a DMF/DMSO mixture (a) and DMSO (b) and $\text{Cs}_3\text{Sb}_2\text{I}_9$ (d). Additionally an image of the different compounds on an FTO substrate is shown, illustrating the clear semi-transparency of the films (c).

In the case of $\text{Cs}_3\text{Bi}_2\text{I}_9$, the addition of DMF to the DMSO solution seems to benefit the crystal formation of the compound. The DMF/DMSO mixture leads to perfect hexagons, while DMSO only solvent shows rather incomplete hexagons and many small crystallites. It should be mentioned that the same annealing temperature was used to verify the influence of the solvent for both synthesis protocols. The difference in color can be possibly explained with the formation of the monoclinic low temperature (LT) structure of $\text{Cs}_3\text{Bi}_2\text{I}_9$ with the space group $C2/c$. The structure of the LT phase is slightly distorted in comparison to the hexagonal phase.^[11] Although no distinct reflection of this phase could be observed in the XRD patterns, even small amounts could influence the optical properties of the film because

of the change in space between Bi and I.^[11] However, the color and morphology of the hexagonal $\text{Cs}_3\text{Bi}_2\text{I}_9$ and $\text{Cs}_3\text{Sb}_2\text{I}_9$ samples are in good agreement with literature reports.^[9, 12] The semi-transparency of all the films arises from the large pinholes between the crystallites. The color difference between the samples is reflected in the UV-vis spectra of $\text{Cs}_3\text{Bi}_2\text{I}_9$ and $\text{Cs}_3\text{Sb}_2\text{I}_9$ (Figure 8-3a).

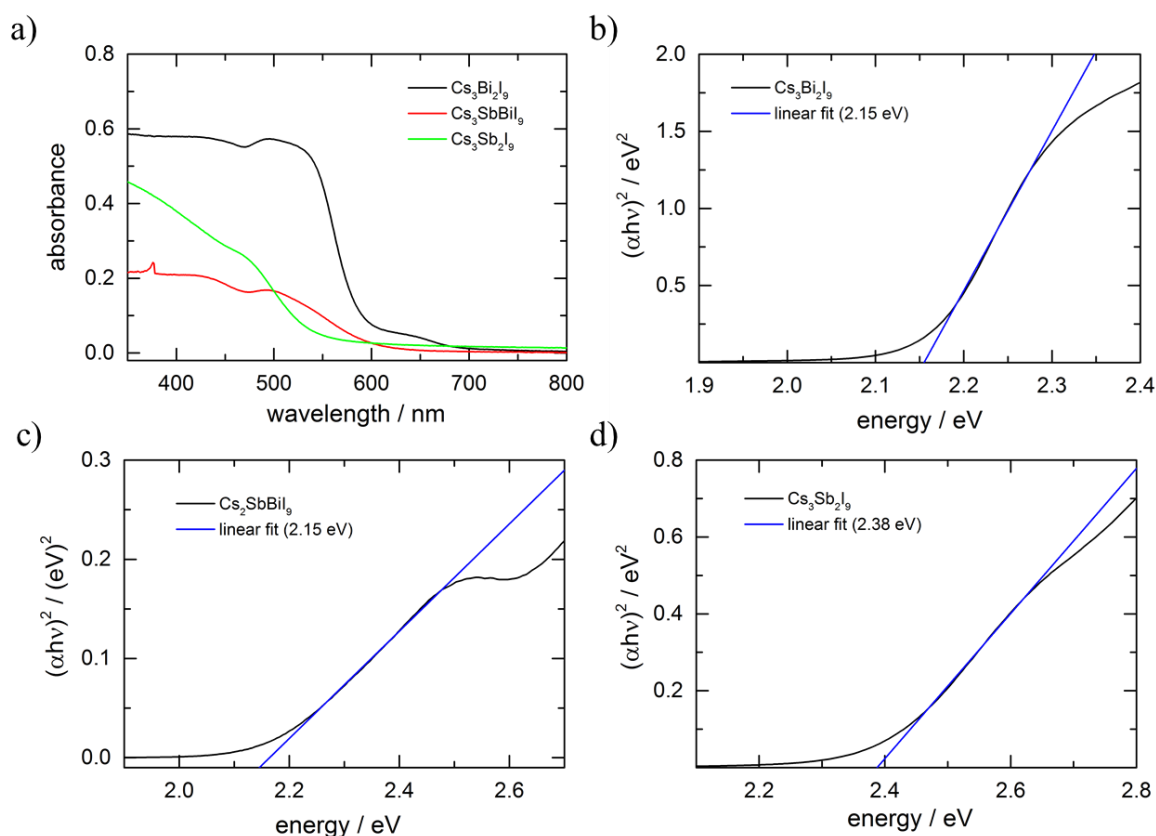


Figure 8-3: UV-Vis measurements of $\text{Cs}_3\text{Bi}_2\text{I}_9$, $\text{Cs}_3\text{SbBiI}_9$ and $\text{Cs}_3\text{Sb}_2\text{I}_9$ (a) plus the corresponding Tauc-Plots (b-d).

$\text{Cs}_3\text{Bi}_2\text{I}_9$ shows the strongest light absorption compared to $\text{Cs}_3\text{SbBiI}_9$ and $\text{Cs}_3\text{Sb}_2\text{I}_9$ for a similar sample thickness as confirmed by Dektak profilometer measurements. With the aid of Tauc-Plots (Figure 8-3b-d), the bandgaps of the corresponding compounds were determined. Interestingly, the incorporation of Sb does not seem to change the bandgap of the material, only the pure Sb compound shows an increased bandgap of 2.4 eV compared to the 2.1 eV for $\text{Cs}_3\text{Bi}_2\text{I}_9$.

8.2 Results and Discussion

In addition to an appropriate bandgap and sufficient light absorption, the presence of photoluminescence (PL) is important for the application in solar cells. For example, the lifetime of the photogenerated species can impact the efficiency of the charge extraction from the absorber layer. Therefore we performed PL measurements and the results are shown in Figure 8-4. It should be noted here that due to the low quantum yield a high intensity laser was needed to determine the PL spectra of the samples. Only the $\text{Cs}_3\text{Bi}_2\text{I}_9$ sample prepared with the DMF/DMSO solution was stable during the measurement. Therefore the PL spectrum of $\text{Cs}_3\text{Sb}_2\text{I}_9$ could not be recorded.

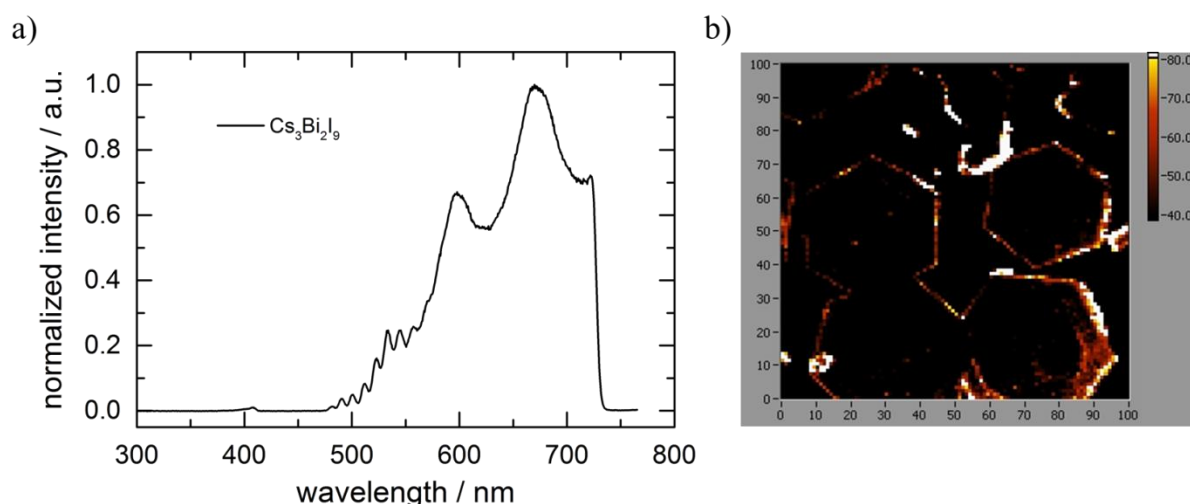


Figure 8-4: Photoluminescence spectra of $\text{Cs}_3\text{Bi}_2\text{I}_9$ (a) and a PL scan over a bigger film area on the substrate (b). The PL signal was detected with short passes at 750nm and 800nm.

In the literature, a PL maximum of $\text{Cs}_3\text{Bi}_2\text{I}_9$ was observed at around 650 nm.^[9] By fitting a Gaussian distribution curve to our spectrum, the PL maximum was also found to be around 650 nm. At this point it is unclear why a splitting of the PL signal occurs. One possible explanation could be the presence of two compounds, or additional effects due to the high intensity laser. For example, similar observations have been made in $\text{Ga}_{0.5}\text{In}_{0.5}\text{P}$ where the PL signal was affected by different temperatures.^[13] In Figure 8-4b an image of the measured area on the substrate is shown illustrating the source of the PL signal. Again we see the

hexagonal structures, as observed in the SEM images, and additionally we observe that the PL arises from the edges of these structures. This indicates the presence of large single crystals of $\text{Cs}_3\text{Bi}_2\text{I}_9$ where the excitation probably originates within the structure. Afterwards, the charges can travel through the lattice and recombine at the edges, or alternatively light is emitted within the crystal and only escapes from the edges. Good charge transport properties in the absorber layer are beneficial for the application in solar cells since the charges can be collected efficiently. However, in the case of $\text{Cs}_3\text{Bi}_2\text{I}_9$ much energy is needed to create free charges because of the high exciton binding energy of 279 meV.^[14] MAPbI_3 on the other hand only features an exciton binding energy of 40 meV.^[15] The high value limits the applicability of $\text{Cs}_3\text{Bi}_2\text{I}_9$ in solar cells^[16]

Nevertheless, Park *et al.* constructed solar cells including $\text{Cs}_3\text{Bi}_2\text{I}_9$ with mesoscopic TiO_2 as the electron extraction layer and spiro-OMeTAD as the hole extraction layer.^[9] These devices showed only poor performance with around 1% PCE. In order to make this material more attractive for solar cells, the crystallization and surface coverage of the material on the FTO / TiO_2 substrate still needs to be optimized.

HDABiI₅ (HAD = 1,6-hexanediammonium)

One way to increase the surface coverage is the use of easy processable organic cations in order to form bismuth-containing hybrid organic-inorganic materials, which have already been investigated as semiconductors for optoelectronic devices.^[17-19] One example is the dicationic alkylidiammonium bismuth halide material (HDABiI_5), where HDA is 1,6-hexanediammonium ($\text{H}_3\text{NC}_6\text{H}_{12}\text{NH}_3$). The use of long alkyl chains has been suggested to enhance the mobility of charge carriers because of the reduction in intermolecular distance between adjacent moieties caused by the intermolecular interaction between the alkyl

8.2 Results and Discussion

chains.^[20] This effect is called molecular-fastener effect.^[20] Therefore HDA is good candidate for the formation of bismuth-based materials with good mobilities for solar cell application. HDABiI₅ crystallizes in a primitive orthorhombic crystal structure with the space group *Pn21a*. Thereby, the BiI₆ octahedra form one-dimensional distorted zig-zag chains where three of these octahedra are connected via a shared iodide ion. The crystal structure of HDABiI₅ is shown in Figure 8-5a.

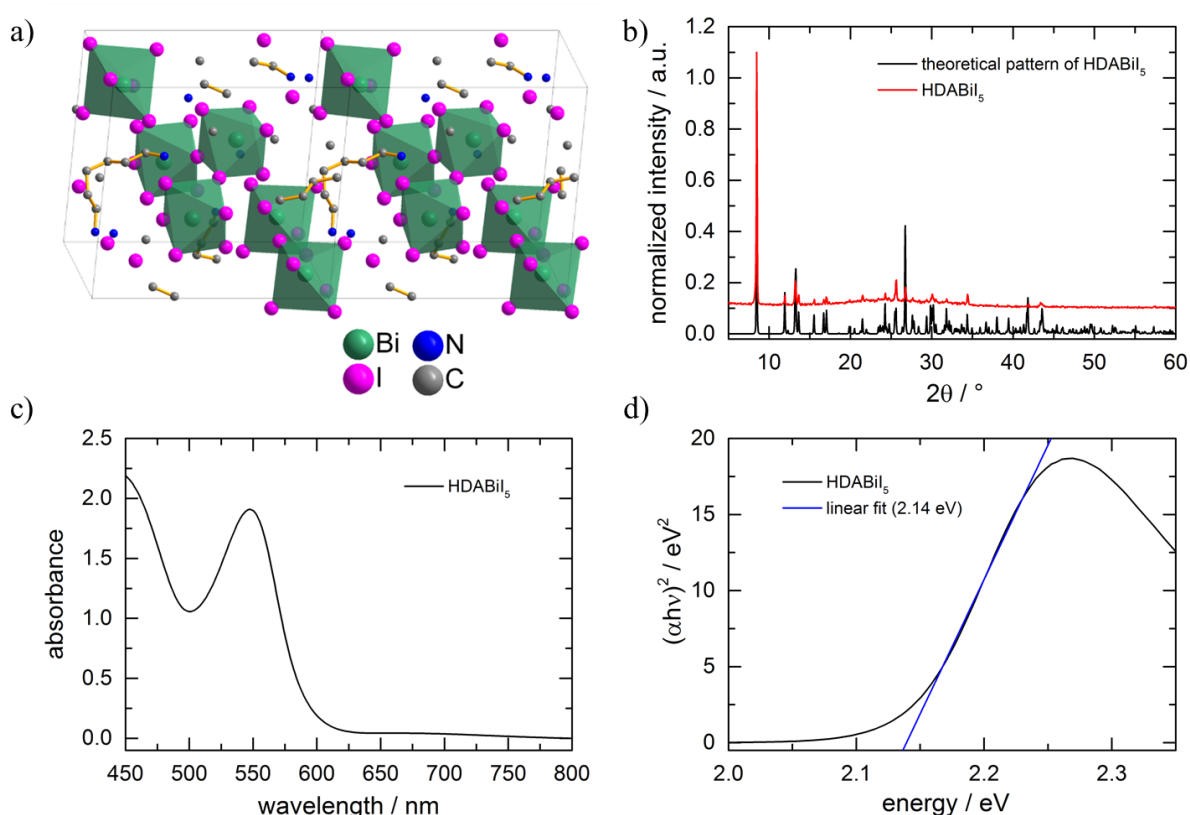


Figure 8-5: Crystal structure of HDABiI₅ (a) and comparison of the XRD patterns of prepared samples and the theoretical pattern (b). Additionally, UV-Vis measurements (c) and the corresponding Tauc-Plot (d) of HDABiI₅ are shown.

The HDABiI₅ samples were prepared according to the synthesis route of Fabian *et al.*^[21] The resulting films exhibit the desired crystal structure, which is visible in comparison with the theoretical XRD pattern of HDABiI₅. The theoretical pattern was simulated with the single crystal data from Mousdis *et al.*^[22] The red-looking films were further characterized with light

absorption spectroscopy and showed a strong absorbance starting from 600 nm. The absorbance of a material can be directly related to the theoretical maximum for the short circuit current (J_{SC}) when incorporated in a solar cell. Therefore the values of the light absorption spectrum (wavelength and absorbance) were substituted in the following equation.

$$J_{SC} = \int_{\lambda_1}^{\lambda_2} \frac{\lambda F(\lambda)(1 - 10^{-A(\lambda)})}{1240} d\lambda \quad (11)$$

Here, λ is the wavelength, $F(\lambda)$ the simulated solar power incident on earth from the AM1.5 solar spectrum and $A(\lambda)$ the wavelength-dependent absorbance of the material. The term $(1 - 10^{-A(\lambda)})$ represent the light harvesting efficiency (LHE) of the sample. In the case of HDABiI₅, a theoretical J_{SC} of 11.9 mA/cm² is estimated; comparable to the values obtained from FAPbBr₃.^[23] Together with a bandgap of 2.1 eV (see Tauc-Plot Figure 8-5d) HDABiI₅ could be a promising candidate for tandem solar cells.

In order to take a look at the optoelectronic properties of HDABiI₅, PL measurements were performed. In contrast to the PL measurements of Cs₃Bi₂I₉, a green LED was used instead of a high intensity laser for the illumination of the sample in order to probe the influence of the connectivity of the octahedra on the needed energy from the source to observe a PL signal. With the increased connectivity a weak signal was observed at around 630 nm (Figure 8-6a) which matches the bandgap of 2.1 eV from the Tauc-Plot. The low intensity of the PL could potentially originate from the observed pinholes on the surface of the film as shown in the SEM topview image in Figure 8-6b. In these pinholes, traps for the photoexcited species may be located and recombination can occur.^[24] Despite that, the FTO / TiO₂ substrate is almost completely covered. The majority of the crystal grains appeared to range in size between 200 nm and 400 nm with no preferential orientation in the plane of the deposited film. This matches the observation of the appearance of almost all reflections of the theoretical pattern

8.2 Results and Discussion

of HDABiI₅ in the observed XRD pattern. The Fermi level and valence band maximum is estimated at around -3.7 eV and -5.6 eV relative to vacuum, respectively.^[21] Similar values are observed for FAPbBr₃, which gives PCEs of almost 7% in a planar heterojunction layout.^[23] Therefore, HDABiI₅ was also incorporated in a stack with TiO₂ and spiro-OMeTAD as the charge extraction layers. The measured *J-V* characteristics are shown in Figure 8-6c.

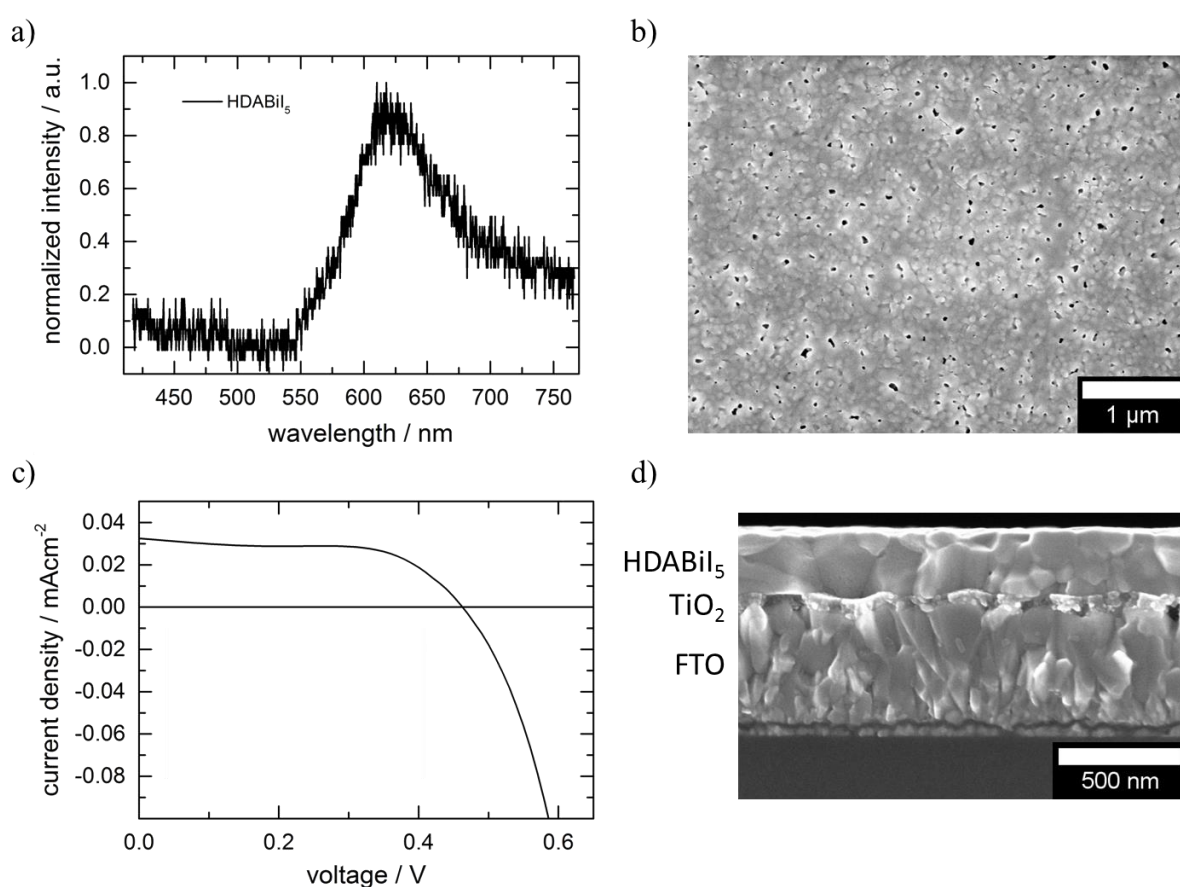
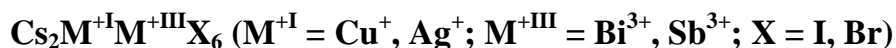


Figure 8-6: PL spectra of HDABiI₅ (a) with the corresponding topview image of the sample (b). *J-V* characteristics of a solar cell incorporating HDABiI₅ (c) and a cross-section of the device (d).

The device exhibits a short-circuit photocurrent density (J_{SC}) of 0.03 mA/cm², an open circuit voltage (V_{OC}) of 460 mV, and a fill factor (FF) of 0.61, which yielded a light-to-electrical energy conversion efficiency of 0.01%. One reason for the low J_{SC} value could be the observed pinholes in the film, however it is clearly visible in the SEM cross-section image

(Figure 8-6d) that HDABiI₅ forms a dense smooth film with a thickness of around 300 nm with no obvious pinholes reaching the FTO / TiO₂ interface. Therefore, we suggest that other causes must lead to the low current. HDABiI₅ devices still require more optimization of film thickness, film quality, dopant density, trap-state density, and selective contact engineering to achieve larger J_{SC} values.



Recently, Slavney *et al.* introduced the double perovskite structure incorporating Bi³⁺ and Ag⁺ with a strong PL signal and a lifetime of the photoexcited species of around 660 ns.^[26] The perovskite Cs₂AgBiBr₆ crystallizes as red-orange truncated octahedra in the cubic space group $Fm\bar{3}m$. The Ag⁺ and Bi³⁺ ions occupy the alternating centers of the octahedra in the ordered double perovskite structure with no disorder between Bi and Ag sites (Figure 8-7a). The unit-cell axis of 11.25 Å is roughly double that of MAPbBr₃ (a = 5.92 Å)^[27] as summarized in Figure 8-7c. Additionally, the structure is tunable with regard to the bandgap by a halide exchange. McClure *et al.* showed the successful synthesis of Cs₂AgBiCl₆ with a larger bandgap of 2.6 eV compared to 2 eV for the bromide compound.^[28] Both structures exhibit the same crystal structure as shown in the Rietveld refinements in Figure 8-7b and d. So far, only single crystals or powder samples of the double perovskite were prepared *via* solid state reactions due to the low solubility of silver halides.^[29] However, the principle of the double perovskite can be expanded to other combinations of 3⁺ and 1⁺ ions as suggested by Volonakis *et al.*^[30]

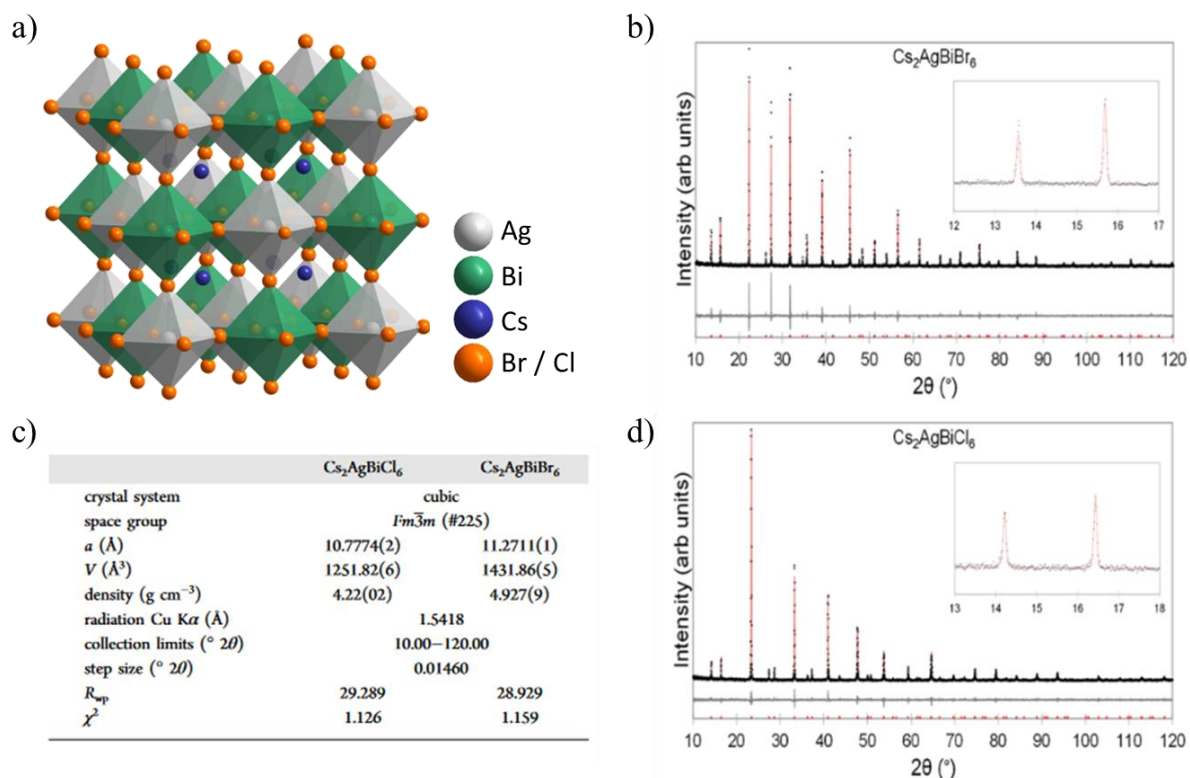


Figure 8-7: Structure of the ordered double perovskite Cs₂AgBiX₆ (with X = Br, Cl) (a), Rietveld refinements of the XRD patterns for Cs₂AgBiCl₆ (d) and Cs₂AgBiBr₆ (b) and the details of the refinement (c).^[32]

A suitable combination is copper (Cu) and antimony (Sb). Both structures are available as halide compounds with the desired oxidation states. The compounds Cs₂CuSbX₆ (with X = I, Br) were synthesized *via* solid state reactions in tantalum crucibles under an inert atmosphere. The XRD patterns of both compounds are shown in Figure 8-8a. So far these compounds have not been reported in the literature, thus the determination of the crystal structures with single crystals is still under investigation.

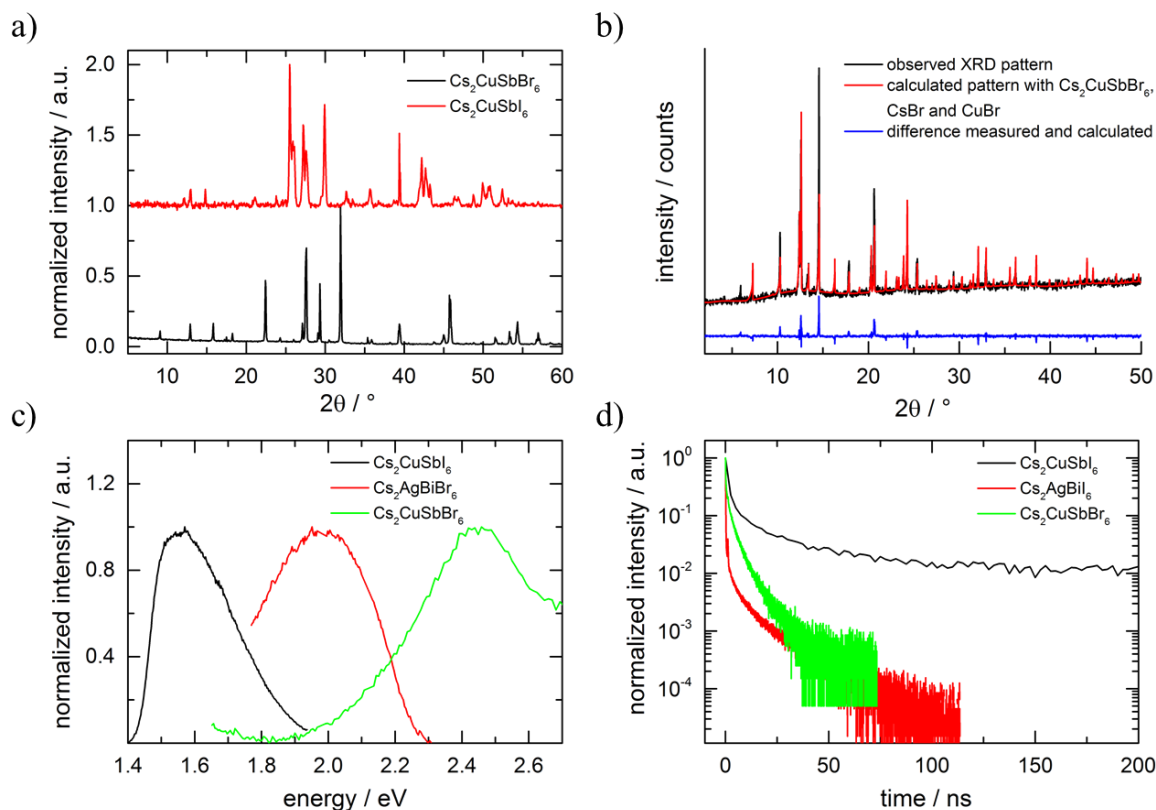


Figure 8-8: XRD patterns of $\text{Cs}_2\text{CuSbX}_6$ ($X = \text{I}, \text{Br}$) (a) and Rietveld refinement of $\text{Cs}_2\text{CuSbBr}_6$ (b). Photoluminescence measurements (c) and time-correlated single photon counting measurements (d) of $\text{Cs}_2\text{CuSbI}_6$, $\text{Cs}_2\text{AgBiBr}_6$ and $\text{Cs}_2\text{CuSbBr}_6$, respectively.

However, some basic information can be extracted from the powder patterns. The most obvious difference in both patterns is the number of observed reflections. For $\text{Cs}_2\text{CuSbBr}_6$ fewer reflections indicate a higher symmetry of the structure. Since a powder sample was used, reflections missing due to a preferred orientation can be excluded. The powder pattern was indexed, which resulted in a cubic symmetry as in $\text{Cs}_2\text{AgBiBr}_6$. A Rietveld refinement was performed for $\text{Cs}_2\text{CuSbBr}_6$; results are depicted in Figure 8-8b. With the inclusion of CsBr and CuBr as impurities, the calculated pattern almost matches the observed pattern as seen in the blue difference curve. Nevertheless, the intensity of the two main reflections of $\text{Cs}_2\text{CuSbBr}_6$, at around $15^\circ 2\theta$ and $21^\circ 2\theta$, does not match the calculated pattern. Additionally, the reflection at around $7^\circ 2\theta$ also cannot be explained by the crystal structure of $\text{Cs}_2\text{AgBiBr}_6$. The mismatch of the intensities is thus a good indication that the space group

8.2 Results and Discussion

used for the refinement is not entirely correct. Especially the centering of the space group has an impact on the intensity of the reflections because of characteristic extinction rules. For example, for a face-centered symmetry (F , $Fm\bar{3}m$ in the case of $\text{Cs}_2\text{AgBiBr}_6$), the reflections should have Miller indices $h k l$ either all odd or all even. In the case of body centered (I), only reflections with $h + k + l = 2n$ indices would appear. If no centering is observed, a primitive lattice (P) is present. The missing reflections in the theoretical pattern can either be explained by another impurity or with a lower symmetry of the crystal structure. In the case of $\text{Cs}_2\text{CuSbI}_6$ it is more difficult to estimate the symmetry from the XRD pattern. Various split reflections are observed, which suggests the presence of lower symmetry than for the bromide compound. Additionally, no systematic overlapping of reflections for both structures is visible, indicating different unit cells. For both new materials, single crystal analysis would be highly desirable to obtain the symmetry, the lattice parameters and the atomic positions in the structure.

To evaluate the suitability of $\text{Cs}_2\text{CuSbX}_6$ ($X = \text{I}, \text{Br}$) for photovoltaic applications, we measured the presence of PL. In comparison to HDABiI_5 , the I/III compounds studied here feature strong PL signal. The spectra are depicted in Figure 8-8c and show a PL maximum for $\text{Cs}_2\text{CuSbI}_6$ at around 1.6 eV and for $\text{Cs}_2\text{CuSbBr}_6$ at around 2.4 eV. For comparison, the PL signal of $\text{Cs}_2\text{AgBiBr}_6$ is also illustrated with its maximum at 2 eV. To determine the fate of the photogenerated carriers, we performed time-correlated single photon counting measurements (TCSPC). The observed decays in Figure 8-8d give the sum of radiative and nonradiative recombination rates of the materials. The PL intensity of all three materials shows a fast initial drop followed by a slower decay. Powders typically have much more defects and surface states than single crystals, which suggests that the short lifetime process may originate from trap and/or surface-state non-radiative recombination.^[26] Nevertheless, the lifetime of $\text{Cs}_2\text{CuSbI}_6$ is several μs and much longer than the lifetimes of $\text{Cs}_2\text{AgBiBr}_6$ and

$\text{Cs}_2\text{CuSbBr}_6$. Long carrier recombination lifetimes are indicators of good photovoltaic performance and with a PL maximum at around 1.6 eV, $\text{Cs}_2\text{CuSbI}_6$ appears to be a very good candidate for solar cell applications. In order to evaluate the absorption properties of these compounds UV-Vis spectra were obtained from powder samples in reflection mode and converted afterwards with the Kubelka-Munk equation (Figure 8-9a). $\text{Cs}_2\text{CuSbI}_6$ shows strong absorption starting from around 600 nm, while the other two compounds start to absorb at around 480 nm. The Tauc Plots revealed direct band gaps for the bromide compounds at around 2.7 eV and an indirect bandgap for $\text{Cs}_2\text{CuSbI}_6$ at around 1.8 eV. Although direct band gaps are more favored for solar cell applications, $\text{Cs}_2\text{CuSbI}_6$ shows the right band gap energy, good absorption and a long carrier lifetime.

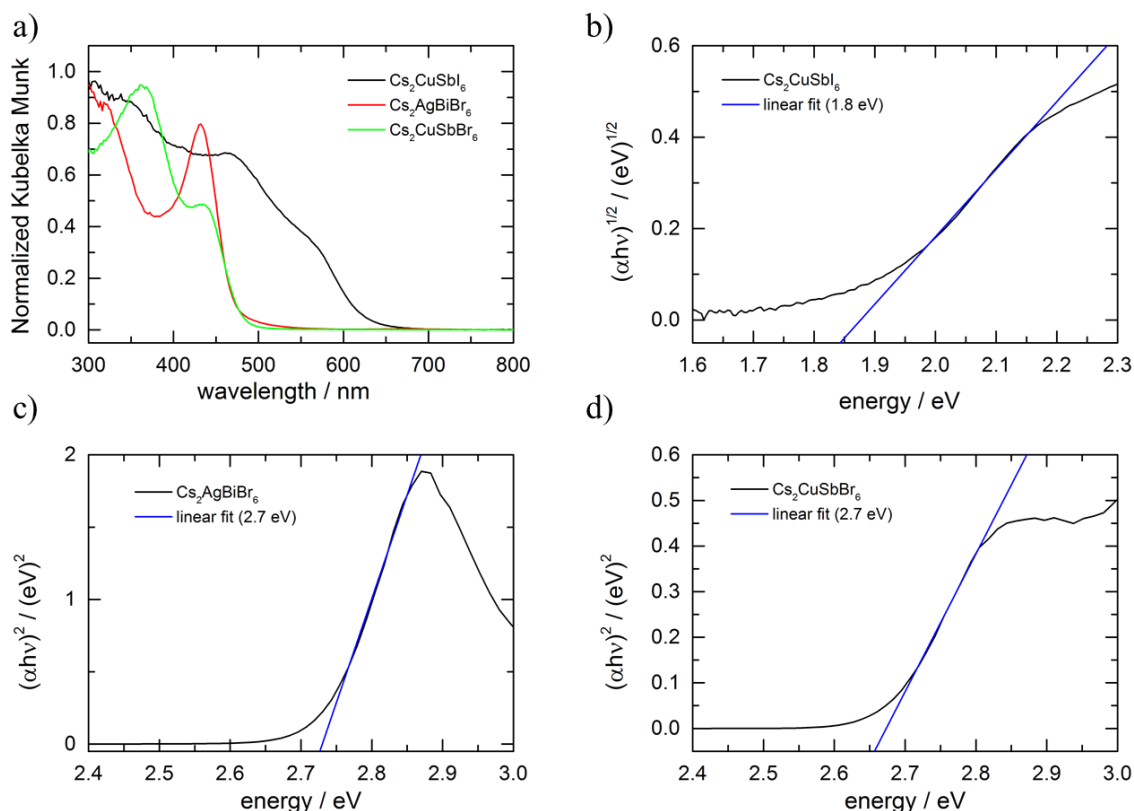


Figure 8-9: UV-Vis spectra of the different double perovskites (a) and the corresponding Tauc Plots (b-d).

8.3 Conclusion

Standard solution-state film deposition techniques are complicated for $\text{Cs}_2\text{AgBiBr}_6$ due to the low solubility of AgBr (K_{sp} at 25 °C is 5×10^{-13}).^[26] In the case of $\text{Cs}_2\text{CuSbI}_6$, CuI is soluble in DMF with the addition of small amounts of HI and is processable via the spin-coating technique. First attempts have been made to develop a solution-based deposition process by spin-coating stoichiometric mixtures on glass substrates. The resulting films were analyzed by XRD and showed the presence of CuI instead of the desired compound. These results suggest that the precipitation of CuI from solution is the thermodynamically favored product rather than the formation of $\text{Cs}_2\text{CuSbI}_6$. Another approach is to start from a CuI layer and deposit the other reactants on top of this layer, followed by thermal processing. During this subsequent annealing step, the CuI could diffuse into the other structure as it was shown with germanium (Ge) to form $\text{Ge}_{1-x}\text{Cu}_x$.^[31] Here we observed, after 6 h of annealing at 150 °C, the formation of $\text{Cs}_3\text{Sb}_2\text{I}_9$ rather than the desired compound. The challenge with higher temperatures is the high volatility of SbI_3 , but this property might make it possible to evaporate SbI_3 to form $\text{Cs}_2\text{CuSbI}_6$. As a final attempt, we mixed CuI and CsI and deposited it on the substrate. However, this mixture resulted in the formation of $\text{Cs}_3\text{Cu}_2\text{I}_5$ which did not react with the SbI_3 vapor. However, the evaporation was performed in a sealed glass petri dish, thus with more controlled evaporation conditions the formation may be possible. Further investigations of alternative methods for forming a high-quality film of $\text{Cs}_2\text{CuSbI}_6$ for photovoltaic devices are still ongoing.

8.3 Conclusion

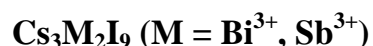
In summary, we have studied different compounds based on Bi and Sb as possible light absorbers for their application in solar cells. For example, the solution-processable inorganic compound $\text{Cs}_3\text{Bi}_2\text{I}_9$ shows strong absorbance starting from 600 nm, a PL emission at around 650 nm and the formation of big single crystals on the substrate. However, the surface is not

completely covered via spin-coating of the compound and the PL emission is only observed with illumination from a high intensity laser, implying that most of the photogenerated species recombine non-radiatively, i.e. via defects or traps. With the high excitation binding energy of $\text{Cs}_3\text{Bi}_2\text{I}_9$ and the apparent high concentration of recombination centers, its application in solar cells may be rather difficult.

One way to get a full coverage of the substrate is the use of the hybrid bismuth compound HDABiI_5 . This material exhibits a weak PL when illuminated with a low intensity green LED, and gives an open circuit voltage of 460 mV with a solar cell layout of $\text{FTO} / \text{TiO}_2 / \text{HDABiI}_5 / \text{spiro-OMeTAD} / \text{Au}$. However, the very low short circuit current of 0.03 mA/cm^2 makes the application in solar cells unlikely.

In order to potentially increase the intensity of the PL emission and the charge transport properties within the structure, we enhanced the connectivity of the octahedra by forming the double perovskite structure $\text{Cs}_2\text{CuSbX}_6$ ($\text{X} = \text{I}, \text{Br}$). These materials exhibit strong PL signals at 1.6 eV for the iodide compound and at 2.5 eV for the bromide compound. Especially $\text{Cs}_2\text{CuSbI}_6$ appears to be promising for applications in solar cells because of the long lifetime (several μs) of the photoexcited species. The deposition of this material on an $\text{FTO} / \text{TiO}_2$ substrate is still challenging because of the preferred formation of either CuI or $\text{Cs}_3\text{Sb}_2\text{I}_9$, but with further experiments this material may offer the potential to replace lead-based solar cells and provide a less toxic photovoltaic system.

8.4 Experimental Section



Sample preparation

The sample preparations were performed in a nitrogen-filled glovebox. The precursor solution for the synthesis of $\text{Cs}_3\text{Bi}_2\text{I}_9$ was prepared by dissolving 974 mg BiI_3 (99%, Sigma–Aldrich) in either a mixture of DMF/DMSO (700 μl DMF and 300 μl DMSO) from Sigma–Aldrich or in pure DMSO (1 mL) at 110 °C. The solution was then filtered and added to 644 mg CsI. This solution was then heated to 100 °C in order to dissolve the precursors and afterwards the solution was filtered to remove small remaining residues of precursors. Subsequently, 100 μL of this solution was spin-coated onto the substrates at 1500 rpm for 20 s. Afterwards the samples were placed on a hotplate at 110 °C for 15 min.

The preparation of $\text{Cs}_3\text{Sb}_2\text{I}_9$ was performed by dissolving 503 mg SbI_3 (98%, Sigma–Aldrich) and 260 mg CsI in 1 mL of DMF at 100 °C. The spin-coating procedure was similar to the preparation of $\text{Cs}_3\text{Bi}_2\text{I}_9$.

Characterization details:

X-ray diffraction analysis was carried out in reflection mode using a Bruker D8 Discover with Ni-filtered $\text{Cu-K}\alpha$ -radiation ($\lambda = 1.5406 \text{ \AA}$) and a position-sensitive semiconductor detector (LynxEye).

Steady-state absorption spectra were acquired with a Lambda 1050 UV-Vis spectrophotometer (Perkin Elmer) using an integration sphere.

Scanning electron microscopy images were acquired on a JEOL JSM-6500F microscope. The different samples were deposited on FTO-coated glass (7 Ω/sq , Pilkington, USA). The latter

was then fixed with silver paint on an aluminum holder. The silver paint was allowed to dry for 3 h in a desiccator. The samples were prepared 10 to 16 h before the measurement and were always stored in a desiccator with <20% relative humidity to avoid decomposition of the moisture-sensitive materials.

Steady state photoluminescence measurements of films were performed with a Mira 900 Laser (Coherent). The excitation wavelength was fixed at 834 nm and a laser excitation power of $\sim 4 \mu\text{W}$ was applied corresponding to a power density of 1.4 kWcm^{-2} . For the detection two short pass filters (750 nm and 800 nm) were used. The PL spectrum was recorded with a spectrometer (Shamrock SR-303i combined with an Andor Newton CCD) and the PL images were obtained with an avalanche photodiode (APD from MPD with a diameter of 50 μm and <100 dark counts). For the latter, the experimental setup is based on a confocal optical microscope equipped with a closed-loop piezo scan stage (sample scan) to raster-scan the sample through the focus of a high NA objective (NA = 1.4).

HDABiI₅ (HAD = 1,6-hexanediammonium)

Preparation of the precursors

To synthesize 1,6-hexanediamine dihydroiodide (HDA•2HI), 260.9 mg of 1,6-hexanediamine (98%, Sigma Aldrich) was dissolved in 5 mL methanol under ambient conditions at RT, and then 1 mL hydriodic acid (33 wt%) was added slowly at 0 °C with stirring, followed by stirring for an additional 30 min. HDA•2HI precipitate was recovered by evaporation of solvents at 40 °C under reduced pressure. The precipitate was rinsed with dry diethyl ether, and vacuum dried at 60 °C for 12 h. A yield of 75% was achieved.

8.4 Experimental Section

Sample preparation

Fluorine doped tin oxide (FTO) coated glass sheets (7 Ω /sq, Pilkington, USA) were patterned by etching with zinc powder and 3 M HCl. They were subsequently cleaned with a 2% Hellmanex solution and rinsed with de-ionized water, ethanol and acetone. Directly before applying the blocking layer, last organic residues were removed by an oxygen plasma treatment for 5 min. The dense TiO₂ blocking layer was prepared from sol-gel precursor solution by spin-coating onto the substrates and calcining at 500 °C in air.^[32] For the sol-gel solution a 27.2 mM solution of HCl in 2-propanol was added dropwise to a vigorously stirred 0.43 mM solution of titanium isopropoxide (99.999 %, Sigma-Aldrich) in 2-propanol. The solution usually stayed clear during the addition and was discarded otherwise.

The sample preparations were performed in a nitrogen-filled glovebox. HDABiI₅ solution was prepared by mixing HDA•2HI and BiI₃ (99%, Sigma–Aldrich) powders at an approximately 1:1 mole ratio (200 mg HDA•2HI and 259 mg BiI₃), in 1 mL anhydrous DMF (99.8%, Sigma–Aldrich) at 70°. This solution was then heated to 100 °C without stirring in order to fully dissolve the starting materials. Subsequently, 100 μ L of the solution were spin-coated with 2000 rpm for 30 s onto the substrate. The film formation was then achieved through annealing at 100 °C for 10 min. Afterwards, the films were covered with a layer of spiro-OMeTAD (Borun Chemicals, 99.5% purity). Typically 100 mg of spiro-OMeTAD were dissolved in 1 mL chlorobenzene (99.8%, Sigma-Aldrich). The solution was filtered and mixed with 10 μ L 4-*tert*-butylpyridine (*t*BP, 96%, Sigma-Aldrich) and 30 μ L of a 170 mg/mL bis(trifluoromethane)sulfonamide lithium salt (LiTFSI, 99.95%, Sigma-Aldrich) solution in acetonitrile. This solution was spin-coated dynamically at 1500 rpm for 45 s. In a second step the sample rotation was accelerated to 2000 rpm for 5 s to allow the solvent to dry

completely. Before evaporating the gold electrodes on the devices, spiro-OMeTAD was left to oxidize in air over night at room temperature and < 20 rel% humidity.

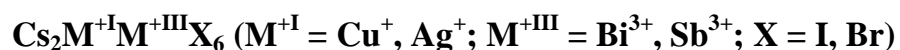
Characterization details:

X-ray diffraction analysis was carried out in reflection mode using a Bruker D8 Discover with Ni-filtered Cu-K α -radiation ($\lambda = 1.5406 \text{ \AA}$) and a position-sensitive semiconductor detector (LynxEye).

Steady-state absorption spectra were acquired with a Lambda 1050 UV-Vis spectrophotometer (Perkin Elmer) using an integrating sphere.

Scanning electron microscopy images were acquired on a JEOL JSM-6500F microscope. The different samples were deposited on FTO-coated glass (7 Ω /sq, Pilkington, USA). The latter was then fixed with silver paint on an aluminum holder. The silver paint was allowed to dry for 3 h in a desiccator. The samples were prepared 10 to 16 h before the measurement and were always stored in a desiccator with <20% relative humidity to avoid decomposition of the moisture-sensitive materials.

Steady state photoluminescence measurements were performed with a 510 nm laser head (LDH-P-C-510, PicoQuant GmbH) with an average power density of 2 mW. For the detection one long pass filter (514 nm) was used. The PL spectrum was recorded with a spectrometer (Shamrock SR-303i combined with an Andor Newton CCD) and a laser intensity of 2.2 μ W.



Sample preparation

The solid-state reactions for the different compounds were prepared in a nitrogen-filled glovebox, where the starting materials CsI (99.999%, Sigma-Aldrich), CsBr (99.999%,

8.4 Experimental Section

Sigma-Aldrich), CuI (99.999%, Sigma-Aldrich), CuBr (99.998%, Alfa Aesar), SbI₃ (99.999%, Alfa Aesar), SbBr₃ (99.995%, Alfa Aesar), AgBr (90%, Sigma-Aldrich) and BiBr₃ (>98%, Sigma-Aldrich) were stored. Typical samples sizes were 500 mg, which consisted of the following ratios of the reactants (see Table 8-1).

Table 8-1: Initial weights of the different compounds.

compound	CsI	CsBr	CuI	CuBr	SbI ₃	SbBr ₃	AgBr	BiBr ₃
Cs ₂ CuSbBr ₆	---	228 mg	---	77 mg	---	194 mg	---	---
Cs ₂ CuSbI ₆	214 mg	---	79 mg	---	207 mg	---	---	---
Cs ₂ AgBiBr ₆	---	200 mg	---	---	---	---	89 mg	211 mg

The reactions were performed in tantalum crucibles ($\varnothing = 10$ mm, $l = 30$ mm), which were welded under inert atmosphere. The following temperature programs were applied (see Table 8-2).

Table 8-2: Temperature programs of the different compounds.

compound	temperature program
Cs ₂ CuSbBr ₆	$RT \xrightarrow{50^\circ C/h} 150^\circ C/h \xrightarrow{10^\circ C/h} RT$
Cs ₂ CuSbI ₆	$RT \xrightarrow{50^\circ C/h} 200^\circ C/h \xrightarrow{10^\circ C/h} RT$
Cs ₂ AgBiBr ₆	$RT \xrightarrow{50^\circ C/h} 250^\circ C/h \xrightarrow{10^\circ C/h} RT$

PL sample preparation

Samples for steady state and time resolved PL measurements were finely ground with pestle and mortar and afterwards stuck with scotch tape onto a glass slide.

Characterization details:

X-ray diffraction analysis was carried out in reflection mode using a Bruker D8 Discover with Ni-filtered Cu-K α -radiation ($\lambda = 1.5406 \text{ \AA}$) and a position-sensitive semiconductor detector (LynxEye). The Rietveld-refinement was done with the software TOPAS Academic 4.^[33]

Steady state and time resolved PL measurements were performed with a Fluotime 300 Spectrofluorometer (Picoquant GmbH). The samples were photo-excited using a 510 nm laser head (LDH-P-C-510, PicoQuant GmbH) pulsed at 500 kHz, with a pulse duration of 117 ps and fluence of $\sim 300 \text{ nJcm}^{-2}$ /pulse. The PL was collected using a high-resolution monochromator and hybrid photomultiplier detector assembly (PMA Hybrid 40, PicoQuant GmbH). The emission for time resolved measurements was monitored at the maximum intensity of the steady state photo-emission.

8.5 Literature

- [1] L. Patrick, *Altern Med Rev* **2006**, 11, 2.
- [2] I. R. Benmessaoud, A.-L. Mahul-Mellier, E. Horvath, B. Maco, M. Spina, H. Lashuel, L. Forro, *Toxicol Res* **2015**, 5, 407.
- [3] R. A. Goyer, T. W. Clarkson, *Toxic Effects of Metals*, Vol. 1236, McGraw-Hill, New York **1996**.
- [4] A. Demayo, M. C. Taylor, K. W. Taylor, P. V. Hodson, P. B. Hammond, *Crit. Rev. Env. Contr.* **1982**, 12, 257.
- [5] R. A. Goyer, *Environ. Health Perspect.* **1990**, 86, 177.
- [6] N. K. Noel, S. D. Stranks, A. Abate, C. Wehrenfennig, S. Guarnera, A.-A. Haghighirad, A. Sadhanala, G. E. Eperon, S. K. Pathak, M. B. Johnston, A. Petrozza, L. M. Herz, H. J. Snaith, *Energy & Environmental Science* **2014**, 7, 3061.
- [7] R. S. Drago, *The Journal of Physical Chemistry* **1958**, 62, 353.
- [8] H. Suzuki, N. Komatsu, T. Ogawa, T. Murafuji, T. Ikegami, Y. Matano, *Organobismuth chemistry*, Elsevier, Netherlands **2001**.
- [9] B.-W. Park, B. Philippe, X. Zhang, H. Rensmo, G. Boschloo, E. M. J. Johansson, *Adv. Mater.* **2015**, 27, 6806.
- [10] A. Arakcheeva, M. Bonin, G. Chapuis, A. Zaitsev, *Zeitschrift für Kristallographie* **1999**, 214, 279.
- [11] A. Arakcheeva, G. Chapuis, M. Meyer, *Zeitschrift für Kristallographie-Crystalline Materials* **2001**, 216, 199.
- [12] B. Saparov, F. Hong, J.-P. Sun, H.-S. Duan, W. Meng, S. Cameron, I. G. Hill, Y. Yan, D. B. Mitzi, *Chem. Mater.* **2015**.
- [13] T. Kanata, M. Nishimoto, H. Nakayama, T. Nishino, *Physical Review B* **1992**, 45, 6637.
- [14] V. F. Machulin, F. V. Motsnyi, O. M. Smolanka, G. S. Svechnikov, E. Y. Peresh, *Low Temperature Physics* **2004**, 30, 964.
- [15] Y. Yang, M. Yang, Z. Li, R. Crisp, K. Zhu, M. C. Beard, *The Journal of Physical Chemistry Letters* **2015**, 6, 4688.
- [16] A. Fahrenbruch, R. Bube, *Fundamentals of Solar Cells: Photovoltaic Solar Energy Conversion*, Elsevier, New York **2012**.

- [17] A. M. Goforth, M. D. Smith, L. Peterson, H.-C. zur Loye, *Inorg. Chem.* **2004**, *43*, 7042.
- [18] D. B. Mitzi, *Inorg. Chem.* **2000**, *39*, 6107.
- [19] D. B. Mitzi, P. Brock, *Inorg. Chem.* **2001**, *40*, 2096.
- [20] S. Ukai, S. Igarashi, M. Nakajima, K. Marumoto, H. Ito, S. Kuroda, K. Nishimura, Y. Enomoto, G. Saito, *Colloids and Surfaces A: Physicochemical and Engineering Aspects* **2006**, 284–285, 589.
- [21] D. M. Fabian, S. Ardo, *J. Mater. Chem. A* **2016**, *4*, 6837.
- [22] G. A. Mousdis, G. C. Papavassiliou, A. Terzis, C. Raptopoulou, *Zeitschrift für Naturforschung B* **1998**, *53*, 927.
- [23] F. C. Hanusch, E. Wiesenmayer, E. Mankel, A. Binek, P. Angloher, C. Fraunhofer, N. Giesbrecht, J. M. Feckl, W. Jaegermann, D. Johrendt, T. Bein, P. Docampo, *The Journal of Physical Chemistry Letters* **2014**, 2791.
- [24] X. Wu, M. T. Trinh, D. Niesner, H. Zhu, Z. Norman, J. S. Owen, O. Yaffe, B. J. Kudisch, X. Y. Zhu, *J. Am. Chem. Soc.* **2015**, *137*, 2089.
- [25] J. Rocha, L. D. Carlos, F. A. A. Paz, D. Ananias, *Chem. Soc. Rev.* **2011**, *40*, 926.
- [26] A. H. Slavney, T. Hu, A. M. Lindenberg, H. I. Karunadasa, *J. Am. Chem. Soc.* **2016**, *138*, 2138.
- [27] D. Z. Weber, *Z. Naturforsch.* **1978**, *33b*, 1443.
- [28] E. T. McClure, M. R. Ball, W. Windl, P. M. Woodward, *Chem. Mater.* **2016**, *28*, 1348.
- [29] D. C. Luehrs, R. T. Iwamoto, J. Kleinberg, *Inorg. Chem.* **1966**, *5*, 201.
- [30] G. Volonakis, M. R. Filip, A. A. Haghighirad, N. Sakai, B. Wenger, H. J. Snaith, F. Giustino, *The Journal of Physical Chemistry Letters* **2016**, *7*, 1254.
- [31] F. C. Frank, D. Turnbull, *Physical Review* **1956**, *104*, 617.
- [32] J. M. Ball, M. M. Lee, A. Hey, H. J. Snaith, *Energy & Environmental Science* **2013**, *6*, 1739.
- [33] A. A. Coelho, *TOPAS-Academic, version 4.1 (Coelho Software)* **2007**, Brisbane (Australia).

9 Conclusions

This thesis focused on some of the challenges perovskite based solar cells have to face in order to become industrially relevant. In the first part the crystallization of MAPbI₃ based on a one-step approach with a chloride-based precursor is studied. Thereby, MAPbCl₃ crystallizes first as a templating phase and while heating up the substrate, MAPbI₃ grows at the expense of MAPbCl₃, which leads to crystals oriented parallel to the substrate. Together with slow evaporation of the solvent before the heat treatment it is shown that the efficiency as well as the reproducibility of the devices increased due to the enhanced conductivity of the perovskite layer.

The structurally related compound FAPbI₃, with a slightly narrower bandgap, is stabilized in order to suppress the formation of the yellow δ -phase instead of the desired dark α -phase and to make FAPbI₃ stable towards the operation temperatures of solar cells. By exchanging a small amount of 15% MA relative to FA, with no accompanying lattice shrinkage, the transition to the yellow δ -phase of FAPbI₃ was completely suppressed between 25-250 °C. We propose that the dipole moment of the organic cation is an important parameter for the formation of stable hybrid perovskites because of the increase in I-H hydrogen bonding and/or the Coulomb interactions within the structure.

Furthermore the scope of the perovskites was extended to wide-bandgap materials through the exchange of the halide from iodide to bromide. We have shown that MAPbBr₃ and FAPbBr₃ can achieve high power conversion efficiencies of up to 7% in planar heterojunction architectures, without the need for a mesoporous scaffold. FAPbBr₃ exhibits charge carrier diffusion lengths that are orders of magnitude longer than with MAPbBr₃, and therefore is able to achieve high charge collection efficiency. However, with a perfect alignment of the

9 Conclusions

cubic crystal planes of MAPbBr₃ parallel to the substrate of the film the efficiency can be increased and the reproducibility is enhanced while the short circuit currents (7 mAcm⁻²) approach their theoretical limit. Both materials are suitable as absorbers for flexible photovoltaic applications as well as the top cell in a tandem configuration with a commercially available silicon or CIGS bottom cell.

Whether considering single perovskite solar cells or the application in tandem systems, the devices have to be collected at the end of their working lifetime, according to international electronic waste disposal regulations. We have established an environmentally sound and cost-efficient recycling process for solar cells based on MAPbI₃ and can re-use the materials without significant losses in device performance. In particular, we show that the toxic PbI₂ and the expensive FTO / glass substrates can be recycled and can be re-used to prepare new devices without any significant loss of device performance.

In addition to the possible recycling of lead-based solar cells, alternative compounds based on Bi or Sb are also studied in this thesis. Especially the bismuth-based compounds show strong absorbance starting from 600 nm, and by using organic cations they are also solution processable with a resulting full surface coverage. However, the PL of these materials is limited by the loss of energy through radiation-less decay or vibrational motions of the BiI₆ octahedra. In addition, we investigate the double perovskite structure Cs₂CuSbX₆ (X = I, Br). These materials exhibit strong PL signals at 1.6 eV for the iodide compound and at 2.5 eV for the bromide compound. Especially Cs₂CuSbI₆ is a promising candidate for applications in solar cells because of the long lifetime (several μs) of the photoexcited species.

Although this thesis tackles some of the challenges for the potential industrial application of perovskite solar cells, there is still a long way ahead for commercialization of these systems. One crucial problem is the upscaling from lab devices to solar panels. First results show that

large aperture areas of the perovskite are possible but so far only efficiencies below 10% have been achieved.

Even with the high efficiencies of the best lead-based perovskite solar cells, the application is limited by the degradation of the active layer by environmental factors. As already known for other photovoltaic systems, encapsulation significantly increases the lifetime of the devices. Several encapsulation techniques are already under investigation for the solar cells in order to obtain a stable performance under certain conditions.

After 5 years of intense research and constant improvement of perovskite-based solar cells, there is still much research and development work left before these materials can enter the photovoltaic market. Nevertheless, probably no material other than MAPbI_3 has ever before experienced such a rapid increase in solar efficiency, and with a growing research community that focuses more and more on aspects relevant for real-world applications, we expect a bright future for this intriguing family of materials.

10 Curriculum Vitae**Persönliche Daten**

Name	Andreas Christian Herbert Binek
Geburtsdatum	21.10.1987
Geburtsort	Schwabmünchen
Staatsangehörigkeit	Deutsch

Schulbildung

1994 – 1998	Grundschule am Spitalplatz Landsberg am Lech
1998 - 2000	Mittelschule Landsberg am Lech
2000 - 2004	Johann-Winklhofer Realschule Landsberg am Lech
15.07.2004	mittlere Reife an der Johann-Winklhofer Realschule
2006 – 2007	staatliche Berufsoberschule Kaufbeuren
27.06.2007	Fachabitur im Bereich Technik an der staatliche Berufsoberschule Kaufbeuren
2007 – 2008	staatliche Berufsoberschule Kaufbeuren
27.06.2008	Fachgebundene Hochschulreife im Bereich Technik an der staatliche Berufsoberschule Kaufbeuren

Ausbildung

2004 – 2006	Ausbildung zum agrartechnischen Assistenten im Fachbereich Lebensmittelanalytik im Agrarbildungszentrum Landsberg am Lech
27.07.2006	Abschluss: Staatlich geprüfter agrartechnischer Assistent Fachrichtung Lebensmittelanalytik (1.86)

Studium

2008 – 2011	Bachelorstudium Chemie und Biochemie LMU München
20.10.2011	Abschluss: B. Sc. Chemie und Biochemie (2.28)
2012 – 2013	Masterstudium Chemie LMU München
06 – 12/2013	Masterarbeit an der LMU München bei Prof. Dirk Johrendt: „Synthesis and Structure Investigations of BaAg ₂ As ₂ and BaAg ₂ Sb ₂ at Different Temperatures“ (1.3)
17.12.2013	Abschluss: M. Sc. Chemie (1.28)

Promotion

04/2014 – heute	Promotion an der LMU München bei Prof. Thomas Bein
-----------------	--

Sonstige Tätigkeiten

seit 04/2014	Verantwortlicher wissenschaftlicher Angestellter für Röntgenbeugung (XRD), Rasterelektronenmikroskopie (REM) Verantwortlicher, Solarzellcharakterisierung, Glovebox Betreuung und Sicherheitsbeauftragter des Labors
seit 04/2014	Betreuung von Praktika in der Anorganischen und Physikalischen Chemie, fachliche Anleitung und Ausbildung von Bachelorranden und Studenten im Hauptstudium, sowie Betreuung von Austauschstudenten des DAAD (Deutscher Akademischer Austausch Dienst) RISE Stipendiums Programms

Sonstiges

03/2015	Poster Award des 4ten International Workshop of the Bavarian interdisciplinary project „Solar Technologies Go Hybrid“
07/2016	Travel Award des Center for NanoScience (CeNS)

Zusatzqualifikationen

Sprachen	Deutsch (Muttersprache)
	Englisch (verhandlungssicher)
EDV	Microsoft Office (sehr gut)
	Origin
	SolidWorks (Grundkenntnisse)

11 Publications and Presentations

11.1 Journals

1. “Efficient Planar Heterojunction Perovskite Solar Cells Based on Formamidinium Lead Bromide”

F. C. Hanusch, E. Wiesenmayer, E. Mankel, A. Binek, P. Angloher, C. Fraunhofer, N. Giesbrecht, J. M. Feckl, W. Jaegermann, D. Johrendt, T. Bein, P. Docampo, *The Journal of Physical Chemistry Letters* **2014**, 5, 2791-2795.
2. “Stabilization of the Trigonal High-Temperature Phase of Formamidinium Lead Iodide”

A. Binek, F. C. Hanusch, P. Docampo, T. Bein, *The Journal of Physical Chemistry Letters* **2015**, 6, 1249-1253.
3. “Control of Perovskite Crystal Growth by Methylammonium Lead Chloride Templating”

A. Binek, I. Grill, N. Huber, K. Peters, A. G. Hufnagel, M. Handloser, P. Docampo, A. Hartschuh, T. Bein, *Chemistry – An Asian Journal* **2016**, 11, 1199-1204.
4. “Synthesis of Perfectly Oriented and Micrometer-Sized MAPbBr₃ Perovskite Crystals for Thin-Film Photovoltaic Applications”

N. Giesbrecht, J. Schlipf, L. Oesinghaus, A. Binek, T. Bein, P. Müller-Buschbaum, P. Docampo, *ACS Energy Letters* **2016**, 1, 150-154.

11.3 Oral presentations

5. „Recycling Perovskite Solar Cells To Avoid Lead Waste”

A. Binek, M. L. Petrus, N. Huber, H. Bristow, Y. Hu, T. Bein, P. Docampo, *ACS Applied Materials & Interfaces* **2016**, 8, 12881-12886.

6. “Two-step vs. One-step Deposition: Optimizing Transport Properties of Perovskite Solar Cells”

K. Handloser, I. Grill, F. C. Hanusch, N. Giesbrecht, A. Binek, Y. Hu, T. Bein, P. Docampo, M. L. Petrus, M. Handloser, A. Hartschuh,
manuscript submitted to *ACS Energy Letters*

11.2 Journal Cover

Cover Picture in *Chemistry – An Asian Journal* for the special issue “Energy Storage and Conversion” **2016**, 11, 1117.

11.3 Oral presentations

1. “Stabilization of the Trigonal High-Temperature Phase of Formamidinium Lead Iodide”

Andreas Binek, Fabian C. Hanusch, Pablo Docampo, Thomas Bein,

International Conference on Hybrid and Organic Photovoltaics (HOPV), **2015**, Rome, Italy.

2. “Bringing Perovskite Solar Cells One Step Closer to Commercial Application”

Andreas Binek, Pablo Docampo, Thomas Bein

Soltech Excursion, **2016**, Nürnberg, Germany.

3. “Controlling the crystal growth and phase stability of hybrid organo-halide perovskite for the commercial application in solar cells”

Andreas Binek, Irene Grill, Niklas Huber, Fabian C. Hanusch, Kristina Peters, Alexander G. Hufnagel, Matthias Handloser, Pablo Docampo, Achim Hartschuh and Thomas Bein

NIM Winter School, **2016**, Tirol, Austria.

4. “Control of Perovskite Crystal Growth by Methylammonium Lead Chloride Templating”

Andreas Binek, Irene Grill, Niklas Huber, Kristina Peters, Alexander G. Hufnagel, Matthias Handloser, Pablo Docampo, Achim Hartschuh, and Thomas Bein

International Conference on Hybrid and Organic Photovoltaics (HOPV), **2016**, Swansea, United Kingdom.

5. “Control of Perovskite Crystal Growth by Methylammonium Lead Chloride Templating”

Andreas Binek, Irene Grill, Niklas Huber, Kristina Peters, Alexander G. Hufnagel, Matthias Handloser, Pablo Docampo, Achim Hartschuh, and Thomas Bein

MRS Fall Meeting & Exhibit, **2016**, Boston, USA.

11.4 Poster presentations

1. “Solution Deposition-Conversion for Planar Heterojunction Mixed Halide Perovskite Solar Cells”

Fabian Hanusch, Pablo Docampo, Andreas Binek, Samuel D. Stranks, Markus Döblinger, Johann M. Feckl, Michael B. Johnston, Henry Snaith, Thomas Bein

International Conference Solution Processed Semiconductor Solar Cells (SSSC), **2014**, Oxford, United Kingdom.

2. “Stabilization of the Trigonal High Temperature Phase of Formamidinium Lead Iodide”

Andreas Binek, Fabian C. Hanusch, Pablo Docampo, Thomas Bein

Soltech Workshop, **2015**, Kloster Banz, Germany.

3. “Controlling the crystal growth and phase stability of hybrid organo-halide perovskite for the commercial application in solar cells”

Andreas Binek, Irene Grill, Niklas Huber, Fabian C. Hanusch, Kristina Peters, Alexander G. Hufnagel, Matthias Handloser, Pablo Docampo, Achim Hartschuh and Thomas Bein

NIM Winter School, **2016**, Tirol, Austria.

4. “Recycling of Perovskite Solar Cells Reducing Environmental Impact and Production Costs”

Andreas Binek, Michiel L. Petrus, Niklas Huber, Helen Bristow, Pablo Docampo and Thomas Bein

Soltech Workshop, **2016**, Munich, Germany.